Transactions of the ASME

The Journal of Fluids Engineering (ISSN 0098-2202) is published quarterly for $100 per year by The American Society of Mechanical Engineers, 345 East 47th Street, New York, NY 10017. Second class postage paid at New York, NY and additional mailing offices. POSTMASTER: Send address changes to The Journal of Fluids Engineering, c/o THE AMERICAN SOCIETY OF MECHANICAL ENGINEERS, 22 Law Drive, Box 2300, Fairfield, NJ 07007-2300.
CHANGES OF ADDRESS must be received at Society headquarters seven weeks before they are to be effective. Please send old label and new address.
PRICES: To members, $24.00, annually: to nonmembers, $100. Add $6.00 for postage to countries outside the United States and Canada.
STATEMENT from By-Laws. The Society shall not be responsible for statements or opinions advanced in papers or . . . printed in its publications (B7.1, Par. 3),

INDEXED by the Engineering Index, Inc.

Journal of Fluids Engineering

Published Quarterly by The American Society of Mechanical Engineers

VOLUME 107 • NUMBER 3 • SEPTEMBER 1985

(Contents continued on page 306)

Contents (Continued)

Vortex Shedding From Bluff Bodies in a Shear Flow: A Review

Owen M. Griffin
Marine Technology Division,
Naval Research Laboratory (Code 5841),
Washington, DC 20375
Fellow ASME

This paper examines the effects of velocity shear on vortex shedding from stationary and vibrating bluff bodies. Experiments with circular cylindrical bodies and other cross sections such as D*-section cylinders and rectangular cylinders, which were limited to conditions with length/diameter ratios less than* L/D = *15 to 20, have shown that the spanwise cellular structure of the vortex shedding is dependent upon end conditions. The vortex shedding also is influenced strongly by the shear flow steepness parameter* $\bar{\beta}$ *which is based upon the incident flow velocity gradient. Experimental evidence is available to show that moderate shear levels of practical importance* ($\bar{\beta} \sim 0.01$ *to* 0.015) *do not appreciably decrease the probability of occurrence of vortex-excited oscillations for flexible structures and cables. The effects of incident shear on vortex shedding from stationary and vibrating bluff structures in both fluid media should be investigated further for long cylinders which have minimal end boundary effects. More definitive bounds for and details of this fluid-structure interaction are needed for applications in the wind engineering design of buildings and structures, and in the design of marine structures and cable systems.*

Introduction

If a fluid is in relative motion past a stationary bluff, or unstreamlined, structure and the vortex shedding frequency approaches one of the natural frequencies of the structure, then resonant flow-induced oscillations of the cylinder can occur when the damping of the system is sufficiently low. These resonant oscillations are accompanied by a "lock-on" or capture of the vortex shedding frequency by the vibration frequency over a range of flow speeds, and this lock-on effect causes the wake and the structure to oscillate in unison. The periodic lift and the mean drag forces are amplified as a result of these vibrations, and changes in these fluid forces are closely related to the changes that occur in the flow field in the near wake of the body. Many practical applications involve lightly damped structures which are situated in flows of air or water that are nonuniform along the length of the structure, e.g., see reference [1]. The primary difference between a uniform flow and a shear flow is the presence and added complexity, in a shear flow, of vorticity whose vector is normal to the plane of the flow. When the incident flow approaches the body this vorticity is turned in direction and it interacts with the vortices which are shed from the body into the wake.

The purpose of this paper is to examine the general problem of the flow about bluff bodies in a shear flow in light of the present state of knowledge for these flows. Experiments with circular cylinders are emphasized, although references also are made to experiments conducted with cylinders having other cross sections such as *D*-section cylinders and rectangular cylinders. Some recent experiments with flexible cables in a shear flow are discussed.

Comments are given concerning the limitations of the work that has been done thus far, and recommendations of possible avenues for future research also are given.

Background and Relevant Parameters

A number of papers which treat various aspects of unsteady flow phenomena and, in particular, the vortex-excited oscillations of bluff bodies and the equivalent forced vibrations have recently appeared. These include the proceedings of two international symposia on flow-induced structural vibrations [2, 3]. Sarpkaya [4] and Bearman [5] recently have reviewed the basic characteristics of vortex shedding as related to vortex-excited oscillations. Griffin and Ramberg [6] have discussed the same topics in the context of marine applications.

Early studies of shear flow past bluff bodies were undertaken by Masch and Moore [7] and by Shaw and Starr [8, 9] and showed the potential importance of characterizing the nonuniform flow in terms of a "steepness or shear parameter" for the incident velocity gradient. The steepness parameter now is defined by

$$\bar{\beta} = \frac{D}{\bar{V}_{\mathrm{REF}}} \frac{d\bar{V}}{d\bar{z}}, \tag{1}$$

where the velocity gradient is given by $d\bar{V}/d\bar{z}$ and the cylinder diameter or other representative transverse dimension by D. The reference velocity $\bar{V}_{\mathrm{REF}}$ is the midspan incident velocity on a finite-length body or it is the velocity at the center of a wind tunnel or water channel. Typical experimental test setups and coordinate systems are sketched in Fig. 1.

Contributed by the Fluids Engineering Division for publication in the JOURNAL OF FLUIDS ENGINEERING. Manuscript received by the Fluids Engineering Division, January 5, 1983; final revision, November, 1984.

Another important parameter to be considered in shear flow experiments is L/D, the ratio of length-to-diameter of the cylinder. Many of the shear flow experiments have been conducted with cylinders of relatively small aspect ratios ($L/D<20$), so that end boundary effects usually were important. Additional important parameters are the Reynolds number $\mathrm{Re} = \bar{V}_{\mathrm{REF}} D/\nu$ and the relative roughness parameter δ/D, where δ is the surface roughness of the cylinder. A roughness Reynolds number can be defined by $\mathrm{Re}_\delta = \bar{V}_{\mathrm{REF}} \delta/\nu$.

In the sections of the paper that follow, reference often is made to the subcritical, critical and supercritical ranges of the Reynolds number. This terminology applies to the circular cylinder where the drag crisis occurs for $\mathrm{Re} \sim 10^5$. These various ranges of Re do not apply, however, to bluff bodies with fixed separation points (rectangular cylinders, for example) where the vortex formation process is relatively uninfluenced by the Reynolds number.

A shear flow can be generated in flowing air or water in a number of ways. The various methods which have been employed thus far are listed as follows:

Curved Screen (air): [10–12, 14, 16, 23, 25];
Array of Rods (air): [13, 15, 18];
Array of Screens (air): [22, 24, 26];
Boundary Layer (air): [13, 17, 29, 32];
Array of Screens (water): [8, 9, 30, 31];
Screen and Mesh (water): [8, 9].

The Characteristics of Shear Flow Past Stationary Bluff Bodies

The essential characteristics of shear flow past bluff bodies now are known in reasonable detail. These conditions are somewhat limited in that most experiments have been concerned with wind-tunnel studies of vortex shedding from relatively short ($L/D<20$), stationary circular cylinders, D-shaped cylinders, and rectangular cylinders. A few studies of shear effects on the flow past circular cylinders have been made in water. All of the work reported thus far has been experimental in nature. The ability to realistically model a turbulent, three-dimensional, high Reynolds number bluff body flow is still beyond the capabilities of existing numerical fluid dynamics algorithms and computational resources.

From all of these experiments the following general features of velocity shear effects have been identified thus far in some detail [21]:

(*i*) The vortex shedding from a D-shaped bluff body takes place in spanwise cells, with the frequency constant over each cell. The Strouhal number is constant for each cell when it is based on the body diameter and a characteristic velocity. The latter is usually the velocity measured at the body's half-span [10, 11].

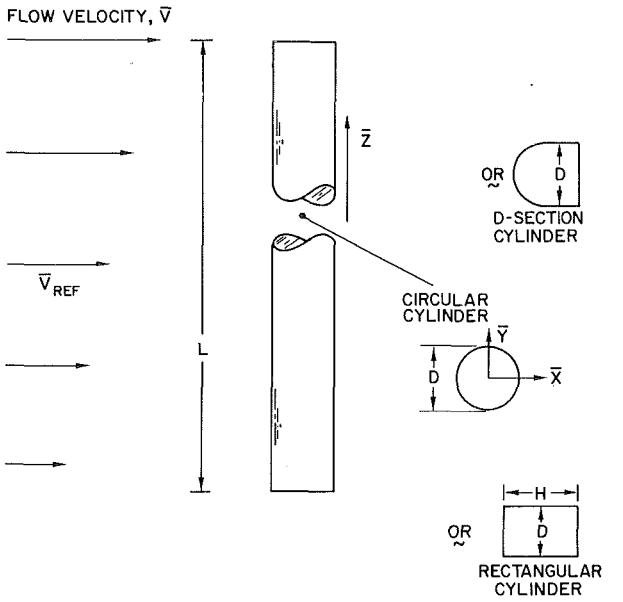

Fig. 1 Typical experimental arrangements for studying shear flow effects on vortex shedding from bluff bodies

(*ii*) The cellular vortex shedding pattern likewise is found for the case of circular and rectangular cylinders spanning a wind tunnel [12, 14, 18, 22]. The number of cells, however, is strongly dependent upon the aspect ratio (L/D) of the cylinder, end effects, etc. [12, 14, 18].

(*iii*) The base pressure or drag force variation along a circular cylinder is dependent on the aspect ratio (L/D) of the body and is highly sensitive to end conditions [12, 17, 18, 22]. The effects of the end condition become more pronounced when the body has a free end and does not completely span the wind tunnel [17].

(*iv*) When the shear flow is highly turbulent ($v'/V \sim 5$ percent or greater), a reduction in the critical Reynolds number by a factor of ten has been observed in the case of a circular cylinder [18]. The effects of the linear shear flow in reducing the critical Reynolds number are similar to a uniform flow of high turbulence level. The shear flow "steepness parameter" was $\bar{\beta} = 0.18$ in these experiments. In another study of the flow around a rectangular cylinder in a highly turbulent stream ($v'/V \sim 10$ percent) the steepness parameter was $\bar{\beta} = 0.09$ to 0.11, also relatively high values [15]. The transition between vortex shedding cells took place over a greater length of the cylinder than for comparable low

Nomenclature

D = cylinder diameter or characteristic dimension (m)
f = vibration frequency (Hz)
f_n = natural frequency of vibration (Hz)
f_s = Strouhal frequency (Hz)
H = width or chord of rectangular cylinder (m)
k_s = reduced damping parameter, $2m\delta/\rho D^2$
L = cylinder length (m)
m = cylinder mass per unit length (kg/m)
Re = Reynolds number, $\bar{V}D/\nu$
St = Strouhal number, $f_s D/\bar{V}$
v' = turbulence level (m/s)
$\bar{V}$ = mean flow velocity (m/s)
$\bar{V}_{\mathrm{REF}}, \bar{V}_M$ = reference mean flow velocity (m/s)
V_r = reduced velocity parameter, $\bar{V}/f_n D$
$\bar{Y}$ = cylinder amplitude of crossflow displacement (m)
$\bar{z}$ = spanwise distance (m)
$\bar{\beta}$ = shear flow steepness parameter $(D/\bar{V}_{\mathrm{REF}})(d\bar{V}/d\bar{z})$
δ = surface roughness (m) or log decrement of structural damping
ν = fluid kinematic viscosity (m^2/s)
ρ = fluid density (kg/m^3)
ζ_s = structural damping ratio

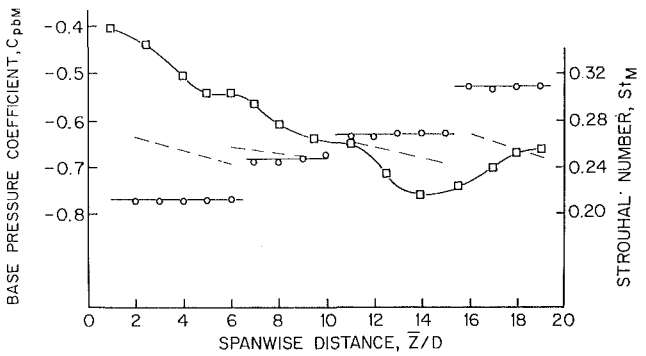

Fig. 2 Base pressure coefficient C_{pbM} and Strouhal number St_M (based upon the centerline velocity $\bar{V}_M$) plotted against the spanwise distance along a D-section cylinder in a linear shear flow; from Maull and Young [11]. Reynolds number $Re_M = 2.8 \times 10^4$; shear flow steepness parameter $\bar{\beta} = 0.025$; cylinder chord/thickness ration $H/D = 6$. Base pressure, □; Strouhal number, 0. Reprinted with permission of the Cambridge University Press.

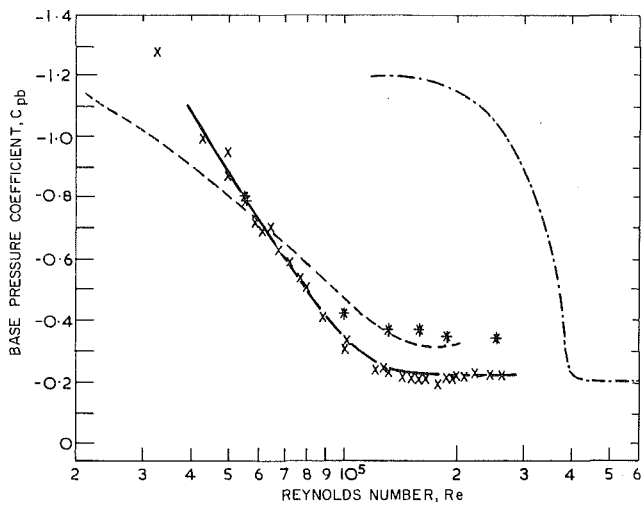

Fig. 3 Base pressure coefficient C_{pbM} at the centerline plotted against the Reynolds number Re_M for a circular cylinder in a shear flow; from Davies [18]. Legend for data: x, centerline value, C_{pbM} ($\bar{\beta} = 0.18$); ···, uniform smooth flow; ----, uniform turbulent flow (Bearman, 1968); *, average value ($\bar{\beta} = 0.18$).

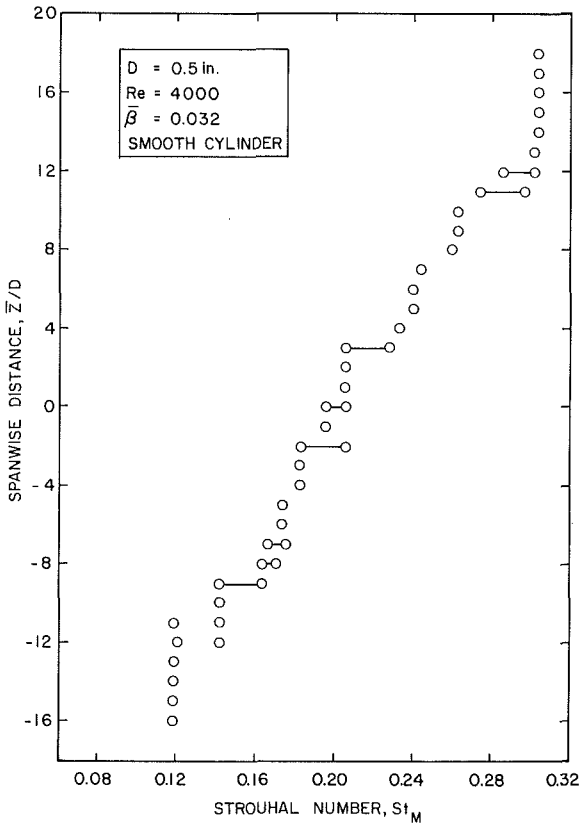

Fig. 4 Strouhal number St_M (based upon the centerline velocity V_M) plotted against the spanwise distance along a circular cylinder in a shear flow; from Woo, Peterka and Cermak [23]

turbulence shear flows. The peaks in the high-turbulence frequency spectra also were much broader.

(*v*) Surface-roughened circular cylinders also exhibit the characteristic cellular vortex shedding pattern in low and moderate-turbulence shear flows [22]. This was observed for both subcritical ($Re < 2\text{-}3 \times 10^5$) and supercritical ($Re > 3 \times 10^6$) Reynolds numbers, with a wide range of steepness parameters, $\bar{\beta} = 0.007$ to 0.04. Any linear shear (as low as $\bar{\beta} = 0.007$) was found to trigger a lengthwise cellular vortex shedding pattern. A general trend toward decreasing cell length with increasing shear and an increase in the average cell length with cylinder roughness was found.

(*vi*) The tendency for strong cells to form usually is highest at the end boundaries of short L/D cylinders. Experiments with cylinders of long aspect ratio ($L/D = 20$ to 50 and larger) have demonstrated in one case no discernible cell structure away from the end influences at subcritical Reynolds number [24] or in another case a slight and irregular cell structure at high shear levels of $\bar{\beta} > 0.005$ [23]. Carefully conducted experiments with a long flexible cable ($L/D \approx 100$) have shown that a discernible cell structure existed at moderate subcritical Reynolds numbers when $\bar{\beta} = 0.005$ [26].

(*vii*) Shear in the flow incident upon a circular cylinder also has an effect on the vortex shedding when the axis of the cylinder is normal to the plane of the shear profile. However, larger values of the steepness parameter $\bar{\beta}$ are required for the shear to have a discernible effect [27].

Some typical results now are discussed in order to document the summary just given. In one of the earliest studies of shear flow past bluff bodies, Maull and Young [10, 11] conducted wind-tunnel experiments to measure the vortex shedding from a D-section cylinder with a blunt base. The base pressure coefficient C_{pbM} and the Strouhal number St_M based upon the centerline velocity $\bar{V}_M$ are shown in Fig. 2. The vortex shedding took place in four cells of constant frequency along the span of the cylinder. One cell extends from $\bar{z}/D = 0$ to 6 and the second from $\bar{z}/D = 7$ to 10. The third cell extends from $\bar{z}/D = 10$ to 15 and the last appears at $\bar{z}/D = 16$.

Frequency spectra showed that cell boundary regions ($\bar{z}/D = 7$, as one example) were marked by two characteristic frequencies, one from each of the adjacent cells. The variation of the base pressure in Fig. 2 shows marked changes at the cell boundaries, with noticeable variations in the C_{pbM} versus $\bar{z}/D$ curve at $\bar{z}/D = 6$ and 10. Within each vortex shedding cell the frequency of shedding was constant while the base pressure varied along the span of the cylinder. A study of flow visualization photographs by Maull and Young indicated that the cells were divided by longitudinal vortices aligned with the free-stream direction [11].

The effect of a highly turbulent incident shear flow on the vortex shedding from a circular cylinder was studied by Davies [18]. The steepness parameter of the flow was quite high, $\bar{\beta} = 0.18$, and the turbulence level was about $v'/V = 5$ percent. End plates were fitted to the cylinder at $\pm 3\,D$ from the centerline of the wind tunnel. The base pressure coefficient at the midspan location on the cylinder is plotted against the Reynolds number in Fig. 3. It is clear that the onset of the critical Reynolds number is reduced in the shear flow by a factor of ten from the uniform smooth flow value

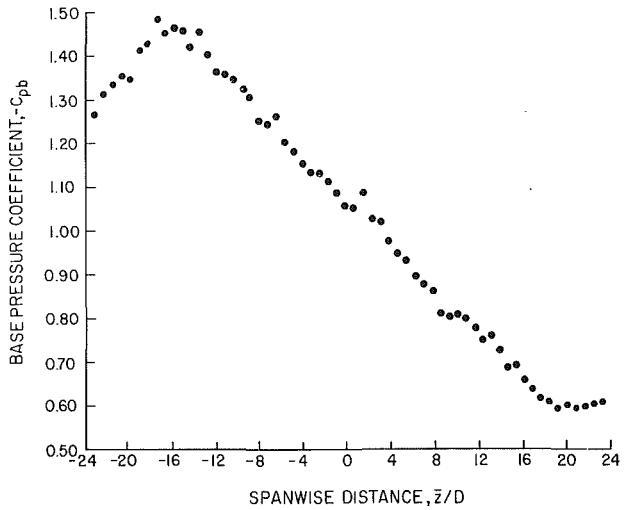

Fig. 5 Spanwise variation of the base pressure coefficient C_{pb} on a rough circular cylinder in a shear flow; from Peltzer and Rooney [24]. Reynolds number $Re_M = 2(10^4)$, shear flow steepness parameter $\bar{\beta} = 0.015$.

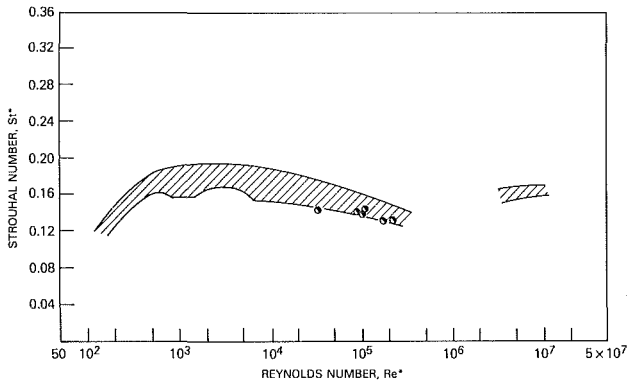

Fig. 6 Universal Strouhal number St* versus the Reynolds number Re*. Shaded region (assorted stationary and vibrating bodies and flow conditions) from Griffin [20]; data points, ϑ, from Peltzer and Rooney [24].

$Re = 2$ to 3×10^5. The reduction in Re_{crit} is similar to that produced by a uniform flow of the same turbulence intensity.

For subcritical conditions a well-defined cell structure with a predominant wake frequency and strong vortex shedding was observed by Davies. Both the base pressure coefficients based on local velocity and the midspan value gave a clear picture of the cell boundaries. The shedding patterns became more irregular as the incident flow velocity was increased, and by $Re = 10^5$ any trace of a vortex shedding peak had disappeared into the turbulent background of the frequency spectrum. The small aspect ratio of the cylinder in this experiment ($L/D = 6$) almost certainly resulted in strong end effects on the cellular structure of the shear flow.

Woo, Peterka, and Cermak [23] have conducted experiments to study the vortex shedding from large aspect-ratio (L/D up to 128), stationary and vibrating circular cylinders and flexible cables in a linear shear flow. Figure 4 shows the Strouhal number based on centerline velocity for $L/D = 34$, $\bar{\beta} = 0.032$ and $Re = 4000$. This figure indicates the presence of two cells at the boundaries and shows a tendency toward a cellular vortex pattern over the central section of the stationary cylinder that probably is free of end effects. Regions with a similar frequency can be identified over a limited distance, but it is not clear that cells with well-defined boundaries exist. When the data from Fig. 4 are presented as Strouhal numbers based on the local velocity [23], the data are grouped around Strouhal numbers of 0.2 to 0.21. There is a weak cell structure, but no clear cell boundaries can be identified in many regions.

The effects of shear on vortex shedding from smooth and rough circular cylinders of relatively high aspect ratio ($L/D = 27$ and 48) at subcritical Reynolds numbers were examined by Peltzer and Rooney [24]. Experiments were conducted at $Re = 2 \times 10^4$ to 1.2×10^5 and at $\bar{\beta} = 0$ to 0.026. The distribution of the base pressure coefficient $-C_{pb}$ along an $L/D = 48$ cylinder with roughness $\delta/D = 0.001$ is shown in Fig. 5. This result is typical in that end effects were apparent adjacent to the end plates of the cylinder. However, at $|\bar{z}/D| < 16$, no cell pattern was observed and the base pressure varied linearly along the cylinder. A similar linear variation also was measured for the Strouhal number St_M, except for $\bar{z}/D = +4$ to $+8$ where a single cell was observed. In general, the vortex shedding patterns were free of constant frequency cells except for short sections adjacent to the end boundaries.

The experiments conducted by Peltzer and Rooney included simultaneous measurements of the Strouhal number, the base pressure coefficient $-C_{pb}$ and the wake width D'. From these parameters the universal Strouhal number [20]

$$St^* = \frac{f_s D'}{V_s} = \frac{St}{K}\left(\frac{D'}{D}\right)$$

can be estimated. Here $K = V_s/V = \sqrt{1 - C_{pb}}$ and St is the usual form of the Strouhal number. St* is plotted against the wake Reynolds number

$$Re^* = \frac{V_s D'}{\nu} = Re\, K\left(\frac{D'}{D}\right)$$

in Fig. 6. The individual data points represent the measurements of Peltzer and Rooney and they are in reasonably good agreement with previous data given by Griffin [19, 20]. The data shown by the shaded region all were measured in uniform flow over a host of stationary and vibrating two-dimensional bluff body cross sections.

It has been pointed out to the author (A. A. Szewczyk, private communication, 1981) that the universal Strouhal number-Reynolds number relationship is not valid when there are appreciable three-dimensional or secondary flow effects in the wake due to the shear flow past the cylinder. Agreement similar to that shown in Fig. 6 is not obtained when the flow in the wake is highly three-dimensional.

As an example, Elsner [25] has investigated the wake flow behind and the pressure distribution on a rectangular cylinder ($L/D = 7$) in a highly sheared flow ($\bar{\beta} = 0.08$ to 0.09). The experiments were conducted in a low turbulence flow ($v'/V \sim 0.05$ percent) at Reynolds numbers from $Re_M = 10^4$ to 8×10^4. Base pressure and drag coefficients were measured along with the wake width D', the local vortex shedding frequency f_s, and the vortex formation region length. The findings from the experiments indicated that no universal Strouhal number St* existed for the highly sheared flow since St* varied continuously along the span of the model.

It was observed by Elsner, from a study of his and previous investigations, that the length of a vortex shedding cell or filament was limited physically to about 5 dia. The idea of a limiting length for the cells is supported by the results of Peltzer and Rooney [22, 24].

Kiya, Tamura and Arie [27] studied the problem of vortex shedding from a circular cylinder when the axis of the cylinder was normal to the plane of the linear velocity shear. For this configuration the shear flow is not affected by the aspect ratio of the cylinder, in this case $L/D = 2$ to 12.5. Blockage corrections were made to take account of confinement effects at the small L/D. The shear parameter $\bar{\beta}$ was defined in the same way as in the present paper and varied from $\bar{\beta} = 0$ to

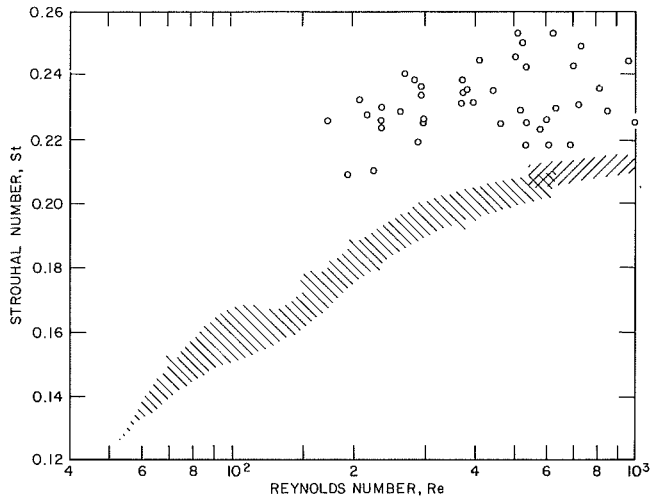

Fig. 7 Strouhal number versus Reynolds number for shear flow, $\bar{\beta} = 0.20$. 0, Kiya, Tamura, and Arie [27]; \\\\, Kiya, Tamura, and Arie [27], uniform flow; ////, Roshko's (1954) data for uniform flow in the range $Re > 550$. Reprinted with permission of the Cambridge University Press.

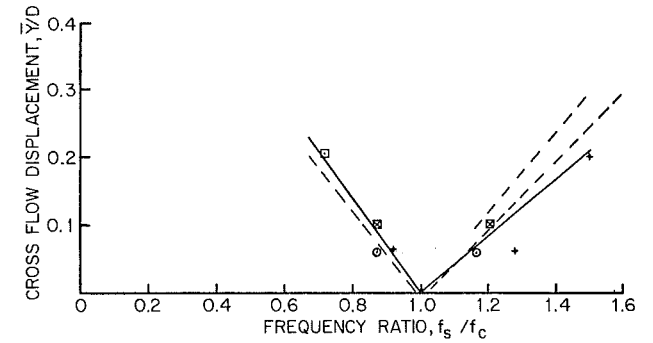

Fig. 8 Boundaries of the crossflow lock-on regime in a shear flow, denoted by the displacement amplitude $\bar{Y}/D$ on the vertical scale, plotted against the ratio f_s/f_c of the Strouhal and vibration frequencies; from Stansby [16]. Reprinted with permission of the Cambridge University Press. Legend for data points: □, $St_{M,c} = f_c D/V_M = 0.168$, $L/D = 9$, $Re_M = 9100$; 0, $St_{M,c} = 0.198$; +, $St_{M,c} = 0.155$ $L/D = 16$, $Re_M = 3700$; □, $St_{M,c} = 0.174$; ---, uniform flow.

0.25. However, the physical meaning of β is obviously different since the velocity gradient is rotated 90 deg from the cases discussed here thus far. A shear parameter of $\bar{\beta} = 0.05$ has little or no effect on the vortex shedding frequency for this case.

When the shear parameter was increased to $\bar{\beta} = 0.2$ the Strouhal number was increased substantially relative to the uniform flow case as shown in Fig. 7. The shear flow results are superimposed over corresponding uniform flow measurements by Kiya, et al., and by Roshko [28]. There also is considerable scatter among the data for St_M at any given Reynolds number. It was concluded generally by Kiya, et al., that shear in the incident flow profile had little or no effect for $\bar{\beta} < 0.1$. At higher values of $\bar{\beta}$ shear effects became more pronounced as shown in Fig. 7.

The Effects of Body Oscillations

The combined effects of velocity gradients and body oscillations are even more difficult to interpret quantitatively. However, the information that does exist suggests that both model and full-scale cylindrical structures certainly will vibrate at large amplitudes of displacement in both air and water even in the presence of nonuniform flow effects when the reduced damping is sufficiently small and the critical reduced velocity is exceeded. The reduced velocity $V_r = V/f_n D$ is the reciprocal of the Strouhal number based upon the cylinder's natural frequency f_n. Some extensive experiments reported by Kwok and Melbourne [29] give strong evidence that a flexible bluff structure with a circular cross section will resonantly vibrate at large displacement amplitudes when a

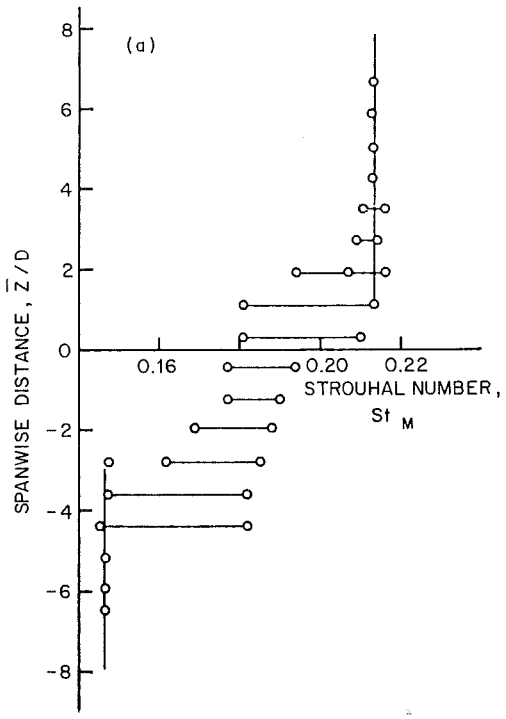

Fig. 9(a) Stationary cylinder. Reynolds number $Re_M \approx 4000$, shear flow steepness parameter $\bar{\beta} = 0.025$, cylinder aspect ratio $L/D = 16$.

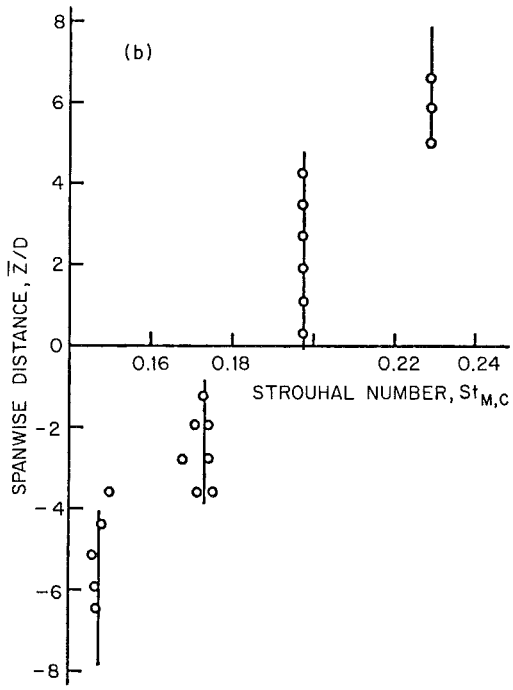

Fig. 9(b) Vibrating cylinder. Same conditions as Fig. 9(a) except that the forced Strouhal number of the crossflow oscillations is $St_{M,c} = 0.198$, displacement amplitude $\bar{Y}/D = 0.06$.

Fig. 9 Strouhal number St_M plotted against the spanwise distance along stationary and vibrating cylinders; from Stansby [16]. Reprinted by permission of the Cambridge University Press.

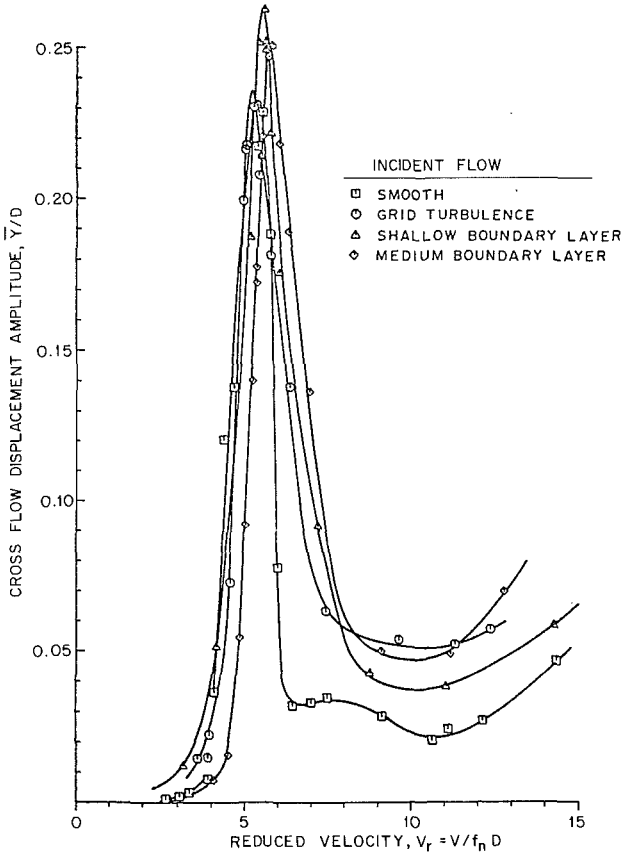

Fig. 10 Peak crossflow displacement amplitude $\bar{Y}/D$ (root-mean-square of $\bar{Y}$) plotted against reduced velocity V_r for a flexibly mounted circular cylinder in uniform and sheared incident flows; from Howell and Novak [32]. Structural damping ratio $\zeta_s = 0.01$; aspect ratio $L/D = 10$. The figure was provided by Dr. John F. Howell, VIPAC Ltd., South Yarra, Vic., Australia.

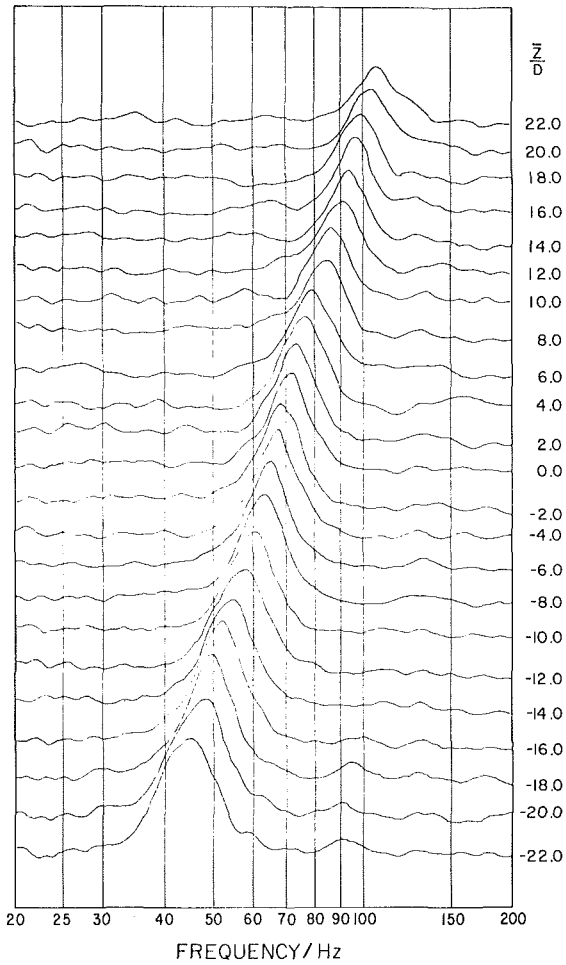

Fig. 11 Frequency spectra at various spanwise locations for a stationary cylinder with $D = 0.25$ in; $L/D = 40$; Re = 735; $\bar{\beta} = 0.016$; from Woo, Peterka, and Cermak [23]

turbulent boundary-layer type of shear flow is incident upon the cylinder.

Stansby [16] investigated the phenomenon of lock-on for the crossflow vibrations of circular cylinders in a linear shear flow and has compared the results to similar experiments in uniform flow. From these experiments Stansby developed empirical equations to predict the bounds for lock-on in a shear flow, based upon the assumption of universal similarity of the flow in the wakes of bluff bodies [19, 20]. The boundaries of the crossflow lock-on regime that were measured by Stansby are shown in Fig. 8. The bounds of the lock-on are in good agreement with comparable measurements made by others; see Sarpkaya [4] and Bearman [5], for example.

The measured Strouhal numbers for stationary and vibrating circular cylinders in a shear flow are compared in Fig. 9. The measurements were reported by Stansby [16] for $\mathrm{Re}_M \approx 4000$ and $\bar{\beta} = 0.025$. The stationary cylinder wake is dominated by two end cells with an irregular type of vortex shedding between these cells. This irregular region is characterized by a wide frequency spectrum which represents a range of cell shedding conditions, and the Strouhal number ranges in Fig. 9(*a*) define the ranges of possible constant-frequency vortex shedding cell formation. When the same cylinder was oscillated at a forced Strouhal number of $\mathrm{St}_{M,C} = 0.198$, the vortex shedding over the center portion of the cylinder was dominated by a single cell from $\bar{z}/D = -1$ to $+4$ that was locked to the vibration frequency as shown in Fig. 9(*b*). The three unforced cells that are distributed along the cylinder show considerably more regularity in shedding frequency than do the corresponding cells on the stationary cylinder.

A recent paper and a report by Fischer, Jones, and King [30, 31] describe some problems that were anticipated during the installation of foundation piles for the Shell Oil production platform in the Cognac field of the Gulf of Mexico. It is clear from the results obtained by Fischer, et al., that a shear flow with $\bar{\beta} = 0.01$ to 0.015 had virtually no effect on the vortex-excited displacement amplitudes in the crossflow direction from the comparable uniform flow results ($\bar{Y} = \pm$ to $1.5\,D$).

Experiments with flexibly mounted cylinders in uniform and shear flows were conducted in a wind tunnel by Howell and Novak [32]. Examples of the cylinder vibrations in four types of incident wind flows are shown in Fig. 10. The character of the shear had little or no effect on the peak response of the cylinder. As the damping ratio was increased to values higher than the one ($\zeta_s = 0.01$) corresponding to the results in Fig. 10, the displacement response of the flexibly mounted cylinders was influenced by the characteristics of the incident flow to the cylinder. The measured displacement amplitudes compare very well with those found by other investigators (a full summary and comparison is given by Griffin and Ramberg in reference [6]), and full lock-on was observed by Howell and Novak for this cylinder with $\zeta_s = 0.01$ and $\bar{Y}/D \approx 0.25$.

A number of other studies with circular, square and rectangular cross section models are discussed in *Proceedings of the Fifth International Conference on Wind Engineering*, held in 1979 [33], and the *Proceedings of the Fourth International Conference on Wind Effects on Buildings and Structures*, held in 1975 [34].

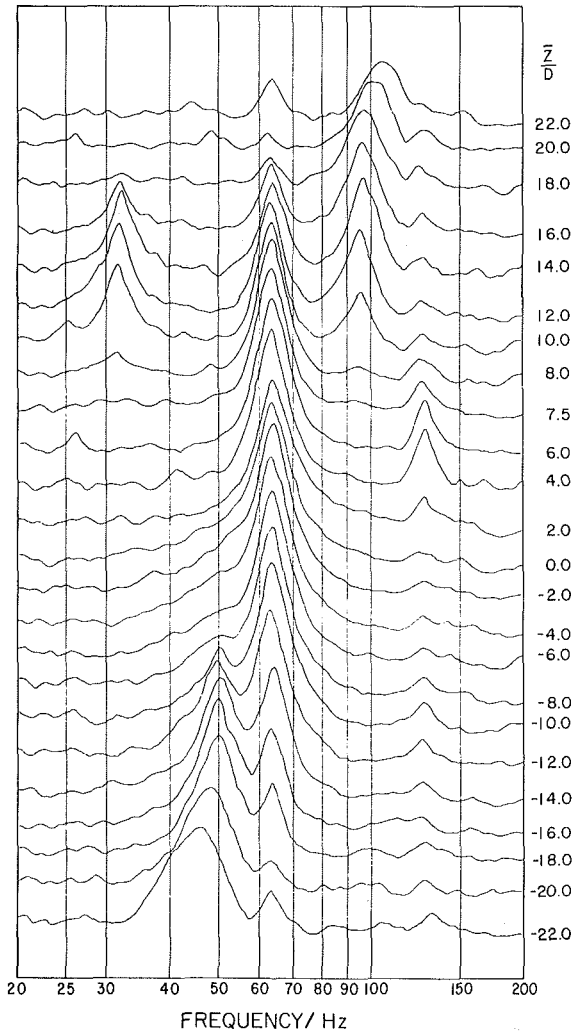

Fig. 12 Frequency spectra at various spanwise locations for an oscillating cylinder with $D = 0.25$ in.; $L/D = 40$; $2\bar{Y}/D = 0.47$; Re = 735; $\beta = 0.016$; from Woo, Peterka, and Cermak [23].

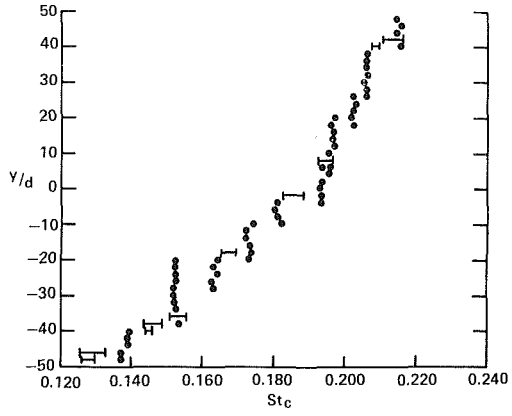

Fig. 13 Strouhal number St_M plotted against spanwise distance along a stationary flexible cable in a linear shear flow; from Peltzer [26]. Reynolds number $Re_M = 2.96 \times 10^3$, shear flow steepness parameter $\hat{\beta} = 0.0053$.

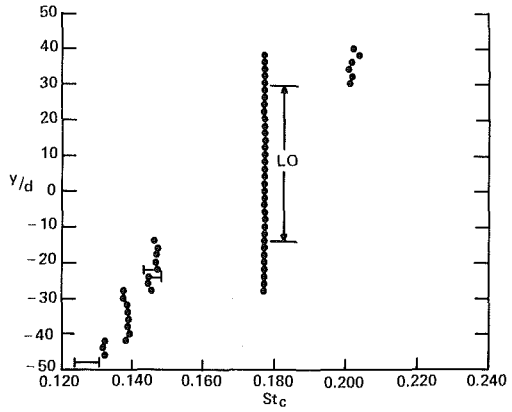

Fig. 14 Strouhal number St_M plotted against spanwise distance along a vibrating flexible cable in a linear shear flow; from Peltzer [26]. Reynolds number $Re_M = 2.96 \times 10^3$, shear flow steepness parameter $\hat{\beta} = 0.0053$, reduced velocity $V_r = 5.6$, displacement amplitude (first mode) $2\bar{Y} = 0.29D$.

An experimental study of the effects of shear on vortex shedding from flexible cables was conducted by Woo, et al. [23]. These experiments were conducted at Reynolds numbers from Re = 700 to 1700 with cables that were forced to oscillate in shear flows with steepness parameters from $\hat{\beta} = 0$ to 0.036. Some typical examples of the results that they obtained with a small-diameter smooth cable (large L/D) are given in Figs. 11 and 12. The frequency spectra from the wake of a stationary cable in a shear flow in Fig. 11 show no cell structure, and the frequency of the vortex shedding appears to vary linearly over the entire span ($L = 40\ D$) of the cable.

When the cable was vibrated normal to the flow at about 88 percent of the center-span shedding frequency and at about a half-diameter (peak-to-peak), the vortex shedding frequency spectra were altered as shown in Fig. 12. There is a lock-on region at a single (vortex shedding and vibration) frequency f from about $\bar{z} = 8\ D$ to $\bar{z} = -4D$, or $\Delta\bar{z} \simeq 12\ D$. For $\bar{z} < -4\ D$ clear peaks are present in the frequency spectra of the local shedding frequency and the vibration frequency (no lock-on). For $z > 8\ D$ again the spectra contain clear peaks at both the local vortex shedding frequency and the vibration frequency. Many of the spectra contain a distinct frequency contribution at the second harmonic $2f$ and some ($z = 8.5\ D$ to $16\ D$) contain an apparent contribution at the difference $(f_{s,z} - f)$ between the local shedding frequency $f_{s,z}$ and the vibration frequency f. Other experiments by Woo, et al. [23] with short cylinders (small L/D) clearly showed the influence of end boundary effects.

Experiments also were conducted by Peltzer [26] to simulate the effects of velocity shear on vortex shedding from stationary and vibrating marine cables. The spanwise Strouhal number variation along the stationary cable in the shear flow is shown in Fig. 13. There are ten cells of constant Strouhal number along the cable span. There is a total change in Strouhal number of $\Delta St_M = 0.067$ over the length of the cable. The clarity of the cellular structure is due to a careful optimization of the location of the hot-wire probe that was used to sense the frequency of vortex shedding from the cable.

The cable was oscillated in its first mode with an antinodal displacement amplitude of $2\bar{Y} = 0.29\ D$ and at a reduced velocity of $V_r = 5.6$. The vortex shedding pattern in Fig. 13 was changed by the oscillations as shown in Fig. 14. The vortex shedding was locked-on to the cable vibration over the central portion of the span from $-14 \le \bar{z}/D \le 30$, so that the locked-on cell was 44-cable-dia long. The remainder of the vortex shedding pattern not influenced by end effects was stabilized as well. Two cells were increased in length to 14 dia each and no fluctuations in the cell boundaries were observed. The change in the Strouhal number across the span was increased to $\Delta St_M = 0.078$ [26].

A recent paper on this subject by Whitney and Nikkel [1] concerns the development of a structural algorithm model for predicting the response of and stresses in long marine risers in shear current profiles. This paper is interesting because it

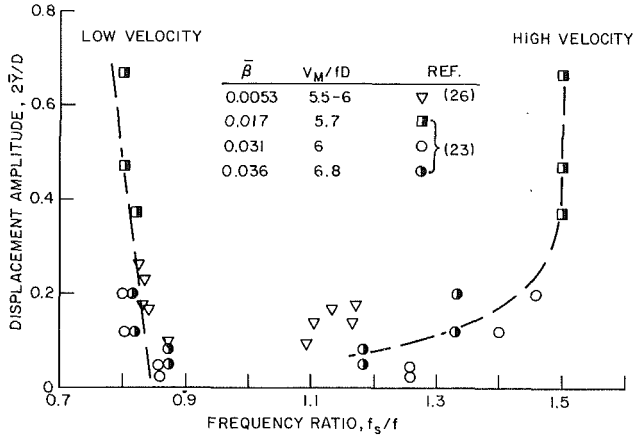

Fig. 15 *Local displacement amplitude and frequency boundaries for lock-on between vortex shedding and cable vibrations in a shear flow; data from Woo, Peterka, and Cermak [23], and Peltzer [26].*

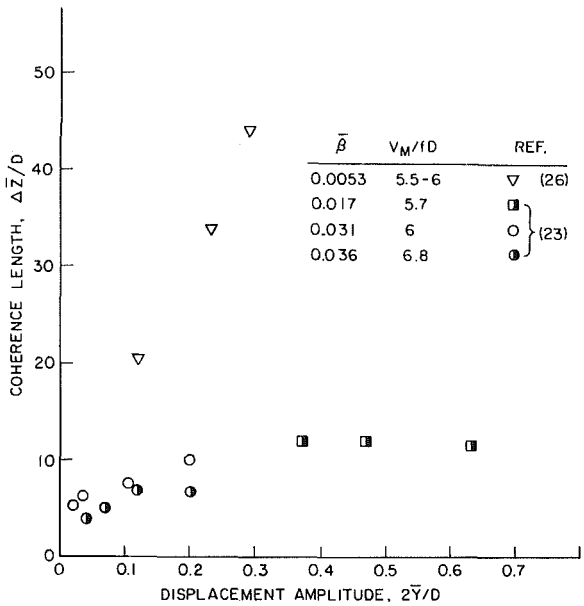

Fig. 16 *Coherence length $\Delta\bar{z}$ of the vortex shedding from a vibrating flexible cable in a shear flow; data from Woo, Peterka, and Cermak [23], and Peltzer [26].*

clearly draws attention to the remaining unsolved problems and relative lack of applicable test data in this somewhat specialized area of fluid/structure interactions.

The Extent of Lock-on in a Shear Flow

The boundaries of the lock-on region along a flexible body with varying amplitude of displacement can be estimated from the results obtained by Woo, et al. [23] and by Peltzer [26]. These results give some useful insights into the effects of shear on the vortex shedding from a long cylinder when end effects are minimal. The bounds of displacement amplitude and frequency are plotted in Fig. 15. The reduced velocities corresponding to these results are typical of the range of V_r ($=5$ to 7) for which large-amplitude oscillations occur in air and in water. The range of steepness parameters $\bar{\beta}$ also is representative of velocity shear conditions which are typically encountered both in laboratory experiments and in practical applications.

The results plotted in Fig. 15 suggest that the frequency boundaries for the lock-on in a shear flow are effectively constant for $2\bar{Y}/D > 0.2$. The result is

$$f_s/f\Big|_{\text{Velocity}}^{\text{High}} - f_s/f\Big|_{\text{Velocity}}^{\text{Low}} \approx 0.7, \quad 2\bar{Y}/D > 0.2$$

and

$$\bar{\beta} = 0.005 \text{ to } 0.036.$$

This result can be employed in recasting the lock-on prediction model of Stansby [16] into a form that is suitable for vibrating flexible cylinders and cables. A more extensive discussion of this prediction model is given in a related report [21].

The coherence length of the vortex shedding, or the span length $\Delta\bar{z}$ over which the cylinder and the wake are oscillating in unison, is plotted in Fig. 16 for the same conditions of reduced velocity and shear parameter as in Fig. 15. An inverse relation between the coherence length and the shear seems evident from the results.

Concluding Remarks

Summary. Most of the experiments conducted up to now with stationary cylinders have demonstrated fairly conclusively that a cellular pattern of vortex shedding exists along the span of a bluff body in a shear flow. Over each cell the vortex shedding frequency is constant, and constant values of the Strouhal number and the base pressure coefficient are obtained when a characteristic velocity scale (usually, the midspan value) is employed. However, the results obtained thus far are limited by the end effects caused by the generally small cylinder aspect ratios, in many cases $L/D < 20$.

Some limited experiments also have been conducted to investigate the effects of turbulence on the response of cylinders in a shear flow. In the case of a linear shear flow with high turbulence level it was observed that the critical Reynolds number for a stationary circular cylinder (usually $\text{Re} \sim 10^5$) was reduced by a factor of ten (to $\text{Re} \sim 10^4$) as had been found for the related case of an incident uniform flow. Some experimental evidence is available to suggest that moderate shear levels do not appreciably decrease the probability of vortex-excited oscillations when the reduced damping k_s of the structure is low enough ($k_s < 16$). In a boundary-layer shear flow, for example, the vortex-excited crossflow response of a circular cylinder was found to be insensitive to the level of incident turbulence when the damping of the structure was small enough to cause the structure and the wake to oscillate in unison. Several experiments have been conducted with long cables and cylinders in a linear shear flow. Vibrations of the cable were observed to lock-in with the vortex shedding as in the case of uniform flow [23, 26].

It would appear in the near term that further studies of shear flow effects will be experimental in nature. The lack of computational resources and numerical algorithms to handle turbulent, three-dimensional, high Reynolds number bluff body flows are limiting factors at this time.

Recommendations. Many of the studies conducted thus far have been small-scale experiments at relatively low Reynolds numbers with limited objectives, and they have been confined to cylinders with small aspect ratios of length/diameter less than $L/D = 15$ to 20. It is important to conduct experiments with cylinders of sufficient length to minimize the effects of the end boundaries. This has been done in a few cases already for L/D's up to about 100 to 120.

The results obtained from experiments such as these will be of particular importance in the design of long, flexible marine structures such as risers and of deep water cable arrays. Risers, for example, in deep water have typical aspect ratios of $L/D = 250$ to 2500 [1]. Boundary-layer shear flow effects on free-ended models of small aspect ratio are of importance in building aerodynamics, and data applicable to this problem

are also limited. More extensive experiments should be conducted to study this latter problem.

There is a need also to investigate further the effects of velocity shear on the crossflow lock-on response of lightly damped structures in air and in water. More definitive bounds for and details of this fluid-structure interaction, and a more extensive data base from experiments are required for applications in both the wind engineering design of buildings and structures in air and the design of structures and cable systems in water.

Acknowledgments

This study was conducted at the Naval Research Laboratory as part of an exploratory development program in marine cable dynamics funded by the Naval Civil Engineering Laboratory. I am grateful to Dick Bajura and the reviewers for their patience and endurance, and to a number of colleagues who allowed the use of figures.

References

1 Whitney, A. K., and Nikkel, K. G., "Effects of Shear Flow on the Vortex-Shedding-Induced Vibration of Marine Risers," Offshore Technology Conference Paper OTC 4595, May 1983.

2 Naudascher, E., ed., *Flow-Induced Structural Vibrations*, Springer, Berlin, 1974.

3 Naudascher, E., and Rockwell, D., eds., *Symposium on Practical Experiences With Flow-Induced Vibrations*, Springer, Berlin, 1981.

4 Sarpkaya, T., "Vortex-Induced Oscillations—A Selective Review," ASME *Journal of Applied Mechanics*, Vol. 46, 1979, pp. 241–258.

5 Bearman, P. W., "Vortex Shedding From Oscillating Bluff Bodies," *Annual Review of Fluid Mechanics*, Vol. 16, 1984, pp. 195–222.

6 Griffin, O. M., and Ramberg, S. E., "Some Recent Studies of Vortex Shedding With Application to Marine Tubulars and Risers," ASME *Journal of Energy Resources Technology*, Vol. 104, Mar. 1982, pp. 2–13.

7 Masch, F. D., and Moore, W. L., "Drag Forces in Velocity Gradient Flow," *Proceedings of the ASCE, Journal of the Hydraulics Division*, Vol. 86, No. Hy 7, 1960, pp. 1–11.

8 Starr, M. R., "The Characteristics of Shear Flows Past a Circular Cylinder," PhD Thesis, University of Bristol, Bristol, UK, 1966.

9 Shaw, T. L., and Starr, M. R., "Shear Flows Past A Circular Cylinder," *Proceedings of the ASCE, Journal of the Hydraulics Division*, Vol. 98, No. Hy 3, 1972, pp. 461–473.

10 Maull, D. J., and Young, R. A., "Vortex Shedding From a Bluff Body in a Shear Flow," in *Flow-Induced Structural Vibrations*, E. Naudascher, ed., 1974, pp. 717–729.

11 Maull, D. J., and Young, R. A., "Vortex Shedding From Bluff Bodies in a Shear Flow," *Journal of Fluid Mechanics*, Vol. 60, 1973, pp. 401–409.

12 Mair, W. A., and Stansby, P. K., "Vortex Wakes of Bluff Cylinders in a Shear Flow," *SIAM Journal of Applied Mathematics*, Vol. 28, 1975, pp. 519–540.

13 Owen, P. R., and Zienkiewicz, K. H., "The Production of Uniform Shear Flow in a Wind Tunnel," *Journal of Fluid Mechanics*, Vol. 2, 1957, pp. 521–531.

14 Fiscina, C., "An Investigation Into the Effects of Shear on the Flow Past Bluff Bodies," MS Thesis, University of Notre Dame, Notre Dame, IN, May 1977.

15 Fiscina, C., "An Experimental Investigation of the Flow Field Around a Bluff Body in a Highly Turbulent Shear Flow," PhD Dissertation, University of Notre Dame, Notre Dame, IN, May 1979.

16 Stansby, P. K., "The Locking-on of Vortex Shedding Due to the Cross-Stream Vibration of Circular Cylinders in Uniform and Shear Flows," *Journal of Fluid Mechanics*, Vol. 74, 1976, pp. 641–667.

17 Vickery, B. J., and Clark, A. W., "Lift or Across-Wind Response of Tapered Stacks," *Proceedings of ASCE, Journal of the Structural Division*, Vol. 98, No. ST1, 1972, pp. 1–20.

18 Davies, M. E., "The Effects of Turbulent Shear Flow on the Critical Reynolds Number of a Circular Cylinder," National Physical Laboratory (U.K.) NPL Report Mar Sci R 151, Jan. 1976.

19 Griffin, O. M., "A Universal Strouhal Number for the "Locking-on" of Vortex Shedding to the Vibrations of Bluff Cylinders," *Journal of Fluid Mechanics*, Vol. 85, 1978, pp. 591–606.

20 Griffin, O. M., "Universal Similarity in the Wakes of Stationary and Vibrating Bluff Bodies," ASME JOURNAL OF FLUIDS ENGINEERING, Vol. 103, Mar. 1981, pp. 52–58.

21 Griffin, O. M., "Vortex Shedding From Cables and Structures in a Shear Flow: State-of-the-Art," Naval Civil Engineering Laboratory Report CR83.004 Nov. 1982.

22 Peltzer, R. D., and Rooney, D. M., "Effect of Upstream Shear and Surface Roughness on the Vortex Shedding Patterns and Pressure Distributions Around a Circular Cylinder in Transitional Re Flows," Virginia Polytechnic Institute and State University Report No. VPI-Aero-110, Apr. 1980.

23 Woo, H. G. C., Peterka, J. A., and Cermak, J. E., "Experiments on Vortex Shedding from Stationary and Oscillating Cables in a Linear Shear Flow," Fluid Mechanics and Wind Engineering Program, Colorado State University, Final Report on Contract N68305-78-C-005 for the Naval Civil Engineering Laboratory, July 1981.

24 Peltzer, R. D., and Rooney, D. M., "Vortex Shedding, Base Pressure and Wake Measurements Behind High Aspect Ratio Cylinders in Subcritical Reynolds Number Shear Flow," ASME Paper 81-WA/FE-10, Nov. 1981.

25 Elsner, S. J., "A Critical Investigation of the Universal Strouhal Number for a Bluff Body in a Linear Shear Flow," MS Thesis, University of Notre Dame, Notre Dame, IN, June 1982.

26 Peltzer, R. D., "Vortex Shedding From a Vibrating Cable With Attached Spherical Bodies in a Linear Shear Flow," Naval Research Laboratory Memorandum Report 4940, Oct. 1982.

27 Kiya, M., Tamura, H., and Arie, M., "Vortex-Shedding From a Circular Cylinder in Moderate-Reynolds Number Shear-Flow," *Journal of Fluid Mechanics*, Vol. 101, 1980, pp. 721–736.

28 Roshko, A., "On the Development of Turbulent Wakes From Vortex Streets," NACA Report 1191, 1954.

29 Kwok, K. C. S., and Melbourne, W. H., "Cross-Wind Response of Structures Due to Displacement Dependent Lock-in Excitation," in *Wind Engineering*, J. E. Cermak, ed., Vol. 2, Pergamon, Oxford, 1980, pp. 699–708.

30 Fischer, F. J., Jones, W. T., and King, R., "Current-Induced Oscillation of Cognac Piles During Installation-Prediction and Measurements," in *Practical Experiences With Flow-Induced Vibration*, E. Naudascher and D. Rockwell, eds., Springer, Berlin, 1980, pp. 570–581.

31 King, R., "Model Tests of Vortex-Induced Motion of Cable Suspended and Cantilevered Piles for the Cognac Platform," BHRA Fluid Engineering Report RR 1453, Jan. 1978.

32 Howell, J. F., and Novak, M., "Vortex Shedding From Circular Cylinders in Turbulent Flow," in *Wind Engineering*, J. E. Cermak, ed., Vol. I, Pergamon, Oxford, 1980, pp. 619–630.

33 Cermak, J., ed., *Wind Engineering, Proceedings of the Fifth International Conference on Wind Engineering*, Pergamon, Oxford, 1980.

34 Eaton, K. J., ed., *Proceedings of the Fourth International Conference on Wind Effects on Buildings and Structures*, Cambridge University Press, Cambridge, UK, 1976.

Experimental Measurements of Hydrodynamic Radial Forces and Stiffness Matrices for a Centrifugal Pump-Impeller

Dimitri S. Chamieh[1]
Assoc. Mem. ASME

Allan J. Acosta
Fellow ASME

Christopher E. Brennen
Mem. ASME

Thomas K. Caughey

California Institute of Technology,
Pasadena, CA 91125

The present work is an experimental investigation of the possible forces of fluid dynamic origin that can act on a turbomachine rotor particularly when it is situated off its normal center position. An experimental facility, the Rotor Force Test Facility, has been designed and constructed in order to measure these kinds of forces acting on a centrifugal pump impeller when the latter is made to whirl in a slightly eccentric circular orbit. The scope of the present experimental work consists of measuring quasi-steady forces on the impeller as it whirls slowly about the axis of the pump rotation. These forces are due to interaction between the impeller and volute; they are decomposed into force components relative to the geometric center of the volute and to those proportional to displacement from this center. These latter are interpreted as stiffness matrices. Such matrices were obtained for two different volutes and both were found to be the sum of a diagonal and a skew-symmetric matrix. It can be shown that a stiffness matrix of this type can lead to dynamic instability of impeller shaft system in certain circumstances. This new experimental finding may explain some operational problems of "high-speed" hydraulic machinery. Comparison is made with various existing theoretical and experimental results.

Introduction

It has become evident in the past few years that hydrodynamic effects due to the presence of the rotor itself, in addition to the seals and bearings, may also cause rotor whirl. Such problems have been experienced not only in steam turbines (Pollman, et al. [13]) but also in large compressors (Thompson [15]) and in high speed pumps (Ek [8]). Here the flow through the turbomachine rotor and its surroundings induces a fluid dynamic force on the rotor shaft that may be a cause for rotor whirl. We have proposed in the past [2] an experiment with the capabilities of measuring impeller forces for any whirling rotor. This paper reports preliminary data from the first stage experiments in which the shaft is orbited at a very low frequency.

Steady State-Radial Force

A major problem centrifugal pump designers must cope with is the radial load on the impeller caused by the nonuniformity of the static pressures and velocities within the volute, particularly at off-design conditions. The reason for this nonuniformity is the mismatching of impeller and volute leading to changes of flow rate and total head around the impeller outlet. The literature dealing with this force is quite extensive. Many of the earlier references are based on the semi-empirical relation quoted by Stepanoff [14]:

$$F_0 = K\Delta P_t d_2 w_2 \tag{1}$$

where K is a parameter depending on the type of volute casing used and on flow rate (see also [14]). Other experimental works followed in the same spirit, namely, those of Agostinelli, et al. [1], Iversen, et al. [10], and Domm and Hergt [7]. Among the theoretical papers on the subject are the source vortex method of Domm and Hergt [7] and Colding-Jorgensen [6] and the actuator disk model of Chamieh and Acosta [3, 4]. Most of these previous works will be compared to the actual experimental findings.

Hydrodynamic Stiffness Matrix

Colding-Jorgensen [6] first introduced the concept of hydrodynamic stiffness matrices in order to express the sensitivity of the radial forces to the position of the impeller. He solved a theoretical model based on the source-vortex model of an impeller inside a logarithmic spiral volute. Here, even at design flow we may still expect a hydraulic force to be exerted on the impeller caused by the distortion of the streamlines within the volute due to displacement of the impeller from the geometric center of the volute.

The displacement of the impeller from the geometric center of the volute can arise from many sources, e.g., manufac-

[1]Presently, Byron Jackson Pump Division, Borg Warner Industrial Products, Inc., Long Beach, CA, 90802.

Contributed by the Fluids Engineering Division for publication in the JOURNAL OF FLUIDS ENGINEERING. Manuscript received by the Fluids Engineering Division, April 2, 1984.

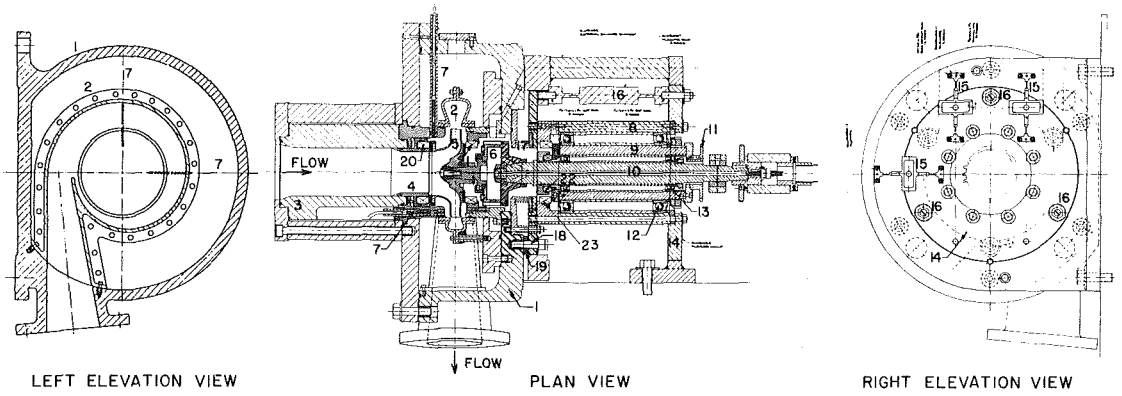

Fig. 1 Machine drawing of the impeller, volute, internal balance, eccentric drive, pump housing and external balance assembly of the Rotor Force Test Facility. Pump housing (1); volute (2); inlet connection (3); inlet bell (4); impeller (5); internal balance (6); proximity probes (7); eccentric drive mechanism: outer bearing carrier (8), inner bearing carrier (9), main shaft (10), orbiting motion sprocket (11) and bearings (12, 13); external balance: flexure face (14), flexure elements (15, not shown in the plan view) and axial flexures (16); bellows (17); bolts linking floating system and ground (18); spacers (19); impeller front face seals (20) and back face seals (21); eccentric drive inner face seals (22) and outer face seals (23). Note: The system is shown in its caged position. Removal of bolts (18) and spacers (19) will make unit float (see also text).

turing tolerances, weight, vibrational disturbances, unbalanced forces or blade cut-water forces etc. In this situation the hydraulic forces caused by the relative displacement of the impeller and volute can be compared in principle to spring forces. In the radial plane of the impeller, this force vector can be linked to the displacement vector (measured from the geometric center of the volute) by a 2 × 2 stiffness matrix. A more mathematical definition of this stiffness matrix will be given in the section under "Data Reduction."

Documentation of hydrodynamic stiffness forces and matrices is exceedingly sparse. For centrifugal pumps, for example, only very limited experimentation by Domm and Hergt [7] and Hergt and Krieger [9] can be found in the literature. Domm and Hergt measured forces on an impeller for two equal eccentricities (but different angular positions) for various flow rates. Their results were not interpreted using the concepts of hydrodynamic stiffness matrices. Hergt and Krieger measured forces on an impeller for three different flow rates but for various eccentricities and angular positions. One of their conclusions is that the forces seemed to be proportional to the eccentricity for the three flow rates tested but there was still no attempt to deduce stiffness matrices. A similar experiment was conducted by Ohashi and Shoji, et al. [12]. Their test impeller was installed in a large vaneless diffuser with the result that the stiffness matrix was small and could not be detected. Besides Colding-Jorgensen [6], Chamieh [4, 5] calculated hydrodynamic stiffness matrices using very simple impeller flow models. We believe this paper is the first to report on the measurement of such matrices.

Rotor Force Test Facility

The facility was described in detail in earlier references [2, 5]. We will merely repeat that the objective of the facility is to impose known orbiting motions of radian frequency ω on the basic rotary motion of a number of typical centrifugal pump impellers (radian frequency, Ω, shaft speed, N). This paper deals only with results obtained for $\omega/\Omega \ll 1$, that is to say a quasi-static offset. The facility is shown in the machine drawing in Fig. 1. Further details can be found in [5].

A five-bladed Byron Jackson centrifugal pump designated Impeller X with an outer diameter of 162 mm and a discharge angle of 25 deg, was used for all the present measurements. A machine drawing as well as photographs can be found in [5]. This impeller was cast in bronze and has a specific speed of 0.57. A well-matched trapezoidal cross-section fiberglass

Nomenclature

A_2 = impeller discharge area = $\pi d_2 b_2$
b_2 = impeller outlet width
C_p = pressure coefficient = $(p - p_{td})/\frac{1}{2}\rho U_2^2$
d_2 = impeller outlet diameter
$\mathbf{e}$ = vectorial deflection of the external balance
$\mathbf{F}$ = impeller total force vector; components F_X and F_Y
F_N = normalizing force = $\rho U_2^2 A_2/2$
$\mathbf{F_0}$ = radial force vector; magnitude F_0 and components F_{0X} and F_{0Y}
$\mathbf{F}_\omega$ = fundamental harmonic component of $\mathbf{F}$
K = Stepanoff's parameter as defined in [14]
$[K]$ = hydrodynamic force matrix; components K_{ij} with $i, j = X, Y$
$[KP]$ = static pressure hydrodynamic force matrix; components KP_{ij} with $i, j = X, Y$
$[K_S]$ = stiffness matrix of the extenal balance system
N = main shaft speed (rpm)
p = static pressure
p_{td} = downstream total pressure
ΔP_t = total pressure rise across the pump
Q = volume flow rate
r_2 = impeller outlet radius
U_2 = impeller tip speed
w_2 = impeller outlet width including the shrouds
X, Y = axes of volute; also impeller center position within the volute axes
δ = instantaneous impeller center position with respect to the center of whirl
δ_V = distance between the volute center and the center of whirl
δ_ω = fundamental harmonic component of δ
ϵ = eccentricity vector
θ = angular position measured from the tongue
ρ = density of water
Φ = pump flow coefficient = $Q/A_2 U_2$
Ψ = pump total head coefficient = $\Delta P_t/\rho U_2^2$
ω = radian frequency of whirl motion
Ω = radian frequency of impeller rotation

Superscript

* = dimensionless quantity

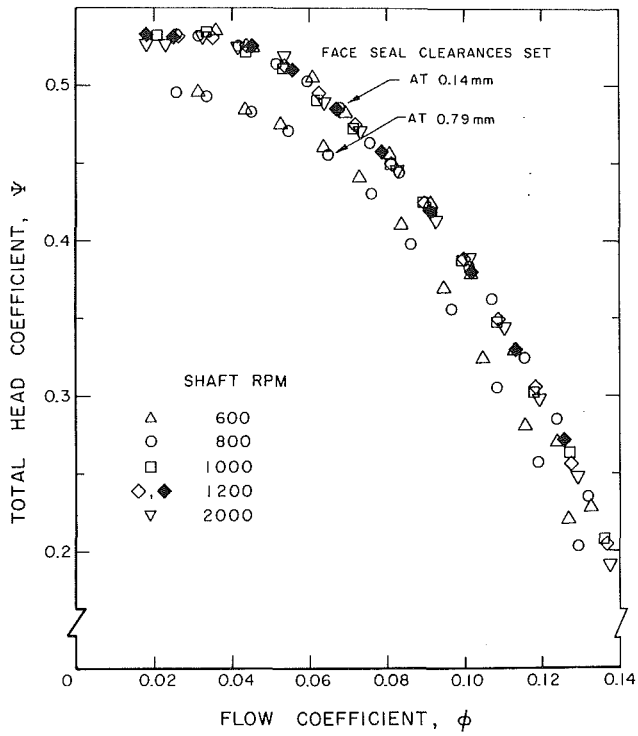

Fig. 2 Performance characteristics of Impeller *X* inside Volute *A* for the front and back face seal clearances of 0.14 and 0.79 mm. Open and closed symbols represent data for $\omega > 0$ and $\omega < 0$ respectively. (Uncertainty in $\Phi = \pm 0.0025$, in $\Psi = \pm 0.01$).

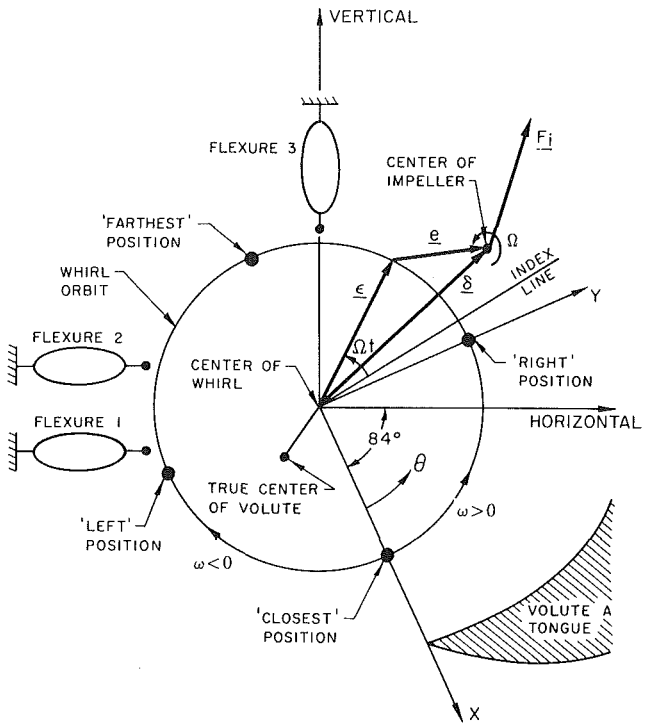

Fig. 3 Schematic of forces and locations within the impeller-volute system as seen from the inlet

volute (Volute *A*) was designed to be used with Impeller *X*. The ratio of the base circle diameter to impeller diameter is 1.13, and the area at the cutwater is 20.75 cm^2 [5]. A deliberately mismatched circular volute (Volute *B*) with a 5.42 cm constant diameter circular cross section [5] was also fabricated.

During the measurements, radial face seals on both sides of the impeller were backed off to prevent interference with the force measurements. These were selected in preference to the usual radial wear rings because the latter would interfere with the measurement of radial forces. Two sets of clearances were investigated with the radial face seals. One was considered a normal clearance in which both face seals are backed 0.14 mm from Impeller *X*. In this configuration, the inlet leakage was then estimated to be around two percent of the design flow rate. The other clearance is a deliberately large maximum clearance of 0.79 mm where inlet leakage losses are about 12 percent of the design flow rate. No experiments were made with the seals in contact. Figure 2 presents the performance characteristic of Impeller *X* for volute *A* for the two face seal clearances and for $\omega = \pm 0.314$ rad/sec.

The force balance, consisting of three strain-gauged aluminum load cells (see Fig. 1), was used with the entire impeller-eccentric drive system floating on soft spring supports attached to the ceiling. Three stainless steel axial flexures parallel with the shaft maintained the alignment in this configuration. A small d-c motor was also mounted on the floating assembly to produce a shaft orbit speed of 3 rpm. The purpose of this was to allow continuous sampling of the forces at all locations of the shaft around a circular orbit with a radius of 1.26 mm. By comparison with the forces at certain fixed locations as well as by imposing a reverse orbiting speed of 3 rpm it was determined that the dynamic effects of this 3 rpm orbit speed were negligible.

Two of the strain-gauged load cells were mounted horizontally (Fig. 1, the right elevation view) for measurement of horizontal force and torque; the other measures the vertical force. Calibrations were performed by known forces applied by systems of wires, pulleys and weights. The linearity of the calibrations was within one percent over the entire range of calibration (−20 to +20 kgf) and the interactions were less than one percent.

Signal processing was accomplished by means of an eight channel digital signal processor which was phase locked to an optical encoder attached to the shaft of the 3 rpm motor. In this way each of the eight channels of data (three load cell signals plus pressure transducers, flow rates, etc.) are sampled at 32 equally spaced positions of each rotation of the eccentricity. Furthermore this sampling was continued for 15 or more rotations in order to obtain averages of the forces for each of the 32 geometric positions.

The flexure signals were also recorded on magnetic tape and processed through a digital spectrum analyzer to investigate their content. The major peak was observed at the 3 rpm whirl frequency. Much smaller peaks also occurred at higher harmonics of this whirl frequency. The largest observed magnitude of the second harmonic was always less than ten percent of the fundamental indicating that the impeller forces at the small eccentricity employed vary quite sinusoidally around the circular eccentric orbit and that this variation can be accurately represented by a stiffness matrix.

Finally, linearity of the stiffness matrix with respect to the imposed eccentricity has been assumed in view of the previously discussed experimental data of Hergt and Krieger [9].

Data Reduction

The geometry and notation of the impeller shaft location, external balance load cells and volute position are shown in Fig. 3 (viewed from the pump inlet). The center of the volute and the center of whirl are made to coincide through proper adjustment of the spring assembly such that δ_V is minimized; ideally δ_V should be zero before any test run. The flexure system, though quite stiff, has some deflections due to the hydrodynamic forces on the impeller: This deflection **e** is

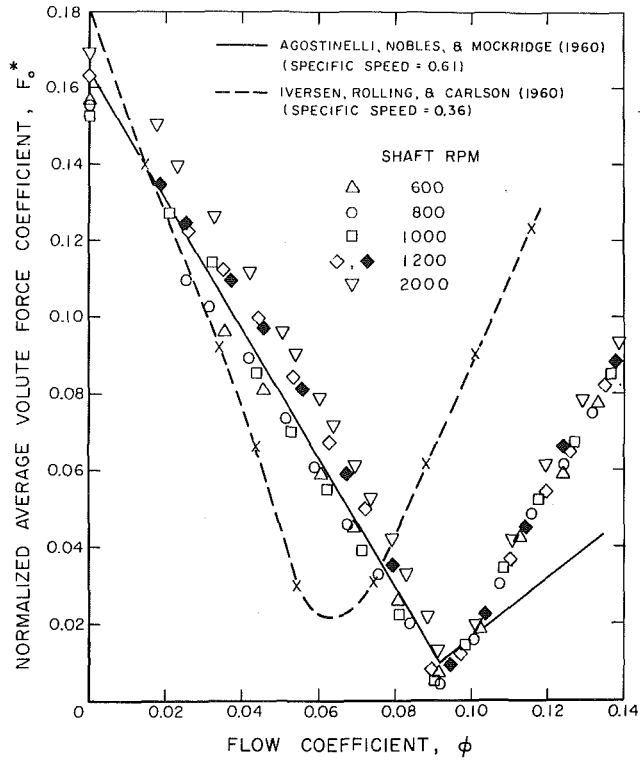

Fig. 4 Normalized average volute force for Impeller *X*, Volute *A* and face seal clearances of 0.14 mm. Open and closed symbols represent data for $\omega > 0$ and $\omega < 0$, respectively. Comparison is made with Iversen, et al. [10], bearing reactions and Agostinelli, et al. [1], experimental data. (Uncertainty in $\Phi = \pm 0.0025$, in $F_0^* = \pm 0.004$).

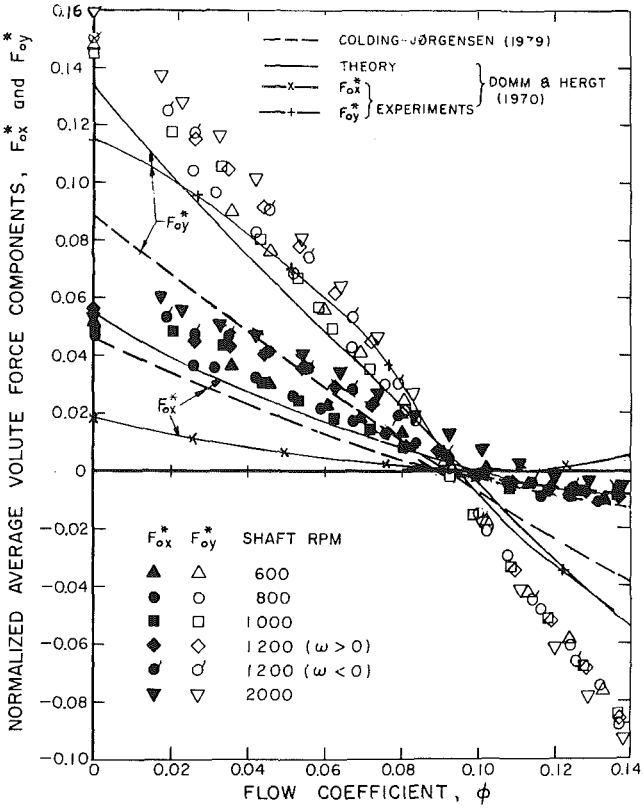

Fig. 5 Normalized average volute force components of Fig. 4 are shown along with the works of Domm and Hergt [7] and Colding-Jorgensen [6] having volute angles of 86.3° and 86°, respectively. Impeller *X*, Volute *A* and face seal clearances of 0.14 mm. (Uncertainty in $\Phi = \pm 0.0025$, in $F_0^* = \pm 0.004$).

monitored by the external balance elements. One consequence of this is that the actual position of the shaft center is a combination of the 1.26 mm eccentricity plus the deflection of the flexure system. All of the data on impeller forces were corrected for this effect. If ϵ is the instantaneous shaft center position due to the imposed eccentricity of 1.26 mm and $[K_S]$ is the stiffness matrix of the flexure system (measured by loading under conditions of no motion), then the actual instantaneous position of the shaft (see Fig. 3) is

$$\delta = \epsilon + \mathbf{e};\ \mathbf{e} = [K_S]^{-1}\mathbf{F} \tag{2}$$

where $\mathbf{F}$ is the instantaneous force acting on the rotor (and therefore on the floating assembly) for a particular test run due to the Ω and ω motions. Tare forces were found to be negligible so that, with proper zeroing of the balance, the forces, $\mathbf{F}$, are entirely hydrodynamic (see the no-impeller results in Fig. 10 for this confirmation).

Fourier decomposition of the data yields the average hydrodynamic force or radial force $\mathbf{F}_0$ associated with the mean position of the shaft center and the first harmonic, $\mathbf{F}_\omega$, associated with the first harmonic of δ, δ_ω. The hydrodynamic force matrix or stiffness matrix, $[K]$ is then defined as

$$\mathbf{F}_\omega = [K]\delta_\omega \tag{3}$$

where δ_ω is the fundamental of $\{\epsilon + [K_S]^{-1}\mathbf{F}\}$ and therefore $[K]$ can be calculated since ϵ, $[K_S]^{-1}$ and $\mathbf{F}_\omega$ are all known. In the present experiments the correction $[K_S]^{-1}\mathbf{F}_\omega$ could be as large as ten percent of δ_ω.

The forces were then nondimensionalized by the factor F_N as defined in the Nomenclature while the force matrices are nondimensionalized by F_N/r_2.

Average Volute Forces: Results and Discussion

The reduced data for the averaged dimensionless volute forces acting on Impeller *X* due to Volutes *A* and *B* are

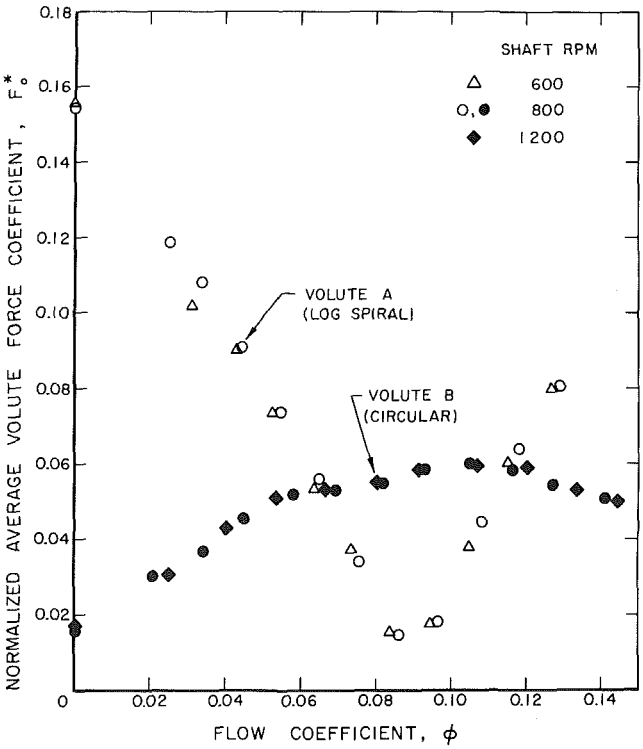

Fig. 6 Normalized average volute force for Impeller *X* and face seal clearances of 0.79 mm. Open and closed symbols represent data for Volutes *A* and *B*, respectively. (Uncertainty in $\Phi = \pm 0.0025$, in $F_0^* = \pm 0.004$).

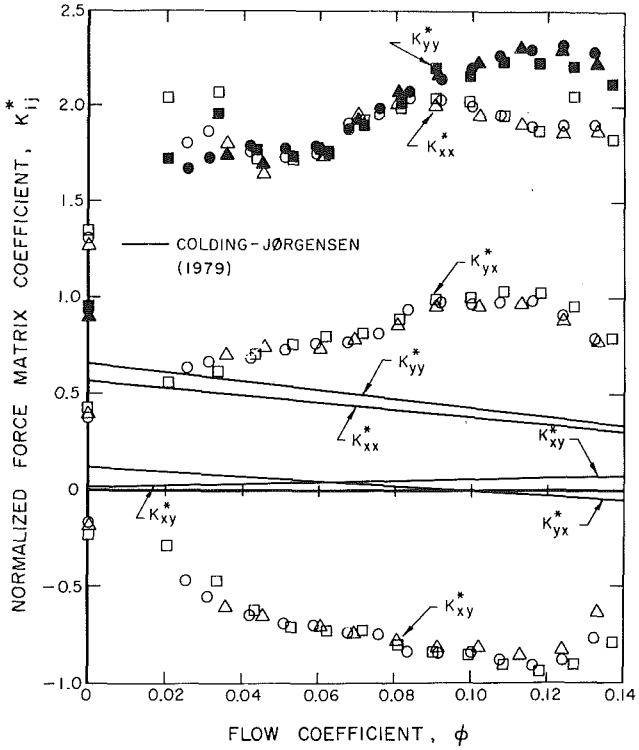

Fig. 7 Normalized force matrix coefficients as defined in text for Impeller X, Volute A and face seal clearances of 0.14 mm. Shaft speed = 600 rpm: △, ▲; 800 rpm: ○, ●; 1000 rpm: □, ■. Values of K^*_{XX}, K^*_{XY} and K^*_{YX} are represented by open symbols; values of K^*_{YY} by closed symbols. Comparison is made with Colding-Jorgensen's [6] theoretical stiffness matrix calculations with a volute angle of 86°. (Uncertainty in $\Phi = \pm 0.0025$, in $K^*_{ij} = \pm 0.05$).

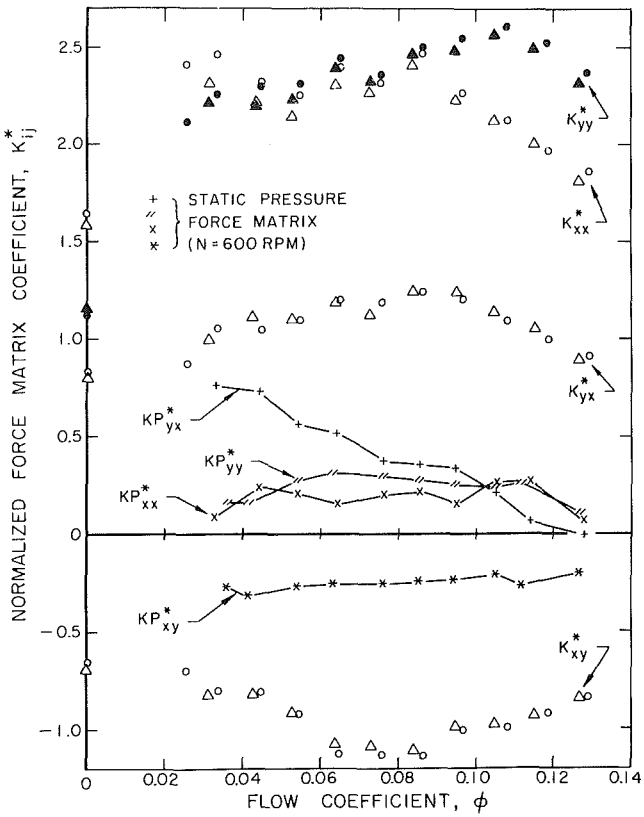

Fig. 8 Normalized force matrix coefficients as defined in text for Impeller X, Volute A and face seal clearances of 0.79 mm. Shaft speed = 600 rpm: △, ▲; 800 rpm: ○, ●. Values of K^*_{XX}, K^*_{XY} and K^*_{YX} are represented by open symbols; values of K^*_{YY} by closed symbols. The normalized static pressure force matrix for a shaft speed of 600 rpm is shown by the symbols +, ‖, × and ∗. (Uncertainty in $\Phi = \pm 0.0025$, in $K^*_{ij} = \pm 0.05$).

presented in Figs. 4–6. The plots include the magnitude and individual components of the forces. The data for the "well-matched" volute (A) at a face seal clearance of 0.14 mm is shown in Fig. 4. Here F^*_0 is plotted versus flow coefficient Φ at various speeds. Some results for both a forward 3 rpm sampling orbit speed ($\omega > 0$) and a reverse orbit speed of 3 rpm ($\omega < 0$) are shown to confirm that this orbit speed had little effect on the results. The nondimensionalized force data for different shaft speeds (600 up to 2000 rpm) is in substantial agreement though there would appear to be a slight increase in the magnitude of the force coefficient at low flow coefficients when rotor speed was increased. It seems likely that this is a Reynolds number effect. From a practical viewpoint, it is clear that the Impeller X and Volute A are well matched at their design flow coefficient of 0.092 since the force on the impeller is virtually zero at this operating point. Values of F^*_0 at shutoff range from 0.155 to 0.17 which is 10–20 percent higher than the calculated value suggested by Stepanoff [14].

Also shown in Fig. 4 are the experimental results of Agostinelli, Nobles, and Mockridge [1] and Iversen, Rolling, and Carlson [10] for pumps with specific speeds of 0.61 and 0.36, respectively. The former are in close agreement with the present results since the specific speed of the present Impeller X/Volute A combination is 0.57. The results of Iversen, et al. for a lower specific speed also appear consistent with the present results. For clarity, another set of experimental results by Domm and Hergt [7] is presented in Fig. 5. These results for a volute having an angle of 86.3 deg appear to be in agreement with the present results shown in Fig. 4.

Figure 5 also presents the dimensionless force components of the average volute force. Note the direction of the total force vector is virtually independent of flow coefficient; it is almost perpendicular to the radius to the cutwater. Included in the plot are the theoretical results of Domm and Hergt [7] and Colding-Jorgensen [6] for volutes with spiral angles of about 86 deg. These theories are based on the impeller being modeled by a source-vortex at its centerline and by assuming potential flow throughout the pump stage. Volute A has a similar angle when projected on the radial plane of the impeller. However Volute A is fully three-dimensional and the equivalent spiral angle obtained by unwrapping its area would be about 82 deg. Under these assumptions the data of Colding-Jorgensen appears more consistent with the experiments than what is actually shown in Fig. 5. Unfortunately we cannot initiate a similar "correction" with the results of Domm and Hergt as the theoretical example of reference [7] featured only a volute angle of 86.3 deg.

We have also investigated the effects of an increase in the face seal clearances and a volute change on the average volute force. Figure 6 shows data for Volutes A and B for the maximum front and back face seal clearances of 0.79 mm. The magnitudes, directions (and therefore also Cartesian components) of the average volute force for Volute A exhibited almost no change for the two face seal clearances at least for the two rotor speeds tested (600 and 800 rpm cf. Fig. 4). This observation is somewhat surprising because the total head changed significantly.

Different results were found for the circular Volute (B). The force is almost constant above $\Phi = 0.07$. Below this flow rate the force coefficient decreases to a shutoff value of about 0.015. Finally, we should point out that the two speeds of 800 and 1200 rpm tested with volute B seemed to be in general agreement with respect to the normalization process.

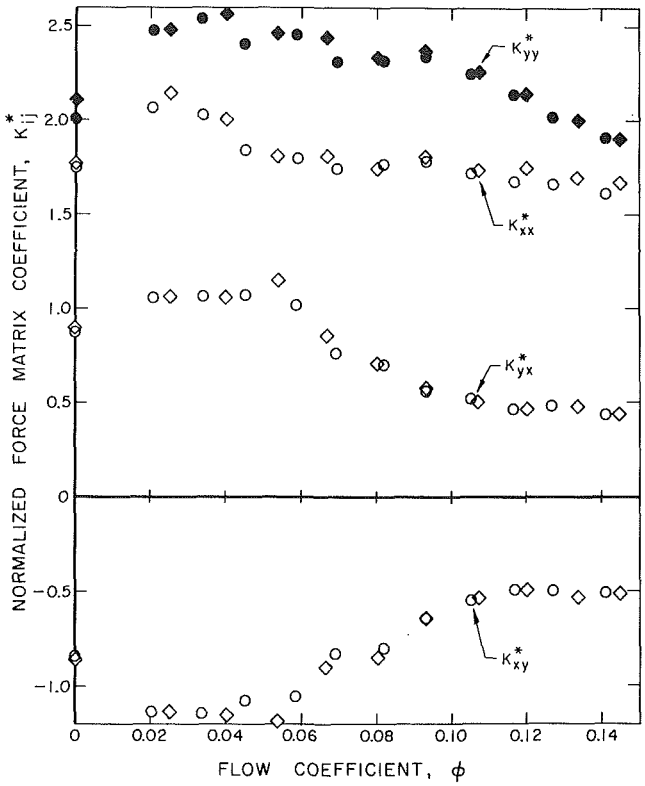

Fig. 9 Normalized force matrix coefficients as defined in text for Impeller X, Volute B and face seal clearances of 0.79 mm. Shaft speed = 800 rpm: ○, ●; 1200 rpm: ◇, ◆. Values of K^*_{XX}, K^*_{XY}, and K^*_{YX} are represented by open symbols; values of K^*_{YY} by closed symbols. (Uncertainty in $\Phi = \pm 0.0025$, in $K^*_{ij} = \pm 0.05$).

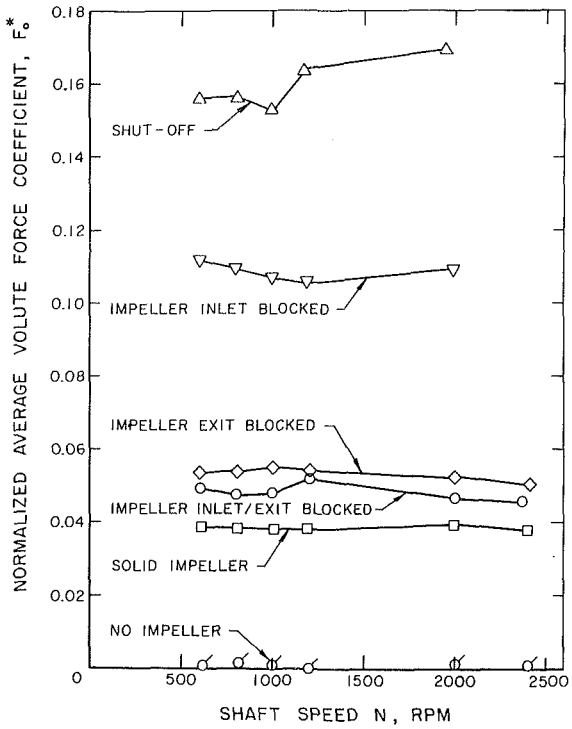

Fig. 10 Normalized average volute force is shown as a function of shaft speed for various auxiliary experiments conducted for Impeller X, Volute A and face seal clearances of 0.14 mm. (Uncertainty in $N = \pm 5$ rpm, in $F^*_0 = \pm 0.004$).

Hydrodynamic Force Matrices

Nondimensional hydrodynamic force matrix coefficients, K^*_{ij}, are presented in Figs. 7–9. These contain all the information on how the forces presented in Figs. 4–6 vary as the position of the impeller center changes when the change is within the linear regime. Figure 7 presents data for Volute A, for face seal clearances of 0.14 mm, for various flow rates and for rotor speeds of N = 600, 800 and 1000 rpm. We observe that the variation with N is consistent with that anticipated by the nondimensionalization and that the components vary only modestly with flow coefficient, Φ, for values above about 0.03. Finally, all of the measured K^*_{ij} show a tendency to drop as we approach shutoff but they do not vanish there.

The theoretical results of Colding-Jorgensen [6] based on the source/vortex model of the impeller and depicted in Fig. 7 exhibit substantial disagreement with the measurements. The diagonal components K^*_{XX} and K^*_{YY} are about one third of those of the present experiments. The off-diagonal or "cross-coupling" terms also differ from the present values and the calculated values of K^*_{YX} exhibit a change in sign unlike its experimental counterpart.

It is worthwhile to examine closely the structure of the $[K^*]$ matrix before presenting the remaining force matrix data. In fact the hydrodynamic force matrix of Fig. 7 implies that the fluid forces tend to excite a whirl motion of the impeller. This force matrix can be presented approximately in the form

$$[K^*] = \begin{bmatrix} 2.0 & -0.9 \\ 0.9 & 2.0 \end{bmatrix} \tag{4}$$

over the range of $0.04 < \Phi < 0.14$. It is therefore a combination of a diagonal and a skew-symmetric matrix. The former will simply reduce the structural stiffness matrix and in many cases this hydrodynamic effect will be small. The skew-symmetric or cross-coupling terms are much more important. The signs of the off-diagonal terms imply that the force component tangential to the whirl orbit is always in the direction of impeller rotation. Hence one important conclusion is that this stiffness matrix has an essential destabilizing rotordynamic effect. Of course the rotordynamic consequences of such excitation will depend on the damping matrix as well. In other words this whirl motion will be suppressed if the damping force due to the whirling motion is sufficient. However since K^*_{XY} and K^*_{YX} are proportional to N^2, it follows that if damping increases more slowly with N, then there will always be a speed above which the excitation will exceed the damping. This indicates that hydrodynamic stiffness due to the flow through the rotor and its surroundings can be a possible cause of "rough-running" of pumps.

We now examine the effect of parameter variation on the normalized force matrix. To accomplish this, rotor speeds higher than those shown in Fig. 7 were carried out. A slight increase in the magnitudes of K^*_{ij} was found at rotor speeds of 1200 and 2000 rpm (see [5]). We take this to be a Reynolds number effect. Data has also been obtained with face seal clearances of 0.79 mm and the results are shown in Fig. 8. These findings are qualitatively similar to those in Fig. 7 except that the magnitude of all the components is up to 20 percent larger for the larger clearances. This figure also contains the static pressure force matrix, the results of which will be explained later.

Results for the circular volute (B) are shown in Fig. 9. These were surprising in the sense that the skew-symmetric effect was even clearer and that, contrary to Volute A, the K^*_{ij} coefficients increased with decreasing flow rate.

In conclusion, no change in the experimental parameters altered the skew-symmetric behavior of the $[K^*]$ matrix. The magnitudes of the K^*_{ij} for different volutes and operating conditions are qualitativey similar.

Combining the volute force results of the previous section along with the hydrodynamic forces matrices of this section

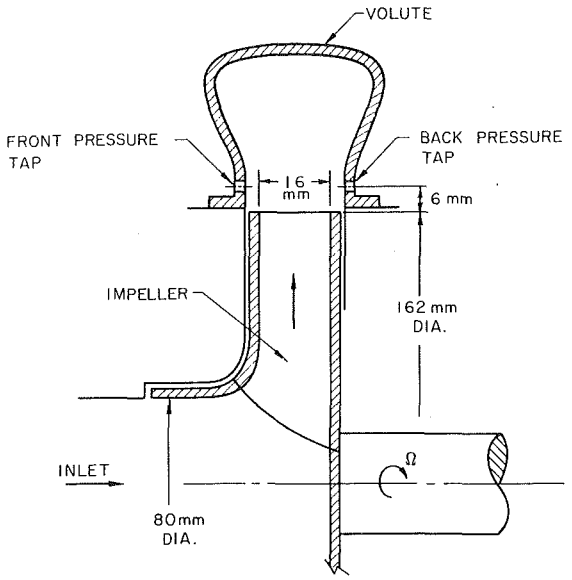

Fig. 11 Schematic showing main dimensions and static measurement points within Volute *A*. There are eight pressure taps more or less equally spaced around the volute circumference on the front and back.

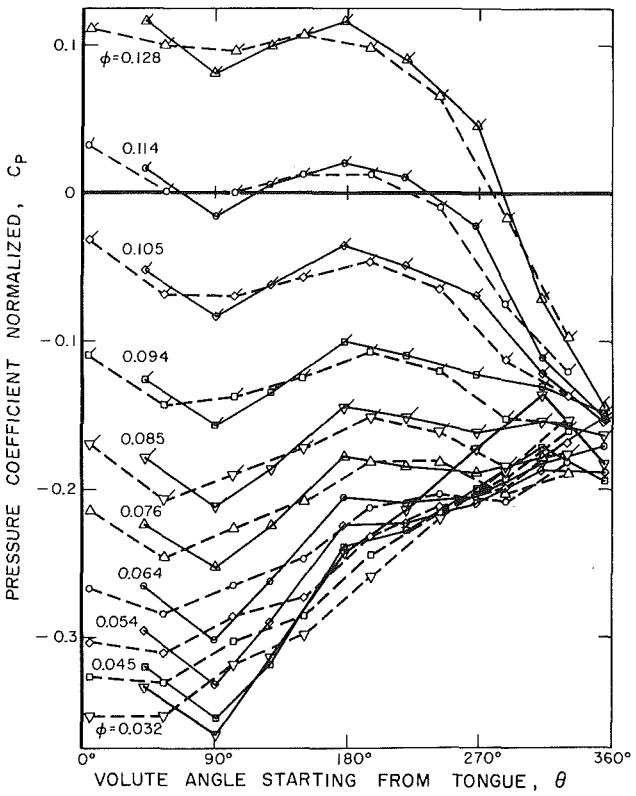

Fig. 12 Pressure coefficients for various flow rates for a rotor speed of 600 rpm. Impeller *X*, Volute *A* and face seal clearances of 0.79 mm. The shaft center position is at the closest point as defined by Fig. 3. Solid lines represent the front pressure taps and dashed lines the back pressure taps of Fig. 11. (Uncertainty in Θ = ±2 deg, in C_p = ±0.007).

gives the geometric position of the impeller within its volute casing such that the total steady-state impeller force is zero. For Volute *A* the locus of these "hydrodynamic centers" exhibits a linear region between the flow coefficients of 0.055 and 0.122 (see reference [5]), which agrees well with the results of Domm and Hergt [7].

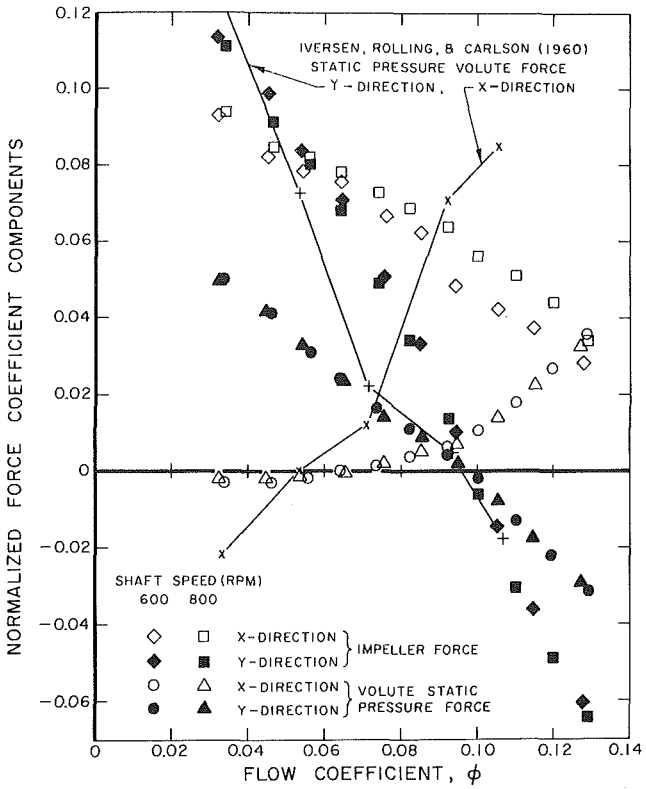

Fig. 13 Normalized impeller forces and static pressure forces of Fig. 12 for rotor speeds of 600 and 800 rpm for Impeller *X*, Volute *A* and face seal clearances of 0.79 mm. The shaft center position is at the closest point as defined by Fig. 3. Comparison is made with Iverson, et al. [10], static pressure volute forces. (Uncertainty in Φ = ±0.0025, in Force = ±0.004).

Auxiliary Experiments

Figure 10 presents the force coefficient data for a number of tests performed with the objective of assessing the source of the large radial forces at shutoff. All of the normalized data presented appeared to be virtually independent of shaft speed indicating that forces are proportional to the square of tip speed. The lack of any appreciable force in the absence of the impeller (No Impeller points) was used *a priori* under "Data Acquisition" to show the forces to be truly due to the presence of the rotor only. Other experiments conducted consisted of testing a solid impeller having the same dimensions of Impeller *X* and of testing Impeller *X* with its inlet and/or exit blocked by a sheet of metal. The data for the solid impeller and for Impeller *X* having its inlet and exit blocked were quite similar for both face seal clearances. We conclude that this force coefficient component (about 0.045) is due to disk friction effects and to the induced pressure gradient acting on the entire exterior surfaces of the impeller. The force coefficient for Impeller *X* with its exit blocked was almost identical to that of the solid impeller. However, the data with the inlet blocked is significantly higher, probably because the outer recirculation effects are greater. The force data for the flow blocked about three diameters upstream of the impeller is higher still.

Dimensionless force matrix coefficients, K_{ij}^*, for each of the experiments in Fig. 10 were also obtained and reported in [5]. The most significant finding is the absence of "stiffness" when the impeller was removed. This confirms the fact that the stiffness force so measured is due to the presence of the rotor. Results for the solid impeller were found to be four times smaller than those at design conditions indicating the contribution of the disk friction effects for the original im-

peller. All of these force matrices remained the sum of diagonal and skew-symmetric matrices [5].

Static Pressure Measurements in the Volute

It would be interesting to learn more about the origins of the impeller hydrodynamic forces. An obvious dissection of these forces should show momentum flux, static pressure and disk friction components. In this section, we measure and discuss the static pressure component of these forces.

Instrumentation. Static pressure distributions within Volute A were measured by means of the static pressure taps shown in Fig. 11 at four fixed positions of the eccentricity (the positions "closest," "farthest," "right" and "left" shown in Fig. 3) at various flow coefficients. A bank of inverted water manometers was used to measure pressure differences for the 16 taps of Fig. 11. The pressure measurements were referenced to the downstream total pressure as measured by an accurate Heise gage. The pressure distributions were then reduced to dimensionless pressure coefficients, C_p, based on the downstream total pressure and the dynamic head at the impeller tip (see Nomenclature). C_p is then plotted against θ, the angle being measured from the cutwater of the volute. Finally, static pressure forces were calculated from these pressure distributions.

Static Pressure Distributions. Figure 12 presents a typical static pressure distribution at the impeller discharge of Impeller X within Volute A at various flow coefficients. The face seal clearances were 0.79 mm and the rotor speed was 600 rpm. The plots represent results from a test at the closest position as shown in Fig. 3. The form and magnitude of the pressure variations are similar to those measured by Iversen, et al. [10] and to those predicted theoretically by Kurokawa [11]. The most important feature is the static pressure discontinuity that occurs in the neighborhood of the cutwater (compare the values of C_p at $\theta = 0°$ and $\theta = 360°$) particularly at off-design flow coefficients. However, at or close to the design value of 0.092, the static pressure is quite uniform around the volute periphery. Finally, we should emphasize the disagreement between the front pressure taps and the back pressure taps measurements of Fig. 11 particularly at low flow coefficients. This suggests that the flow coming out of the impeller is not symmetrical with respect to the centerline of the volute cross section.

Static Pressure Forces. Figure 13 presents the X and Y components of the static pressure force expressed in the coordinates of Volute A for the closest eccentric position (see Fig. 3) and compares them with the total force components on the impeller measured by the external balance for the same impeller location. Note that the static pressure component is not sufficient in itself to explain the measured total force. This is contrary to the results obtained by Iversen, et al. [10]; they observed significant agreement between these forces. They exhibit the same general trend as ours but are much larger in magnitude; this is perhaps due to the lower specific speed of the pump (0.36 instead of 0.57). We conclude that the nonisotropy of the momentum flux leaving the impeller is an important contributor to the impeller forces.

Static Pressure Force Matrix. Hydrodynamic force matrices, $[KP]$, due to the static pressure force components were also calculated and these are shown in Fig. 8 for a rotor speed of 600 rpm and for face seal clearances of 0.79 mm. It transpires that the components of this matrix represent only about 20 percent of the magnitude of the corresponding total hydrodynamic force matrix components. In addition we have shown earlier that disk friction contributes to about 25 percent of this matrix. We therefore conclude that the nonisotropy of the momentum flux is the primary contributor to the "stiffness" matrix. This fact emphasizes the need for direct measurement of the forces on the impeller rather than estimating the latter by integrating pressure distributions around the base circle of the volute.

Measurements Error

Rotor speeds and pump flow rates were read by digital voltmeters and showed negligible drifts or oscillations. The maximum error for the smallest values of these quantities (except for shutoff) was less than one percent. The net eccentricity has a relative error of 0.4 percent while impeller dimensions were measured to $\pm$ 0.2 percent. It was felt the accuracy of the slopes of calibration of the pressure transducers and of the force balance load cell elements was well within a one percent relative error. Finally, the phase angle of the measured forces with respect ot the volute's cutwater are determined to within $\pm$ 3 deg due to the uncertainties in exactly locating the data sampling "start" position.

Concluding Remarks

We have presented measurements of the steady-state hydrodynamic forces on a centrifugal pump impeller as a function of position within two geometrically different volutes. These correspond to the forces experienced by the impeller at zero whirl frequency. The hydrodynamic force matrices derived from these measurements exhibit both diagonal and off-diagonal terms of substantial magnitude. The off-diagonal or cross-coupling terms are of the form which would tend to excite a whirl motion in a rotordynamic analysis of the pump. This may be the cause of "rough running" reported in many pumps.

Static pressure measurements in the impeller discharge flow show that the hydrodynamic force on the impeller contains a substantial component due to the nonisotropy of the net momentum flux leaving the impeller. Moreover a similar breakdown of the contributions to the stiffness matrices reveals that the major component of these matrices results from the nonisotropy of the momentum flux.

Fugure plans include direct measurement of the forces due to the momentum flux leaving the impeller and the study of other impeller/volute configurations particularly vaned diffusers. Finally measurement of forces at nonzero whirl frequencies will be initiated in order to obtain a complete picture of the rotordynamic consequences of these hydrodynamic forces.

Acknowledgments

This work was supported by the National Aeronautics and Space Administration under contract No. NAS8-33108 and by a Byron Jackson Fellowship in Fluid Machinery. This support is gratefully acknowledged.

References

1 Agostinelli, A., Nobles, D., and Mockridge, C. R., "An Experimental Investigation of Radial Thrust in Centrifugal Pumps," ASME *Journal of Engineering for Power*, Vol. 82, Apr. 1960, pp. 120–126.

2 Brennen, C. E., Acosta, A. J., and Caughey, T. K., "A Test Program to Measure Fluid Mechanical Whirl-Excitation Forces in Centrifugal Pumps," First Workshop on Rotordynamic Instability Problems in High-Performance Turbomachinery, Texas A&M University, NASA Conference Pub. 2133, 1980, pp. 229–235.

3 Chamieh, D. S., and Acosta, A. J., "Dynamic Forces on a Whirling Centrifugal Rotor," *Proceedings 6th Conference on Fluid Machinery*, Akademiai Kiado, Budapest, Hungary, 1979, pp. 210–219.

4 Chamieh, D. S., "Calculation of the Stiffness Matrix of an Impeller Eccentrically Located Within a Volute," Cavitation and Polyphase Flow Forum, Joint ASME/ASCE Conference, Boulder, CO, 1981, pp. 51–53.

5 Chamieh, D. S., "Forces on a Whirling Centrifugal Pump-Impeller," *PhD Thesis, Division of Engineering and Applied Sciences, California Institute* of Technology, Pasadena, CA, 1983.

6 Colding-Jorgensen, J., "The Effect of Fluid Forces on Rotor Stability of

Centrifugal Compressors and Pumps," PhD Thesis, Department of Machine Design, Technical University of Denmark, 1979.

7 Domm, H., and Hergt, P., "Radial Forces on Impeller of Volute Casing Pumps," Flow Research on Blading," Dzung, L. S., ed., Elsevier Publishing Co., The Netherlands, 1970, pp. 305–321.

8 Ek, M. C., "Solution of the Subsynchronous Whirl Problem in the High Pressure Hydrogen Turbomachinery of the Space Shuttle Main Engine," Paper No. 78-1002, AIAA/SAE 14th Joint Propulsion Conf., Las Vegas, NV, July 25–28, 1978.

9 Hergt, P., and Krieger, P., "Radial Forces in Centrifugal Pumps With Guide Vanes," Advance Class Boiler Feed Pumps," *Proceedings, Institution of Mechanical Engineers*, Vol. 184, Pt 3N, 1969–1970, pp. 101–107.

10 Iversen, H. W., Rolling, R. E., and Carlson, J. J., "Volute Pressure Distribution, Radial Force on the Impeller and Volute Mixing Losses of a Radial Flow Centrifugal Pump," ASME *Journal of Engineering for Power*, Vol. 82, Apr. 1960, pp. 136–144.

11 Kurokawa, J., "Theoretical Determinations of the Flow Characteristics in Volutes," IAHR/AIRH Symposium, Tokyo, Japan, 1980, pp. 623–634.

12 Ohashi, H., Shoji, H., Yanagisawa, S., and Tomita, K., "Experimental Study of Fluid Forces on Whirling Centrifugal Impeller in Vaneless Diffuser," Symp. Fluid/Structures Interactions in Turbomachinery, Thompson, W. E., ed., ASME Winter Annual Meeting, 1981, pp. 57–62.

13 Pollman, E., Schwerdtfeger, H., and Termuehlen, H., "Flow Excited Vibrations in High Pressure Turbines (Steam Whirl)," ASME *Journal of Engineering for Power*, Vol. 100, Apr. 1978, pp. 219–228.

14 Stepanoff, A. J., *Centrifugal and Axial Flow Pumps*, 2nd ed., Wiley, New York, 1957.

15 Thompson, W. E., "Fluid Dynamic Excitation of Centrifugal Compressor Rotor Vibrations," ASME JOURNAL OF FLUIDS ENGINEERING, Vol. 100, Mar. 1978, pp. 73–78.

Centrifugal Compressors and Pumps," PhD Thesis, Department of Machine Design, Technical University of Denmark, 1979.

7 Domm, H., and Hergt, P., "Radial Forces on Impeller of Volute Casing Pumps," Flow Research on Blading," Dzung, L. S., ed., Elsevier Publishing Co., The Netherlands, 1970, pp. 305-321.

8 Ek, M. C., "Solution of the Subsynchronous Whirl Problem in the High Pressure Hydrogen Turbomachinery of the Space Shuttle Main Engine," Paper No. 78-1002, AIAA/SAE 14th Joint Propulsion Conf., Las Vegas, NV, July 25-28, 1978.

9 Hergt, P., and Krieger, P., "Radial Forces in Centrifugal Pumps With Guide Vanes," Advance Class Boiler Feed Pumps," *Proceedings, Institution of Mechanical Engineers*, Vol. 184, Pt 3N, 1969-1970, pp. 101-107.

10 Iversen, H. W., Rolling, R. E., and Carlson, J. J., "Volute Pressure Distribution, Radial Force on the Impeller and Volute Mixing Losses of a Radial Flow Centrifugal Pump," ASME *Journal of Engineering for Power*, Vol. 82, Apr. 1960, pp. 136-144.

11 Kurokawa, J., "Theoretical Determinations of the Flow Characteristics in Volutes," IAHR/AIRH Symposium, Tokyo, Japan, 1980, pp. 623-634.

12 Ohashi, H., Shoji, H., Yanagisawa, S., and Tomita, K., "Experimental Study of Fluid Forces on Whirling Centrifugal Impeller in Vaneless Diffuser," Symp. Fluid/Structures Interactions in Turbomachinery, Thompson, W. E., ed., ASME Winter Annual Meeting, 1981, pp. 57-62.

13 Pollman, E., Schwerdtfeger, H., and Termuehlen, H., "Flow Excited Vibrations in High Pressure Turbines (Steam Whirl)," ASME *Journal of Engineering for Power*, Vol. 100, Apr. 1978, pp. 219-228.

14 Stepanoff, A. J., *Centrifugal and Axial Flow Pumps*, 2nd ed., Wiley, New York, 1957.

15 Thompson, W. E., "Fluid Dynamic Excitation of Centrifugal Compressor Rotor Vibrations," ASME JOURNAL OF FLUIDS ENGINEERING, Vol. 100, Mar. 1978, pp. 73-78.

DISCUSSION

H. Ohashi[2]

As one who has the same interest in the hydrodynamic forces of whirling centrifugal impellers, I would like to express my respect for carrying out such delicate and complex experiments successfully. Following are a few comments on your result.

1 Despite a remarkable difference in the average volute forces F_0 of Volute A and B, the difference in the stiffness matrices of both volutes is surprisingly small. This may imply that stiffness matrices are insensitive to the configuration of volute casing. It is, however, still unknown how stiffness is affected by impeller geometries.

The result for centrifugal impellers in vaneless diffuser obtained by our test facility [16] showed a smaller diagonal term (about one quarter of equation (4)) and cross-coupling term which was destabilizing at lower flow rate and stabilizing around design flow rate.

Therefore, the stiffness matrices can be quite different from one impeller to another and the result approximately presented by equation (4) seems applicable to a specific impeller.

2 Since the hydrodynamic stiffness of impeller vanes and shrouds are different in nature, the fraction of outlet width b_2 to total width w_2 is an important parameter. Please give the value of the test Impeller X.

3 At lower flow rate close to shutoff, the flow in the impeller becomes quite turbulent and the fluid force fluctuates violently. Have you experienced any measurement problems associated with this phenomena?

Additional Reference

16 Ohashi, H., Shoji, H., and Kato, C., "Experimental Study of Fluid Forces on Whirling Centrifugal Impeller (1st Report; Impeller in Vaneless Diffuser)," *Trans. JSME*, Vol. 51, No. 467, July 1985, pp. 2373-2381 (in Japanese) or NASA CP 2338, 1985, pp. 109-122.

[2]Mechanical Engineering, University of Tokyo, Bunkyo-Ku, Tokyo 113, Japan.

Authors' Closure

The authors wish to thank Professor Ohashi for his continuing interest in this paper in particular, and this research field in general. The work presented herein was concluded in late 1982 and has since been validated and extended at the Caltech Rotor Force Test Facility to inlcude the full dynamic effect of whirl [17, 18]. Currently additional research was also initiated to study the effects of cavitation inception and net positive suction head on the magnitudes of the stiffness matrix coefficients [19]. While we agree that the similarities between the stiffness matrices of Volutes A and B are relatively striking, additional experiments by Jery, et al. [17] for 7 different volutes/diffusers and 2 different impellers of about the same specific speed seem to validate that fact. The stiffness matrices Professor Ohashi obtained in his very valuable study are much lower than those presented here probably because of the large collector case used in his experiment. An impeller discharging in an infinite medium should have no stiffness coefficients.

The width of the impeller discharge including the shrouds is 26 mm. The internal width of the discharge is 16 mm as shown in Fig. 11. We believe that the latter dimension is the important one.

No wild fluctuation in forces were observed at shutoff for the steady-state measurements presented in this paper. In a communication with B. Jery [17, 18], it also seems that their experimental results were quite consistent and repeatable.

Additional References

17 Jery, B., Brennen, C. E., Caughey, T. K., and Acosta, A. J., "Forces on Centrifugal Pump Impellers," *Proceedings of the 2nd International Pump Symposium*, Houston, TX, April 30-May 2, 1985, pp. 21-32.

18 Jery, B., Acosta, A. J., Brennen, C. E., and Caughey, T. K., "Hydrodynamic Impeller Stiffness, Damping and Inertia in the Rotordynamics of Centrifugal Flow Pumps," *Workshop on Rotordynamic Instability Problems in High-Performance Turbomachinery*, Texas A&M University, NASA Conference Publication 2338, 1984, pp. 137-160.

19 Franz, R., Acosta, A. J., Brennen, C. E., and Caughey, T. K., "Effects of Cavitation on the Radial Forces in a Centrifugal Pump," to be published, Oral presentation by C. E. Brennen at the 2nd Joint ASCE/ASME Mechanics Conference, University of New Mexico, Albuquerque, June 23-26, 1985.

E. F. Brown
Virginia Polytechnic Institute
and State University,
Blacksburg, VA

G. L. Hamilton

D. W. Kwok

McDonnell Douglas Corporation,
Douglas Aircraft Company,
Long Beach, CA

A Comparison of Three Critical Flow Venturi Designs

Three critical flow venturi designs have been examined from the standpoint of their sensitivity to initial boundary-layer thickness, inlet flow nonuniformity, separation, and transition point location. These sensitivity studies were carried out with a finite-difference computer code which represents a coupled solution of the inviscid potential core and the viscous boundary layer. Since it makes good sense to select a design that is least sensitive to these effects, it is expected that this information will be of interest to potential users of these devices. Differences between the sensitivities of the various designs were found to be small; however, a slight advantage is seen in designs which employ a circular arc entrance section and a circular arc throat.

Introduction

The advantages of critical flow venturis for mass flow measurements are well known and their use is common in aircraft propulsion systems testing. Throughout the past 20 years, a number of critical flow venturi designs have evolved. An early design proposed in 1962 by Smith and Matz [1] featured a circular arc (toroidal) inlet and throat section mated to a 6-deg conical diffuser. This design was selected to facilitate the theoretical calculation of the discharge coefficient and to minimize uncertainties involved in the calculation of centrifugal and boundary-layer effects. In 1966, Jaumotte [2] described a critical flow venturi which in this paper will be called the LMEF venturi (for the Laboratoire de Mécanique Expérimentale des Fluides of the University of Paris where this design was developed). Like the Smith and Matz venturi, the inlet section is a toroid. The throat section, rather than being a continuation of the torus, is cylindrical, having a length of two throat radii. This is connected to a 3.5-deg conical diffuser. An advantage claimed for this design is its insensitivity to variations in the shape of the inlet section. In 1969, Dudzinski [3] tested a critical flow venturi design which featured an inlet and throat designed in accordance with ASME standards for low beta ratio, long radius-type flow nozzles coupled to an offset 4-deg conical diffuser. In this paper, this design will be called the ASME critical flow venturi. An obvious advantage of this design is that it is built around an already accepted standard. Other designs have been proposed, such as that of Stratford [4] but none have gained the degree of acceptance which the previously mentioned three designs have.

Although critical flow venturi devices have been used for many years to measure steam and gas flows (see, for example, Arnberg [5]), the authors have limited themselves to the designs of references [1–3] in the belief that these provide both a representative sample of modern critical flow venturi designs and sufficient experimental data to verify the accuracy of the numerical calculations.

Contributed by the Fluids Engineering Division for publication in the JOURNAL OF FLUIDS ENGINEERING. Manuscript received by the Fluids Engineering Division, July 10, 1985.

Despite considerable efforts both here and abroad, there is at present no national or international standard for critical flow venturi design. Consequently, it is up to the user to choose the venturi design and the manner of its installation. Once the venturi has been fabricated, it must be calibrated before it can be used. Despite the best of intentions, there will be unavoidable differences between the facility in which the venturi was calibrated and the facility in which it will ultimately be used. Accordingly, in addition to such obvious considerations as manufacturability and cost, a critical flow venturi design cannot be selected without considering the degree of confidence one has in the transferability of the measured discharge coefficient from the laboratory environment to the workplace. For example, questions such as the following need to be asked with regard to the chosen design:

1 Assuming that the turbulence level will be significantly different between the calibration rig and the test facility, what is the sensitivity of the venturi's discharge coefficient to laminar/turbulent transition?

2 Assuming that the degree of uniformity of the inlet flow may differ between the calibration rig and test facility, what is the venturi's sensitivity to inlet flow distortions?

3 Assuming that the location and extent of any zones of separated flow may be strongly facility-dependent, what is the venturi's sensitivity to changes in the effective inlet geometry by varying degrees of flow separation?

4 Assuming that the boundary-layer history (including boundary-layer conditioning) may differ between calibration rig and test facility, what is the venturi's sensitivity to different inlet boundary-layer thicknesses?

The purpose of this paper is to provide answers to these questions for the Smith and Matz, LMEF, and ASME designs.

Description of Method

The sensitivites of the three critical flow venturi designs were assessed by means of a numerical method which is

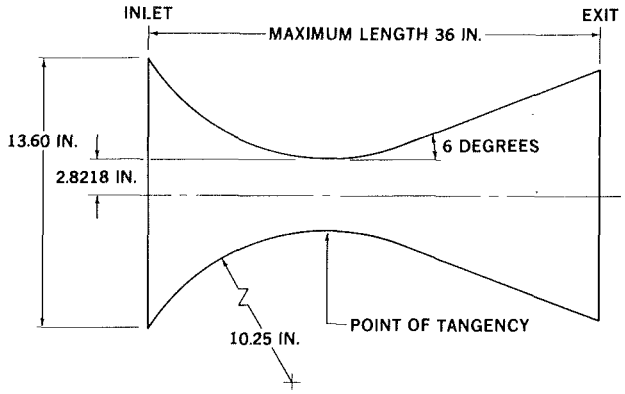

Fig. 1 Smith and Matz venturi geometry

particularly well suited to accurate calculation of such viscous internal flows. The numerical solution in fact is the consolidation of two highly developed and well-documented programs. For the core flow (that is, for the region excluding the boundary layers) the MTRAN program developed by Brown, et al. [6] was used. For the boundary-layer calculations, the well-known Cebeci boundary-layer code was used.

Core Flow Calculations

The MTRAN program, which was used for the core flow calculations, solves the equations of inviscid rotational transonic flow by a type-dependent differencing scheme. The program is especially well suited to the performance comparisons considered in this paper since it is accurate and considerably more flexible, comprehensive, and efficient than other methods reported in the literature for predicting critical flow venturi performance. An indication of the accuracy of the program is provided in reference [6] where the MTRAN calculations are compared with the well-known series expansion solution of Oswatitch and Rothstein [7]. Excellent agreement was observed between the computed and theoretical results. Additional test cases have been run at Douglas Aircraft Company which further confirm the accuracy of the calculations. An indication of the efficiency of the MTRAN code can be obtained by a comparison with the time-dependent methods used by Smith and Matz in their 1973 paper [8]. They report computational times on an IBM 370 amounting to approximately 1 hr. For a comparable calculation the MTRAN code requires less than 3 min. A large class of venturi geometries can be considered with the MTRAN code. This contrasts sharply with series expansion solutions such as those used by Szaniszlo [9] wherein only nozzles with throats of circular arc cross section can be considered. Not only does this restrict the class of geometries which may be considered but excludes the possibility of interactive boundary-layer calculation since the effect of a boundary layer produces an effective throat shape which is far from circular even for a circular-arc throat design. In addition, in series expansion solutions, the shape of the inlet is excluded from the calculations, whereas the MTRAN code includes the entire venturi geometry in the calculations. Finally, because the MTRAN code allows rotational flow effects to be included, the effects of inlet flow distortion on venturi performance can be easily predicted.

Boundary-Layer Program

For the boundary-layer calculations, Cebeci's method was used. This method is currently used by a large number of jet engine and airframe manufacturers and by many government agencies. It employs an efficient and accurate two-point finite-difference scheme [10] and an algebraic eddy-viscosity formulation developed by Cebeci and Smith [11]. It has been employed for a wide range of external and internal geometries and boundary conditions, and its accuracy has been demonstrated to be very satisfactory [12].

Coupling Method

Because of the demands of high accuracy and the inclusion of zones of separated flow required for the venturi performance comparisons made in this paper, it was necessary to couple the core flow and boundary-layer calculations. This produces what is known as a strongly interactive calculation in that the effects of the boundary layer on the core flow are acknowledged by the core flow calculations. This is accomplished by an iterative procedure in which the core flow is first calculated with the actual nozzle geometry providing the boundaries of the flow. With the edge conditions provided by this inviscid calculation, the boundary-layer calculations are then carried out and a displacement thickness along the venturi wall obtained. This displacement thickness is then used to modify the venturi geometry and the core flow calculations are run once again. As a consequence of the displacement effects of the boundary layer, the edge conditions are now slightly different and the boundary-layer calculations must accordingly be repeated. The procedure of calculating first the core flow and then the boundary-layer flow is repeated until subsequent calculations show an insignificant change in the edge conditions. Up to four iterations have been investigated in order to assure that adequate convergence has been obtained; however, in most cases satisfactory accuracy results from only a single iteration.

Calculation Details

Attention was first focused on the matter of choosing the number of computational points to be used in calculations. For this purpose, a number of runs were made with up to 49 points in the radial direction and 97 points in the axial direction. The computational points were uniformly distributed in both directions. It was finally decided to use 49 points in the axial direction and 23 points in the radial direction since no appreciable change in the results was evident when a finer mesh was used. Obviously, using such a coarse mesh would be unthinkable in a Navier-Stokes calculation; however, it should be remembered that in the present case the flow at the wall is to be computed by a separate boundary-layer program.

For the initial inviscid calculations, the venturi geometry was supplied by analytical relations; however, in the subsequent boundary layer corrected calculations a point-by-point specification of the adjusted venturi geometry was used to vary the throat Reynolds number. Values of the reference static pressure from 500 to 40,000 psi were used. This corresponds to throat Reynolds numbers from 1×10^4 to 7×10^6.

Venturi Geometries

The toroidal venturi used by Smith and Matz is shown schematically in Fig. 1. This design is based on a throat radius of curvature-to-radius ratio of 3.635. The throat connects directly to the 6-deg conical diffuser section. In the tests conducted by Smith and Matz, the venturi was installed in a 30-in-dia pipe by a mounting flange located just downstream of the throat section.

The ASME venturi used in this investigation is shown in Fig. 2. The inlet section is a standard ASME low beta ratio flow nozzle with a throat diameter of 8 in. and a beta ratio of 0.42. In accordance with ASME standards, the inlet section is a quarter ellipse with a semimajor axis equal to the throat

diameter and a ratio of major to minor axes of 1.5. The throat is cylindrical, 6 in. in length, and is connected to a conical diffuser with a half-angle of 3.75 deg. In the experiments of reference [8], the venturi was mounted in a 20-in-dia pipe.

The design of the LMEF venturi shown in Fig. 3 is taken from Vincent [13]. It features a toroidal inlet with a 1.024-in. (26-mm) radius of curvature and a 1.024-in. (26-mm) dia cylindrical throat which is 1.024 in. (26 mm) long. The conical diffuser has a half angle of 3.5 deg. Tests were conducted with this venturi mounted in a 2.362-in. (60-mm) dia pipe.

A Preliminary Validation Study

Before specifically addressing the four calibration-related problems mentioned in the Introduction, the accuracy of the calculation method used in this study will be determined. For this purpose the calculated values of the discharge coefficients of the Smith and Matz, ASME, and LMEF venturis will be compared with experimental data. For these calculations the venturi geometries described in references [1, 3, 13] were used. The results are shown in Figs. 4–6.

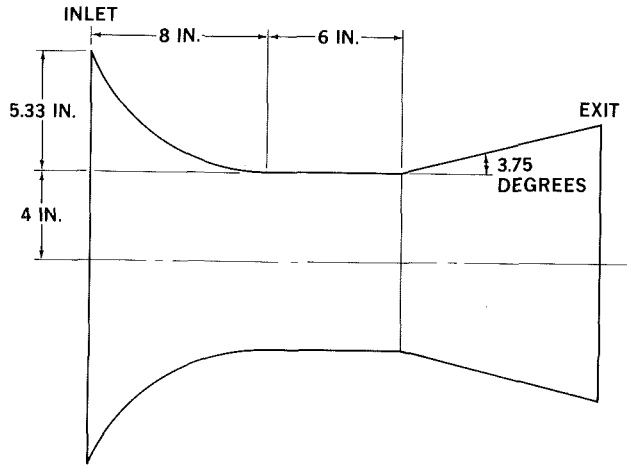

Fig. 2 Low beta ratio ASME venturi geometry

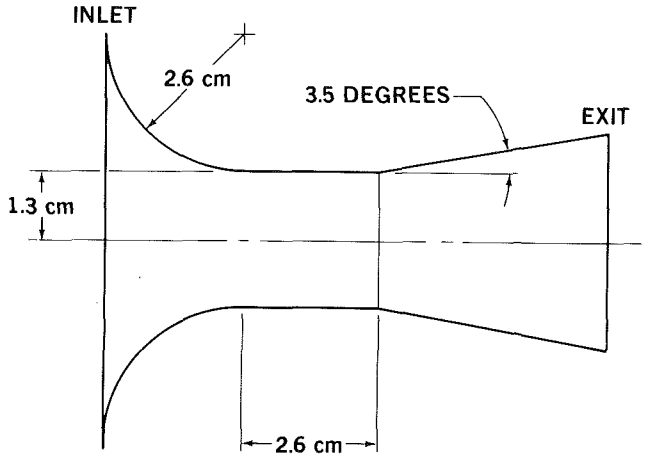

Fig. 3 LMEF venturi geometry

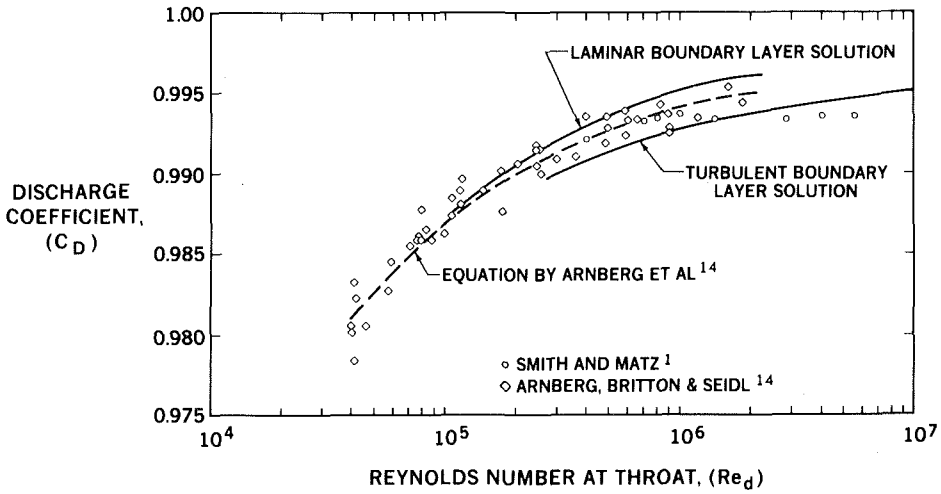

Fig. 4 Smith and Matz critical flow venturi performance

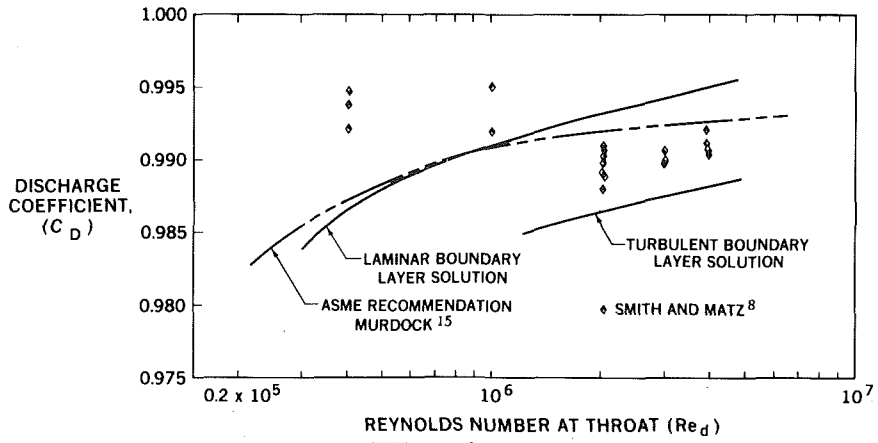

Fig. 5 ASME venturi performance

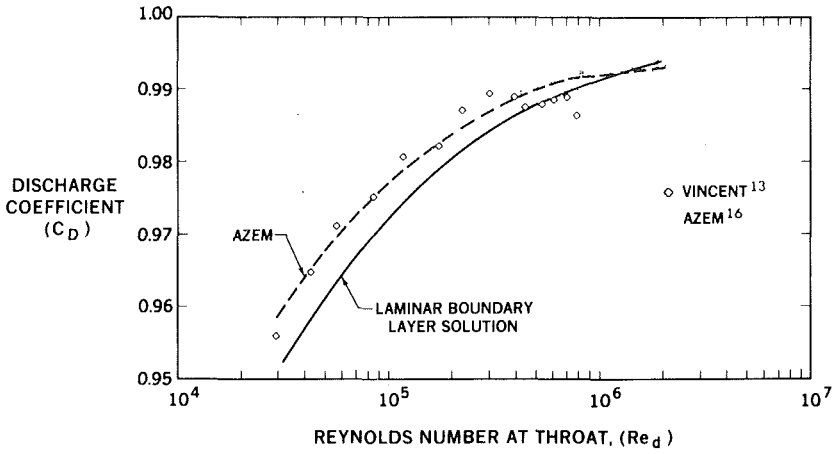

Fig. 6 LMEF venturi performance

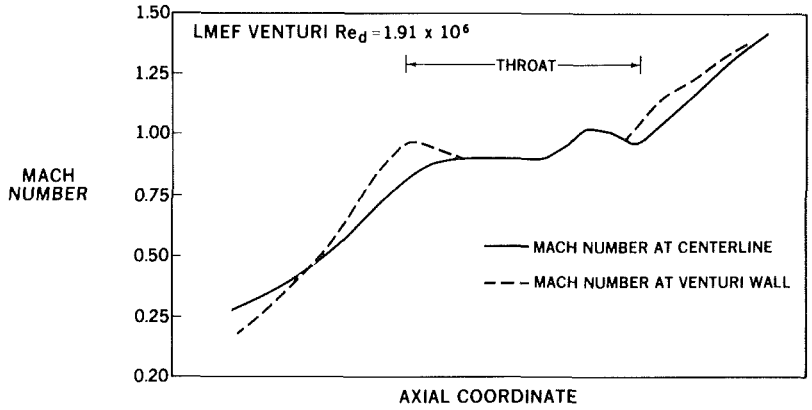

Fig. 7 Axial Mach number distributions

The agreement of the calculated results with experiments is particularly good for the Smith and Matz venturi where an accuracy of approximately 0.1 percent is seen. In addition, agreement is equally good with the correlation of Arnberg [14]. The inability to calculate as accurately the discharge coefficients for the ASME and LMEF designs may be associated with the discontinuity in the radius of curvature at the junction of the inlet and throat sections of these designs. This produces a strong local acceleration of the flow, which is clearly seen in Fig. 7, where in the LMEF venturi, the Mach number quickly rises toward sonic values at the beginning of the throat section. This causes a rapid decrease in the boundary-layer thickness which may not be well predicted by the boundary-layer calculations.

It should be pointed out that the difference between the laminar and the turbulent values of the discharge coefficients shown in Figs. 4–6 is a measure of the uncertainty of the discharge coefficient, since in the transition region it is unknown whether the flow is laminar or turbulent. Note that the difference between the laminar and turbulent calculations is only about 0.2 percent for the Smith and Matz venturi and more than 0.6 percent for the ASME venturi. The effect of transition will be more thoroughly considered in the following section. Comparison of the calculated results with experiment show that the transition Reynolds number is approximately 0.5 to 2.0 $\times$ 10^6 for both the Smith and Matz and ASME venturis.

These figures show a tendency of the experimental data to level off at high Reynolds numbers while the calculated results continue to rise. However, until additional experimental data at high Reynolds numbers are obtained, there is insufficient evidence to determine if, in fact, a discrepancy exists.

Laminar-Turbulent Transition

In Fig. 8 the discharge coefficients calculated for the three venturis for various positions of the transition point are shown. For these calculations the location of the transition point was manually set and corresponded to locations varying from the venturi inlet to the beginning of the diffuser. It can be seen from Fig. 8 that the discharge coefficient of the Smith and Matz venturi gradually increases as the transition point location is moved downstream. This contrasts with the behavior of the ASME and LMEF venturis where, rather than monotonically increasing as the transition point is moved downstream, the discharge coefficient first increases and then decreases as the transition point is moved into the throat region. Considering only the ASME venturi for a moment, the "overshooting" adds to the already large difference between the laminar and turbulent discharge coefficients previously alluded to and further contributes to the uncertainty of the discharge coefficient in the transition region. Some experiments have also shown evidence of this overshooting or "humped" behavior of the discharge coefficient; see, for example, Hall [17]. Experiments by Szaniszlo [9] showed that the overshoot is much more severe in the ASME venturi than it is for nozzles which feature continuous wall curvature such as the Smith and Matz design. Our calculations confirm these results.

Inlet Flow Nonuniformity

The wall boundary layer considered in the previous sections is in reality a type of inlet flow nonuniformity; a nonuniformity in which the total pressure at the centerline is greater than the value at the wall. An upstream elbow

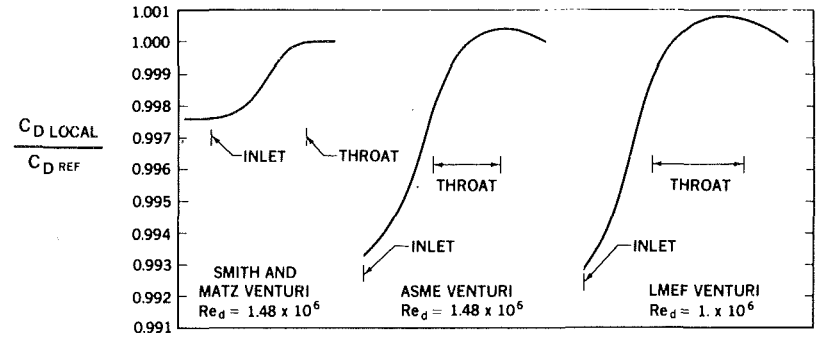

Fig. 8 Effect of transition point location

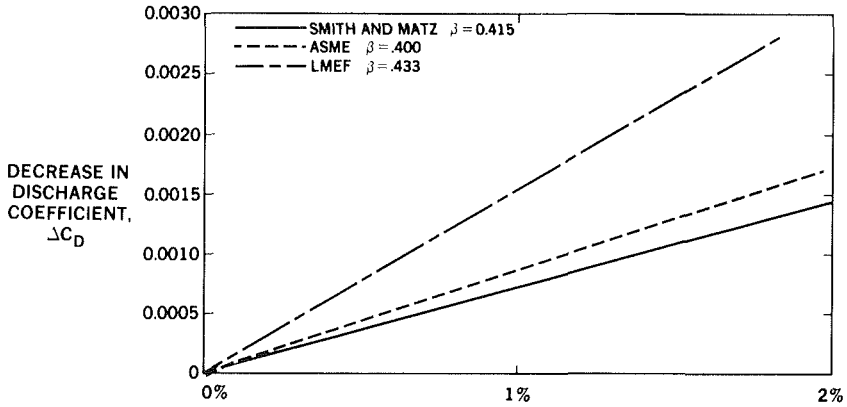

Fig. 9 Effect of pressure distortion

produces just the opposite effect. In this case, the total pressure at the wall is greater than at the centerline. This latter effect will be investigated in this section. Therefore, a linearly distorted total pressure profile will be used which has its minimum value at the centerline and its maximum value at the venturi wall. The distortion is expressed in terms of a ratio defined by

$$\frac{P_{max} - P_{min}}{P_{min}}$$

Since the presence of the boundary layer was not expected to change the results of these comparisons, only inviscid calculations were made. In addition, the diameter of the section upstream of the venturi was reduced from the diameter of the pipe to the diameter of the venturi inlet in order to avoid a numerical stability problem encountered in the use of the program for distorted inlet flows. In the calculations the maximum total pressure distortion was limited to 2 percent.

The results of these calculations, which appear in Fig. 9, clearly show that the Smith and Matz venturi has the least sensitivity to entrance flow pressure distortions. For a 2-percent pressure distortion the Smith and Matz discharge coefficient varies by 0.14 percent from its undistorted inlet flow value. The discharge coefficient of the LMEF venturi, on the other hand, changes by more than twice this amount.

Separation Effects

In conventional installations, the critical flow venturi is mounted in a large pipe. As a consequence, the flow in the pipe experiences a very large contraction prior to entering the venturi. A fluid particle near the wall of the pipe will not follow the contour of the wall, change direction suddenly, and flow into the inlet of the venturi. Instead, the flow will detach from the wall of the pipe and reattach to the venturi at some point in the inlet section. The location of the separation point depends on the local Reynolds numbers, the roughness of the pipe, the contraction ratio, and the turbulence intensity of the flow. The result of this separation is an uncontrollable change in the effective inlet shape which can have a significant effect on venturi performance.

To examine the effect of flow separation, several cases were investigated in which the zone of separated flow was approximated by a conical streamtube. Various cone half-angles were tried. The following cases are reported here: for the Smith and Matz venturi, cone half-angles of 30 and 60 deg; and for the LMEF venturi, cone half-angles of 45 and 60 deg. For all but the 60-deg Smith and Matz case, the conical streamtube was positioned so that it was locally tangent to the venturi inlet. For the Smith and Matz venturi, the maximum inlet wall angle was only 52.3 deg, and thus the 60-deg streamtube was positioned at the inlet lip. As in the previous calculations, the MTRAN program was first run to get the pressure gradient for the boundary-layer calculations. These calculations were conducted for a throat Reynolds number of about 1×10^6. Since at this Reynolds number the condition of the flow in the venturi was transitional, both laminar and turbulent calculations were made.

The results in Fig. 10 show that the Smith and Matz and ASME designs are almost completely insensitive to separation point location. For the LMEF venturi, the discharge coefficient decreased slightly from the 45-deg to the 60-deg configurations. The decrease was 0.09 percent for the laminar case and 0.18 percent for the turbulent case. These results do not substantiate the assertions of the proponents of the LMEF design which claim it to have limited sensitivity to the configuration of the inlet.

Initial Boundary-Layer Thickness

To examine the effect of increased boundary-layer thickness, the boundary layer was increased to correspond to an inlet pipe length which was 20 dia longer than the test

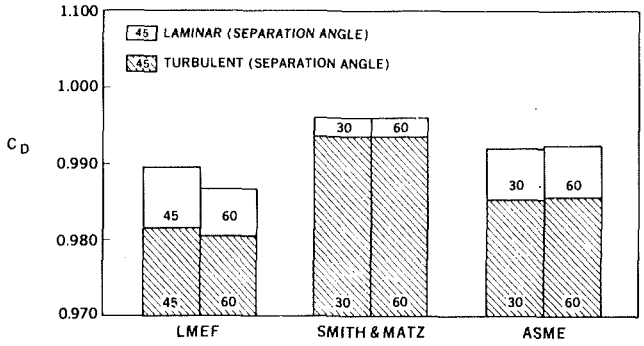

Fig. 10 Effect of separation

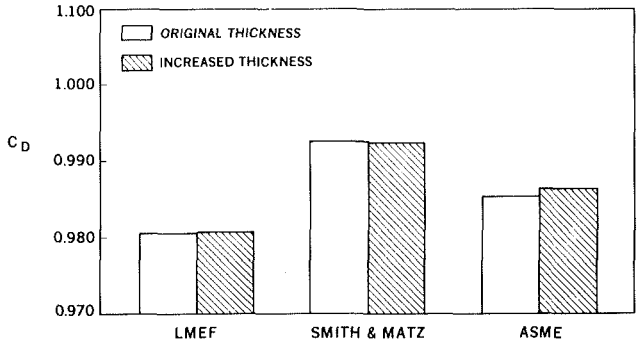

Fig. 11 Effect of boundary-layer thickness ($Re_d \cong 1 \times 10^6$)

conditions specified for each venturi. For the calculation of the discharge coefficient, additional computational points were introduced to accommodate this additional inlet section and still maintain a mesh spacing equal to that used in the original calculations. For both the turbulent and laminar flow calculations, there was no effect on the value of the discharge coefficient. This is shown in Fig. 11. There was one exception. For the turbulent ASME venturi calculations, the discharge coefficient was found to increase by 0.11 percent. This change was unexpected for two reasons: first, in no other case was a change in discharge coefficient observed and, second, the discharge coefficient (if it did change) would be expected to decrease and not increase. We are hypothesizing that the change in discharge coefficient observed for the ASME venturi is a result of the complicated nature of the flow in the throat which is produced by the previously mentioned discontinuity in wall curvature. It may even be possible that the flow in the throat may contain shock waves which would cause a rapid growth of the boundary layer not accounted for by the present calculations. In any event it appears that an accurate calculation of the flow may require more sophisticated modeling procedures that are contained in the present program, and therefore our calculations are overpredicting the values of the discharge coefficient.

Conclusions

The results reported here verify the accuracy of the computational technique and point to the superiority of the Smith and Matz venturi to the other designs investigated. In particular,

- For the Smith and Matz venturi, the experimentally measured discharge coefficients were predicted to within 0.1 percent. This tends to indicate that the flow in the venturi is for the most part "well-behaved." In other designs, discontinuities in the wall curvature produced regions of rapidly accelerating flow which might result in local regions of shock-induced boundary-layer separation. This makes the flow more difficult to model and introduces a mechanism for increased uncertainty in the experimental evaluation of the discharge coefficient.
- For the Smith and Matz venturi, the transition point location does not significantly affect the value of the discharge coefficient. Moreover, what variation there is occurs monotonically. With other designs the discharge coefficient varies by as much as 1 percent and there is a tendency of the discharge coefficient to overshoot.
- Of the three designs investigated, the Smith and Matz venturi showed the least sensitivity to inlet flow distortion.
- The Smith and Matz venturi (similar to the other designs) showed little sensitivity to either upstream separation effects or increases in the wall boundary layer thickness.

References

1 Smith, R. E., Jr., and Matz, R. J., "A Theoretical Method of Determining Discharge Coefficients for Venturis Operating at Critical Flow Conditions," ASME JOURNAL OF FLUIDS ENGINEERING, Dec. 1962, pp. 434-446.

2 Jaumotte, A. L., "Calculation of the Flow Coefficient of Nozzles by Means of the Boundary-Layer Theory," NASA TT-F-12475, Sept. 1969.

3 Dudzinski, T. J., Johnson, R. C., and Krause, L. N., "Venturi Meter With Separable Diffuser," ASME *Journal of Basic Engineering*, Mar. 1969, pp. 116-170.

4 Stratford, B. S., "The Calculation of the Discharge Coefficient of Profiled Choked Nozzles and the Optimum Profile for Absolute Air Flow Measurements," *Journal of the Royal Aeronautical Society*, Vol. 68 (640), Apr. 1964, pp. 237-245.

5 Arnberg, B. T., "Review of Critical Flow Meters for Gas Flow Measurements," ASME *Journal of Basic Engineering*, Dec. 1962, pp. 447-460.

6 Brown, E. F., Brecht, T. J. F., and Walsh, K. E., "A Relaxation Solution of Transonic Nozzle Flows Including Rotational Flow Effects," *Journal Aircraft*, Vol. 14 (10), Oct. 1977, pp. 944-951.

7 Oswatitch, K., and Rothstein, W., "Flow Pattern in a Converging-Diverging Nozzle," NACA Tech Memo No. 1215, 1949.

8 Smith, R. E., Jr., and Matz, R. J., "Performance Characteristics of an 8-in-dia ASME Nozzle Operating at Compressible and Incompressible Conditions," ASME JOURNAL OF FLUIDS ENGINEERING, Dec. 1973, pp. 542-550.

9 Szaniszlo, A. J., "Experimental and Analytical Sonic Nozzle Discharge Coefficients for Reynolds Numbers Up to 8×10^6," ASME Paper No. 74-WA/FM-8, 1974.

10 Cebeci, T., and Bradshaw, P., *Momentum Transfer in Boundary Layers*, McGraw-Hill/Hemisphere, Washington, D.C., 1977.

11 Cebeci, T., and Smith, A. M. O., *Analysis of Turbulent Boundary Layers*, Academic Press, New York, 1974.

12 Bradshaw, P., Cebeci, T., and Whitelaw, J. H., *Engineering Calculation Methods for Turbulent Flows*, Academic Press, London, 1981.

13 Vincent, J., "Sur la détermination expérimentale du coefficient de débit des tuyères soniques," C. R. Academic Society of Paris, t. 267, Apr. 1968, pp. 337-340.

14 Arnberg, R. T., Britton, C. D., and Seidl, N. F., "Discharge Coefficient Correlations for Circular-Arc Venturi Flowmeters at Critical (Sonic) Flow," ASME Paper No. 73-WA/FM-8, 1973.

15 Murdock, J. W., "A Rational Equation for ASME Coefficients for Long-Radius Flow Nozzle Employing Wall Taps at 1D and 1/2D," ASME Paper No. 64-WA/FM-7, 1964.

16 Azem, M., "Contribution à la mesure du débit au moyen de tuyères soniques, et de diaphragmes a l'aspiration," Societe d'Etude et de Diffusion des Industries Thermiques et Aérauliques, 8e annee No. 31, Dec. 1971, pp. 32-42.

17 Hall, G. W., "Application of Boundary-Layer Theory to Explain Some Nozzle and Venturi Flow Peculiarities," *Proceedings of the Institution of Mechanical Engineers*, London, Vol. 173, No. 36, 1959, pp. 837-870.

Coupled Parallel Flows in a Channel and a Bounding Porous Medium of Finite Thickness

N. Rudraiah
UGC-DSA Centre in Fluid Mechanics,
Department of Mathematics,
Central College,
Bangalore University,
Bangalore-560 001, India

The steady laminar flow in a parallel plate channel bounded below by a porous layer of finite thickness and above by a rigid impermeable plate moving with a uniform velocity is studied. The two cases, viz., the porous medium bounded below (i) by a static fluid and (ii) by a rigid impermeable stationary wall, are considered separately. The modified slip condition involving the thickness of the porous layer is derived using the variation of velocity in the porous medium with the proper matching conditions based on the physical considerations. It is shown that when the thickness of the porous layer tends to infinity our modified slip condition tends to the slip condition postulated by Beavers and Joseph [3]. Methods to estimate the viscosity factor λ and relative permeability are discussed. The velocity profiles in the porous layer are shown to exhibit the boundary-layer type very near the porous surface; they increase with increase in depth of the porous medium and decrease with increases in λ. We find that the effect of the finite thickness of the porous medium is significant only for large values of λ and small values of the porous parameter σ.

1 Introduction

In recent years considerable interest has been evinced in the study of flow past a porous medium [1] because of its natural occurrence and importance in many engineering problems such as porous bearings [2–7], porous rollers [8], porous layer insulation consisting of solid and pores [9] and, in biomathematics, particularly, in the study of blood flow in lungs [10, 11], in arteries [12], etc. It involves the study of fluid flow above and through a porous medium. The former flow is governed by the Navier-Stokes equation and the latter either by the Darcy equation or by a non-Darcy equation depending on the structure and depth of the porous medium. These two flows are coupled through a proper boundary condition at the porous surface. The crux of the problem here is to specify suitable boundary conditions. It has been customary to assume that the no-slip boundary condition is valid at the surface of the porous material. However, Beavers and Joseph (hereafter called BJ) [13] have shown that this no-slip condition is no longer valid at the permeable surface and have postulated the slip boundary condition

$$\frac{du}{dy} = \frac{\alpha(u_B - Q)}{\sqrt{k}} \tag{1}$$

called the BJ-slip condition which admits a nonzero tangential velocity at the porous surface. Here, u is the velocity parallel to the surface (Fig. 1), u_B is the slip velocity at the permeable surface $y = 0+$, Q is the Darcy velocity, k is the permeability and α is the slip parameter assumed to be independent of velocity. Actually, Q should have been the velocity of the porous medium at the permeable surface $y = 0-$, but the porous medium that they [13] have considered is such that the Darcy velocity is valid uniformly throughout the medium. They [13] have also performed experiments and the results are reported with a view to test the validity of the boundary condition. Subsequently, many investigators [14–17] have refined the experimental results of BJ [13] and Saffman [18] has provided a rigorous theoretical basis via average arguments for this slip velocity model. Taylor [15], Richardson [19], Rajasekhara [16], Rudraiah and Veerabhadraiah [20, 21] and Ranganna [17] have also investigated, both analytically and experimentally, the plane Couette flow bounded by a permeable material and an excellent agreement was found to prevail between the results for the slip velocity model and the experiments.

We note that the BJ condition (1) is valid only in a densely packed porous medium of large thickness so that the variation

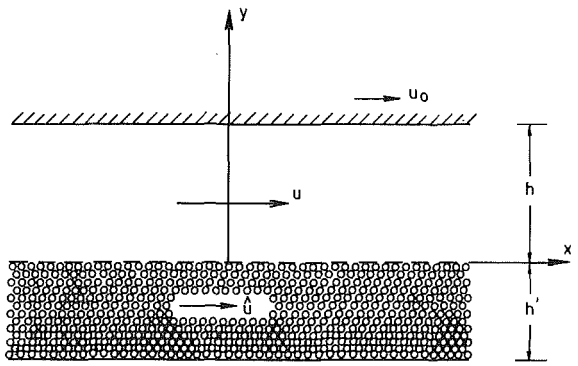

Fig. 1 Physical model of the channel bounded on one side by a porous media

Contributed by the Fluids Engineering Division for publication in the JOURNAL OF FLUIDS ENGINEERING. Manuscript received by the Fluids Engineering Division, July 11, 1983.

of velocity in it can be ignored and the flow is governed by the Darcy equation. However, many engineering problems cited earlier involve porous layers of shallow depth and of porosity close to unity. In such porous layers the velocity is no longer uniform and the distortion of velocity gives rise to the usual viscous shear. Therefore, instead of using the Darcy equation, one has to use a modified Darcy equation involving both the usual viscous force and the Darcy resistance. This will take care of the streamwise moving fluid in a thin boundary layer, just beneath the nominal surface, envisaged in the BJ-condition (1).

Williams [22] has investigated the flow of an incompressible viscous fluid through a porous medium incorporating the terms which account for capillary forces, drag forces and viscous shear effects. These equations, however, involved three unspecified coefficients and he has suggested the procedure to evaluate them. To determine the viscosity factor λ, one of the three unspecified coefficients, he has proposed the study of Poiseuille flow past a permeable material of finite thickness. The fluid flow through the porous material is governed by the Brinkman [23] equation with the physical conditions specified at the porous surface together with the no-slip condition at the rigid plate bounding the porous medium. We note that care must be taken in imposing the no-slip condition at the rigid plate bounding the porous medium. The no-slip condition is valid only when we invoke the concept of boundary layer which inevitably arises when the Brinkman [23] equation is used to describe the flow through a porous medium (see Rudraiah and Veerabhadraiah [21]. The work of Williams [22] is free from this boundary-layer concept and we discuss this in Section 3. Further, the work of Williams [22] pertains only to the determination of the viscosity factor λ but is silent about the nature of velocity distribution and the effect of the thickness of the porous layer on ther mass flow rate and the friction factor which are discussed in detail in this paper.

For this purpose, we consider a special type of porous medium of porosity close to unity made up of small identical spherical particles of radius d_p and number density N. Since the porosity, $\phi = 1 - (4/3)\pi d^3 N$, is close to unity, we choose d_p such that $d_p^3 N \to 0$ while $d_p N$ remains finite as $N \to \infty$, so that the force ($=6\pi\,\mu d_p\,Nu$) offered by the solid particles to the fluid remains finite. In this porous medium, the distortion of velocity gives rise to viscous forces. Thus we have to use the Brinkman [23] equation with suitable boundary conditions. This would provide a necessary understanding of the mechanism leading to skewing of the velocity profile and would explain the basis for the streamwise moving fluid in a thin layer of porous medium.

We consider the following two cases: (*i*) the porous layer bounded below by an impermeable wall and (*ii*) the porous layer bounded below by a stationary fluid. The motivation for the case (*i*) stems from the study of flow in porous bearings [2–7] and that for the case (*ii*) stems from the study of flow in biomechanics. Case (*i*) is similar to the one discussed by Williams [22] with the exception that the upper rigid plate (Fig. 1) is moving with a uniform velocity U_0, and to invoke the boundary-layer concept which inevitably arises when the Brinkman equation is used to incorporate the no-slip condition at the rigid wall bounding the porous medium.

The plan of this study is as follows: The basic equations and the corresponding boundary and matching conditions are discussed in Section 2. Solutions for the two cases mentioned above are obtained in Section 3.

Section 4 is devoted to detailed discussions. Methods to evaluate the viscosity factor λ and the relative permeability k' are also given in Section 4. It is shown that the velocity in the porous medium is large because the fluid is apt to slip at the porous wall.

2 Basic Equations and Boundary Conditions

The physical configuration illustrating the problem under consideration is shown in Fig. 1. It consists of a parallel plate channel bounded below by a special type of porous medium of porosity close to unity and bounded above by a rigid impermeable moving plate moving with a uniform velocity U_0. The height of the channel and the thickness of the porous medium are, respectively, h and h'. We use the Cartesian coordinate system (x, y) with the x-axis parallel to the surface and the y-axis perpendicular to it. The porous layer may be bounded below either by a thick layer of static fluid (i.e., the porous medium is sandwiched between two fluids, one of which is static) or by a rigid stationary wall. These two cases are studied separately. To obtain the required basic equations we make the following approximations:

(*i*) The fluid is Newtonian, viscous and incompressible.

(*ii*) The flow in the channel and in the porous medium, driven by a common uniform pressure gradient $\partial p/\partial x$ and by a shear produced by the motion of the upper plate, is steady, laminar, fully developed unidirectional, and parallel to the walls. This type of flow is called Poiseuille-Couette flow.

(*iii*) The flow in the channel in the porous medium is coupled through proper boundary conditions.

(*iv*) The viscosity of the fluid in the porous medium, $\hat{\mu}$, is assumed to be different from that of pure viscous fluid, μ, in the channel because the porous matrix may present less window for a fluid to react on itself or may enhance the drag. In this paper, following Williams [22], we use

$$\hat{\mu} = \lambda \Phi^2 \mu \tag{2}$$

where Φ is the porosity and λ, a positive constant, is a viscosity factor. The value of λ can be determined by identifying it with the slip parameter α in (1) which is independent of the velocity of fluid. We note that since the porous medium considered here is assumed to be made of sparsely distributed spherical particles of porosity close to unity, there will be a viscous shear produced by the distortion of the velocity in the bed. Therefore, we can measure λ using simple viscometers governed by

$$\frac{d^2u}{dy^2} = 0 \quad \text{and} \quad \frac{d^2\hat{u}}{dy^2} - \frac{\hat{u}}{\lambda k} = 0 \tag{3}$$

where u is the velocity of fluid above the bed, $\hat{u}$ is that in the bed and k is the permeability of the bed. It is also possible to obtain λ by identifying it with α, the slip parameter measured by BJ [13].

Under these approximations, the velocity field $u(y)$ in the channel must obey the Navier-Stokes equation

$$\frac{d^2u}{dy^2} = \frac{1}{\mu}\frac{\partial p}{\partial x} \tag{4}$$

and the velocity $\hat{u}(y)$ in the porous medium must obey the Brinkman equation

$$\frac{d^2\hat{u}}{dy^2} - \frac{1}{\lambda k}\hat{u} = \frac{1}{\hat{\mu}}\frac{\partial p}{\partial x}, \tag{5}$$

where k is the permeability of the porous material (which has the unit of length squared).

The velocity distribution in the channel and in the porous medium cannot be derived until the boundary conditions are prescribed. This is based on the following matching procedure [22]. The velocity $\hat{u}$ in the porous layer is related to the velocity in the channel by the relation

$$u = \Phi\hat{u}. \tag{6}$$

The viscous shear due to the distortion of the velocity in the porous layer should be taken into account because the fluid occupies almost all parts of the porous medium. Therefore, we propose that the fluid and the solid each receive a shearing

stress from the external stream. Then following Williams [22], we assume that the shear produced by the fluid in the channel (namely, $\Phi\mu\,\partial u/\partial y$) must be proportional to that in the porous layer (namely, $\lambda\,\phi^2\,\mu\,\partial u/\partial y$). Hence, the second matching condition is

$$\frac{\partial u}{\partial y} = \phi\lambda\frac{\partial \hat{u}}{\partial y}. \tag{7}$$

These matching conditions have to be supplemented with the boundary conditions.

To obtain the required boundary conditions, we consider as stated earlier, the following two cases:

Case 1: Corresponds to the porous layer bounded below by a thick layer of static fluid.

Case 2: Corresponds to the porous layer bounded below by an impermeable rigid wall.

For Case 1, the boundary conditions are

$$u = u_0 \quad \text{at} \quad y = h \tag{8}$$

$$\frac{du}{dy} = \sqrt{\lambda}\tanh(\delta h')(u_B - \phi\lambda Q)/\sqrt{k} \quad \text{at} \quad y = 0+ \tag{9}$$

$$u = \Phi\hat{u} \quad \text{at} \quad y = 0+. \tag{10}$$

$$\frac{d\hat{u}}{dy} = 0, \quad \text{at} \quad y = h' \tag{11}$$

where

$$\delta = (\lambda k)^{-1/2}.$$

u_B is the slip-velocity at $y = 0+$ and $Q = -(k/\lambda\phi\mu)(\partial p/\partial x)$ is the Darcy velocity which is valid away from the porous surface. Condition (9) or (12) is identical with (7). To compare these with BJ [13] condition we have transformed (7) to the form (9) or (12).

For the Case 2, the boundary conditions are (8) and (10) together with

$$\frac{du}{dy} = \lambda\delta\left[\frac{Q\lambda\phi}{\sinh(\delta h')} + (u_B\lambda\Phi)\coth\right] \quad \text{at} \quad y = 0+ \tag{12}$$

and

$$\hat{u} = 0 \quad \text{at} \quad y = h'. \tag{13}$$

Conditions (9) and (12) are the modified BJ-slip conditions which will be derived in the next section using the solution of (5) and the matching condition (7). As stated in the previous sections, the no-slip condition (13) is valid only when we use the concept of boundary layer, which inevitably arises when the Brinkman equation is used. Now we must consider the range of validity of this equation. For this purpose we introduce a typical characteristic length scale h of the problem i.e., large-scale flow. The ratio of the magnitude of the viscous force $\hat{\mu}\,\partial^2\hat{u}/\partial y^2$, to Darcy resistance $\hat{\mu}/\lambda k\,\hat{u}$ in (5) is $\lambda k/h^2$. Since, the viscosity factor λ is of order unity and k/h^2 is small if h is a macroscopic length scale, the viscous force term is small in the bulk of the porous medium and hence the Brinkman equations (5) reduces to the Darcy equation. In that case the fluid cannot sustain the usual shear so that the no-slip condition (13) is not valid. To use the no-slip condition (13), however, we should select the appropriate length scale h (i.e., small scale) which will correspond to the pore size so that k/h^2 is of order unity and hence Brinkman equation (5) is valid. Rudraiah and Veerabhadraiah [21] have shown that there exists a boundary layer, an extremely thin layer of fluid of thickness $k^{1/2}$, very close to the fluid-solid boundary in the medium where the no-slip condition (13) is valid.

We note that in the limit of $\delta h' \to \infty$, both (19) and (20) tend to the slip-condition

$$\frac{du}{dy} = \sqrt{\lambda}\frac{(u_B - Q')}{\sqrt{k}} \tag{14}$$

where $Q' = -k/\mu\,\partial p/\partial x$ is the Darcy velocity as used in BJ [13]. Condition (4) coincides with the BJ-slip condition (1) if $\sqrt{\lambda} = \alpha$. In other words, the slip parameter α used by BJ [13] has the physical meaning of the viscosity factor.

3 Solutions of the Problem

Solutions for the cases when the porous layer is bounded below either by a thick layer of static fluid or by an impermeable rigid wall are determined separately in this section.

3.1 Solutions When the Porous Layer is Bounded Below by a Static Fluid. Solutions of (4) and (5), satisfying the conditions (8)–(11) are

$$u = \frac{Ph^2}{2}\left[\eta^2 + \frac{2\delta_1}{\sigma^2}\eta\right] + (1 + \delta_1\eta)u_B, \tag{15}$$

$$\hat{u} = -\frac{Ph^2}{\sigma^2\phi}\{1 - \cosh[\delta_2(\epsilon+\eta)]/\cosh(\epsilon\delta_2)\}$$

$$+ \frac{u_B}{\phi}\cosh[\delta_2(\epsilon+\eta)]/\cosh(\epsilon\,\delta_2) \tag{16}$$

where

$$P = \frac{1}{\mu}\frac{\partial p}{\partial x},$$

$$u_B = -\frac{Ph^2}{2}f_0 \tag{17}$$

$$f_0 = \frac{(\sigma^2 P_0 + 2\delta_1)}{2\sigma^2(1+\delta_1)} \tag{18}$$

$$P_0 = 1 + \frac{2\mu U_0}{\left(-\frac{\partial p}{\partial x}\right)h^2}, \tag{19}$$

$\eta = y/h$, $\sigma = h/\sqrt{k}$, $\epsilon = h'/h$, $\delta_1 = \sigma\sqrt{\lambda}\tanh(\epsilon\delta_2)$, $\delta_2 = \sigma/\sqrt{\lambda}$.

Equation (7) using (16) leads to (10). We note that if $U_0 = 0$, i.e., $P_0 = 1$, we get the results of Poiseuille flow. If $\bar{u}$ is the mean velocity in the channel, (15) can be written in the form

$$\frac{u}{\bar{u}} = -\frac{6}{(3P_0 - 2)(1+f)}\left(\eta^2 + \frac{2\delta_1\eta}{\sigma^2}\right) + (1 + \delta_1\eta)\frac{u_B}{u} \tag{20}$$

$$\frac{u_B}{u} = \frac{6}{3 + \frac{\sigma^2(3P_0 - 2)(1+\delta_1)}{(\sigma^2 P_0 + 2\delta_1)}} \tag{21}$$

$$f = \frac{3(\sigma^2 P_0 + 2\delta_1)}{\sigma^2(3P_0 - 2)(1+\delta_1)} \tag{22}$$

We note that since $P_0 \geq 1$, $3P_0 - 2 \neq 0$.

It is readily verified that as $\epsilon \to \infty$ (20) and (21) tend to those given by Beavers, et al. [14] for large thickness of the porous layer. Thus the velocity in the porous medium exhibits boundary-layer nature near the surface and at large distances it approaches the Darcy velocity.

It is of interest to extract from the solution relations that involve quantities which may be measured through experiments. Among these are the mass flow rate and friction factor [14] in the channel. If M is the mass rate of flow per unit channel width, then

$$M=\int_0^h u\,dy=\rho\bar{u}h=-\frac{\rho Ph^3}{12}(3p_0-2)(1+f) \tag{23}$$

On the other hand, for a channel bounded by impermeable walls, the mass rate of flow is given by

$$M^*=-\frac{\rho Ph^3(3p_0-2)}{12} \tag{24}$$

where the asterisk is used to denote the solid-wall case. For the condition of equal pressure gradient and channel heights, the ratio of (23) and (24) yields.

$$M/M^*=1+f. \tag{25}$$

Since f is always positive, it follows that the presence of porous wall results in a higher mass flow.

Another physical phenomenon which can be measured easily in the laboratory is the friction factor C_f. Upon evaluating the definition [14],

$$C_f=\frac{4(-\partial p/\partial x)h}{\rho\bar{u}^2} \tag{26}$$

one finds

$$C_f\,\mathrm{Re}=96/1+f. \tag{27}$$

where $\mathrm{Re}=2\bar{u}h/\nu$. From this it is clear that the effect of the porous medium is to diminish the friction factor relative to that for a solid-walled channel for which $(C_fR_e)^*=96$.

Thus

$$\frac{C_fR_e}{(C_fR_e)^*}=\frac{1}{1+f} \tag{28}$$

From (27) it is clear that, C_fR_e product is a constant (i.e., independent of the Reynolds number) for a channel of fixed height, given porous bounding wall and for a given uniform velocity of the moving plate. From (28), it follows that the effect of the porous medium is to diminish the friction factor compared to that for a solid-walled channel.

3.2 Solutions When the Porous Layer Is Bounded Below by a Rigid Impermeable Plate. In this case, solutions of (4) and (5) satisfying the conditions (8), (10), (12) and (13) are

$$u=\frac{Ph^2}{2}\left[\eta^2+\frac{2\delta_3\eta}{\delta_2}-\frac{2\eta}{\delta_2\sinh(\epsilon\delta_2)}\right]+(1+\lambda\delta_3\delta_2\eta)u_B \tag{29}$$

$$\hat{u}=-\frac{Ph^2}{\sigma^2\phi}\left[1+\frac{\sinh(\delta_2\eta)}{\sinh(\epsilon\delta_2)}-\frac{\sinh\delta_2(\epsilon+\eta)}{\sinh(\epsilon\delta_2)}\right]+\frac{\sinh\delta_2(\epsilon+\eta)}{\sinh(\epsilon\delta_2)}\frac{u_B}{\phi} \tag{30}$$

$$u_B=-\frac{Ph^2(P_0\delta_2+2\delta_3)}{2\delta_2(1+\lambda\delta_3\hat{o}_2)}(1-g_0) \tag{31}$$

$$g_0=\frac{2}{(P_0\delta_2+2\delta_3)\sinh(\epsilon\delta_2)},\quad \delta_3=\coth(\epsilon\delta_2) \tag{32}$$

Equation (7) using (30) leads to (12). Note that if $u_0=0$, i.e., $P_0=1$, we get the results of Poiseuille flow. Even in this case, (12) tends to the BJ-slip condition (1) in the limit of $\delta h'\to\infty$ with $\sqrt{\lambda}=\alpha$.

If $\bar{u}$ is the mean velocity in the channel, (29) can be written as

$$\frac{u}{\bar{u}}=-\frac{6}{(3P_0-2)(1+g)}\left[\eta^2+\frac{2\delta_3\eta}{\delta_2}-\frac{2\eta}{\delta_2\sinh(\epsilon\delta_2)}\right]+(1+\lambda\delta_3\delta_2\eta)\frac{u_B}{\bar{u}} \tag{33}$$

$$u_B=\frac{6}{3+\dfrac{(3P_0-2)(1+\lambda\delta_3\delta_2)}{\left(P_0+\dfrac{2\delta_3}{\delta_2}\right)(1-g_0)}} \tag{34}$$

$$g=\frac{3\left(P_0+\dfrac{2\delta_3}{\delta_2}\right)(1-g_0)}{(3P_0-2)(1+\lambda\delta_3\delta_2)}. \tag{35}$$

As in Section 3.1, the expressions for the ratio of mass flow rates and the ratio of friction factors are, respectively, given by

$$M/M^*=1+g \tag{36}$$

$$\frac{C_fR_e}{(C_fR_e)^*}=\frac{1}{1+g}. \tag{37}$$

Here also we see that the presence of a porous layer increases the mass flow rate and decreases the friction factor.

4 Numerical Results and Discussions

The modified BJ-slip condition to describe the Poiseuille-Couette flow past a permeable material of finite thickness has been derived by solving the Brinkman equation for flow through a porous medium. The physical explanation for the validity of no-slip condition at the surface of a rigid boundary bounding the porous medium is given based on the existence of a boundary layer that arises inevitably when the Brinkman equation is used. It is found that the modified BJ-slip condition tends to the condition derived by Williams [22] if $P_0=1$ (i.e., $U_0=0$). With this new boundary condition, the physical problem is shown to involve two constants, the viscosity factor λ and the permeability k.

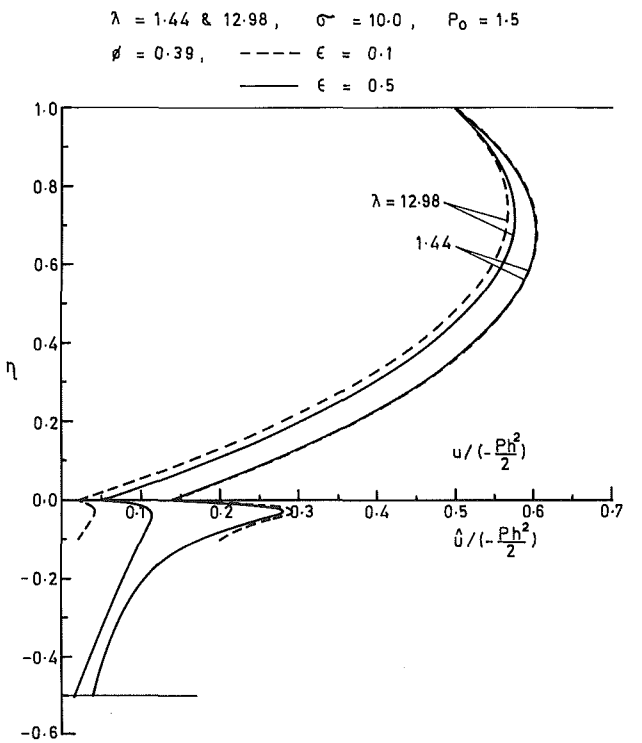

Fig. 2 Velocity profiles in the channel and porous space with slip condition at $y=-h'$

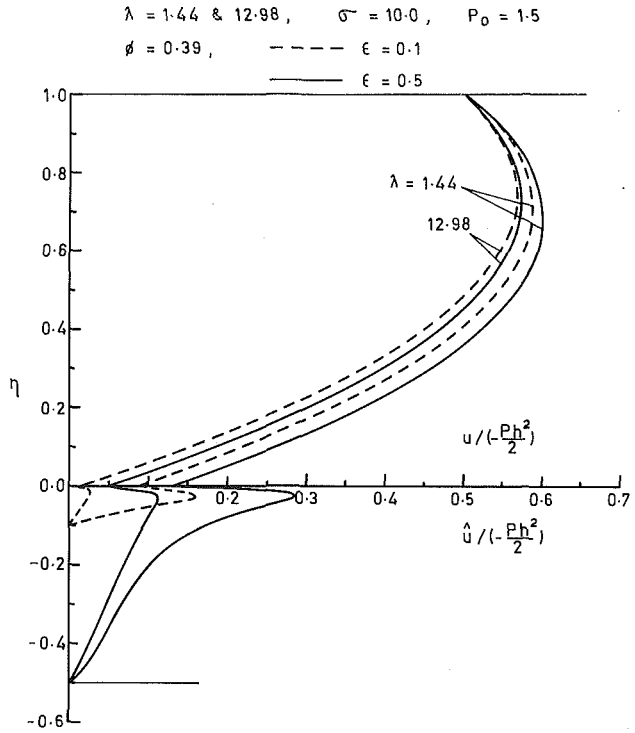

Fig. 3 Velocity profiles in the channel and porous space with no-slip condition at $y = -h'$

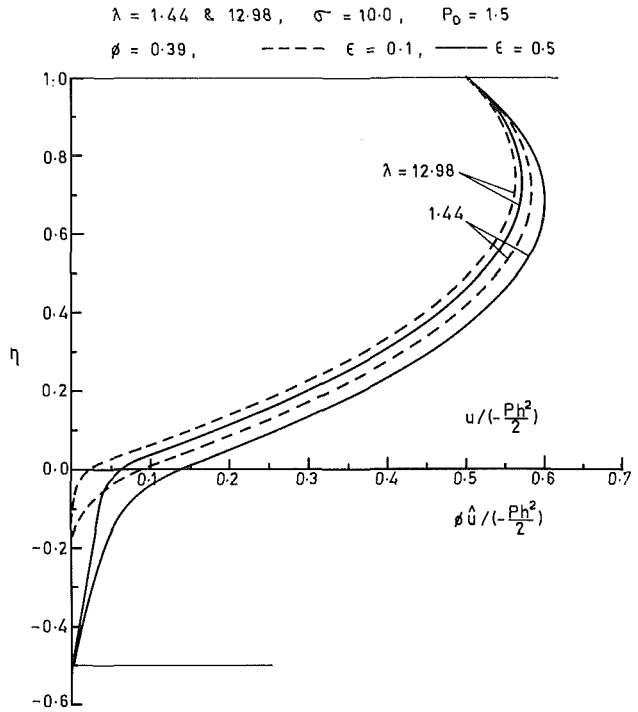

Fig. 5 Velocity profiles in the channel and porous space with no-slip condition at $y = -h'$

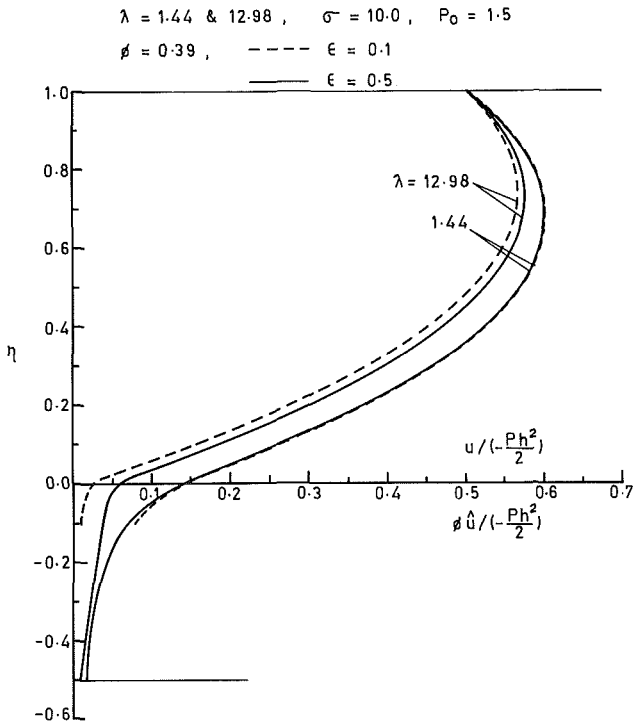

Fig. 4 Velocity profiles in the channel and porous space with slip condition at $y = -h'$

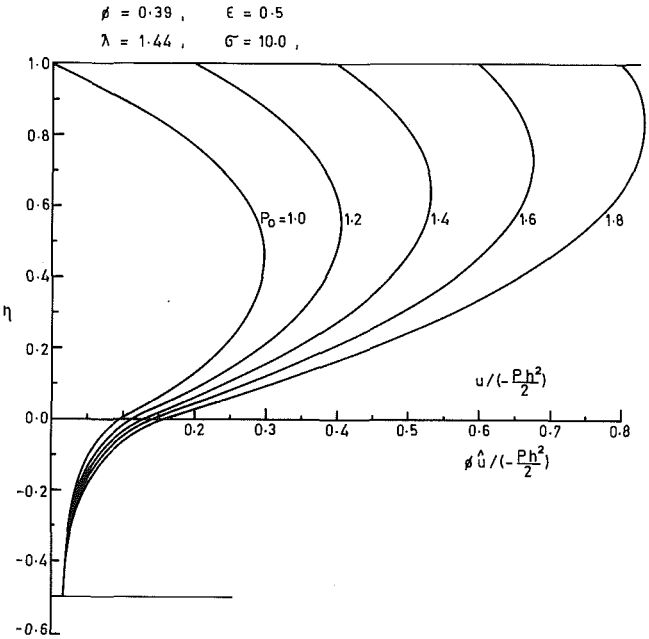

Fig. 6 Velocity profiles in the channel and porous space with slip condition at $y = -h'$

Comparing (1) and (14), we find that $\sqrt{\lambda} = \alpha$. In other words, the slip parameter α has the interpretation of the viscosity factor. The experiments of Taylor [15], Rajasekhara [16], and Ranganna [17] for couette flow and that of Rajasekhara [16] and Ranganna [17] for the case of Poiseuille flow (i.e., $P_0 = 1$) show that α is independent of the velocity profile and has the value in the range 0.1 to 4 for various porous media. Thus we can presume $0.01 \leq \lambda \leq 16$ for that class of porous materials. We note that Einstein's [24] formula for suspension of particles gives $\lambda = 12.98$ for $\phi = 0.39$ which lies in the range obtained from the experiments in [13], [14], and [17] for a particular porous medium. Therefore, we can conclude that Einstein's formula for the case of suspension of particles may be used, to a first approximation, to determine the value of λ. We also conclude that λ may be measured directly using simple viscometers. For this purpose, following Williams [22], we compute a simple shear solution for the two cases discussed in Section 3. For the Case 1, where the porous medium is bounded below by a static fluid, the solution for a plane couette flow driven purely by the shear produced by the motion of the upper plate, is

$$u = u_0 - A(1 - y/h), y > 0, \tag{38}$$

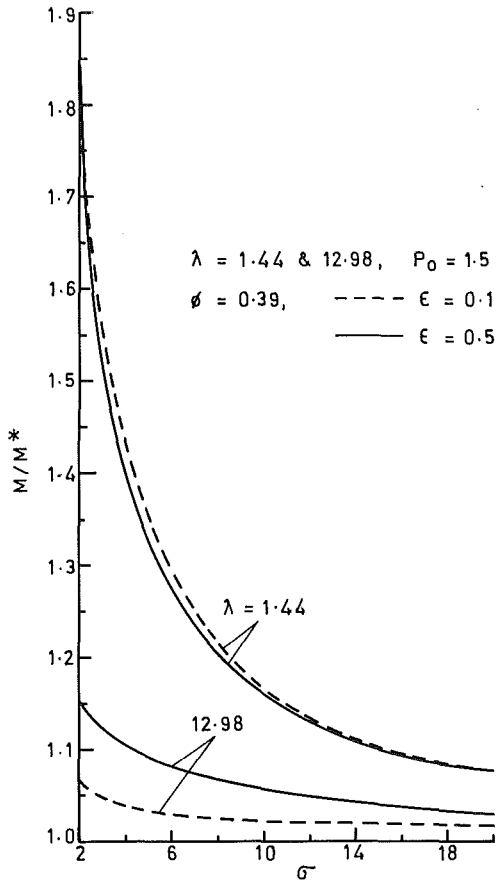

Fig. 7(*a*) Mass flow rate versus porous parameter with slip condition at $y = -h'$

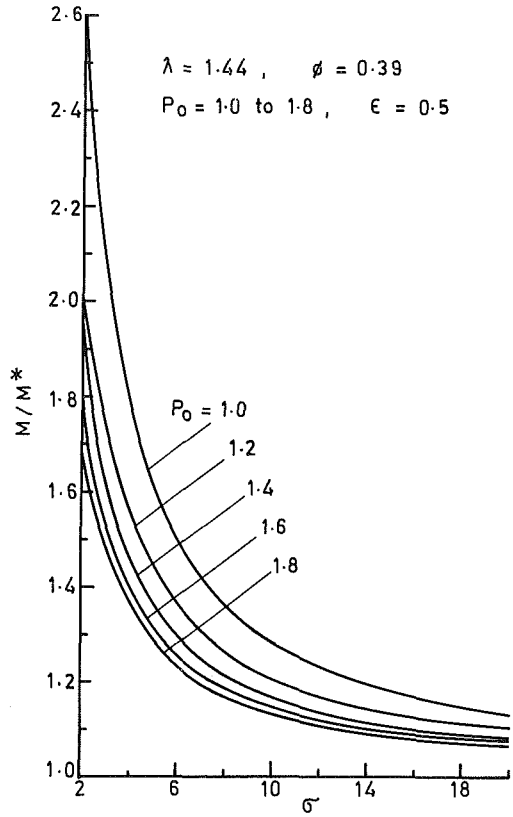

Fig. 8(*a*) Mass flow rate versus porous parameter with slip condition at $y = -h'$

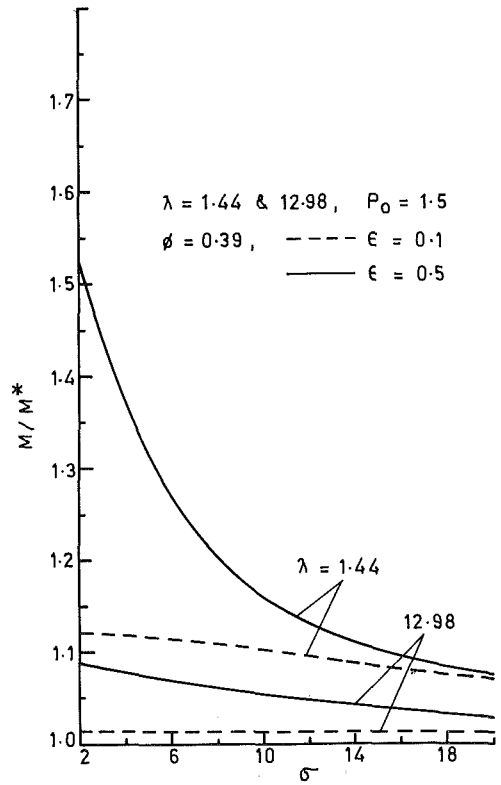

Fig. 7(*b*) Mass flow rate versus porous parameter with no-slip condition at $y = -h'$

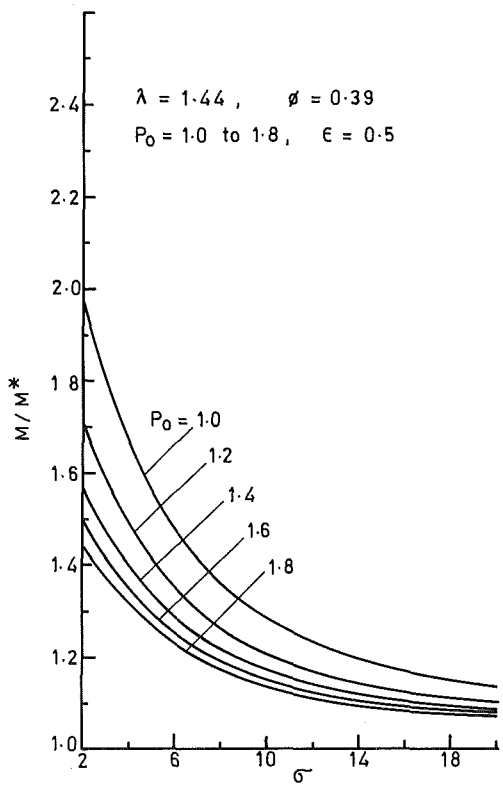

Fig. 8(*b*) Mass flow rate versus porous parameter with no-slip condition at $y = -h'$

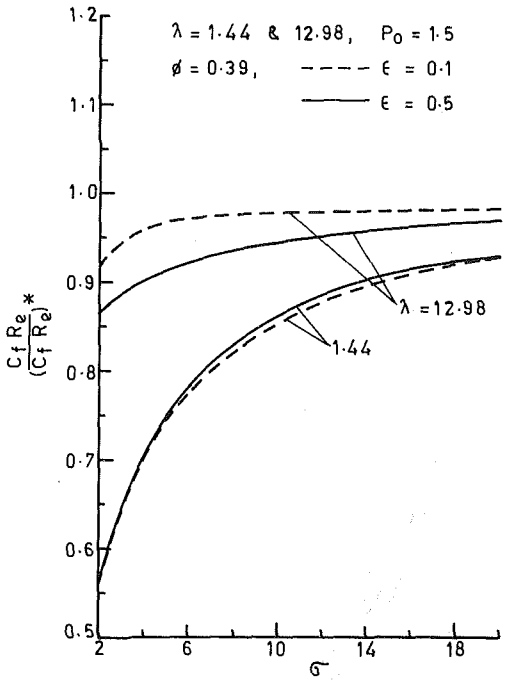

Fig. 9(*a*) Friction coefficient versus porous parameter with slip condition at $y = -h'$

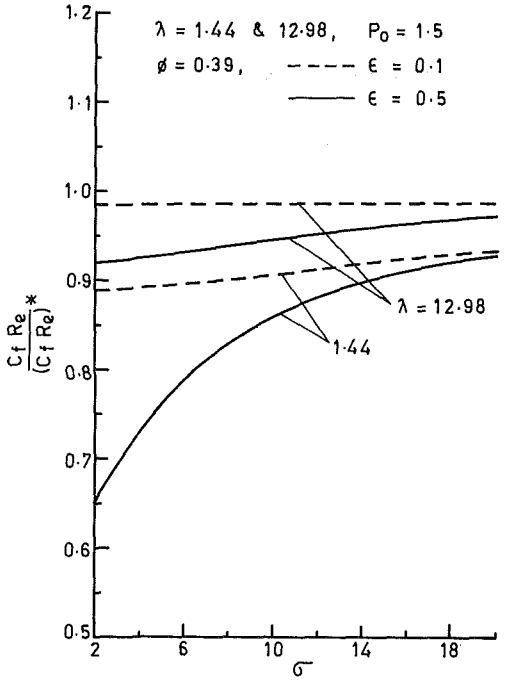

Fig. 9(*b*) Friction coefficient versus porous parameter with no-slip condition at $y = -h'$

$$\hat{u} = \frac{A}{\phi\delta_1}\left[\sinh \delta y + \frac{\cosh \delta y}{\delta_1}\right], \quad y<0 \tag{39}$$

where

$$A = u_0\delta_1 / 1 + \delta_1 \tag{40}$$

The shear force per unit area required to drive the motion in this case is

$$\mu \frac{u_0}{h + \dfrac{\coth(\delta h')}{\lambda\sigma}} \tag{41}$$

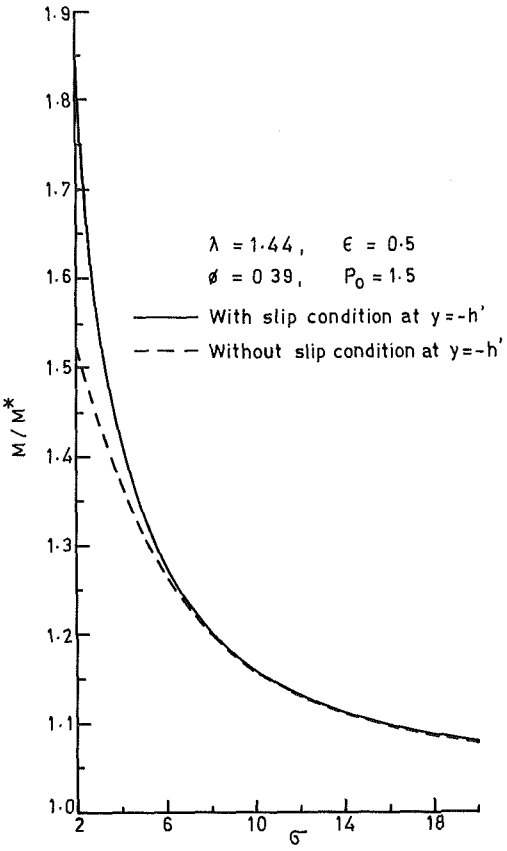

Fig. 10(*a*) Mass flow rate versus porous parameter

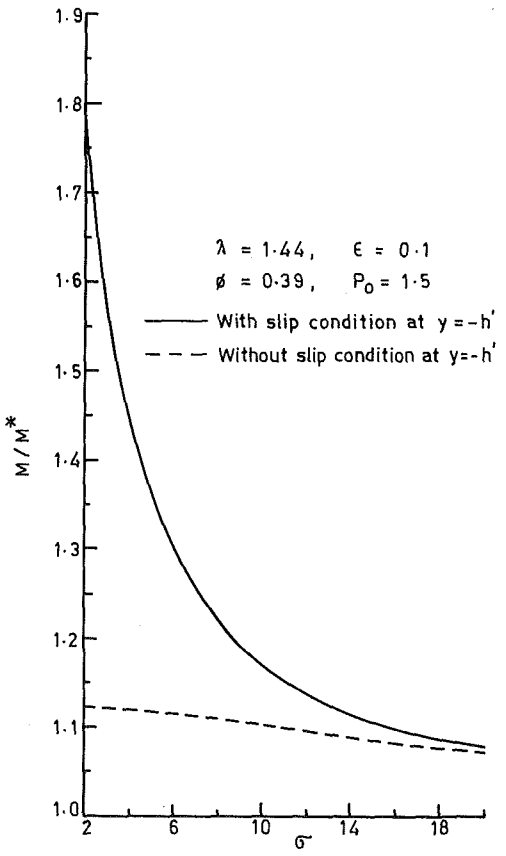

Fig. 10(*b*) Mass flow rate versus porous parameter

The measurement of this then yields λ. We also conclude that, the viscometer with the porous base has an effective width, given by

$$h + \frac{\sqrt{k}\coth(\delta h')}{\sqrt{\lambda}}.$$

In the second case where the porous medium is bounded below by a rigid plate, the viscometer has an effective width given by

$$h + \frac{\tanh \delta h')}{\lambda\delta}$$

which is identical to the one given by Williams [22].

The permeability k may be measured in the laboratory using a constant head permeameter [13, 17]. Since we allow the variation of velocity in the porous medium by considering the Brinkman equation (5), there may be an apparent permeability say $\hat{k}$. This can be obtained by computing the average volume flux, $\bar{q}$, in the porous medium. For Case 1, from (16), we obtain

$$\bar{q} = -Pk\left[1 + \frac{(\sigma^2 P_0 - 2)}{2(1+\delta_1)}\frac{\tanh(\delta h')}{\delta h'}\right] \tag{42}$$

From (42), it follows that the apparent permeability $\hat{k}$ is given by

$$\hat{k} = k\left[1 + \frac{(\sigma^2 P_0 - 2)}{1+\delta_1}\frac{\tanh(\delta h')}{\delta h'}\right] \tag{43}$$

Similarly, we can obtain the apparent permeability for the second case. Once we know the permeability k, we can determine $\hat{k}$ from (43).

Numerical calculations of u, $\hat{u}$, $\phi\hat{u}$ corresponding to (15), (16), (29) and (30) are carried out for different values of ϵ, λ and P_0 and the typical results are plotted in Figs. 2–5. Figures 2 and 3 correspond to the velocity distribution in the channel and in the porous medium while Figs. 4 and 5 correspond to the velocity distribution using the matching condition (10). Figure 6 represents the effect of P_0 on velocity.

From these we conclude the following:

(*i*) The velocity distribution in the porous medium has a boundary-layer character very near to the surface as expected from the Brinkman equation. Outside this layer, i.e., at large distances from the surface, $\hat{u}$ is almost a constant and approaches the Darcy velocity. This means that an effectively Darcy interior flow meets a Brinkman boundary layer on the nominal surface.

(*ii*) The velocity in the porous medium is large near the porous surface because the fluid is apt to slip at the porous surface.

(*iii*) The increase in λ and decrease in ϵ reduce the velocity. The effect of the thickness of the layer (i.e., ϵ) is significant when large values of viscosity factor λ and small values of σ are considered.

(*iv*) The increase in P_0 increases the velocity. The numerical calculations of the ratio of mass rate of flow, M/M^* given by (25) and (26) and the ratio of friction factors $(C_f R_e)/(C_f R_e)^*$ given by (28) and (37) are carried out for different values of ϵ, λ and P_0 and the results are shown in Figs. 7–10. Figures 7 and 8 depict, respectively, the effect of thickness of the porous layer and P_0 on the mass flow rate. Figure 9 depicts the effect of the thickness of the porous layer on friction factor. Figure 10 shows the effect of porous parameter σ on M/M^*. From these we conclude the following:

(*i*) The effect of the presence of porous bounding wall of finite thickness is to increase the mass flow and to decrease the friction factor relative to those for laminar flow in a solid-walled channel.

(*ii*) The decrease in ϵ and increase in λ decrease the mass flow and increase the friction factor relative to those in solid-walled channel. These effects are significant for small values of σ.

(*iii*) The increase in P_0 decreases the mass flow and increases the friction factor relative to those in the solid-walled channel.

(*iv*) λ may also be measured using M/M^* or $C_f\,Re/(C_f\,R_e)^*$ because all the quantities except λ involved in them are known experimentally and hence can be measured.

Acknowledgment

The financial support from the UGC under the DSA program is gratefully acknowledged.

References

1 Rudraiah, N., Chandrasekhara, B. C., Veerabhadraiah, R., and Nagaraja, S. T., "Some Flow Problems in Porous Media," PGSAM Series, Bangalore University, Vol. 2, 1979.

2 Morgan, V. T., and Cameron, A., "Mechanism of Lubrication in Porous Metal Bearings," *Proceedings Conference on Lubrication and Wear*, Institution of Mechanical Engineers, London, 1957, pp. 151–157.

3 Cameron, A., Morgan, V. T., and Stainsby, A. E., "Critical Conditions for Hydrodynamic Lubrication of Porous Metal Bearing," *Proceedings of the Institution of Mechanical Engineers*, Vol. 176, 1962, pp. 761–769.

4 Joseph, D. D., and Tao, L. N., "Lubrication of a Porous Bearing—Stokes' Solution," ASME *Journal of Applied Mechanics*, Vol. 88, Series E, No. 3, 1966, pp. 753–760.

5 Shir, C. C., and Joseph, D. D., "Lubrication of a Porous Bearing—Reynolds Solution," ASME *Journal of Applied Mechanics*, Vol. 88, Series E, No. 3, 1966, pp. 761–767.

6 Rhodes, C. A., and Rouleau, W. T., "Hydrodynamic Lubrication of Partial Porous Metal Bearings," ASME *Journal of Basic Engineering*, Vol. 88, Series D, No. 1, 1966, pp. 53–60.

7 Chandrasekhara, B. C., Rajani, K., and Rudraiah, N., "Effect of Slip on Porous-Walled Squeeze Films in the Presence of a Magnetic Field," *Applied Scientific Research*, Vol. 34, 1978, pp. 393–411.

8 Tao, L. N., and Joseph, D. D., "Fluid Flow Between Porous Rollers," ASME *Journal of Applied Mechanics*, Vol. 84, Series E, No. 2, 1962, pp. 429–433.

9 Masuoka, T., "Convective Current in a Horizontal Layer Divided by a Permeable Wall," *Bulletin of the JSEM*, Vol. 17, No. 14, 1974, pp. 225–237.

10 Tang, H. T., and Fung, Y. C., "Fluid Movement in a Channel With Permeable Walls Covered by Porous Media—A Model of Lung Alveolar Sheet," ASME *Journal of Applied Mechanics*, Vol. 97, Series E, No. 1, 1975, pp. 45–50.

11 Dulal Pal, Veerabhadraiah, R., Shivakumar, P. N., and Rudraiah, N., "Longitudinal Dispersion in a Channel Bounded by Porous Media Using Slip Condition."

12 Shivakumar, P. N., Nagaraj, S., Veerabhadraiah, R., and Rudraiah, N., "Fluid Movement in a Channel of Varying Gap With Permeable Walls Covered by Porous Media," *Bulletin of Math. Biology*, 1983 (submitted for publication).

13 Beavers, G. S., and Joseph, D. D., "Boundary Conditions at a Naturally Permeable Wall," *Journal of Fluid Mechanics*, Vol. 30, 1967, pp. 197–207.

14 Beavers, C. S., Sparrow, E. M., and Magnuson, R. A., "Experiments on Coupled Parallel Flows in a Channel and a Bounding Porous Medium," ASME *Journal of Basic Engineering*, Vol. 92, Series D, No. 1, 1970, pp. 843–848.

15 Taylor, G. I., "A Model for the Boundary Condition of a Porous Material," *Journal of Fluid Mechanics*, Vol. 29, 1971, pp. 319–326.

16 Rajasekhara, B. M., "Experimental and Theoretical Study of Flow Past a Porous Medium," PhD Thesis, Bangalore University, India, 1974.

17 Ranganna, G., "Theoretical and Experimental Study of Flow of Fluids Past Porous Media," PGSAM—Bangalore University, Vol. 5, No. 2, 1982, pp. 1–108.

18 Saffman, P. G., "On the Boundary Conditions at the Surface of a Porous Medium," *Studies in Applied Mathematics*, Vol. 50, 1971, pp. 93–101.

19 Richardson, S., "A Model for the Boundary Conditions of a Porous Material," Part II, *Journal of Fluid Mechanics*, Vol. 29, 1971, pp. 327–336.

20 Rudraiah, N., and Veerabhadraiah, R., "Temperature Distribution in Couette Flow Past a Permeable Bed," *Proceedings of the India Academy of Sciences*, Vol. 86, 1977, pp. 537–547.

21 Rudraiah, N., and Veerabhadraiah, R., "Buoyancy Effect on the Plate Couette Flow Past a Permeable Bed," *Journal of Mathematical and Physical Sciences*, Vol. 13, 1979, pp. 523–538.

22 Williams, W. O., "Constitutive Equations for a Flow of an Incompressible Viscous Fluid Through a Porous Medium," *Quarterly of Applied Mathematics*, 1978, pp. 255–267.

23 Brinkman, H. C., "A Calculation of Viscous Force Exerted by a Flowing Fluid on a Dense Swaram of Particles," *Applied Scientific Research*, Vol. A1, 1949, pp. 27–36.

24 Landau, D. D., and Lifschitz, E. M., *Fluid Mechanics*, Pergamon Press, Oxford, 1963, pp. 76–79.

A Schwarz-Christoffel Method for Generating Two-Dimensional Flow Grids

K. P. Sridhar
Assistant Professor,
Department of Mechanical Engineering,
Loyola Marymount University,
Los Angeles, CA 90045

R. T. Davis
Professsor,
Department of Aerospace Engineering
and Applied Mechanics,
University of Cincinnati,
Cincinnati, OH 45221

A new coordinate generation technique, developed by Davis for external flows, is extended to allow for accurate grid generation for a variety of complex internal flow configurations. The approach is based on numerical integration of the Schwarz-Christoffel transformation for polygonal surfaces. It is shown to be second-order accurate with mesh size due to analytic treatment of boundary singularities. The method is flexible enough to allow for treatment of severe internal geometries, for a high degree of control of mesh spacing, and for generation of either orthogonal or nonorthogonal grids. In addition, this technique directly provides the two-dimensional incompressible potential flow solution for internal flows, as well as a simple expression for calculating the grid metric coefficients. Sample cases include symmetric and asymmetric channel, diffuser, and cascade flows.

Introduction

Accurate solution of high Reynolds number, viscous, internal flow problems involving complex arbitrary geometries is a continuing concern in fluid dynamics. One of the difficulties related to these problems is the fast and accurate generation of coordinate systems ideally suited to the geometries involved. In high Reynolds number flows, where thin viscous regions and shocks may appear, the choice of a coordinate system plays a crucial role in the efficient and accurate solution of a problem. For viscous problems the coordinate system can determine the form of the flow equations, the ease of expression of boundary conditions, and the amount of truncation error due to difference approximations of the flow equations.

Generation of a proper coordinate system for a given complex geometry is difficult, since the coordinate system should facilitate the formulation and numerical solution of the problem, while minimizing the errors in the viscous flow solver. Ultimately, the coordinate generator should be interactive with the viscous flow solver via an adaptive mesh system, such that viscous problems are handled with a minimum number of mesh points.

Many authors have addressed the grid generation problem, with efforts concentrated in the areas of analytic conformal mapping and differential systems techniques. Moretti [1] and Ives [2] have used conformal mappings to generate grids for a variety of geometries. Analytic conformal mappings, of course, have no problems with orthogonality, but selective mesh densing and large cascade solidities can present difficulties.

Differential systems techniques abound in the literature. Thompson, et al. [3–5] developed an interesting method for generating coordinate systems by solving elliptic boundary-value problems. Originally Laplace equations were solved for the coordinates [3], and later Poisson equations were used [4]. Sorenson and Steger [6] developed a method to solve for the Poisson equation forcing functions as part of the coordinate system solution, and they were able to control orthogonality at the boundary. Coleman [7] has developed a method to achieve orthogonal coordinates everywhere in the field as well as mesh control at boundaries, but his method has difficulty with severe geometries (large curvature change, corners, etc.). Hyperbolic systems have been considered, with good results, by Barfield [8], Starius [9], and Steger and Sorenson [10], among others, but elliptic systems have greater flexibility since general closed boundaries can be specified.

The aforementioned methods are all based on the numerical solution of partial differential equations, and are inflexible to some degree. Specification of orthogonality and mesh spacing are often mutually exclusive, while severe geometries present additional difficulties.

The limitations of elliptic and hyperbolic boundary-value methods make boundary integral methods, such as the Schwarz-Christoffel transformation, more attractive. Singularities due to corners can be removed during the integration process, and once the mapping of the boundary has been performed, mesh coordinates are determined by integration of the mapping function in any convenient direction in the flow field. Because the Schwarz-Christoffel transformation is a conformal mapping, orthogonal coordinates can be generated; but the flexibility of this boundary integral method allows for generation of many different coordinate systems, depending upon the choice of the direction of integration.

Several authors have dealt numerically with the Schwarz-Christoffel transformation. Trefethen [11] presented a

Contributed by the Fluids Engineering Division and presented at the Winter Annual Meeting, Washington, D.C., November 15–20, 1981 of THE AMERICAN SOCIETY OF MECHANICAL ENGINEERS. Manuscript received by the Fluids Engineering Division, September 30, 1983.

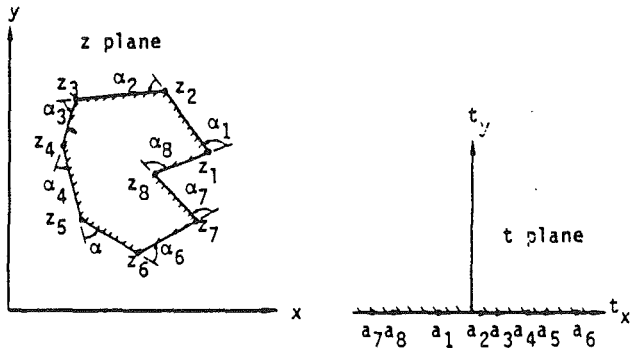

Fig. 1 Polygon mapping to upper half plane

method for integration of the transformation for polygons. Anderson [12] has used the Schwarz-Christoffel transformation to generate streamline-potential line coordinates for curved channels approximated by polygonal (straight) elements. Davis [13] has detailed the removal of boundary singularities for flows around isolated bodies approximated by straight elements. In addition, an interesting extension of the transformation to curved elements, presented in Woods [14], has been developed by Davis [13] for external flow problems.

In this paper, we will use Davis's method for removal of boundary singularities from the Schwarz-Christoffel transformation to accurately generate coordinate systems for a variety of complex two-dimensional internal flow configurations. For channels approximated by polygonal (straight) elements we will first present a one-step mapping to a parallel wall channel (ζ plane). An alternate two-step channel mapping will also be developed, where integration steps are defined in the ζ plane, while the actual integration is performed in an intermediate half plane. For both mappings we will show how the numerical integration can be accurately performed through the removal of singularities which occur at corners. Further, the effects of improved accuracy due to removal of boundary singularities on both the coordinates and the metric coefficients will be explored. Channel, diffuser, and cascade cases will be presented with orthogonal and nonorthogonal grids to show the flexibility of the method.

One-Step Mapping to a Straight Channel

Integration of the Transformation Function. The Schwarz-Christoffel transformation is well known [15] and is given by

$$\frac{dz}{dt} = M \prod_{i=1}^{I} (t - a_i)^{\alpha_i/\pi}, \tag{1}$$

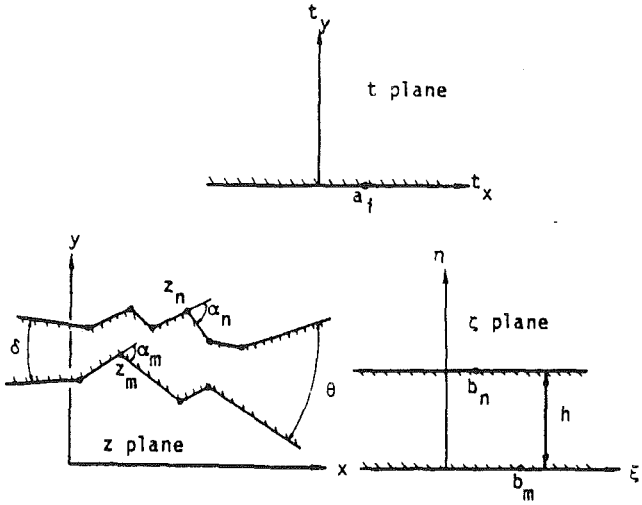

Fig. 2 Mapping of arbitrary channel to straight channel via intermediate t-plane

where the geometry is shown in Fig. 1. The transformation maps the interior of the polygon onto the upper half of the transformed plane (or onto a circle). This transformation can also be applied to a polygon with several vertices at infinity, i.e., a channel. We first must write the equivalent of equation (1) to map the channel in the physical (z)-plane onto the upper half of the intermediate t-plane (see Fig. 2), with upstream and downstream infinity mapped symmetrically about the t_y-axis. Similarly, the transformation to the t-plane can be written for a straight channel of height, h, in the ζ-plane. Elimination of the intermediate t-plane yields a one-step mapping from the z-plane to the ζ-plane, with the transformation function of the form

$$\frac{dz}{d\zeta} = K \exp\left[(\theta+\delta)\frac{\zeta}{2h}\right] \frac{\prod_{m=1}^{NL}\left[\sinh\frac{\pi}{2h}(\zeta - b_m)\right]^{\alpha_m/\pi}}{\prod_{n=1}^{NU}\left[\cosh\frac{\pi}{2h}(\zeta - b_n)\right]^{\alpha_n/\pi}}, \tag{2}$$

where K is a constant, b_m is the location in the transformed plane of the mth corner on the lower channel wall, α_m is the turning angle at the mth corner in the physical plane, and b_n and α_n are similar quantities for the upper channel wall. Here α_m and α_n are taken to be positive for a clockwise rotation when the upper and lower surfaces are traversed from left to right. For the case of parallel upstream and downstream walls ($\theta = \delta = 0$) the transformation function becomes

Nomenclature

a_i = upper half plane (t-plane) images of the physical corners, z_i
A = constant relating mapping to potential flow
b_i, ξ_i = images (real) of physical corners in the transformed (ζ) plane
C = constant of integration defined by equation (5)
h = channel height in the transformed (ζ) plane
$\hat{h}, \hat{h}_\xi, \hat{h}_\eta$ = grid metric coefficients
i = index, also, $\sqrt{-1}$
K = complex constant defined by equation (6)
M = complex constant defined by equation (22)
NL = number of corners on the lower channel surface
NU = number of corners on the upper channel surface
r_1, r_2 = upstream and downstream channel heights (physical plane)
s = arc length
t = upper half plane
u, v = velocity components in the physical plane
V = magnitude of the velocity
V_∞ = uniform free-stream velocity
w = complex potential
x, y = Cartesian coordinates, physical plane
z_i = corner coordinates in the physical plane
α_i = turning angle at a corner in the physical plane
δ = upstream divergence angle
ϕ = potential function
ψ = stream function
θ = downstream divergence angle
ξ, η = Cartesian coordinates, transformed (ζ) plane
ζ = transformed (parallel wall channel) plane

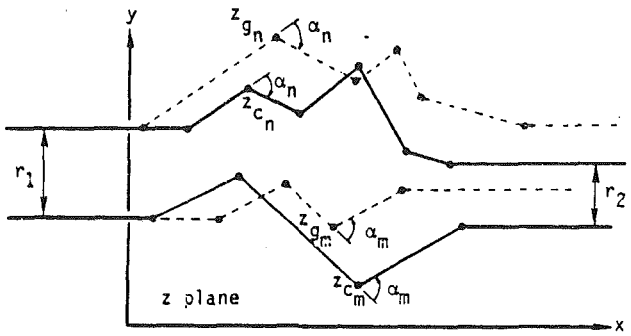

Fig. 3 Channel calculated during iteration procedure. — z_c = $z_{correct}$; ····· z_g = $z_{guessed}$ (calculated).

$$\frac{dz}{d\zeta} = Kf(\zeta) = K \frac{\prod_{m=1}^{NL} \left[\sinh \frac{\pi}{2h}(\zeta - b_m)\right]^{\alpha_m/\pi}}{\prod_{n=1}^{NU} \left[\cosh \frac{\pi}{2h}(\zeta - b_n)\right]^{\alpha_n/\pi}}. \tag{3}$$

Integration of equation (3) yields

$$z = K\int_0^{\zeta} \frac{\prod_{m=1}^{NL} \left[\sinh \frac{\pi}{2h}(\zeta - b_m)\right]^{\alpha_m/\pi}}{\prod_{n=1}^{NU} \left[\cosh \frac{\pi}{2h}(\zeta - b_n)\right]^{\alpha_n/\pi}} d\zeta + C. \tag{4}$$

For a given configuration z_n, z_m, α_n, α_m in the physical plane, the complex constants, K and C, and the real parameters, b_m and b_n, must be determined. From the Riemann mapping theorem we know that three of the parameters may be chosen arbitrarily. Denoting the lower channel wall by l and the upper channel wall by u, the choice is made to let

$$C = z_{l_1} \quad \text{and} \quad b_{u_1} = 0 \tag{5}$$

Since the lower limit of integration in equation (4) corresponds to C, our choice of C implies that $b_{l_1} = 0$. The rest of the parameters must be determined as part of the solution.

For the parallel (horizontal) inlet and exit case, determination of the constant, K, is made simple through examination of the asymptotic behavior of the transformation function both far upstream and far downstream. It is easily shown that

$$K = \sqrt{\frac{r_1 r_2}{h^2}}, \tag{6}$$

where r_1 and r_2 are, respectively, the upstream and downstream heights in the physical plane, as shown in Fig. 3. This is the equivalent of saying that far upstream and downstream the flow is uniform. With this in mind, then, it is clear that $b_{l_1} = 0$ and $b_{u_1} = 0$, ($\zeta_{u_1} = ih$) correspond to z_{l_1} and $z_{u_1} = z_{l_1} + ir_1$, respectively. It remains only to calculate $b_{u_2} \ldots b_{u_{NU}}$ and $b_{l_2} \ldots b_{l_{NL}}$ by integrating the transformation function along the channel walls. The equations that must be solved for b_n and b_m are therefore

$$z_{k+1} - z_k = K\int_{\zeta_k}^{\zeta_{k+1}} f(\zeta)\, d\zeta, \tag{7}$$

where k refers to either the upper or lower surface.

Performing the integrations indicated in equation (7) is the numerical essence of this mapping problem. Numerical integration of expressions like (7) using a trapezoid or midpoint rule results in large errors near corners, due to the singular behavior of $f(\zeta)$ there. Errors in the boundary mapping will result in errors in the coordinates generated, and therefore in the metric coefficients. The significance of these errors will be demonstrated in a later section.

To achieve accurate integration of the mapping function, even in the region near a singularity, we have used the procedure developed by Davis [13] to exactly integrate any nonanalytic term which occurs at a corner. Using this procedure we developed the following multiplicative composite integration formula, which is valid everywhere and removes the (integrable) singularities at each corner:

$$z_{k+1} - z_k = \frac{K}{\Delta\zeta^{(NL+NU-1)}}$$

$$\prod_{m=1}^{NL} \left\{ \left[\frac{\sinh \frac{\pi}{2h}(\zeta_{\text{mid}} - b_m)}{\zeta_{\text{mid}} - b_m} \right]^{\alpha_m/\pi} \cdot \left[\frac{(\zeta_{k+1} - b_m)^{\frac{\alpha_m}{\pi}+1} - (\zeta_k - b_m)^{\frac{\alpha_m}{\pi}+1}}{\frac{\alpha_m}{\pi}+1} \right] \right\}$$

$$\cdot \prod_{n=1}^{NU} \left\{ \left[\frac{\zeta_{\text{mid}} - b_n - ih}{\cosh \frac{\pi}{2h}(\zeta_{\text{mid}} - b_n)} \right]^{\frac{\alpha_n}{\pi}} \cdot \left[\frac{(\zeta_{k+1} - b_n - ih)^{1-\frac{\alpha_n}{\pi}} - (\zeta_k - b_n - ih)^{1-\frac{\alpha_n}{\pi}}}{1 - \frac{\alpha_n}{\pi}} \right] \right\}; \tag{8}$$

where K refers to either the upper or lower channel surface, and $\zeta_{\text{mid}} = (\zeta_k + \zeta_{k+1})/2$. Equation (8) can be termed a modified midpoint rule since it uses the midpoint integration rule away from singularities, and exact integration near singularities. This integration formula retains the accuracy of the midpoint rule; it is second-order accurate even when singularity-producing corners are present. The midpoint rule was chosen since its second-order accuracy is sufficient to match the second-order finite differencing used in typical flow solvers.

Solution Procedure. Armed with the integration formula (8), we can now iteratively solve for the mapping parameters in equation (7) as follows:

1 Guess the values for the unknown $b_{u_2} \ldots b_{u_{NU}}$ and $b_{l_2} \ldots b_{l_{NL}}$. Recall that $b_{u_1} = b_{l_1} = 0$, and the rest of the parameters must be chosen such that $b_{u_n} < b_{u_{n+1}} < b_{u_{n+2}}$ and $b_{l_m} < b_{l_{m+1}} < b_{l_{m+2}}$. Calculate K from equation (6). Note that although K is generally a complex constant, it will be purely real for channels with horizontal inlet and exit sections.

2 Integrate by the composite formula (8) the expression in equation (7), using the guessed values of b and the calculated value of K. With z_{u_1} and z_{l_1} known and set far upstream, calculate the left-hand side of equation (7), obtaining values for $z_{u_2} \ldots z_{u_{NU}}$ and $z_{l_2} \ldots z_{l_{NL}}$, based on the guessed values of the parameters. The form of the Schwarz-Christoffel transformation guarantees that the angles at the corners of the calculated polygon in the z-plane (for any guess in the ζ-plane) will be correct. The location of the corners, and therefore the element lengths, will be in error for some arbitrary guess of the parameters, and the calculated channel may look as shown in Fig. 3.

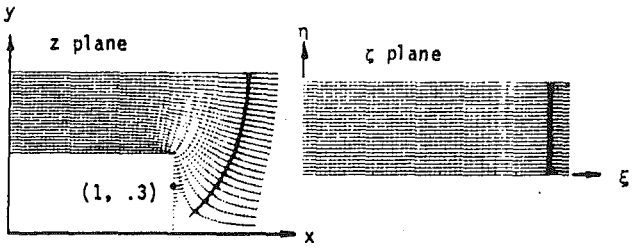

Fig. 4 Mapping of a sudden expansion

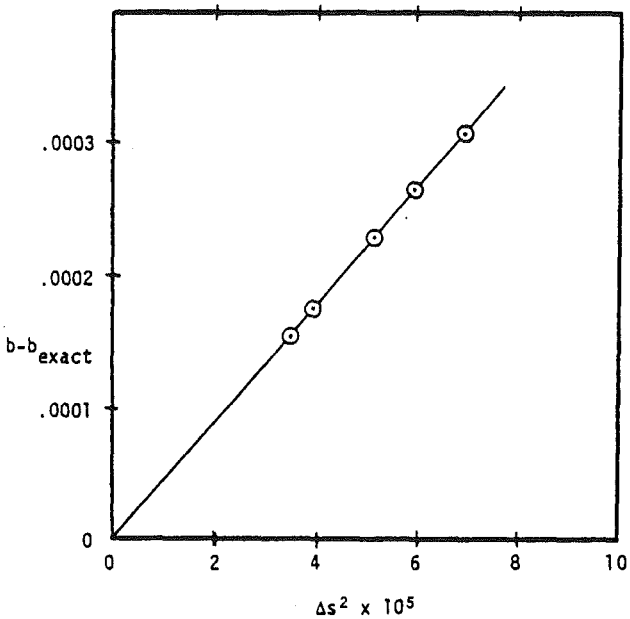

Fig. 5 Step-size study: transformed value of an arbitrary point plotted versus Δs^2

3 Following Davis's procedure, a new guess is made on $b_{u_2} \ldots b_{u_{NU}}$ and $b_{l_2} \ldots b_{l_{NL}}$ based on the scalings indicated by the errors in length of the elements in the z-plane. Denoting correct values by the subscript c and old or guessed values by the subscript g, updating is done according to

$$\frac{b_{c_{k+1}} - b_{c_k}}{b_{g_{k+1}} - b_{g_k}} = \frac{|z_{c_{k+1}} - z_{c_k}|}{|z_{g_{k+1}} - z_{g_k}|}, \tag{9}$$

where k refers to either the upper or lower channel wall.

4 Steps (2) and (3) are repeated, and the procedure is iterated to convergence.

This procedure typically converges in less than 15 iterations. In the cases presented, accuracy is to five decimal places. For internal flow problems the convergence rate is independent of the number of elements used to describe the channel. This is in agreement with Davis's result for external flows. However, the convergence rate does seem to be related to the severity of the geometry; for cases like Fig. 8, where the maximum difference between inlet slope and element slope is more than 90 deg, the convergence rate is less than that for cases like Fig. 6, where the maximum slope change is only 45 deg.

Results in Fig. 5 verify that the method is second-order accurate with mesh size. In this step-size study, the transformed value of an arbitrary boundary point in the sudden expansion shown in Fig. 4 is plotted versus the square of the integration step-size; the linear error dependence as Δs approaches zero shows the second-order accuracy.

Grid Generation. Once the mapping parameters have reached their converged values along the walls of the straight channel in the ζ-plane, the coordinate system can be generated

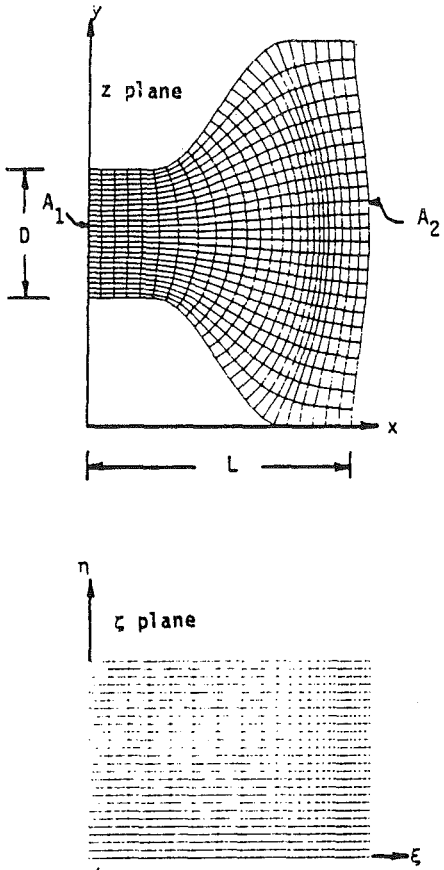

Fig. 6 Mapping of a nozzle with area ratio, $A_2/A_1 = 9$, $L/D = 2$

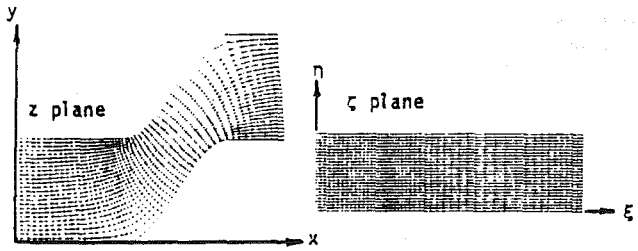

Fig. 7 Mapping of an interstage duct between turbine or compressor components

by integrating the (now known) transformation function (3) in any convenient direction. For example, Fig. 7 shows the grid in the physical plane resulting from integration along lines of constant ξ and η in the transformed plane. The duct walls were divided into elements of equal arc length, and these element end points were mapped onto the walls of the straight channel in the ζ-plane. The converged values of b on the *lower* channel wall were then used as the starting points for the upward integration along lines of constant ξ. The lines of constant η are those which result from a constant spacing of $\Delta\eta = 0.1\ ih$ in the transformed plane. Because the mapping is conformal, generation of the rectangular orthogonal grid in the ζ-plane results in an orthogonal grid in the z-plane. Also note that conformality permits elements of equal arc length to be maintained in the physical grid only along the wall from which the lines of constant ξ eminated. Wall elements of equal arc length in the physical grid can be maintained on both walls only for symmetric channels like those in Figs. 4, 6, and 16.

Examples of grids generated by this mapping method are shown in Figs. 4, 6–11. Orthogonal families of coordinate

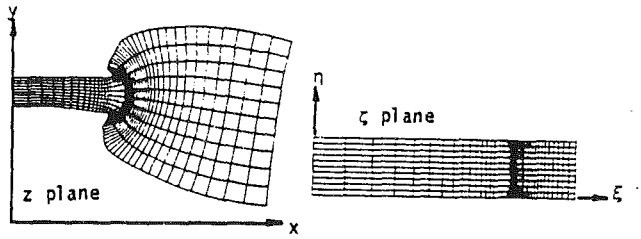

Fig. 8 Mapping of a prediffuser/combustor combination showing ξ-line densing

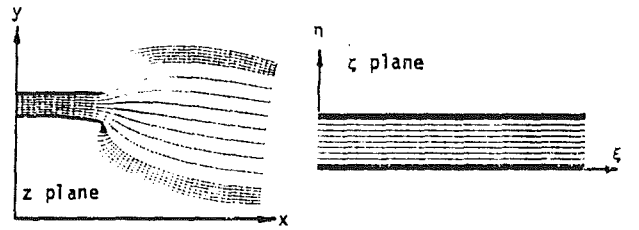

Fig. 9 Mapping of a prediffuser/combustor combination showing η-line densing

lines in Figs. 4, 6–10 are two-dimensional streamlines and potential lines, as discussed in the following section.

Figure 6 shows a symmetric nozzle mapping ($A_1/A_2 = 9$, $L/D = 2$), and Fig. 7 represents an interstage duct between turbine or compressor components. These figures illustrate orthogonal grids for geometries with high curvatures. Figures 8 and 9 show the mapping of a gas turbine prediffuser/combustor combination. These cases demonstrate the ability of the method to accurately calculate orthogonal grids for problems with severe geometries, as does the sudden expansion case shown in Fig. 4. In Figs. 4, 8, and 9 the corners are sharp and are 90 deg or more. The grids remain smooth, even near large corners, due to analytic treatment of singularities. Figure 8 also shows the effect of densing the ξ family of coordiante lines (potential lines), while Fig. 9 shows a densing of the η family of coordinate lines (streamlines). In Fig. 9 the η lines are dense only near the channel walls, but the η spacing could just as easily be varied smoothly from wall to wall. The mesh size in both the ξ and η-directions can be varied gradually or suddenly, with the same result in the z-plane. And significantly, the method allows for control of mesh spacing in both directions simultaneously. A final turbomachine application is shown in Figs. 10 and 11. In Fig. 10, the rectangular grid in the ζ-plane yields the orthogonal, nonperiodic streamline-potential line grid for the cascade of airfoils in the z-plane. This grid is not particularly useful for a practical cascade solution since a suitable grid should be periodic in the y-direction for application of the boundary conditions. For the same cascade, the periodic, nonorthogonal grid in Fig. 11 was generated by changing the path of integration in the ζ-plane as shown, where *LE* and *TE* refer to the leading and trailing edges of the airfoil. This case was included to further illustrate the flexibility of the method.

Potential Solution and Metric Coefficients. A convenient property of the mapping to the straight channel is the direct relation of the mapping function (3) to the two-dimensional incompressible potential solution. The complex potential, $w = \phi + i\psi$, is simply a constant multiple of ζ. That is

$$w = A\zeta, \tag{10}$$

and therefore

$$\frac{dw}{d\zeta} = A, \tag{11}$$

where A is a constant to be determined. The complex velocity at any point in the physical plane is given by

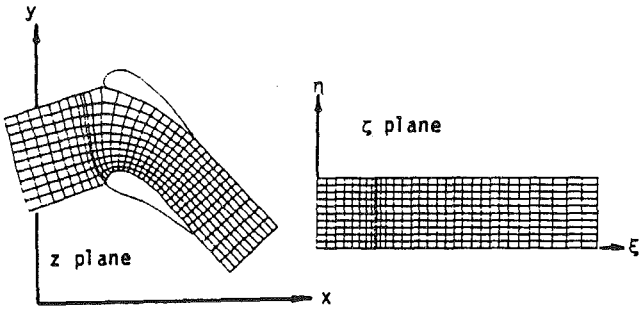

Fig. 10 Orthogonal, nonperiodic cascade grid

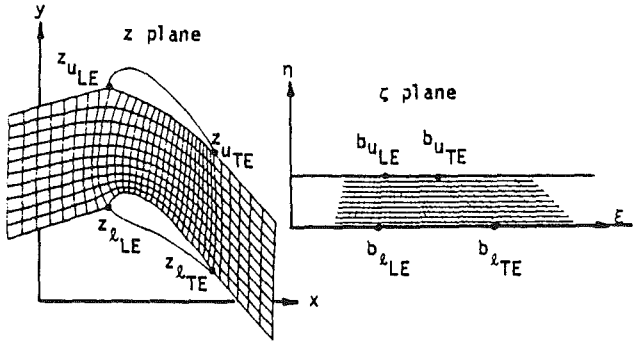

Fig. 11 Nonorthogonal, periodic cascade grid

$$u - iv = \frac{dw}{dz} = \frac{dw/d\zeta}{dz/d\zeta} = \frac{A}{dz/d\zeta}. \tag{12}$$

The constant, A, is determined by letting $u = V_\infty$ at $\zeta \to -\infty$ in equation (12), and we obtain for the velocity components

$$u - iv = V_\infty \sqrt{\frac{r_1}{r_2}} \frac{\prod_{n=1}^{NU} \left[\cosh \frac{\pi}{2h}(\zeta - b_n)\right]^{\alpha_n/\pi}}{\prod_{M=1}^{NL} \left[\sinh \frac{\pi}{2h}(\zeta - b_m)\right]^{\alpha_m/\pi}}. \tag{13}$$

The metric coefficients, which give the ratios of differential distances in the z-plane to differentials of the coordinate parameters in the ζ-plane, are defined as

$$\hat{h}_\xi = \sqrt{\left(\frac{\partial x}{\partial \xi}\right)^2 + \left(\frac{\partial y}{\partial \xi}\right)^2}, \quad \hat{h}_\eta = \sqrt{\left(\frac{\partial x}{\partial \eta}\right)^2 + \left(\frac{\partial y}{\partial \eta}\right)^2}. \tag{14}$$

For this conformal mapping it can be shown that

$$\hat{h}_\xi = \hat{h}_\eta = \left|\frac{dz}{d\zeta}\right| = \hat{h}, \tag{15}$$

and that $\hat{h}$ is related to the velocity in (13) by

$$V = (u^2 + v^2)^{1/2} = \frac{V_\infty}{\hat{h}} \sqrt{\frac{r_1}{r_2}}. \tag{16}$$

The metric coefficient can, therefore, be easily calculated from (15) once the transformation function has been determined, as can the velocity or the velocity components.

To illustrate the effect of coordinate system accuracy on the metric coefficients, the sudden expansion shown in Fig. 4 was mapped using two different integration schemes. First, the mapping was performed using the midpoint rule throughout, i.e., without the removal of singularities at the two corners. The procedure was repeated using the composite integration formula (8), which allows for removal of boundary singularities. The metric coefficients were calculated for both integration procedures by using increasingly smaller in-

Table 1 Error in metric coefficient for analytic integration and for midpoint rule at several streamline locations

Streamline Number (lower wall = 1)	η	Number of Streamwise Integration Steps per Wall	% Error in $\hat{h}$ Midpoint Rule	% Error in $\hat{h}$ Analytic Integration
13	.48	80	.9	.001
		40	1.8	.02
5	.16	80	1.3	.06
		40	2.5	.17
2	.04	80	3.1	.11
		40	5.8	.29
1	0.0	80	3.5	.10
		40	6.5	.28

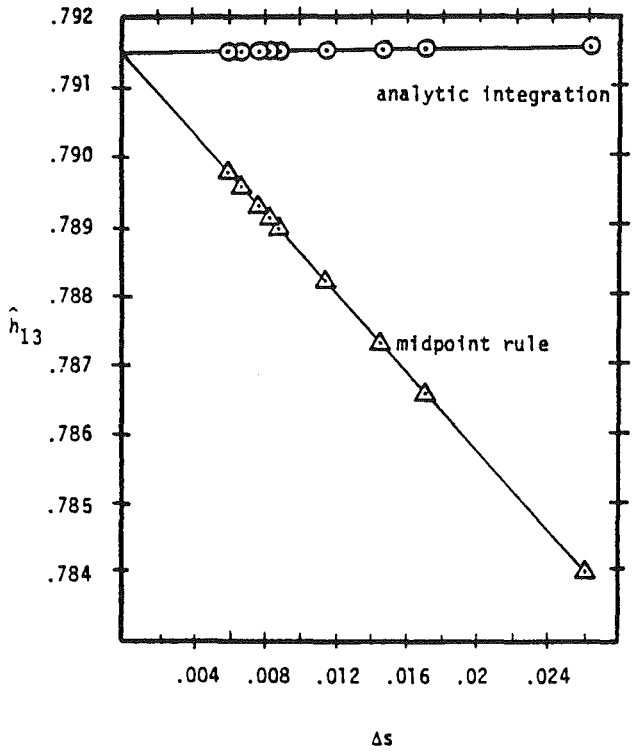

Fig. 12 Metric coefficient, $\hat{h}$ at $\eta = 0.48$ versus step-size for analytic and midpoint integration schemes

tegration steps along the walls. In particular, the metric coefficients along the potential line eminating from the boundary point (1, 0.3) (between the two corners) were examined. Figure 12 shows the metric coefficient on this potential line at the 13th streamline location plotted versus the integration step size for both integration methods. The largest step size corresponds to 80 equal divisions along the wall, while the smallest corresponds to 340 equal divisions. Both curves approach the same $\hat{h}$ intercept, but high accuracy is maintained if singularities are removed, even for large step sizes. Indeed, the metric coefficients on the top curve, calculated via our analytic formula (8), are practically insensitive to step size. For straight midpoint rule integration, the mapping is first-order accurate, as indicated by the linear $\hat{h}$ versus Δs relationship. Replotting $\hat{h}$ versus $(\Delta s)^2$ verifies that the analytic integration formula (8) actually yields second-order accurate metric coefficients, as expected.

The accuracy arguments are convincing, but calculations based on the figure show that even the less accurate midpoint rule method results in an $\hat{h}$ error of only 0.9 percent for the largest step size plotted (taking the $\hat{h}$ intercept as the correct value). However, if we examine the metric coefficient on this potential line at streamline locations increasingly close to the lower wall, the error increases for the midpoint rule, while it

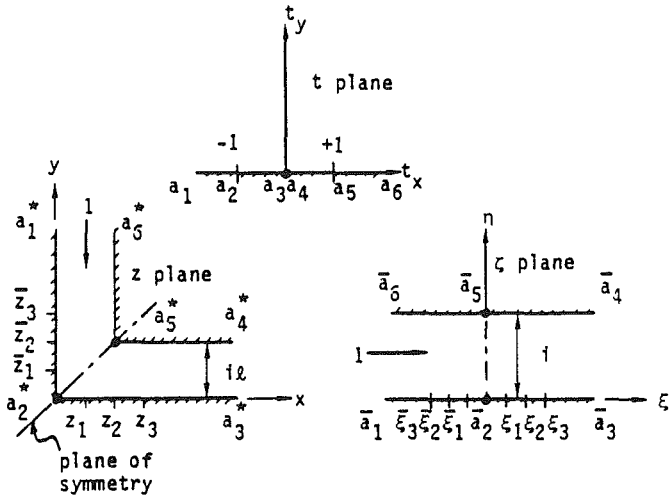

Fig. 13 Channel mapping with a plane of symmetry

remains small for the analytic integration, as shown in Table 1. It is clear, then, that accurate integration using equation (8) yields accurate metric coefficients near the wall.

Two-Step Mapping to a Straight Channel

Transformation Functions. As an alternative to the one-step mapping to a straight channel, we will demonstrate how the Schwarz-Christoffel transformation for polygons is used to develop a two-step numerical channel mapping method. This method resembles somewhat the method of Anderson [12], where the mapping parameters in equation (1) are determined in the upper half (t)-plane.

Referring to Fig. 13, if the channel inlet ($z = i\infty$) is mapped to $t = \infty$, and if the exit ($z = \infty$) is mapped to $t = 0$, equation (1) becomes

$$\frac{dz}{dt} = M \prod_{i=1}^{NC} (t - a_i)^{\alpha_i/\pi} / t, \tag{17}$$

where α_i is measured clockwise with the channel vertices numbered counterclockwise. NC is the number of corners (vertices) on the channel, excluding the corners at the channel ends.

Except for the denominator, t, equation (17) represents the same type of mapping function as Davis's [13] obtained for external flows, and its singularities may be addressed in a similar manner. In fact, the computer program written for external flows is easily modified to do channel flows. In the channel case we take the mapping one step further and map the t-plane to a ζ-plane, which consists of a channel with parallel walls a unit distance apart (see Fig. 13). This second step of the mapping is given in closed form by

$$\zeta = i - \ln(t)/\pi, \tag{18}$$

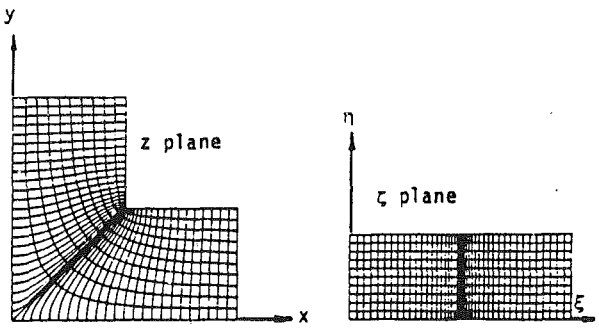

Fig. 14 Corner mapping

or

$$t = -e^{-\pi\zeta} \tag{19}$$

Solution Procedure. As an example of how a typical two-step mapping is performed numerically, consider the case shown in Fig. 13. Letting $t \to \infty$, we find that from equation (17)

$$\frac{dz}{dt} \to \frac{M}{t} \quad \text{as} \quad t \to \infty \tag{20}$$

for this case. If the velocity in the ζ-plane is taken to be unity, the complex potential, w, is ζ. Letting the upstream velocity in the physical plane be unity, we find from equations (18) and (20) that upstream

$$u - iv = i = \frac{dw}{dz} = \frac{dw}{d\zeta}\frac{d\zeta}{dt}\frac{dt}{dz} = -\frac{1}{\pi M} \tag{21}$$

and therefore

$$M = i/\pi \tag{22}$$

for this case. Other cases are done in the same manner, but M may have both real and imaginary parts, depending on the angle the inlet makes with the horizontal.

Next, we observe that this problem has the plane of symmetry shown and that, therefore, a_2^* and a_5^* map to $\bar{a}_2$ and $\bar{a}_5$ in the ζ-plane. Now we divide the channel into elements with corner locations $z_1, z_2, \ldots z_N$ to the right of the symmetry plane shown. We place elements above the symmetry plane with nodes at the locations $\bar{z}_1, \bar{z}_2, \ldots \bar{z}_N$, which are the reflections of z_i locations. Due to symmetry, these element end points must also be symmetric about the η-axis in the ζ-plane. Examination of equation (18) reveals that this symmetry implies that the locations of the element end points on the t_x-axis in the t-plane satisfy

$$\bar{t}_{x_i} = \frac{1}{t_{x_i}}, \tag{23}$$

which is true for any problem for which the upstream and downstream flows in a channel are symmetric about some plane.

Problems of this type are solved numerically in almost exactly the same manner as symmetric external flow cases [13]. The composite integration formula, however, is modified to analytically address the singular behavior of (17) near the origin in the t-plane with the result

$$z_{k+1} - z_k = \frac{M}{(t_{k+1} - t_k)^{NC}} \prod_{i=1}^{NC} \left\{ \frac{(t_{k+1} - a_i)^{\frac{\alpha_i}{\pi}+1} - (t_k - a_i)^{\frac{\alpha_i}{\pi}+1}}{\frac{\alpha_i}{\pi}+1} \right\} \cdot \ln\left(\frac{t_{k+1}}{t_k}\right) \tag{24}$$

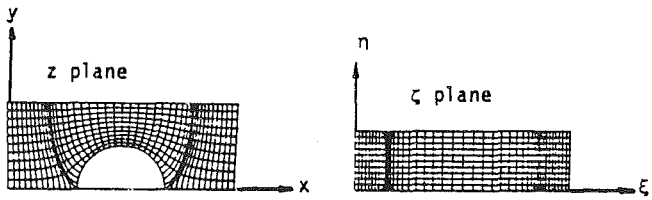

Fig. 15 Channel mapping with a half cylinder on boundary

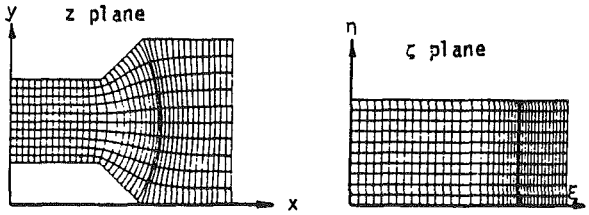

Fig. 16 Mapping of a divergent channel

As in the one-step channel mapping above, and in the external flow mappings [13], the integration formula (24) retains the inherent second-order accuracy of the midpoint rule. The solution proceeds as follows:

1 Guess values for the locations in the t-plane of the element end points for the region to the right of the symmetry plane ($-1 \le t_{x_i} \le +1$). Use equation (23) to determine the locations for the elements to the other side of the symmetry plane. M is determined from equation (22) and equation (24) is used for integration, where the range of integration is from $t_x = -1$ to $t_x = +1$. The resulting z_i-values will not be at the proper locations. Call these values z_{g_i}.

2 For the guessed t_{x_i}-values in part (1), calculate the equivalent ξ_g locations from equation (18) and predict new ξ_c locations from an equation equivalent to (9):

$$\frac{\xi_{c_{i+1}} - \xi_{c_i}}{\xi_{g_{i+1}} - \xi_{g_i}} = \frac{|z_{c_{i+1}} - z_{c_i}|}{|z_{g_{i+1}} - z_{g_i}|} \tag{25}$$

3 Using equation (19), convert these calculated ξ_{c_i} locations in the ζ-plane to t_{x_i} locations, and repeat the process.

This method appears to always converge and converges at about the same rate as was found in the external flow case (approximately ten iterations independent of the number of elements). It is important that the interpolation be done in the ζ-plane for physically obvious reasons. Attempts to iterate for the element end points in the t-plane resulted in either a much slower convergence rate or even divergence in some cases.

Figure 14 shows the result of this mapping. The elements were taken to be equally spaced on both surfaces in the z-plane in order to perform the mapping. The coordinates are generated by upward integration along lines of constant ξ, beginning at ξ_i, the images of the element end points in the ζ-plane. With ξ held constant at an element end point value, η is incremented to calculate Δt from equation (19), and equation (24) is used to perform the integration.

Figure 15 shows another mapping which was performed in exactly the same manner. Here the symmetry plane extends from the top of the cylinder to the upper wall.

As in the one-step mapping, the metric coefficients and the potential flow complex velocity can be directly computed numerically from $d\zeta/dz$. In both cases examined for the two-step mapping, the wall tangential velocities show excellent agreement with more exact or analytical results.

Figure 16 shows a geometry with a different type of symmetry. In this case, the symmetry is about the centerline of the channel. Again, the same type of mapping is performed with the channel inlet placed on the η-axis in the ζ-plane. If we

subdivide the upper and lower surfaces in the z-plane with the same element spacings, the mapping will be completely symmetric about the t_y-axis. We need only to integrate in the region $0 \leq t_x \leq +1$ and then reflect the element end points about the t_y-axis. The interpolation is again performed in the ζ-plane to update the guessed element end points in the t-plane. The convergence rate is about the same as in the other two-step mapping cases. The coordinate lines in Fig. 16 are again generated by integrating vertically from the element end points in the ζ-plane.

In problems with symmetry of the types previously discussed, the numerical problem becomes much simpler than for a problem which has no symmetry. This occurs since, for both types of symmetry, we know the location of the points in the z-plane which map to $\zeta = 0 + i0$ and $\zeta = 0 + il$ in the ζ-plane. In problems with no symmetry, we must be sure to take an initial plane far enough upstream so that the flow is essentially parallel in the physical plane and then assume that the upper and lower points at this location map to $\zeta = 0 + i0$ and $\zeta = 0 + il$ in the ζ-plane. This same assumption was made in the one-step channel mapping just discussed, and results in a small error which diminishes as the location of the initial station is moved further upstream. A method to improve the results would be to assume that symmetry exists about the initial plane even though it does not. This error would not be serious as long as the initial station (assumed symmetry plane) is far enough upstream of the region of interest.

Comparisons. The nozzles shown in Fig. 6 was mapped using both the one and two-step procedures for comparison. The one and two-step mappings for this case converged to 5 decimal places in 9 and 11 iterations, respectively, and required 56 to 58 s of computer time, respectively, to complete the mapping and generate a 41 × 11 grid. Calculations were done on an IBM 3033 computer.

The mappings are comparable for this case, but for more highly curved geometries or for geometries with very large corners, the two-step mapping appears to converge in fewer iterations. In addition, because of the hyperbolic functions involved in equations (3) and (8), the time per iteration is greater for the one-step mapping than for the two-step mapping.

Conclusions

A new coordinate generation technique, developed by Davis for external flows, has been extended to two-dimensional internal flows. The method is second-order accurate with mesh size due to analytic treatment of channel boundary singularities. The method allows for treatment of severe internal geometries, for a high degree of control of mesh spacing, and for generation of either orthogonal or nonorthogonal grids. In addition, this technique directly provides the two-dimensional incompressible potential flow solution for internal flows, as well as a simple expression for calculating the grid metric coefficients. The extension of the method to higher-order accuracy via a curved-element channel approximation is in progress.

Acknowledgments

The authors are indebted to Dr. M. Werle for many valuable discussions during this project and gratefully acknowledge his efforts. The authors also wish to thank Dr. T. Barber and Mr. J. Dannenhoffer for helpful discussions and Mr. R. VanVogelpoel for his assistance with programming.

References

1 Moretti, G., "Conformal Mappings for Computations of Steady, Three-Dimensional, Supersonic Flows," Num./Lab. Comp. Methods in Fl. Mech., Vol. 13, ASME, 1976.

2 Ives, D. C., "A Modern Look at Conformal Mappings Including Doubly-Connected Regions," AIAA Paper 75-842, 1975.

3 Thompson, J. F., Thames, F. C., and Mastin, C. W., "Automatic Numerical Generation of Body-Fitted Curvilinear Coordinate System for Field Containing Any Number of Arbitrary Two-Dimensional Bodies," *Journal of Computational Physics*, Vol. 15, 1974, pp. 299–319.

4 Thompson, J. F., Thames, F. C., Mastin, C. W., and Shanks, S. P., "Use of Numerically Generated Body-Fitted Coordinate Systems for Solution of the Navier-Stokes Equations," *Proc. of the AIAA 2nd Comp. Fl. Dyn. Conf.*, Hartford, CT, 1975.

5 Thompson, J. F., Thames, F. C., and Mastin, C. W., "TOMCAT—A Code for Numerical Generation of Boundary-Fitted Curvilinear Coordinate Systems on Fields Containing Any Number of Arbitrary Two-Dimensional Bodies," *Journal of Computational Physics*, Vol. 24, 1977, pp. 274–302.

6 Sorenson, R. L., and Steger, J. L., "Numerical Generation of Two-Dimensional Grids by the Use of Poisson Equations with Grid Control at Boundaries," *Proc. of NASA Workshop on Num. Grid Generation Tech.*, Hampton, VA, 1980, pp. 449–462.

7 Coleman, R. M., "Generation of Orthogonal Boundary-Fitted Coordinate Systems," *Proc. of NASA Workshop on Num. Grid Generation Tech.*, Hampton, VA, 1980, pp. 213–220.

8 Barfield, W. D., "An Optimal Mesh Generator for Lagrangian Hydrodynamic Calculations in Two Space Dimensions," *Journal of Computational Physics*, Vol. 6, 1970, pp. 417–429.

9 Starius, G., "Construction of Orthogonal Curvilinear Meshes by Solving Initial Value Problems," *Numerische Mathematik*, Vol. 28, 1977, pp. 25–48.

10 Steger, J. L., and Sorenson, R. L., "Use of Hyperbolic Partial Differential Equations to Generate Body-Fitted Coordinates," *Proc. of NASA Workshop on Num. Grid Generation Tech.*, Hampton, VA, 1980, pp. 463–478.

11 Trefethen, L. N., "Numerical Computation of the Schwarz-Christoffel Transformation," *SIAM J. Sci. Stat. Comp.*, Vol. 1, 1980, pp. 82–102.

12 Anderson, O. L., "Calculation of Internal Viscous Flows in Axisymmetric Ducts at Moderate to High Reynolds Numbers," *Computers and Fluids*, Vol. 8, 1980, pp. 391–411.

13 Davis, R. T., "Numerical Methods for Coordinate Generation Based on Schwarz-Christoffel Transformations," AIAA Paper 79-1463, 4th Computational Fluid Dynamics Conference, July, 1979.

14 Woods, L. C., *The Theory of Subsonic Plane Flow*, Cambridge University Press, 1961.

15 Polya, G., and Latta, G., *Complex Variables*, Wiley, 1974.

16 Wassmuth, R. H., "Some Complex Numerical Integrations of the Schwarz-Christoffel Transformation and Application to Potential Flow," PhD, Mathematics, Oregon St. University, 1966.

17 Sridhar, K. P., "Coordinate System Generation for Internal Flow Problems Via Schwarz-Christoffel Transformations," PhD, Mechanical Engineering and Mechanics, West Virginia University, 1981.

Pai-Mow Lee
Associate Professor,
School of Engineering,
Lakehead University,
Thunder Bay, Ontario, P7B5E1 Canada

Sui Lin
Professor,
Mechanical Engineering Department,
Concordia University,
Canada

Pressure Distribution for Radial Inflow Between Narrowly Spaced Disks

In the study of the subject flow, various forms of integral solution were often employed [1-5] to find out the pressure distribution along a radius. Recognizing the fact that an integral solution is intended to satisfy the mean characteristics over the whole thickness of a boundary layer, Kwok [1] directly assumed a velocity profile satisfying the boundary and compatible conditions to determine the pressure distribution; others [2-5] generated velocity profiles. But in the end, all the resulting pressure equations ([1, equation (10)] and [3, equations (20) and (21)]) were able to produce predictions with an approximately equal degree of accuracy as can be seen from [1]. In fact, due to the narrow space between the disks it is difficult to experimentally verify the velocity profiles, assumed or derived, and hence the experimental pressure data are still the final criteria used to judge the validity of a solution. Indeed, these disk-type devices have many engineering applications in which pressure distributions are the major design concerns (see references quoted in [4]). In this connection, references [2-5] presented only limited experimental evidences; on the other hand, reference [1] was able to present abundant data except that they were not properly organized and plotted in dimensionless form. Thus this paper attempts a differential solution to directly obtain a pressure equation without having to derive or assume any velocity profile. It can be seen that the equation can predict pressure distribution in better agreement with experimental data.

Analysis

Consider a steady, laminar, nonswirling inflow of an incompressible fluid between two parallel stationary disks, Fig. 1. The disks are narrowly spaced, i.e., the arrangement has a low aspect ratio, defined as h/r_0. As a result, the only significant component of flow velocity is the radial component, the axial component being comparatively insignificant. Thus the Navier-Stokes equations in cylindrical coordinates for constant density and viscosity [6] are simplified as

$$\frac{1}{\mu}\frac{dp}{dr} = \frac{\partial^2 v_r}{\partial z^2} - \frac{\rho}{\mu} v_r \frac{\partial v_r}{\partial r} \tag{1}$$

The continuity equation [6] is

$$\frac{v_r}{r} + \frac{\partial v_r}{\partial r} = 0 \tag{2}$$

Equation (1) is linearized by replacing v_r with mean radial velocity ($v = -\dot{m}/4\pi hr\rho$),

$$\frac{1}{\mu}\frac{dp}{dr} = \frac{\partial^2 v_r}{\partial z^2} + \left(\frac{\dot{m}}{4\pi\mu hr}\right)\frac{\partial v_r}{\partial r} \tag{1a}$$

Then, using (2), equation (1a) is reduced to

$$\frac{1}{\mu}\frac{dp}{dr} = \frac{\partial^2 v_r}{\partial z^2} - \omega^2 v_r \tag{3}$$

where $\omega = \sqrt{\dot{m}/4\pi h\mu}\ /r$. Such a linearizing technique was used by Langhaar [7] and Slezkin (see Discussion [8, p. 46]). Equation (3) is a linear second-order differential equation and one particular solution is

$$v_r = -\frac{1}{\mu\omega^2}\frac{dp}{dr} \tag{4}$$

It then suffices to solve the characteristic equation

$$\lambda^2 - \omega^2 = 0 \tag{5}$$

Thus the general solution to (3) is

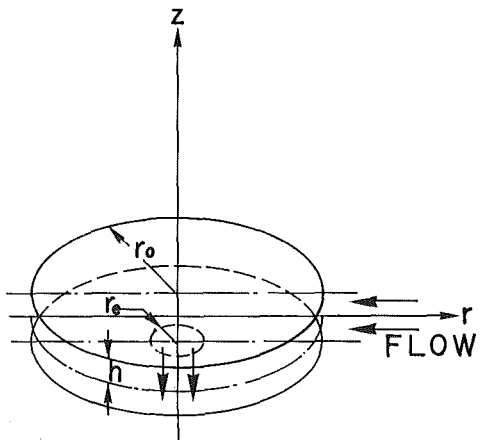

Fig. 1 Definition

Contributed by the Fluids Engineering Division of THE AMERICAN SOCIETY OF MECHANICAL ENGINEERS and presented at the Fluids Engineering Conference, Albuquerque, NM, June 24-26, 1985. Manuscript received by the Fluids Engineering Division, March 24, 1984.

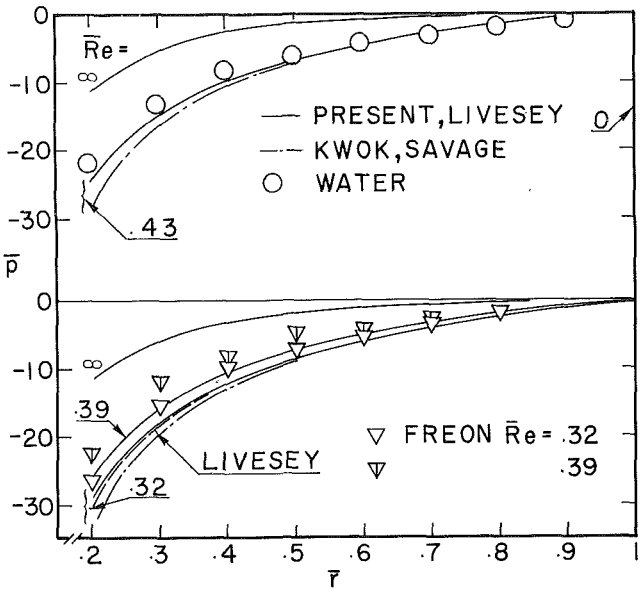

Fig. 2 Pressure distribution

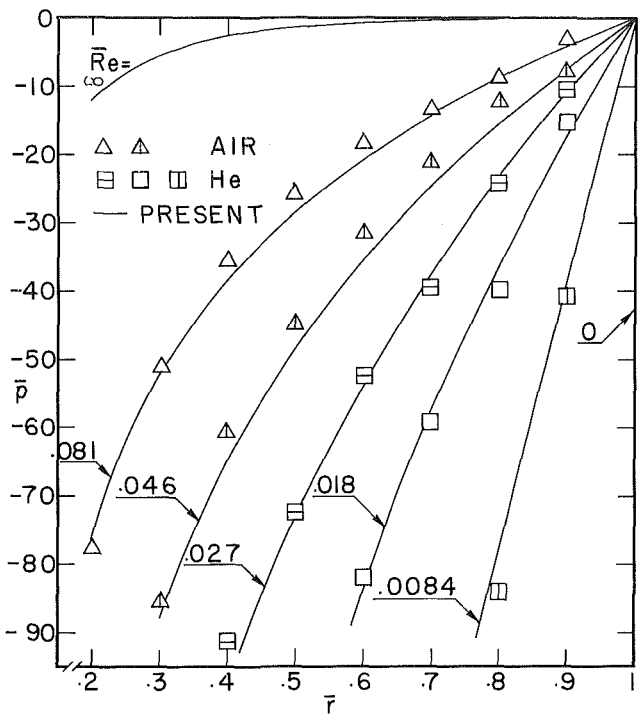

Fig. 3 Pressure distribution

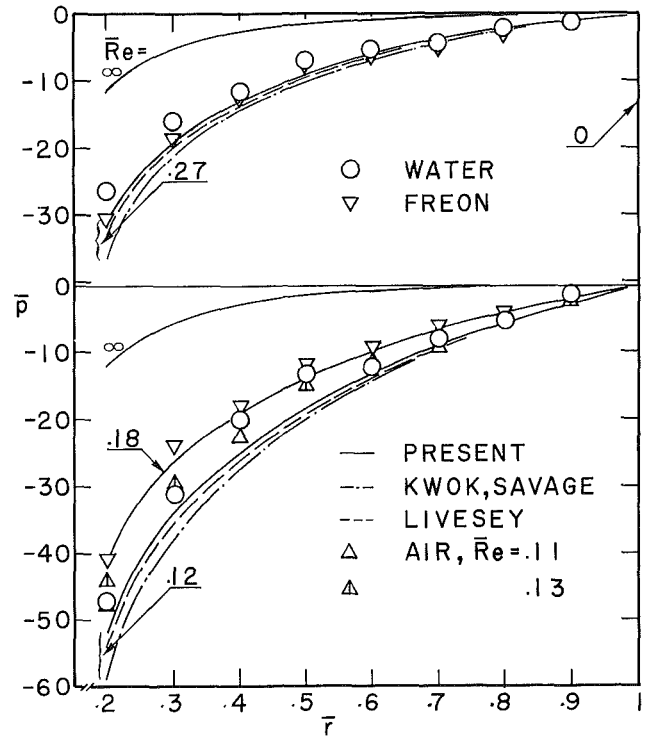

Fig. 4 Pressure distribution

$$v_r = Ae^{\omega z} + Be^{-\omega z} - \frac{1}{\mu\omega^2}\frac{dp}{dr} \tag{6}$$

At $z = 0$, $\partial v_r/\partial z = 0$, hence $A = B$ and (6) reduces to

$$v_r = C\cosh(\omega z) - \frac{1}{\mu\omega^2}\frac{dp}{dr} \tag{7}$$

where $C = 2A$. At $z = h$, $v_r = 0$, hence

$$C\cosh(\omega h) = \frac{1}{\mu\omega^2}\frac{dp}{dr} \tag{8}$$

Using the continuity equation again

$$-2\int_0^h \rho v_r (2\pi r)\, dz = \dot{m}$$

one obtains

$$C\sinh(\omega h) = \omega\left(-\frac{\dot{m}}{4\pi\rho r} + \frac{h}{\mu\omega^2}\cdot\frac{dp}{dr}\right) \tag{9}$$

Dividing (9) with (8), the result is

$$\frac{dp}{dr} = \frac{1}{1 - \dfrac{\tanh(\omega h)}{\omega h}}(\rho v^2)\frac{1}{r} \tag{10}$$

Introducing the following definitions:

Re = Reynolds number $= \rho v_0 h/\mu$;

$\bar{\text{Re}}$ = reduced Reynolds number $= \text{Re}\zeta$;

$\bar{r} = r/r_0$; $\bar{p} = p/\rho v_0^2$,

equation (10) is then rendered dimensionless as

$$\frac{d\bar{p}}{d\bar{r}} = \frac{1}{1 - \dfrac{\tanh(\sqrt{\bar{\text{Re}}}/\bar{r})}{(\sqrt{\bar{\text{Re}}}/\bar{r})}}\cdot\frac{1}{(\bar{r})^3} \tag{11}$$

Nomenclature

$\dot{m}$ = mass flowrate
p = static pressure
p_0 = static pressure at $r = r_0$, Fig. 1
$\bar{p}$ = dimensionless pressure ($\equiv p/\rho v_0^2$) or $(p - p_0)/\rho v_0^2$, Fig. 2-4)
Re = Reynolds number ($\equiv \rho v_0 h/\mu$)
$\bar{\text{Re}}$ = reduced Reynolds number ($\equiv \text{Re}\,\zeta$)
$\bar{r}$ = dimensionless radius ($\equiv r/r_0$), Fig. 1
v_r = radial component of flow velocity
v = mean radial velocity ($\equiv -\dot{m}/4\pi hr\rho$)
v_0 = mean radial velocity at $r = r_0$, Fig. 1
ζ = aspect ratio ($\equiv h/r_0$), Fig. 1
μ = absolute viscosity
ρ = density

Table 1

Fluid	Water		
Disc outside radius, r_o, mm	119		
exit radius, r_e, mm	9.53		
Distance, 2h, mm	0.51	0.28	0.28
Aspect ratio, $\zeta \times 10^3$	2.1	1.2	1.2
Initial pressure, p_o, kPa	136	274	400
Temperature C	22		
Absolute viscosity, mPa·s	1.0		
Mass flowrate, $\dot{m}$, kg/s	0.315	0.159	0.343
Dimensionless pressure, $\bar{p}_o$	200	480	154
Reduced Reynolds No. $\bar{R}e$	0.43	0.12	0.27

Equation (11) is solved using the Runge-Kutta method [9] and is plotted in Figs. 2-4 as theoretical curves of $\bar{p}$ versus $\bar{r}$, $\bar{R}e$ being used as parameters. It is noticed that the general trend of the curves seems to suggest they approach an upper and right-hand limiting position as $\bar{R}e$ approaches ∞ or zero, respectively. Indeed, this is the case. For instance, if $\bar{R}e \to \infty$, then

$$\frac{d\bar{p}}{d\bar{r}} = \frac{1}{1 - \dfrac{\tanh(\infty)}{\infty}} \frac{1}{(\bar{r})^3}$$

Applying L'Hospital's rule

$$\lim_{\bar{R}e \to \infty} \frac{\tanh(\infty)}{\infty} \to 0$$

and $d\bar{p}/d\bar{r} = 1/(\bar{r})^3$ defining the upper limiting curve.

Similarly, if $\bar{R}e \to 0$, then

$$\lim_{\bar{R}e \to 0} \frac{\tanh(0)}{0} \to 1$$

and $d\bar{p}/d\bar{r} \to \infty$ defining the right-hand limiting curve.

The aforementioned theoretical curves are now verified with experimental data.

Experiment and Discussion

Hayes, et al. [10] conducted extensive experiments for the subject flow; the experimental conditions are summarized in Tables 1 and 2. After rendering dimensionless the data are superimposed in Figs. 2-4 in accordance with pertinent $\bar{R}e$. It can be seen that the data fit more closely with the present theory. Further, in comparison with Kwok's [1] graphs, the present ones plotted in dimensionless variables display concisely experimental evidences. As suggested earlier in this report, there are two limiting positions for $\bar{p} - \bar{r}$ curves, i.e., upper and right-hand positions corresponding to $\bar{R}e \to \infty$ and $\bar{R}e \to 0$, respectively. Thus one may surmise that the latter represents a creeping motion, while the former a potential flow. The following derivation proves this statement.

For creeping motion, (1) reduces to

$$\frac{dp}{dr} = \mu \frac{\partial^2 v_r}{\partial z^2} \tag{13}$$

Using boundary and symmetry conditions,

$$z = \pm h,\ v_r = 0 \quad \text{and} \quad z = 0,\ \frac{\partial v_r}{\partial z} = 0,$$

the solution to (13) is

$$v_r = \frac{1}{2\mu}(h^2 - z^2)\frac{dp}{dr} \tag{14}$$

Table 2

Fluids	Air	Freon	Helium
Disc outside radius, r_o, mm	119		
exit radius, r_e, mm	9.53		
Distance, 2h, mm	0.18		
Aspect ratio, $\zeta \times 10^4$	7.6		
Temperature, C	16		
Absolute viscosity, μPa·s	18.2	12.3	20
	Initial pressure, p_o = 33.8 kPa		
Mass flowrate, $\dot{m} \times 10^2$, kg/s	0.164	0.431	0.0325
Reduced Reynolds No. $\bar{R}e$	0.046	0.18	0.0084
	p_o = 67.4		
$\dot{m} \times 10^2$	0.280	0.631	0.0692
$\bar{R}e$	0.081	0.27	0.018
	p_o = 101		
$\dot{m} \times 10^2$	0.373	0.781	0.105
$\bar{R}e$	0.11	0.32	0.027
	p_o = 135		
$\dot{m} \times 10^2$	0.470	0.949	0.141
$\bar{R}e$	0.13	0.39	0.036

Using the continuity equation again

$$-2\int_0^h \rho v_r (2\pi r)\, dz = \dot{m}$$

and nondimensionizing the resulting equation, one obtains

$$\frac{d\bar{p}}{d\bar{r}} = \frac{3}{4}\frac{1}{\bar{R}e\,\bar{r}} \tag{15}$$

As $\bar{R}e \to 0$, $d\bar{p}/d\bar{r} \to \infty$, which represents the right-hand $\bar{p} - \bar{r}$ curves, Figs. 2-4.

On the other hand, if $\bar{R}e \to \infty$ then in equation (1), the inertial term dominates and the viscous term may be ignored. Thus

$$\frac{dp}{dr} = -\rho v_r \frac{\partial v_r}{\partial r} \tag{16}$$

or

$$dp + \frac{\rho}{2}\partial(v_r)^2 = 0 \tag{17}$$

Clearly, equation (17) represents Bernoulli's equation for frictionless flow. Using the continuity equation (2), (16) reduces to

$$\frac{dp}{dr} = \rho \frac{v_r^2}{r} \tag{18}$$

Since the flow is frictionless, v_r will have a uniform profile. Again, from continuity, $\dot{m} = -(4\pi\rho h)\, v_r\, r$, it can be seen $v_r/v_0 = r_0/r$.

Hence, equation (18) can be rendered dimensionless as

$$d\bar{p}/d\bar{r} = 1/\bar{r}^3 \tag{19}$$

which is identical to (12), defining the upper limiting curves, Figs. 2-4.

Conclusion

An equation of motion, simplistic yet with sufficient engineering accuracy, to describe the subject flow is given by equation (3), a linear second-order differential equation. Indeed, to judge the validity of a solution to the subject flow, the final criterion is pressure. In this connection, velocity profiles, assumed or generated, will not serve as effective criteria because they are difficult to be verified experimentally. Thus the paper directly obtains a dimensionless

pressure-gradient equation, equation (11), which is capable of predicting pressure distribution in closer agreement with experimental data. The pressure distribution curves are shown to spread between two limiting positions representing creeping and potential flow, and the flow characteristic number is shown to be the reduced Reynolds number.

References

1 Kwok, C., and Lee, P. M., "Integral Equation Method for Compressible Flow Between Parallel Disks," *Trans. CSME*, Vol. 5, No. 1, 1979, pp. 55–58.

2 Boyack, B. E., and Rice, W., "An Integral Solution for Laminar Radial Outflow of Viscous Fluid Between Parallel Stationary Disks," ASME *Journal of Basic Engineering*, Sept. 1970, pp. 662–663.

3 Savage, S. B., "Laminar Radial Flow Between Parallel Plates," ASME *Journal of Applied Mechanics*, Dec. 1964, pp. 594–595.

4 Woolard, H. W., "A Theoretical Analysis of Viscous Flow in Narrowly Spaced Radial Diffuser," ASME *Journal of Applied Mechanics*, Vol. 79, 1957, pp. 9–15.

5 Livesey, J. L., "Inertia Effects in Viscous Flows," *International Journal of Mechanical Sciences*, Vol. 1, 1960, pp. 84–85.

6 Daily, J. W., and Harleman, D. R. F., *Fluid Dynamics*, Addison-Wesley, 1966.

7 Langhaar, H. L., "Steady Flow in the Transition Length of a Straight Tube," ASME *Journal of Applied Mechanics*, Vol. 64, 1942, pp. A55–58.

8 Campbell, W. D., and Slattery, J. C., "Flow in the Entrance of a Tube," ASME *Journal of Basic Engineering*, Mar. 1963, pp. 41–46.

9 Kuo, S. S., *Numerical Methods and Computers*, Addison-Wesley, 1965.

10 Hayes, W. F., and Tucker, H. G., "Theoretical Radial Pressure Distribution for Viscous Fluid Inflow Within a Thin Disk Chamber," National Research Council of Canada, CS-51, 1973.

B. Bar-Haim
Instructor.

D. Weihs
Professor.

Department of Aeronautical Engineering,
Technion—Israel Institute of Technology,
Haifa, Israel

Boundary-Layer Control as a Means of Reducing Drag on Fully Submerged Bodies of Revolution

The drag of axisymmetric bodies can be reduced by boundary-layer suction, which delays transition and can control separation. In this study, boundary-layer transition is delayed by applying a distributed suction technique. Optimization calculations were performed to define the minimal drag bodies at Reynolds numbers of 10^7 and 10^8. The saving in drag relative to optimal bodies with non-controlled boundary layers is shown to be 18 and 78 percent, at Reynolds numbers of 10^7 and 10^8, respectively.

Introduction

The design of low drag axisymmetric hydrodynamic bodies has attracted considerable attention in recent years. There are both civil and military aspects to this interest: reduction of drag means reduction of fuel costs in underwater and air transportation, as well as faster and more quiet naval underwater vehicles.

Drag reduction may be achieved by two different approaches. The first is the design of low drag bodies by shape manipulations for a maximum downstream displacement of the transition point [1,2]. Parsons [1] applied optimization techniques to define the best shape from families of bodies with five to eight parameters. His optimal designs were shown to have very low drag coefficients (for example, for X-35 body, the optimal design at $\mathrm{Re}=10^7$, a drag coefficient of $C_D=0.0051$ was achieved), but the bodies were highly curved and thus less attractive for underwater applications. Furthermore, these low drag shapes are totally dependent on the transition criterion selected, and Zedan and Dalton [2] have shown that the application of a different criterion may cause a 40 percent change in the predicted drag reduction. A somewhat different approach was adopted by Hess [3] who postulated that at high Reynolds numbers (above 10^7) there cannot exist a significant run of laminar boundary layer along underwater bodies, considering the natural turbulence conditions in the sea. Thus the shape manipulations mentioned are inefficient due to the fact that the turbulent boundary layer is essentially insensitive [3] to the detailed body shape.

A totally different approach is manifested by applying passive or active boundary-layer control (BLC) methods to prevent the boundary-layer transition or to decrease the turbulent skin friction, and sometimes to delay separation. Examples of passive methods of BLC are compliant surfaces [4] and skin riblets [5]. While the first technique is difficult to apply and its drag reduction capability not easily estimated, the second technique is very simple but its capability of decreasing the drag is limited to a few percent only. As for prevention of separation, an interesting passive device based on a trapped vortex had been suggested by Ringleb [6] and adopted later by Goldschmied [7].

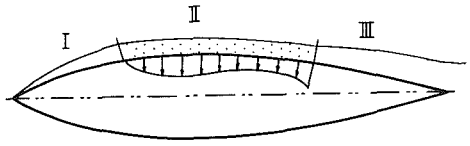

Fig. 1 Axisymmetric two parameter body with schematic description of boundary-layer development: (I) Laminar boundary layer; (II) Suction controlled boundary layer; (III) Turbulent boundary layer

Active devices are the most versatile and efficient means of boundary-layer control, but in contrast to the passive methods, their application is energy demanding. Therefore, in considering the energy savings in this type of drag reduction, one must add the control energy introduced in the system, in order to fully evaluate the efficiency of the method.

The best-known methods of active BLC are body heating [8] and suction. Heating may decrease the skin-friction coefficient but has no influence on boundary-layer separation. Goldschmied [9] suggested the application of strong suction from a slot to prevent separation while allowing the boundary layer to be turbulent along the whole body. In contrast, Wieghardt [10] applied a combined suction-blowing procedure to maintain the boundary layer stable on two bodies of revolution. While this combined technique was able to delay substantially the onset of boundary-layer instability, it demanded the application of mass transfer along almost the whole body length, even at a relatively low Reynolds number of $\mathrm{Re}=1.6\times10^6$.

In this paper, we investigate the drag characteristics of axisymmetric shapes whose boundary layer is controlled by distributed suction. The application of this suction BLC is in conjunction with shape manipulations, to define the bodies of least drag in axisymmetric, incompressible, nonseparating and noncavitating flow. The technical difficulties arising from the design of suction mechanisms and systems are not

Contributed by the Fluids Engineering Division of THE AMERICAN SOCIETY OF MECHANICAL ENGINEERS and presented at the Energy Sources Technology Conference, New Orleans, LA, February 1984. Manuscript received by the Fluids Engineering Division, March 26, 1984; final revision, July 10, 1985.

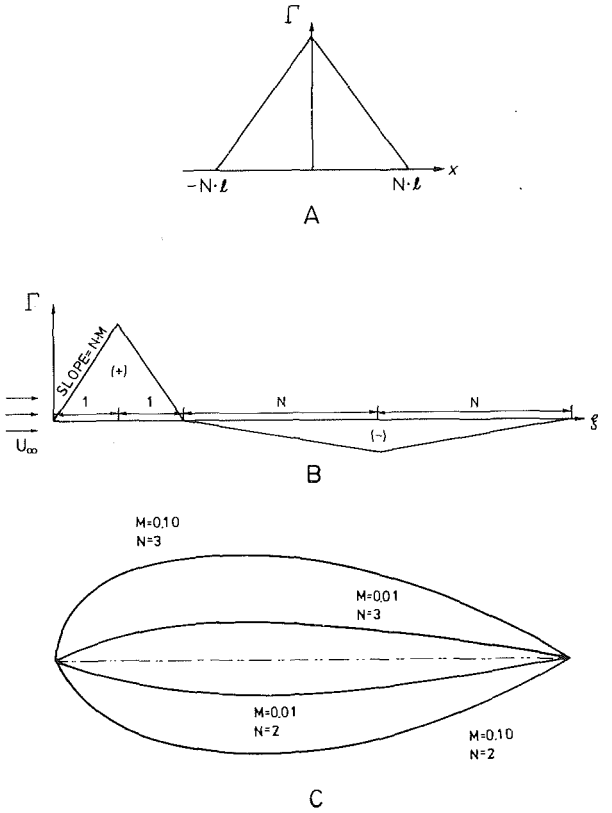

Fig. 2 (*A*) Triangular distribution of source strength; (*B*) Source/sink strength distribution to form a two-parameter closed body; (*C*) Four typical members of the two-parameter family of bodies

dealt with here, but an attempt is made to define bounds to the drag reduction capabilities of this method. These bounds will enable the practical applicability of the suction methods to be ultimately judged.

Analysis

Definition of the Optimization Goal. A crucial part of the present approach is to define properly the optimization goal. This definition is difficult due to the considerable number of parameters involved and the complexity of the drag model (to be described). Furthermore, the optimization procedure is meaningful only in context with a definite drag reduction scheme which was determined to be (see Fig. 1):

A Free development of the laminar boundary layer from the body apex up to the point where the boundary layer is neutrally stable.

B Application of distributed suction whose strength is the local minimum required to maintain the stability of the boundary layer.

C Areas along which the boundary layer has regained local natural stability are not subject to mass transfer.

D Deletion of the suction from the point where the boundary layer is expected to separate. As a result of stopping the BLC, a turbulent boundary layer is developed along the remaining body length.

This drag reduction procedure is by no means unique. Other schemes may be defined, resulting in somewhat different optimal bodies. Nevertheless, it was felt that this procedure is the most logical one according to the following points:

1 The suction area is to be minimized due to technological problems. There is no suction up to the point of onset of instability, and there is no blowing at points where stability is naturally maintained.

2 Delaying laminar separation by suction is inefficient due to the large suction velocities involved. Therefore, the boundary layer is allowed to behave naturally from this point on.

Another restriction on the optimization procedure is the family of bodies from whom the optimal shape is to be selected. In this study it was decided to define a limited two-parameter family which allows describing both the body coordinates and the potential flowfield analytically.

We now define the optimization goal: In a two-parameter family of axisymmetric bodies, determine the nonseparated body whose drag (composed of the skin friction and suction energy contributions) is minimal according to the prescribed BLC technique.

Nomenclature

C_D = drag coefficient ($= \text{drag}/\frac{1}{2}\rho U_\infty^2 V^{2/3}$)
C_F = friction drag coefficient
C_S = suction drag coefficient
D = body maximum diameter
F = distributed source/sink nondimensional stream function
f = transformed stream function ($= \psi/\sqrt{U\nu x}$)
L = body length
L_S = length of arc along with suction is applied
l = distributed source base semilength
M = slope of sink strength function
N = source to sink distribution lengths ratio
n = exponent
P = pressure
P_0 = stagnation pressure
Q = volume of fluid withdrawn by suction per unit time
q_∞ = dynamic pressure ($= \frac{1}{2}\rho U_\infty^2$)
Re = Reynolds number ($= U_\infty V^{1/3}/\nu$)
r_0 = body local radius
S = velocity gradient parameter $\left(= \frac{x}{U}\frac{dU}{dx}\right)$
T = radius gradient parameter $\left(= \frac{x}{r_0}\frac{dr_0}{dx}\right)$
U = local potential velocity
U_∞ = vehicle velocity
(u,v) = axial and radial velocity components in (x,r) system of coordinates, respectively
V = body volume
v_0 = suction velocity
(x,r) = cylindrical system of coordinates
(x,y) = fixed to the body contour system of coordinates
Δx = boundary-layer calculation interval
$\bar{y}$ = Falkner-Skan coordinate $\left(= \sqrt{\frac{U}{x\nu}}y\right)$
Γ = source strength function
ν = kinematic viscosity
(ξ,η) = nondimensionalized system of coordinates
(ξ_0,η_0) = point at which the stream function is to be calculated
ρ = fluid density
ψ = stream function
Ω = combined stream function of distributed source, distributed sink and uniform flow system

The Two-Parameter Family of Bodies. The two-parameter family of bodies, which defines the mathematical domain in which the optimization is to be performed, is described by an equilateral triangular source distribution and an equilateral triangular sink distribution positioned in tandem in a uniform flow.

In order to construct the mathematical relations of this family (i.e., the body coordinates and the corresponding potential flow), let us first introduce the stream function of an isolated equilateral triangular distributed source. When the source is positioned symetrically around the origin between points $-Nl$ and $+Nl$ on the x-axis of the cylindrical coordinate system (x,r), (Fig. 2(*a*)), its nondimensional stream function is

$$F(\xi_0,\eta_0,N)=\frac{\psi}{\Gamma_0}\frac{N}{l}=-\xi_0[\xi_0^2+\eta_0^2]^{1/2}+\frac{1}{2}(\xi_0+N)[(\xi_0+N)^2+\eta_0^2]^{1/2}+\frac{1}{2}(\xi_0-N)[(\xi_0-N)^2+\eta_0^2]^{1/2}-\frac{1}{2}\eta_0^2 Ln\frac{\{[(\xi_0+N)^2+\eta_0^2]^{1/2}-(\xi_0+N)\}\{[(\xi_0-N)^2+\eta_0^2]^{1/2}-(\xi_0-N)\}}{[(\xi_0^2+\eta_0^2)^{1/2}-\xi_0]^2} \quad (1)$$

where (ξ,η) is the nondimensional coordinate system, $\xi=x/l$, $\eta=r/l$. (ξ_0,η_0) is the point in which the nondimensional stream function F is calculated, and Γ_0 is the value of the source strength function at $\xi=0$.

Figure 2(*b*) describes the full system of sources and sinks positioned in a uniform flow of unit velocity. When equating the total source and sink effluxes (in order to form a closed body), we obtain the total nondimensional stream function,

$$\Omega = N^2 M\,\mathrm{SGN}(\xi_0-1)F(\mathrm{ABS}(\xi_0-1),\eta_0,1) - M\,\mathrm{SGN}(\xi_0-N-2)F(\mathrm{ABS}(\xi_0-N-2),\eta_0,N)-\frac{1}{2}\eta_0^2, \quad (2)$$

where M is the slope of the sink strength function, and the functions SGN and ABS are written in a computer-oriented form. Once the stream function is known, the locus of $\Omega=0$ is easily calculated to form the axisymmetric body. The cylindrical velocity components (u,v) are derived from

$$u = 1-\frac{1}{\eta_0}\left[N^2 M\,\mathrm{SGN}(\xi_0-1)\frac{\partial F}{\partial \eta_0}(\mathrm{ABS}(\xi_0-1),\eta_0,1) - M\,\mathrm{SGN}(\xi_0-N-2)\frac{\partial F}{\partial \eta_0}(\mathrm{ABS}(\xi_0-N-2),\eta_0,N)\right] \quad (3a)$$

$$v = \frac{1}{\eta_0}\left[N^2 M\frac{\partial F}{\partial \xi_0}(\mathrm{ABS}(\xi_0-1),\eta_0,1) - M\frac{\partial F}{\partial \xi_0}(\mathrm{ABS}(\xi_0-N-2),\eta_0,N)\right] \quad (3b)$$

and the potential flowfield is obtained.

Figure 2(*c*) describes four members of the family of bodies. The two parameters M and N completely define the body. The parameter M regulates the maximum body thickness, and the parameter N controls its longitudinal location.

Members of the family of bodies, although described by only two parameters, are surprisingly similar to well-known streamlined low drag bodies such as the Gertler family [11] and Parsons' *I*-36 all-turbulent body [1]. Therefore, it may be assumed that the optimal body belonging to this family will represent a good indication of the obtainable theoretical limit of low drag.

Boundary Layer Calculations. Once the axisymmetric body coordinates and its potential flowfield are known, boundary-layer calculations can be performed. Here the laminar axisymmetric boundary-layer equations with suction boundary conditions were solved with a predictor-corrector version of the numerical method of lines [12].

Applying the Falkner-Skan transformation to the axisymmetric boundary-layer equations [13], we obtain the partial differential equation for the stream function,

$$f'''+\left(\frac{S+1}{2}+T\right)ff''+S(1-f'^2)=x\left(f'\frac{\partial f'}{\partial x}-f''\frac{\partial f}{\partial x}\right) \quad (4)$$

where $f=\psi/\sqrt{U\nu x}$

$$S=\frac{x}{U}\frac{dU}{dx},\ T=\frac{x}{r_0}\frac{dr_0}{dx},$$

the coordinates (x,y) are fixed to the body contour, $(\ )'$ represents derivatives with respect to the Falkner-Skan coordinate

$$\bar{y}=\sqrt{\frac{U}{x\nu}}y,U$$

is the local potential velocity and r_0 the local body radius. The boundary conditions to equation (4) are

$$\begin{aligned} y=0: \quad f_0 &= -\frac{1}{r_0}\frac{1}{\sqrt{U\nu x}}\int_0^x r_0 v_0\,dx \\ f_0 &= 0 \\ y\to\infty: \quad f_\infty &= 1 \end{aligned} \quad (5)$$

where v_0 is the suction velocity.

Equation (4) is traditionally solved by approximating the x-derivatives with finite differences and thus obtaining an ordinary differential equation for each x station (see, for example, Smith and Clutter [13]). The obtained set of two-point boundary-value problems is solved by an iterative procedure on f_0'' which converges when the infinity boundary condition is fulfilled. To initiate these iterations, one needs a first guess to f_0''; a bad guess can cause a divergence of the iteration procedure, or at least can increase the total number of these time-consuming calculations. If this first guess of f_0'' at station $x+\Delta x$ can be predicted from the known solution at station x, the number of iterations will be significantly decreased.

In this study, we calculated the longitudinal derivative of f_0'', $\partial f_0''/\partial x$, according to an approximate analytical solution of the axisymmetric boundary-layer equations. A four-parameter velocity profile was assumed and these parameters were calculated from the boundary-layer equation and its three derivatives at $y=0$ (for details, see Bar-Haim and Weihs [14]). Incorporating the analytical expression to $\partial f_0''/\partial x$ in the solution scheme, it becomes possible to define the first choice for f_0'' at the $x+\Delta x$ station (predictor),

$$f_0''|_{x+\Delta x}=f_0''|_x+\Delta x\frac{\partial f_0''}{\partial x} \quad (6)$$

and refine this value with a conventional shooting method procedure (corrector) until the infinity boundary condition is achieved. This way, the iterative procedure is accelerated and final convergence is ensured.

Downstream of the neutral stability point of the laminar boundary layer, which depends on the local velocity profile only, disturbance waves are intensified to form the final transition to turbulence. There are simple criteria to calculate the neutral stability point location under suction conditions (for example, Wazzan, et al. [8] and Weighardt [10]) but the influence of the suction on the transition location is not entirely understood.

In the present study, the universal stability criterion of Wazzan, et al. [8] was incorporated and the suction velocity at each x station was adjusted to maintain the neutral stability of the boundary layer. By applying a stability criterion instead of

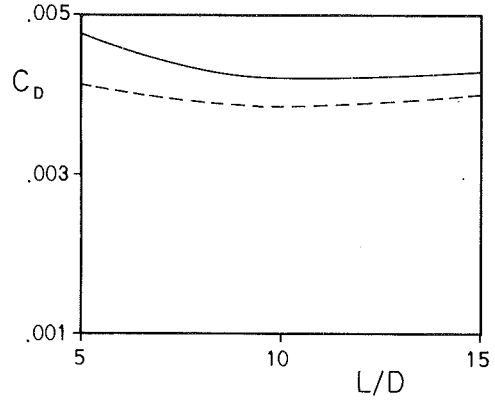

Fig. 3 Minimum obtainable drag coefficient versus fineness ratio at Re = 10^7; broken line represents the skin-friction contribution

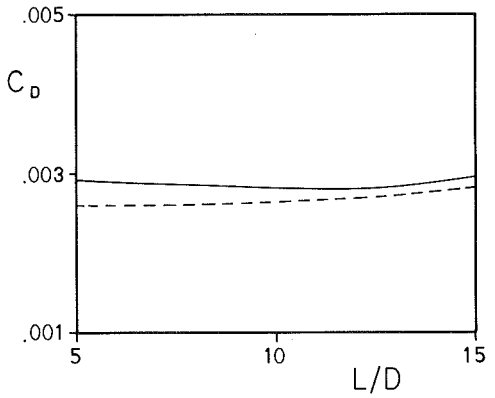

Fig. 4 Minimum obtainable drag coefficient versus fineness ratio at Re = 10^8; broken line represents the skin-friction contribution

a hypothetical transition criterion (for example, the e^n criterion, where n is dependent on the free-stream turbulence, surface roughness, etc.), we cause the definition of a larger suction area along the body. Nevertheless, it was felt that the optimal design should not depend on *a priori* unknown parameters such as the natural turbulent conditions in the sea; therefore the design is based on a stability criterion, which is more conservative, with the acceptable penalty of an increase in the suction area.

At the point along the body where the local friction coefficient becomes negative, laminar separation is assumed to be present, which for streamlined bodies is manifested by the appearance of a small separation bubble and the reattachment of a turbulent layer (see reference [1] and reference [12, pp. 366–367]). Suction is no longer applied downstream of this point and the turbulent boundary layer is calculated along the remaining body length by Nash's integral method [16]. Bodies along which the turbulent boundary layer is separating are excluded from the optimization procedure.

Drag Computation. The total drag of an axisymmetric body with distributed suction is composed of three parts: friction drag, from drag and suction drag. For shapes with impermeable surface, the drag is computed according to integral formulas such as the Young [16] or Granville [17] equations. These equations do not account for the momentum transfer during the suction procedure and thus are not suitable for our purpose. Here, the friction drag coefficient C_F was calculated by integrating the computed friction coefficient along the body surface, and normalizing the integral by $V^{2/3}$, where V is the body volume. Cebeci, et al. [18] have shown that the form drag is only about 6 percent of the total drag for bodies with impermeable wall with length-to-maximum-diameter ratio of 4. The form drag is expected to be even less significant for suction controlled boundary layers on axisymmetric bodies, and therefore was neglected in this paper. Suction causes boundary layer thinning and so no second-order viscous corrections were made to the external velocity field.

The suction contribution to the total drag coefficient is composed of the theoretical power required to pump the ingested fluid to a point at the stagnation pressure, normalized by the dynamic pressure q_∞, the body velocity U_∞ and the reference area $V^{2/3}$,

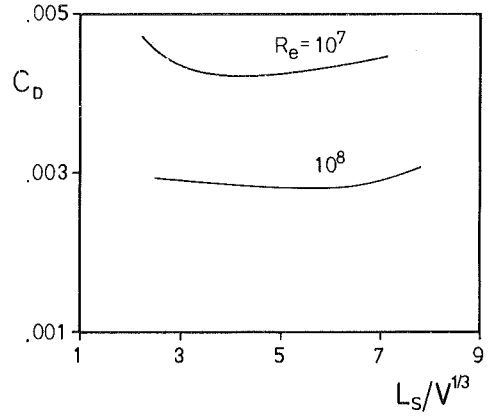

Fig. 5 Minimum obtainable drag coefficient versus nondimensional suction arc length, for various Reynolds numbers

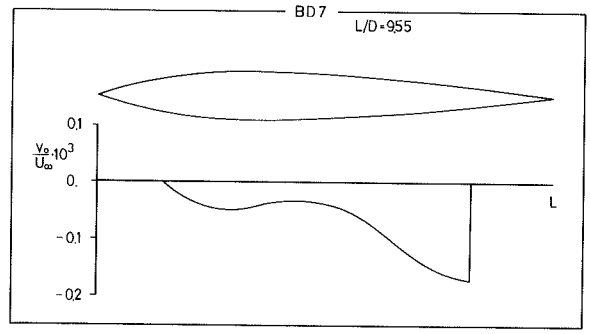

Fig. 6 Minimum drag body BD7 with suction velocity distribution at Re = 10^7

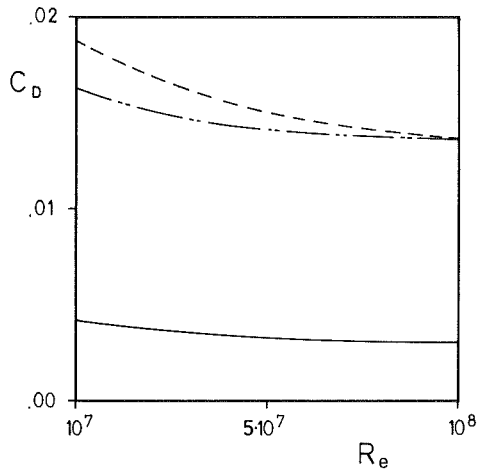

Fig. 7 Drag coefficient of body BD7 as function of Re: _____ suction controlled boundary layer; _ _ _ _ _ _ _ _ fully turbulent boundary layer; ___ _ _ ___ laminar-turbulent boundary layer with transition location calculation

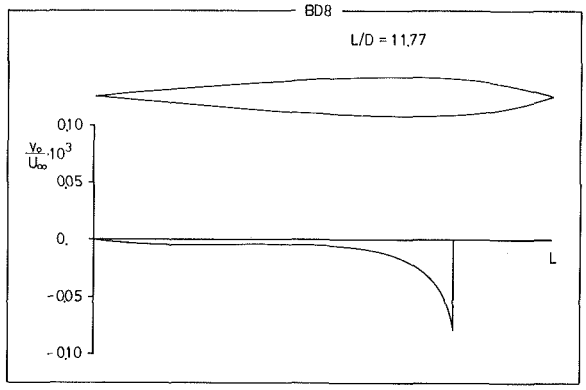

Fig. 8 Minimum drag body BD8 with suction velocity distribution at Re = 10^8

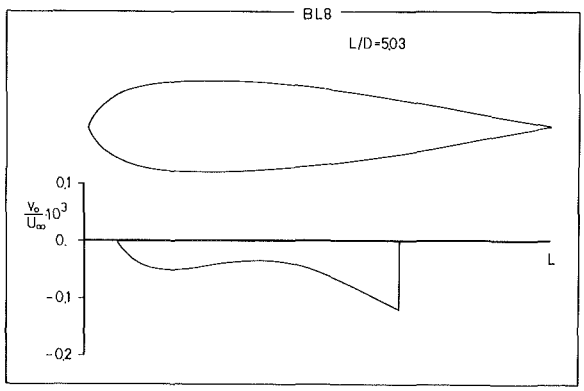

Fig. 9 Minimum drag body BL8 with suction velocity distribution at Re = 10^8

$$C_S = \frac{1}{q_\infty \cdot U_\infty \cdot V^{2/3}} \cdot \int_0^L (P_0 - P)dQ \tag{7}$$

where Q is the volume of the fluid sucked per unit time. Finally, the total drag coefficient is expressed by the addition of the two terms,

$$C_D = C_F + C_S \tag{8}$$

The suction drag coefficient is not fully representative of the actual energy required to perform the suction BLC, in the same way that C_F does not represent the energy that has to be supplied to the propulsion system. These terms, referred to as drag contributions, have only a comparative meaning relative to the theoretically calculated external drag of other bodies.

Optimization Technique. The mathematical formulation of the optimization problem is to find

$$\min C_D(M,N) \tag{9}$$

subject to the constraint,

$$x_S > x_{TE}. \tag{10}$$

Here $(\ )_S$ represents separation and $(\ )_{TE}$ trailing edge.

The two-variable direct search was conducted according to the linear method of Hooke and Jeeves [19]. Due to the fact that the number of optimization variables is only two, there was no need to especially treat the separation constraint. Instead, the boundary of the feasible region has been investigated by "riding" the constraint, whenever the linear search arrived close to it.

Results and Discussion

Optimization searches have been conducted to define the body of minimal drag at Reynolds number of 10^7 and 10^8, based on $V^{1/3}$. The body length-to-maximum-diameter ratio (L/D) and the arc length over which suction is required,

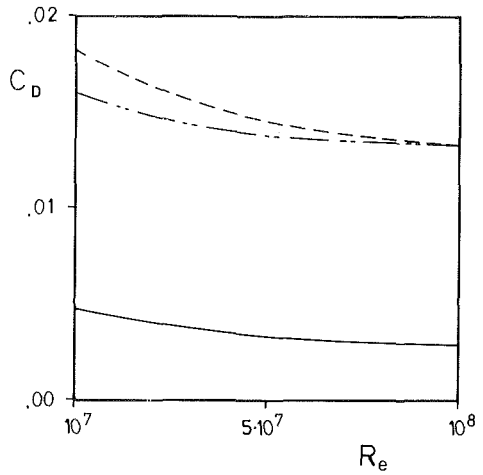

Fig. 10 Drag coefficient of body BL8 as function of Re: _____ suction controlled boundary layer; _ _ _ _ _ _ _ _ fully turbulent boundary layer; ___ _ _ ___ laminar-turbulent boundary layer with transition location calculation

normalized by $V^{1/3}$ ($L_S/V^{1/3}$) are essential parameters in all practical designs, so that minimum drag calculations have also been performed as functions of these two quantities.

Figure 3 describes the minimum obtainable drag as a function of L/D at $\mathrm{Re} = 10^7$. Each point on the solid line is the minimum line obtained for a body of given L/D. The broken line represents the friction drag coefficient C_F of the bodies forming the solid line. It may be observed that the gap between the two lines represent the suction drag, which decreases as L/D increases. This is due to the fact that as L/D grows, within the range of this parameter studied here, less and less suction energy is required to prevent the boundary layer from becoming unstable. The total drag line has a well-defined minimum at $L/D = 9.55$ which represents the body of least drag of the two-parameter family studied here.

Figure 4 describes the minimum obtainable drag as a function of L/D, at $\mathrm{Re} = 10^8$. Here the suction drag is at a minimum for $L/D = 11$. The total drag line has again a minimum at $L/D = 11.77$. When comparing Figs. 3 and 4 it may be observed that the suction drag contribution is smaller for $\mathrm{Re} = 10^8$. This is due to the fact that when the Reynolds number is increased, the boundary layer becomes thinner and less mass has to be taken out by suction in order to maintain stability.

Figure 5 describes the minimum obtainable drag as a function of the nondimensional suction arc length $L_S/V^{1/3}$ at $\mathrm{Re} = 10^7$ and 10^8. At first, the total drag decreases as the suction arc length is increased because the body area on which there is a turbulent boundary-layer run is reduced. Then, the increase in the laminar friction coefficient caused by suction becomes more and more significant, and the total drag increases.

Figure 6 describes the minimum drag body at $\mathrm{Re} = 10^7$ (called BD7) with the required suction velocity distribution. Suction starts at a point 14 percent of the body length and ends at 76 percent length when turbulent transition occurs. The maximum local suction velocity is only 0.016 percent of the body velocity U_∞. The BD7 body drag coefficient is 0.0042, 18 percent less than Parsons' X-35 optimal body [1]. Figure 7 describes the total drag of the BD7 body under suction condition as a function of Re, as well as this body's fully turbulent drag and normal drag (when no BLC is applied), calculated with transition estimated by Crabtree's criterion [20]. It may be observed that the distance between the two upper curves decreases with growing Re due to the fact that the transition point is displaced upstream as the Reynolds number is decreased.

Figure 8 describes the minimum drag body at $\mathrm{Re} = 10^8$

(called BD8) with the required suction velocity. The suction, although with a surprisingly small maximum velocity, is distributed almost over the whole body, and the resulting drag coefficient equals 0.0028, only 22 percent of that of Parsons' *I*-36 optimal body [1]. Due to the fact that the large suction area required for body BD8 may prevent practical application of this body, we also show body BL8 (Fig. 9) which has the minimal suction arc length parameter at $\mathrm{Re} = 10^8$. The BL8 body has a drag coefficient of 0.0029, but its suction length parameter is reduced by 60 percent relative to the BD8 body. Figure 10 describes the drag behavior of body BL8 as a function of the Reynolds number.

The shallow minima of the drag functions in Figs. 3 and 4 are encouraging from the practical point of view. It indicates that the designers of suction controlled bodies do not have to be limited to impractical L/D or $L_S/V^{1/3}$ ratios. Instead, more suitable parameters may be chosen with only a small penalty in the drag obtained. The crucial design parameter is shown to be the Reynolds number, and while BLC designs at $\mathrm{Re} = 10^7$ have only moderately lower drags than the optimal impermeable wall bodies, at the higher Reynolds number of 10^8 great improvements in drag, by a factor of 4 or more, are obtained. These savings are large enough to offset the added complexity (and cost) of suction BLC systems.

References

1 Parsons, J. S., "The Optimum Shaping of Axisymmetric Bodies for Minimum Drag in Incompressible Flow," PhD Thesis, School of Mechanical Engineering, Purdue University, Lafayette, IN, 1972.

2 Zedan, M. F., and Dalton, C., "Viscous Drag Computation for Axisymmetric Bodies at High Reynolds Numbers," AIAA 11th Fluid and Plasma Dynamics Conference, Seattle, WA, 1978, AIAA Paper 78-1183.

3 Hess, J. L., "On the Problem of Shaping an Axisymmetric Body to Obtain Low Drag at Large Reynolds Numbers," *Journal of Ship Research*, Vol. 20, 1976, pp. 51-60.

4 Bushnell, D. M., "Turbulent Drag Reduction for External Flows," AIAA 21th Aerospace Science Meeting, Reno, NV, 1983, AIAA Paper 83-0227.

5 Walsh, M. J., "Riblets as a Viscous Drag Reduction Technique," *AIAA Journal*, Vol. 21, 1983, pp. 485-486.

6 Ringleb, F. O., "Separation Control by Trapped Vortices," *Boundary Layer and Flow Control*, edited by Lachmann, G. V., Pergamon Press, Oxford, 1961.

7 Goldschmied, F. R., "Aerodynamic Hull Design for HASPA LTA Optimization," *Journal of Aircraft*, Vol. 15, 1978, pp. 634-638.

8 Wazzan, A. R., Gazley, C., and Smith, A. M. O., "Tollmien-Schlichting Waves and Transition," *Progress in Aerospace Science*, Vol. 18, edited by Bagley, J. A., and Finley, P. J., Pergamon Press, Oxford, 1979.

9 Goldschmied, F. R., "Integrated Hull Design, Boundary-Layer Control and Propulsion of Submerged Bodies: Wind Tunnel Verification," AIAA/SAE/ASME 18th Joint Propulsion Conference, Cleveland, OH, 1982, Paper 82-1204.

10 Wieghardt, K., "Zur Berechnung Ebener und Drehsymmetrischer Grenzschichten mit Kontinuierlicher Absaugung," *Ingenieur-Archiv*, Vol. 22, 1954, pp. 368-377.

11 Gertler, M., "Resistance Experiments on a Systematic Series of Streamlined Bodies of Revolution—for Application to the Design of High-Speed Submarines," The David W. Taylor Model Basin Report C-297, 1951.

12 Cebeci, T., and Bradshaw, P., *Momentum Transfer in Boundary Layers*, McGraw-Hill Book Company, New York, 1977.

13 Smith, A. M. O., and Clutter, D. W., "Solution of the Incompressible Laminar Boundary-Layer Equations," *AIAA Journal*, Vol. 1, 1963, pp. 2062-2071.

14 Bar-Haim, B., and Weihs, D., "Boundary-Layer Flow Over Long Cylinders With Suction," ASME *Journal of Applied Mechanics* (in print).

15 Nash, J. F., "Turbulent Boundary Layer Behaviour and the Auxiliary Equation," ARC CP 835, London, 1965.

16 Young, A. D., "The Calculation of the Total and Skin-Friction Drags of Bodies of Revolution at Zero Incidence," ARC R&M 1874, 1939.

17 Granville, P. S., "The Calculation of the Viscous Drag of Bodies of Revolution," The David W. Taylor Model Basin Report 849, 1953.

18 Cebeci, T., Mosinskis, G. J., and Smith, A. M. O., "Calculation of Viscous Drag of Two-Dimensional and Axisymmetric Bodies in Incompressible Flow," AIAA 10th Aerospace Science Meeting, San Diego, CA, AIAA Paper 72-1.

19 Hooke, R., and Jeeves, T. A., "Direct Search Solution of Numerical and Statistical Problems," *Journal of the Association for Computing Machinery*, Vol. 8, 1961, pp. 212-229.

20 Crabtree, L. F., "Prediction of Transition in the Boundary Layer on an Aerofoil," *Journal of the Royal Aeronautical Society*, Vol. 62, 1958, pp. 525-528.

The Formation of Stratified Combustible Mixtures in Closed Tubes by Molecular and Convective Diffusions

O. Badr
Mechanical Engineering Department,
Building 19,
Lehigh University,
Bethlehem, PA 18015

This paper describes a theoretical study on the formation of stratified combustible mixtures in closed long vertical flame tubes. The concentration profiles of the fuel (methane) in air, just before ignition took place, were predicted using a one-dimensional model involving molecular and convective diffusional processes. Phenomenological and experimental justification of the one-dimensional assumption was given and some of the predicted data were compared with experiment for different test conditions. The model appears to have successfully predicted the concentration profiles in some situations where other models failed.

Introduction

Stratified combustible atmospheres are frequently encountered in practice such as those associated with the leakage of fuels from storage tanks or pipelines, with oil or gas spills during transportation, with the formation of gas pockets in coal mine galleries, and with the operation of stratified charge internal combustion engines. If such a mixture is ignited at a point, the formed flame front propagates with a velocity which depends on local conditions. The present work was a part of an overall program to study the characteristics of flames propagating through stratified methane-air mixtures in closed circular tubes. The objective of this work is to predict *just before ignition*, the concentration profiles of methane in air formed by molecular and convective diffusion within such tubes.

Molecular diffusion is the transfer of the molecules of a stagnant fluid through another under the influence of a concentration gradient. When a heavy layer of fluid is placed on top of a lighter one, a gross movement is initiated by natural convection. The motion of such unstably stratified fluid has two extreme situations [3]. Rayleigh-Taylor flow, in which diffusion of momentum and density is ignored, is clearly an unconditionally unstable situation. On the other hand, the Benard-Rayleigh flow is a situation in which the combined stabilizing action of the diffusion of both momentum and density is important. The physical problem considered in this paper involves a Benard-Rayleigh-type flow.

Experimental Setup. The flame tube used in this work was made of a 274.3-cm long and 6.35-cm ID plexiglass tube as shown in Fig. 1. The tube was mounted on a vertical rotating disk to allow the study of flame propagation in the three main directions (upward, horizontal, and downward). A quick action plate valve was inserted at the middle of the tube to separate two different initially homogeneous methane-air mixtures. Thus diffusion could be initated by retrieving that valve and producing over a certain period of time a stratified gas mixture.

In some experiments, when the flame was to propagate upward from a rich methane-air mixture (lighter) to a lean mixture (heavier) or to propagate downward from a lean mixture to a rich mixture (i.e., a layer of heavy gas on top of a lighter one), combined molecular and convective diffusion of Benard-Rayleigh type was the way to prepare the unburned mixtures. Moreover, the time required to form a certain stratified mixture by both molecular and convective diffusion was two-orders-of-magnitude less than that required by molecular diffusion only.

Literature Review. Buoyant convection phenomena such as the motion of plumes from isolated sources [20], and heat transfer by natural convection from vertical walls [1] have been studied extensively. However, Benard-Rayleigh type of buoyant convection in enclosures has received relatively little attention because it is considerably more complex [11].

Sparrow, Husar, and Goldstein observed some thermals ascending the fluid environment (water) above a heated horizontal surface. The thermals were generated at fixed sites which were spaced more or less regularly along the heated surface [18]. In an experimental study of the response of a thin rotating layer of silicon oil when heated from below, Rossby noticed a number of unstable cells with dimensions and geometry dependent on the rate of rotation and Rayleigh number [13]. Similar shapes were observed by Krishnamurti [8] and Schmidt and Saunders [15]. Considering a fluid bounded above and below by horizontal rigid, conducting walls and bounded on the sides by vertical rigid, insulating walls with aspect ratio ≤ 1.0, Elder observed an array of blobs rapidly growing above the lower heated surface. This was followed by a gradual appearance of large-scale thermals

Contributed by the Fluids Engineering Division for publication in the JOURNAL OF FLUIDS ENGINEERING. Manuscript received by the Fluids Engineering Division, April 23, 1984.

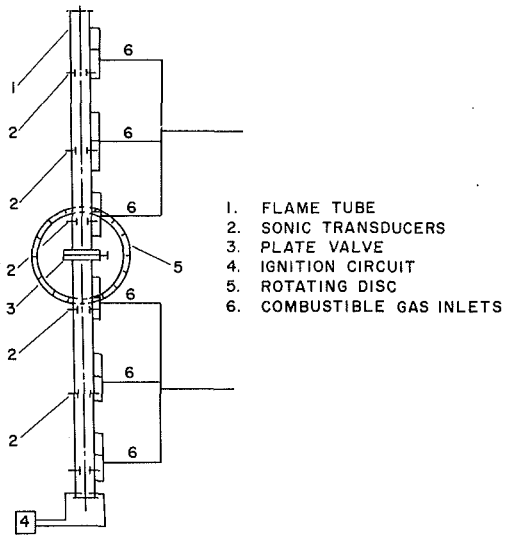

Fig. 1 Schematic diagram of the apparatus

in the vertical direction and of a cellular pattern in the horizontal direction [3].

In a one-dimensional theoretical study of natural convection in a vertical enclosure heated from below, Elder [4] and Herring [6] simplified the problem by assuming a horizontal mixing wave moving vertically. Although Elder [4] could not confirm that experimentally, he claimed some physical validity based on the known heat transfer mechanism outside the heat sublayer. Moreover, he stated: "The reader unfamiliar with the ruthless approximations needed to cope with turbulence studies may be surprised that the approximation works at all."

In an experimental and theoretical study of stratified combustion in flame tubes, Tsang [19] predicted the concentration profiles of methane in air in such tubes and then checked them using sonic transducers. He reported a difference between theory and experiment of up to 50 percent of measured values.

The previous work sited by the author, except that of Tsang [19], dealt with problems of different geometry, boundary conditions, initial conditions, and objectives. However, their observations of such Benard flows were helpful in developing the present model.

This paper describes the numerical solution developed to predict the isothermal axial concentration profiles of methane in air when a heavier gas is placed on top of a lighter one in a vertical tube with both ends *closed*.

Governing Equations. When the closed tube is in the vertical position with a heavier gas in the upper half, a lighter gas in the lower half, and with the middle valve fully open, mixing of the two gases occurs by natural convection and molecular diffusion. In such a case, the mass of gases in an elemental control volume is not conserved but the volume is. Therefore, across a horizontal plane, a mass flowing upward (due to density difference) would cause a downward flow with the same velocity. Purely for thre derivation of the equations, and outside the boundary-layer zone (i.e., neglecting wall effects), the flame tube is imagined to consist of an infinite number of vertical stream tubes of equal cross-sectional areas such that the flow velocities in any two adjacent tubes, at the same axial location, are equal in magnitude and opposite in direction; the heavier mixture flows downward in one stream tube and the lighter mixture flows upward in the other. Such infinitesimally small stream tubes simulate the vertical thermals observed by many researchers when a fluid layer was heated from below [3, 8, 13, 18]. The velocities of the mixtures in the imagined stream tubes are fictitious and used only to predict the concentration profiles. Assuming axial symmetry and that the flow away from the ends of the flame tube is one-dimensional and neglecting the wall effects, the governing equations of the upward flow in one stream tube, as derived in Appendices 1 and 2, are shown as follows.

Table 1 Comparison of values of diffusion coefficient of methane into air at room temperature and pressure

References Number	Basis of Evaluation	Diffusion Coefficient (cm^2/s)
5	Experiment	0.2535
5	Analytical	0.2336
7	Analytical	0.2339
9	Analytical	0.1966
10	Analytical	0.2417
16	Analytical	0.2383
Present Work	Experimental	0.2120

A Conservation of Mass:

$$\frac{\partial c}{\partial t} = D\frac{\partial^2 c}{\partial y^2} - \frac{\partial (c \cdot v)}{\partial y} \tag{1}$$

B Conservation of Momentum:

$$\rho \frac{\partial v}{\partial t} = \frac{1}{2} v^2 \frac{\partial \rho}{\partial y} + \frac{4}{3}\mu \frac{\partial^2 v}{\partial y^2} \tag{2}$$

Available information on the binary diffusion coefficient or methane-air mixtures [5, 7, 9, 10, 16] showed differences up to 30 percent as shown in Table 1. Thus the diffusion coefficient was measured using the apparatus described here. Two different methane air mixtures were placed into the two halves of the vertical tube with the heavier mixture in the

Nomenclature

A = cross-sectional area of an infinitesimally small stream tube
C = relative concentration by volume
D = molecular diffusion coefficient
G = nondimensional constant
g = gravitational acceleration
H = normalized time element
K = normalized distance element
L = total length of the flame tube
M = molecular weight
m = mass
P = pressure
$\tilde{p}$ = total or stagnation pressure
$\tilde{R}$ = universal gas constant
TM = absolute temperature
T = nondimenional parameter in time
t = time
U = nondimensional parameter in velocity
v = velocity component in the y-direction
Y = nondimensional parameter in distance (y)
y = distance in the y-direction measured from the bottom of the flame tube
α = a ratio $= K/H^2$
λ = wavelength
σ = surface tension between two fluids
ρ = density
μ = dynamic viscosity
ν = kinematic viscosity
Δ = small increment

Subscripts

a = air
CH_4 = methane
0 = initial
t = at time t
y = at axial location y

Superscripts

$\cdot$ = per unit time
n = time level

lower half. The molecular diffusion process was started by opening the midplate valve and the concentration of methane with respect to time was monitored at various points along the tube using sonic transducers [12]. The measured diffusion coefficient of methane into air was 0.212 cm^2/s. Moreover, an average viscosity of 0.01735 g/(m•s) for methane-air mixtures was calculated from Wilke's formula [21].

The density of the mixture at a point in the flame tube can be expressed in terms of the local concentration of methane and the densities of air and methane as

$$\rho = (K_1 c + K_2)p \tag{3}$$

where

$$K_1 = \frac{M_{CH_4} - M_a}{\bar{R} \cdot TM} \text{ and } \quad K_2 = \frac{M_a}{\bar{R} \cdot TM} \tag{4}$$

Differentating equation 3 w.r.t. distance y, the density gradient is

$$\frac{\partial \rho}{\partial y} = pK_1 \frac{\partial c}{\partial y} + (K_1 c + K_2) \frac{\partial p}{\partial y} \tag{5}$$

Cancelling $\partial p/\partial y$ between equations (5) and (29) (Appendix 2) and substituting equation (3), equation (5) becomes

$$\left(\frac{1}{K_1 c + K_2} + \frac{1}{2} V^2\right) \frac{\partial \rho}{\partial y} = \frac{pK_1}{K_1 c + K_2} \cdot \frac{\partial c}{\partial y} - p(K_1 c + K_2)\left(g + v \frac{\partial v}{\partial y}\right) \tag{6}$$

Using the maximum value of (v) predicted by Tsang [19] [$v = 5$ cm/s] and an average value for c[$c = 10$ percent $= 0.10$], the second term within the brackets on the left-hand side of equation (6) is some eight-orders-of-magnitude less than the first term. Thus, neglecting the second term, equation (6) becomes

$$\frac{\partial \rho}{\partial y} = pK_1 \frac{\partial c}{\partial y} - p(K_1 c + K_2)^2 \left(g + v \frac{\partial v}{\partial y}\right) \tag{7}$$

Substituting ρ from equation (3) and $\partial \rho/\partial y$ fom equation (7) in equation (2), the equation of conservation of momentum becomes

$$\frac{\partial v}{\partial t} = \frac{v^2 K_1}{2(K_1 c + K_2)} \cdot \frac{\partial c}{\partial y} - \frac{1}{2} v^2 (K_1 c + K_2)\left(g + v \frac{\partial v}{\partial y}\right) + \frac{4}{3} \nu \frac{\partial^2 v}{\partial y^2} \tag{8}$$

Initial and Boundary Conditions

Since the tube is closed at both ends, i.e., there is no mass flow at these ends, the boundary conditions are

$$\begin{aligned} \frac{\partial c}{\partial y} &= 0 \quad \text{at} \quad y = 0 \quad \text{and} \quad y = L \\ v &= 0 \quad \text{at} \quad y = 0 \quad \text{and} \quad y = L \end{aligned} \tag{9}$$

Before the removal of the plate valve separating the two different initially homogeneous gas mixtures of methane and air, the two mixtures are stagnant. Thus the initial conditions are

$$\begin{aligned} c &= c_{01} \quad \text{for} \quad 0 < y < \frac{1}{2}, \quad \text{and} \quad t < 0 \\ c &= c_{02} \quad \text{for} \quad \frac{L}{2} < y < L, \quad \text{and} \quad t < 0 \end{aligned} \tag{10}$$

and

$$v = 0 \quad \text{for} \quad \text{all } y, \quad \text{and} \quad t < 0$$

Normalization

To normalize equations (2), (8)-(10), a reference length L, a reference time L^2/D, and a reference velocity $\sqrt{gL}$ are used. The new dimensionless variables are

$$\begin{aligned} Y &= y/L \\ T &= tD/L^2 \\ U &= v/\sqrt{gL} \end{aligned} \tag{11}$$

After normalization and rearranging, the equation of conservation of mass (2) becomes

$$\frac{\partial c}{\partial T} = \frac{\partial^2 c}{\partial Y^2} - G_1 \cdot \frac{\partial cU}{\partial Y} \tag{12}$$

and the equation of motion (8) becomes

$$\frac{\partial U}{\partial T} = \frac{1}{2} G_1 \frac{U^2}{(c + G_2)} \cdot \frac{\partial c}{\partial Y} - G_3 (c + G_2) \cdot U^2 \left(1 + U \frac{\partial U}{\partial Y}\right) + \frac{4}{3} G_4 \frac{\partial^2 U}{\partial Y^2} \tag{13}$$

where G_1, G_2, G_3 and G_4 are dimensionless constants defined as

$$\begin{aligned} G_1 &= g^{1/2} L^{3/2}/D \\ G_2 &= K_2/K_1 = \frac{M_a}{M_{CH_4} - M_a} \\ G_3 &= g^{3/2} L^{5/2} K_1/2D \\ G_4 &= \nu/D \end{aligned} \tag{14}$$

The normalized boundary conditions are

$$\begin{aligned} \frac{\partial c}{\partial Y} &= 0 \quad \text{at} \quad Y = 0 \quad \text{and} \quad Y = 1.0 \\ U &= 0 \quad \text{at} \quad Y = 0 \quad \text{and} \quad Y = 1.0 \end{aligned} \tag{15}$$

and the normalized initial conditions are

$$\begin{aligned} c &= c_{01} \quad \text{for} \quad 0 < Y < \frac{1}{2} \quad \text{and} \quad T < 0 \\ c &= c_{02} \quad \text{for} \quad \frac{1}{2} < Y < 1.0 \quad \text{and} \quad T < 0 \\ U &= 0 \quad \text{for} \quad \text{all } Y \quad \text{and} \quad T < 0 \end{aligned} \tag{16}$$

Method of Solution

A finite-difference scheme based on Crank-Nicolson implicit method [2] was used to approximate the derivatives of velocity and concentration with respect to time and space. At a point $(i, n + \frac{1}{2})$, where i represents the axial position and n represents the time level, the equation of conservation of mass (12) becomes

$$\begin{aligned} &[-\alpha/2 - G_1 \alpha H U_{i-1}^{n+1}/2] \cdot C_{i-1}^{n+1} + [1 + \alpha + G_1 \alpha H (U_i^{n+1} \\ &+ U_{i-1}^{n+1})/2] \cdot C_i^{n+1} + [-\alpha/2 - G_1 \alpha H U_i^{n+1}/2] \cdot C_{i+1}^{n+1} \\ &= (\alpha/2) C_{i-1}^n + (1 - \alpha) C_i^n + (\alpha/2) C_{i+1}^n - (G_1 \alpha H/2)(C_i^n U_i^n \\ &- C_{i-1}^n U_{i-1}^n + C_i^n U_{i-1}^n - C_{i+1}^n U_i^n) \end{aligned} \tag{17}$$

and the equation of conservation of momentum (13) becomes

$$U_i^{n+1} = U_i^n + (U_i^{n+1} + U_i^n)^2 \left[\frac{KG_1}{16H} \cdot \frac{(C_{i+1}^{n+1} - C_{i-1}^{n+1} + C_{i+1}^n - C_{i-1}^n)}{(C_i^{n+1} + c_i^n + 2G_2)}\right.$$

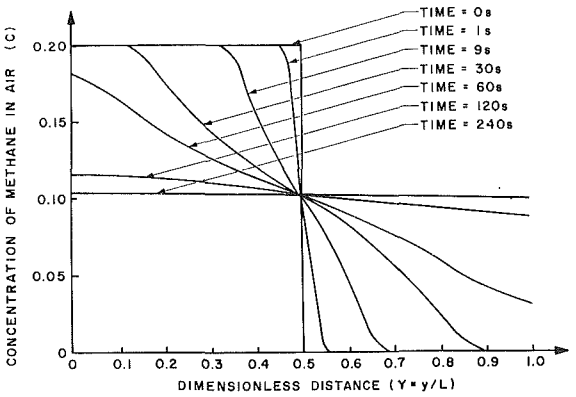

Fig. 2 Predicted concentration profiles after different periods of upward diffusion of a mixture of 20 percent methane in air into pure air

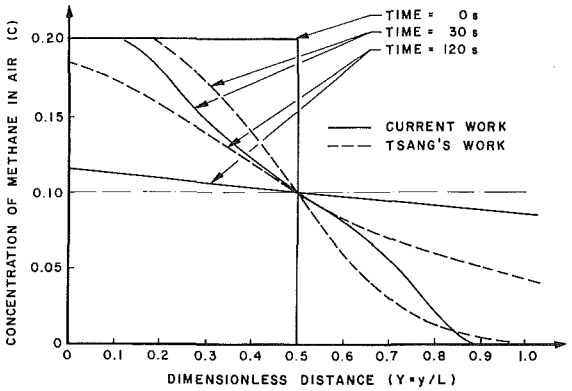

Fig. 3 Comparison between the present results and Tsang's results [10] of concentration profiles

$$-\frac{KG_3}{8}(C_i^{n+1}+C_i^n+2G_2)\left\{1+\frac{1}{8H}(U_i^{n+1}+U_i^n)(U_{i+1}^{n+1}-U_{i-1}^{n+1}+U_{i+1}^n-U_{i-1}^n)\right\}+\frac{2KG_4}{3H^2}(U_{i-1}^{n+1}-2U_i^{n+1}+U_{i+1}^{n+1}+U_{i-1}^n-2U_i^n+U_{i+1}^n) \quad (18)$$

where $H = \Delta Y$, $K = \Delta T$, and $\alpha = K/H^2$.

The dependent variables C and U in equation (17) and (18) were approximated by using Euler's and Newton's iterative techniques, respectively [17]. The time increment was 0.1 s for the initial stages of diffusion for the convergence of computation particularly with the discontinuity and step gradient in concentration profile. It was increased to 1 sec at longer diffusion times. Meanwhile, the distance increment was 2.8 cm, throughout the whole computation.

Results and Discussion

Figure 2 shows the concentration profiles in the flame tube resulting from the upward diffusion of a mixture of 20 percent methane in air into pure air after various diffusion times.

A comparison between the concentration profiles predicted by the present work and those of Tsang [19] after a diffusion time of 30 sec showed a slight difference while after a diffusion time of 120 sec the difference was large, as shown in Fig. 3. The presently predicted time to obtain a certain concentration profile was almost one-half of what Tsang found. Depsite all of the differences in test conditions and apparatus dimensions, it is believed that the main reason for the discrepancy between the two results was Tsang's neglect of the dynamic part of the pressure ($1/2\ \rho v^2$) in his derivation of

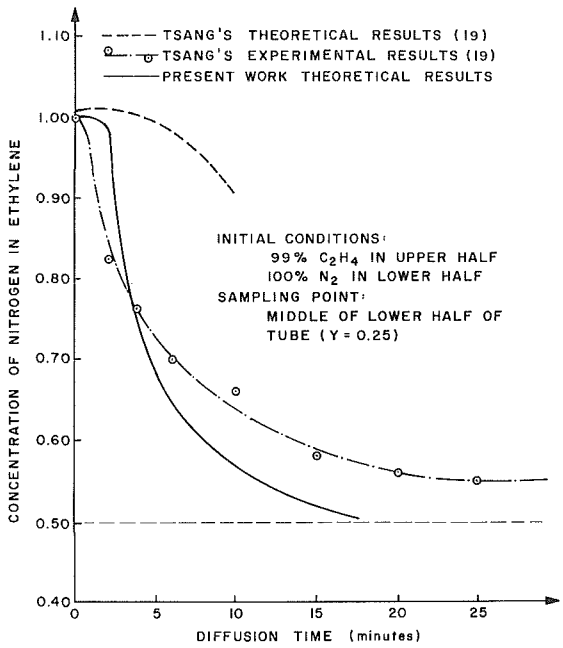

Fig. 4 Comparison between the present theoretical results and Tsang's theoretical and experimental results [10]

the equation of conservation of momentum (see Appendix 2). Because the velocities were low, neglecting the dynamic part of the pressure was acceptable when dealing with the absolute value of pressure, equation (28). However, when it came to pressure gradients, equation (29), neglecting the effect of the dynamic part of the pressure meant neglecting the terms ($\rho v\ \partial v/\partial y + 1/2\ v^2\ \partial \rho/\partial y$). These terms might have large values at the middle section of the tube especially at the early stages of the diffusion process.

To check the accuracy of the present convective diffusion model, a case in which Tsang's model had failed to predict the concentration profile satisfactorily was chosen for comparison. Nitrogen and 90 percent pure ethylene were chosen for their relatively similar molecular weights (28.016 and 28.052, respectively). With the slightly heavier ethylene in the upper half of the tube and nitrogen in the lower half, Tsang [19] measured the concentration of nitrogen in ethylene at the middle point of the lower half of the tube ($Y = 0.25$). Tsang's predicted values had grossly underestimated the diffusion rate while the presently predicted values had slightly overestimated it, as shown in Fig. 4. It is expected that the accuracy of the present model would have been even better if radial velocity components were accounted for.

Justification for the One-Dimensional Approach

Using the present apparatus, Fig 1, with tobacco smoke (which had a density approximately equal to that of air) in the upper half of the tube and a mixture of 20 percent methane in air in the lower one, it was observed that the interface between the two mixtures uniformly propagated downward, which meant that the wavelength of any ripples (equivalent to thermals in heat tranfser situations) at that interface was very small. Zuber [22] gave a formula for the wavelength of stable ripples established at the interface between two fluids, even in the case where the upper fluid had a higher density, as

$$\lambda = 2\pi\left[\frac{\sigma}{g(\rho_u-\rho_l)}\right]^{1/2} \quad (19)$$

where

λ = wavelength of the ripples
σ = surface tension between the two fluids
ρ_u, ρ_l = densities of upper and lower fluids, respectively

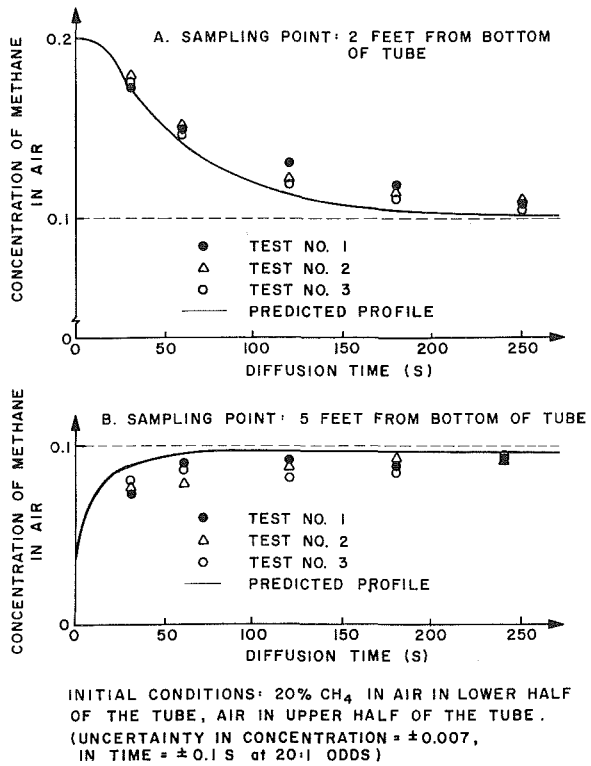

Fig. 5 Comparison between the predicted and measured (concentration-time) data at two sampling points

Since the surface tension between any two gases is very small, the wavelength of the ripples established at the interface, according to equation (19), is very small which agrees with the present observations.

The one-dimensional approach was not strictly correct at the ends of the tube. The velocity must be dissipated horizontally at the end walls, causing recirculation and possibly turbulence. Due to the large length-to-diameter ratio of the flame tube ($L/D \simeq 44$), the recirculation was restricted to the ends of the tube and the larger portion of the flow could be assumed one-dimensional. However, from the present visual study, the recirculation at the ends of the vertical tube was not evident and the disturbance due to the removal of the plate valve was negligible.

Experimental Verification of Concentration Profiles

To check the accuracy of the present model, experimental and predicted values of concentration of methane in air were compared to each other. Sonic transducers [12], Appendix 3, were used at two axial locations in the flame tube to measure, with respect to time, the concentration of methane in air. Each experiment was carried out three times to show the repeatability of measurements as shown in Fig. 5. The experimental profiles followed the general trend of the calculated ones. However, differences of 10 percent (or less) of readings between the predicted and the average measured concentrations were observed. The theoretical model, as expected, had slightly overestimated the rate of diffusion. This was probably due to the neglect of the radial velocity component in the derivation of the momentum equation. The present model, however, predicted with reasonable accuracy the concentration and concentration gradient profiles which were essential for the study of flame propagation within stratified combustible mixtures.

Summary

A one-dimensional theoretical model for the prediction of concentration profiles of gaseous fuels in stratified combustible mixtures has been presented. The physical and phenomenological basis of the model have been described. Justification for the one-dimensional approach has been given. A comparison between predicted and measured concentrations of methane in air has shown a reasonable agreement (± 10 percent of reading). However, for closer agreement, radial velocity components should be considered in the derivation of the momentum equation.

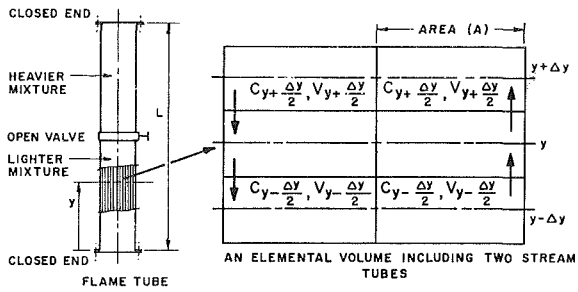

Fig. 6 Diagram of a flame tube consisting of an infinite number of small tubes

Acknowledgment

The author wishes to express his gratitude to Professor G. A. Karim for his encouragement and many stimulating discussions.

References

1 Catton, I., "Natural Convection in Enclosures," International Heat Transfer Conference, 6th, Toronto, Ontario, Canada, Vol. 6, 1978, p. 13.

2 Crank, J., and Nicolson, P., "A Practical Method for Numerical Evaluation of Solutions of Partial Differential Equations of the Heat Conduction Type," *Proceedings of the Cambridge Philosophical Society*, Vol. 43, 1947, p. 50.

3 Elder, J. W., "The Unstable Thermal Interface," *Journal of Fluid Mechanics*, Vol. 32, 1968, p. 69.

4 Elder, J. W., "The Temporal Development of Convection," *Journal of Fluid Mechanics*, Vol. 23, 1969, p. 77.

5 Fuller, E., Schettler, and Giddings, C., "A New Method For Prediction of Binary Diffusion Coefficients," *Ind. Eng. Chem.*, Vol. 58, No. 5, 1966, p. 19.

6 Herring, J. R., "Investigation of Problems in Thermal Convection: Rigid Boundaries," *J. Atmospheric Science*, Vol. 21, 1964, p. 277.

7 Hirschfelder, Curtiss, and Bird, *Molecular Theory of Gases and Liquids*, John Wiley & Sons, Inc., New York, 1954, p. 9.

8 Krishnamurti, R., "On the Transition of Turbulent Convection," *Journal of Fluid Mechanics*, Vol. 42, 1970, p. 295.

9 Sissom, L. E., *Elements of Transport Phenomena*, McGraw-Hill Book Co., New York, 1972, p. 189.

10 Ning, H., "New Generalized Equation for Gas Diffusion Coefficients," *J. Chem. and Eng. Data*, Vol. 7, No. 1, 1962, p. 37.

11 Ostrach, S., "Natural Convection in Enclosures," *Advances in Heat Transfer*, Vol. 8, 1972, p. 161.

12 Reid, A. M., "Gas Analysis by Sonic Phase Measurements," *J. British Inst. of Radio Engineers*, Nov. 1962, p. 381.

13 Rossby, H. T., "Benard Convection With and Without Rotation," *Journal of Fluid Mechanics*, Vol. 36, 1969, p. 309.

14 Schlichting, H., *Boundary-Layer Theory*, McGraw-Hill Book Co., New York, 1969, p. 61.

15 Schmidt, R. J., and Saunders, O. A., "On the Motion of a Fluid Heated From Below," *Proceedings of the Royal Society of London*, Series A, Vol. 165, 1938, p. 216.

16 Sherwod, T. K., Pigford, R. L., and Wilke, C. R., *Mass Transfer*, McGraw-Hill, Inc., 1975, p. 19.

17 Smith, G., Numerical Solution of Partial Differential Equations, Oxford University Press, 1974.

18 Sparrow, E. M., Husar, R. B., and Goldstein, R. J., "Observations and Other Characteristics of Thermals," *Journal of Fluid Mechancis*, Vol. 41, 1970, p. 793.

19 Tsang, P., "Flame Propagation Through Methane-Air Mixtures Involving Concentration Gradients Formed by Mass Transfer Phenomena," PhD Thesis, Department of Mechanical Engineering, The University of Calgary, 1974.

20 Turner, J. S., *Buoyancy Effects in Fluids*, Cambridge University Press, 1973, p. 165.

21 Wilke, C. R., "A Viscosity Equation for Gas Mixtures," *J. Chem. Phys.*, Vol. 18, 1950, p. 517.

22 Zuber, N., "On the Stability of Boiling Heat Transfer," TRANS. OF ASME, Vol. 80, No. 3, Apr. 1958, p. 711.

APPENDIX 1

Derivation of the Equation of Conservation of Mass. Consider an elemental control volume crossing two of the infinitesimally small stream tubes of equal cross-sectional area, as shown in Fig. 6. The downward flow of the heavier mixture in one stream tube causes an upward flow of the higher mixture in the adjacent stream tube. At any axial location (y), the two flows have velocities of equal magnitudes and opposite directions. Thus the average velocity over any cross section of the flame tube is zero.

The time variation of methane concentration at any point is due to molecular and convective diffusional processes. The rate of change of methane concentration due to molecular diffusion, at axial location y and time t, is given by Fick's second law [7] as

$$\left.\frac{\partial c_{y,t}}{\partial t}\right]_{\text{Molecular diffusion}} = D\frac{\partial^2 c_{y,t}}{\partial y^2} \tag{20}$$

The effect of convective diffusion is obtained by considering the equation of conservation of mass of methane for an elemental control volume on one of the infinitesimally small stream tubes (Fig. 6). The convective change in the mass of methane in the elemental control volume during a time (Δt) is due to inlet and outlet flows, i.e.,

$$(\dot{m}_{\mathrm{CH_4,in}} - \dot{m}_{\mathrm{CH_4,out}})\Delta t = \rho_{\mathrm{CH_4}}\,(C_{y,t+\Delta t/2} - C_{y,t-\Delta t/2})A \cdot \Delta y \tag{21}$$

where

$$\dot{m}_{\mathrm{CH_4,in}} = \rho_{\mathrm{CH_4}} \cdot C_{y-\Delta y/2,t} \cdot v_{y-\Delta y/2,t} \cdot A$$

$$\dot{m}_{\mathrm{CH_4,out}} = \rho_{\mathrm{CH_4}} \cdot C_{y+\Delta y/2,t} \cdot v_{y+\Delta y/2,t} \cdot A$$

Thus equation (21) becomes

$$-\rho_{\mathrm{CH_4}} \cdot A\,(C_{y+\Delta y/2,t} V_{y+\Delta y/2,t} - C_{y-\Delta y/2,t} v_{y-\Delta y/2,t}) \cdot \Delta t = \rho_{\mathrm{CH_4}} \cdot A\,(C_{y,t+\Delta t/2} - C_{y,t-\Delta t/2})\Delta y \tag{22}$$

rearrange to get

$$(C_{y,t+\Delta t/2} - C_{y,t-\Delta t/2})/\Delta t = -[(CV)_{y+\Delta y/2,t} - (CV)_{y-\Delta y/2,t}]/\Delta y \tag{23}$$

Taking the limits when $\Delta t \to 0$ and $\Delta y \to 0$, equation (23) becomes

$$\left.\frac{\partial C_{y,t}}{\partial t}\right]_{\text{convective diffusion}} = -\frac{\partial (CV)_{y,t}}{\partial y} \tag{24}$$

Thus the total rate of change of methane concentration, at distance y and time t, due to molecular and convective diffusional process is

$$\frac{\partial C}{\partial t} = D\frac{\partial^2 c}{\partial y^2} - \frac{\partial (C \cdot v)}{\partial y} \tag{25}$$

APPENDIX 2

Derivation of the Equation of Conservation of Momentum. The momentum equation in the y-direction for a one-dimensional flow is [14]

$$\rho\left(\frac{\partial v}{\partial t} + v\frac{\partial v}{\partial y}\right) = -\rho g - \frac{\partial p}{\partial y} + \frac{4}{3}\mu\frac{\partial^2 v}{\partial y^2} \tag{26}$$

It has been seen for the assumed fictitious flow, that the average velocity over a horizontal cross section of the vertical flame tube is zero. Therefore, at any elevation (y), the stagnation pressure is equal to the hydrostatic pressure. Accordingly, the gradient of stagnation pressure is

$$\frac{\partial \bar{p}}{\partial y} = -g\rho \tag{27}$$

At a local point where the fictitious velocity is v (upward or downward), the static pressure can be approximated as

$$p = \bar{p} - \frac{1}{2}\rho v^2 \tag{28}$$

Differentiating equation (28) and utilizing equation (27), the static pressure gradient is given by

$$\frac{\partial p}{\partial y} = -g\rho - \rho v\frac{\partial v}{\partial y} - \frac{1}{2}v^2\frac{\partial \rho}{\partial y} \tag{29}$$

Substituting equation (29) into equation (26), the momentum equation becomes

$$\rho\frac{\partial v}{\partial t} = \frac{1}{2}v^2\frac{\partial \rho}{\partial y} + \frac{4}{3}\mu\frac{\partial^2 v}{\partial y^2} \tag{30}$$

APPENDIX 3

Gas Analysis Using Sonic Transducers. Sonic gas analysis is a nonintrusive technique for measuring the concentration of a certain species in a binary mixture of gases without sampling and consequent mixture disturbance. Such a technique is based on the realtionship between the speed of sound in a gas and its density.

In the present work, the local speed of sound was determined by measuring the time interval between emitting and receiving a sound signal using two similar sonic transducers mounted diametrically across the flame tube. The time interval was the average of 50 readings collected by an electronic circuit. A calibration chart for the concentration of methane in air as a function of speed of sound was thus developed and used for concentration measurements.

D. S. Weaver
Professor.

A. Abd-Rabbo
Research Assistant.

Department of Mechanical Engineering,
McMaster University,
Hamilton, Ontario, Canada

A Flow Visualization Study of a Square Array of Tubes in Water Crossflow

A flow visualization technique has been developed to study the flow behavior in tube arrays in water crossflow. The technique is used to examine flow development in a square array with a pitch ratio of 1.5. Results are presented for turbulence, vortex shedding and fluid-elastic instability including visualization photographs and associated frequency spectra and response curves.

Introduction

It is generally accepted that the principal excitation mechanisms for tube arrays in a crossflow of water are turbulence, vortex or vorticity shedding and fluid-elastic instability. While there is little debate about turbulence, the other two mechanisms exist primarily in name only and their precise nature is not well understood. An excellent critical review of the state of knowledge in this area is given by Paidoussis [1].

Early studies [2–4] attributed large amplitude vibrations in heat exchangers to vortex shedding resonance. Owen [5] disputed this possibility and argued that the phenomenon was caused by a peak in the turbulence spectrum. This debate has still not been resolved. However, it has been accepted that, whatever the phenomenon is, it is distinct from so-called fluid-elastic instability and that the latter is potentially much more destructive.

The concept of fluid-elastic instability was discussed by Connors [6], and has been the subject of many investigations as noted by Paidoussis [1]. Chen [7, 8] is of the opinion that this mechanism is different for tube arrays in water or air. On the other hand, Weaver and Lever [9] have shown theoretically that the observed behavior can be explained by a single mechanism, tube motion dependent flow redistribution associated with a phase lag due to fluid inertia. The magnitude of the phase lag varies significantly with mass ratio and will generally not be indicative of either pure fluid stiffness or pure fluid damping.

Through all this, relatively little research has been conducted to examine the details of the flow behavior in tube arrays. Y. N. Chen has discussed various excitation mechanisms and sketched general flow patterns [10] but the latter are based primarily on intuition. Zdravkovich and Namork [11, 12] have measured pressure distributions around tubes in tube arrays and various studies have examined hot-wire anemometer data inside tube banks (see, for example, references [13] and [14]). However, no systematic flow visualization studies have been reported which attempt to study excitation mechanisms.

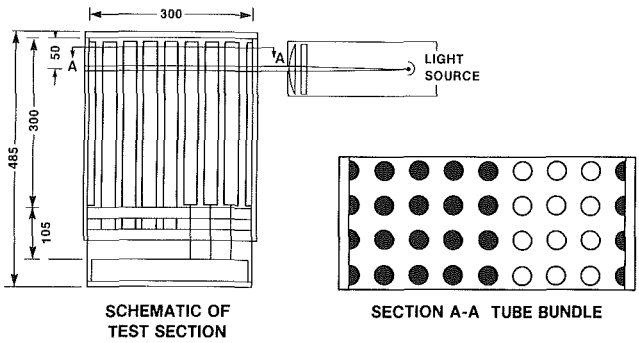

Fig. 1 Test section and tube bundle; ○ flexible tubes, ● rigid tubes; (dimensions in mm)

The purpose of the research reported in this paper was to develop a flow visualization technique to study flow phenomena in heat exchanger tube arrays in a crossflow. In particular, it was hoped that such studies would help provide insights into the various excitation mechanisms. The method was used with a square array of pitch ratio 1.5 and results are presented for the entire flow velocity range from very low Reynolds numbers to those high enough to cause tube-to-tube clashing.

Experimental Facility

The experiments were conducted in the McMaster University water tunnel which was specially designed for this kind of research [15]. The flow upstream of the test section is conditioned through a settling chamber and contraction such that a low turbulence intensity ($< 1/2$ percent), flat velocity profile (less than 1 percent velocity variation outside the boundary layers) is produced. The test section is approximately 0.30 m square and the flow velocity is determined using a Brooks bypass rotameter type 1110-82-2-C1A across an orifice plate. The rotameter was calibrated using a pitot-static probe in the test section. The uncertainty in the upstream flow velocity measurements, V_u, is considered to be of

Contributed by the Fluids Engineering Division and presented at the Symposium on Flow Induced Vibrations, Winter Annual Meeting, New Orleans, LA, December 5–10, 1984. Manuscript received by the Fluids Engineering Division, August 20, 1984.

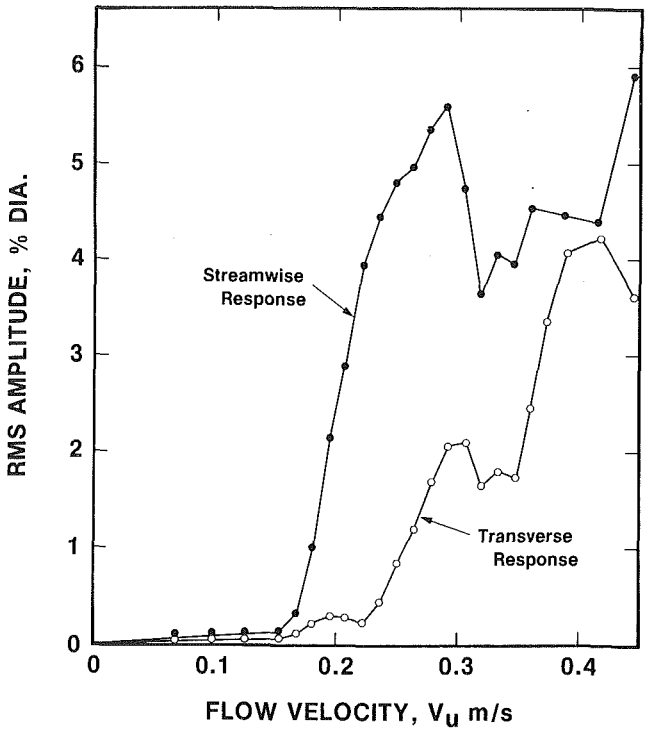

Fig. 2 Response of 2nd row tube (uncertainty in rms amplitude, ± 0.1 percent dia, in V_u, ± 0.005 m/s)

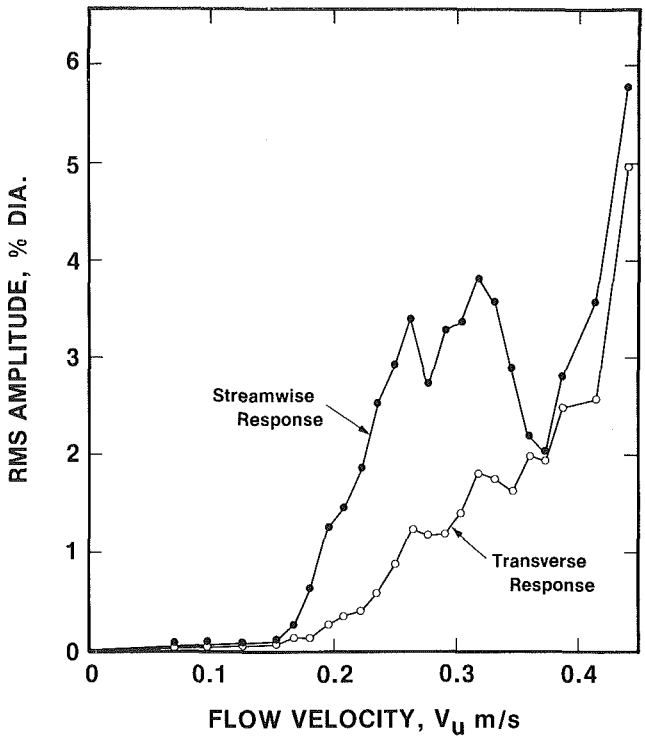

Fig. 3 Response of 3rd row tube (uncertainty in rms amplitude, ± 0.1 percent dia, in V_u, ± 0.005 m/s)

the order of ± 0.005 m/s in the range $0.07 < V_u < 0.80$ m/s. The very low flow velocities (< 0.07 m/s) reported in this paper were measured from flow visualization particle streak lengths in photographs taken upstream of the tube bundle. The uncertainty in the latter measurements is of the order of ± 5 percent.

The test section and tube bundle are shown schematically in Fig. 1. The array is a normal square configuration with a pitch-to-diameter ratio of 1.5. The tubes are made from acrylic rods 25 mm in diameter. The flexibly mounted tubes shown as open circles in section A-A are 300-mm long and mounted as cantilevers on 6-mm-dia steel rods. The latter are screwed into a heavy steel plate to minimize mechanical coupling through the base. The remaining tubes, shown as filled in circles in section A-A of Fig. 1, are also 25-mm-dia acrylic rods but are fixed below the test section so that they are effectively rigid.

The central tubes among the flexibly mounted ones were instrumented for response due to flow using strain gauges at the base of their support rods. Thus response measurements were obtained for second and third row tubes which were completely surrounded by flexibly mounted tubes. The strain gauge signals were processed using a Vishay 2310 signal conditioner and frequency spectra were obtained using a Spectral Dynamics 375 Fourier Analyzer. The strain gauge output was calibrated in terms of tube tip displacement and the response was found to be linear up to displacements sufficient to cause tube-to-tube clashing.

Before commencing the experiments, all of the flexibly mounted tubes were tuned in air to a frequency of 25.5 ± 0.2 Hz. The logarithmic decrement of damping was also measured in air using a simple pluck test and found to be 0.014 ± 0.001. The logarithmic decrement of damping in quiescent water was also determined from a pluck test but, in this case, all of the remaining flexibly mounted tubes were locked up to prevent distortion of the time decay traces by energy transfer between tubes through fluid coupling. This method has been shown to give a good estimate of the damping of a single tube in a fully flexible tube bundle in quiescent fluid [16]. The logarithmic decrement of damping in water was found to be 0.037 ± 0.004.

Figure 1 also shows the arrangement used for flow visualization. The light source is nine 300 W Sylvania ELH Tungsten Halogen projector bulbs arranged in a pattern to minimize the shadows produced by light diffraction through the various tubes. The light is passed through a slit and cylindrical collimating lens such that a sheet of light about 10-mm thick passes through the tube array at right angles to the

Nomenclature

d = tube diameter (25.4 mm)
f = frequency of vortex shedding
p = tube pitch (38.1 mm)
$\mathrm{Re} = Vd/\nu$ = Reynolds number
Re_u = Reynolds number based on upstream flow velocity
$\mathrm{S} = fd/V$ = Strouhal number
$\mathrm{S}_g, \mathrm{S}_u$ = Strouhal number based on gap and upstream velocity respectively
T = transverse tube spacing (38.1 mm)
V = flow velocity
V_u = upstream flow velocity
V_{cr} = critical or threshold flow velocity based on V_u
$V_p = \frac{p}{p-d} V_u$ = pitch velocity
V_{gcr} = critical velocity based on gap velocity
$V_g = \frac{T}{T-d} V_u$ = gap velocity
V_{cr}/fd = critical reduced velocity
ν = kinematic viscosity of fluid

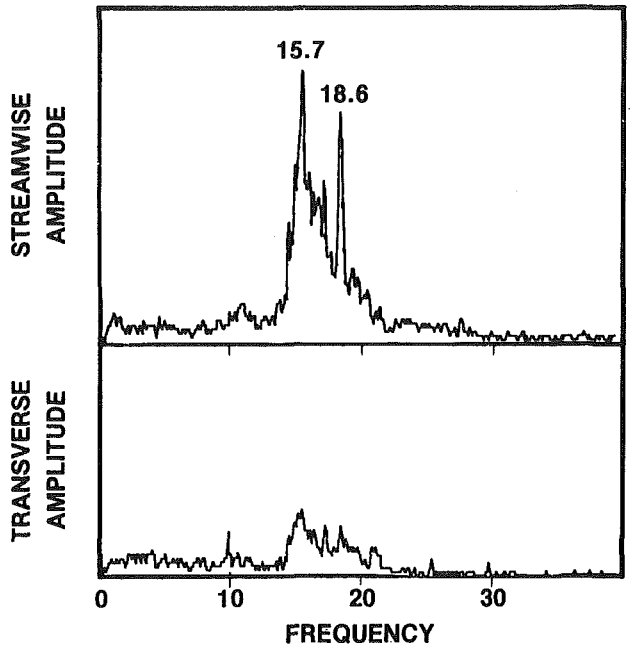

Fig. 4(a) $V_u = 0.15$ m/s

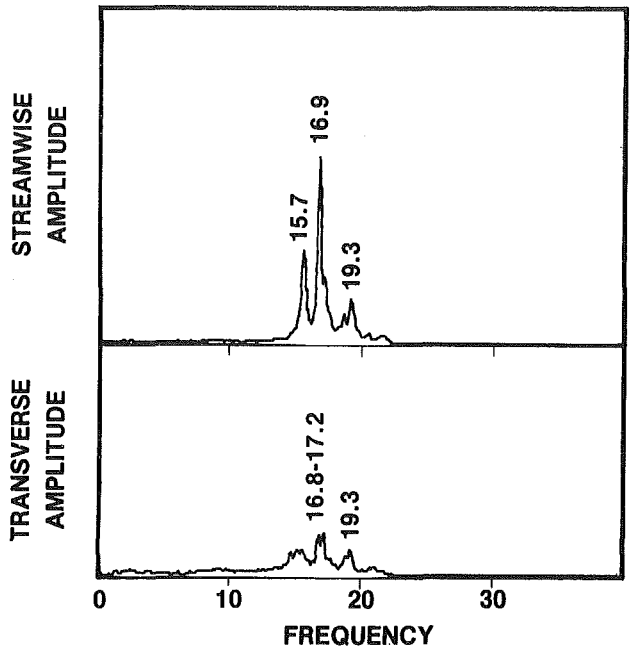

Fig. 4(c) $V_u = 0.35$ m/s

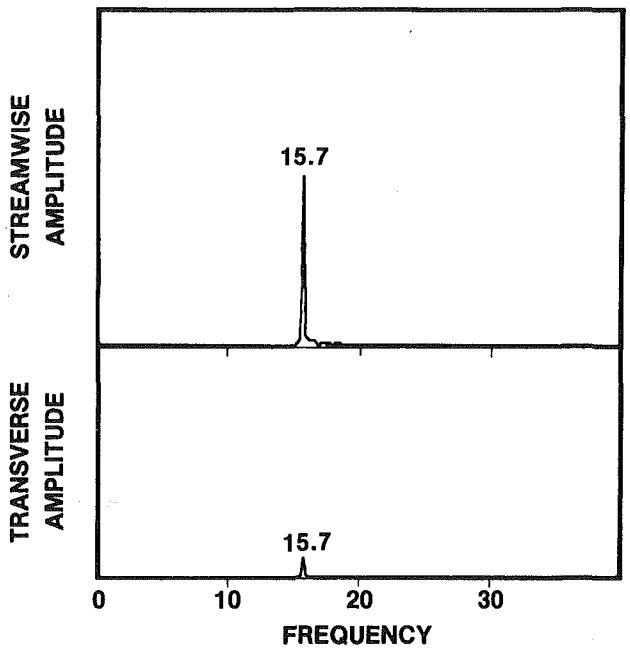

Fig. 4(b) $V_u = 0.19$ m/s

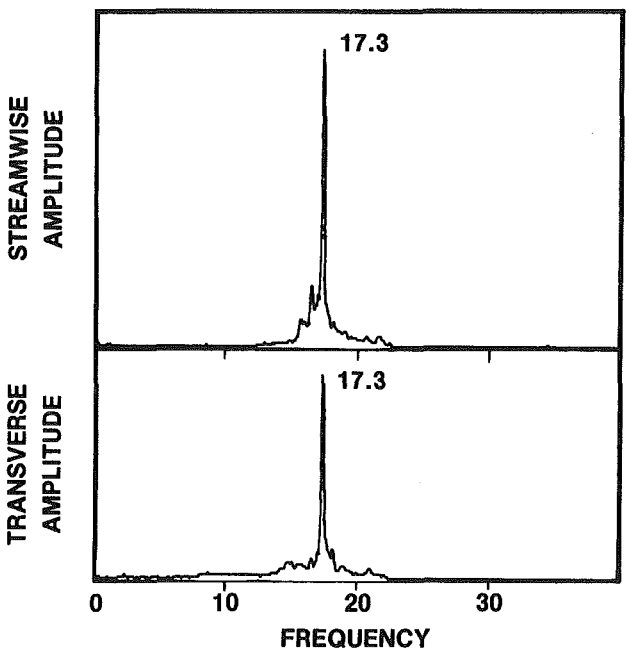

Fig. 4(d) $V_u = 0.37$ m/s

Fig. 4 Tube response spectra (uncertainty in V_u, ± 0.005 m/s)

tube axes and about 50-mm below the top of the test section. Thus the flow patterns observed are not affected by the test section boundary layer or free surface effects. The flow was seeded using aluminum particles which provide maximum reflection at about 90° to the incident light. This arrangement therefore was ideally suited to making observations from the top of the test section. The flow patterns were recorded using a Graflex 4 × 5 press camera and Plus-X or Tri-X film. Cine films were taken using a Locam model 51 high-speed camera (up to 500 frames per sec) and Kodak Plus-X film.

Experimental Procedure

The tuned tube bundle was inserted into the bottom of the test section such that the flow was across the entire length of the 300-mm tubes and the cantilever supports were in quiescent fluid below the water tunnel. The flow was started at some low velocity and allowed to stabilize for several minutes. The tube response of the monitored tubes was then recorded for both the streamwise and transverse directions to the flow. The rms response amplitudes and frequency spectra recorded were the result of 200 sample averages from the Fourier analyzer. The overall rms tube response is computed from the square root of the sum of squares of the measured transverse and streamwise responses.

When measurements and observations were complete, the flow velocity was incremented and the entire process repeated. The experiment was teminated when the tube amplitudes were sufficiently large to nearly cause tube clashing. The tube response behavior was then studied in order to determine

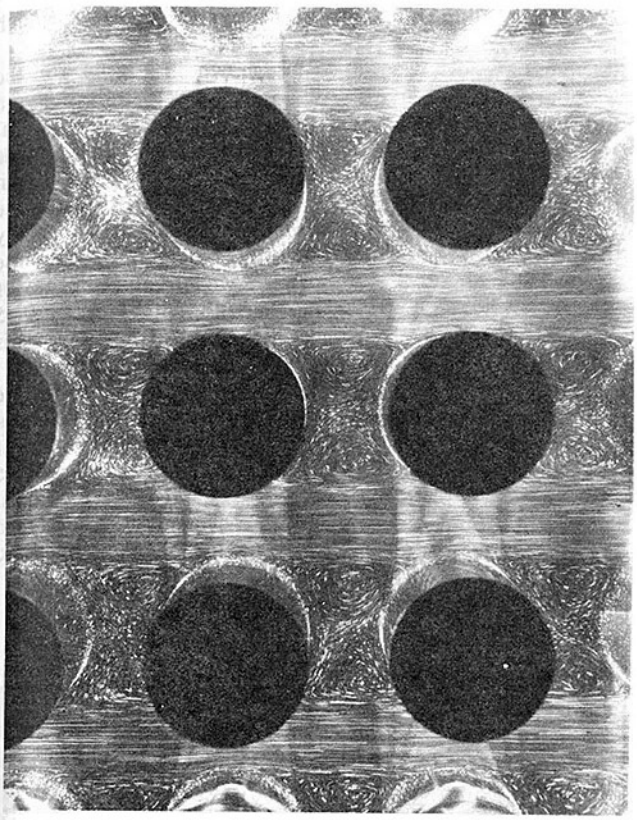

Fig. 5(*a*) $V_u = 0.0043$ m/s, ($Re_u = 110$)

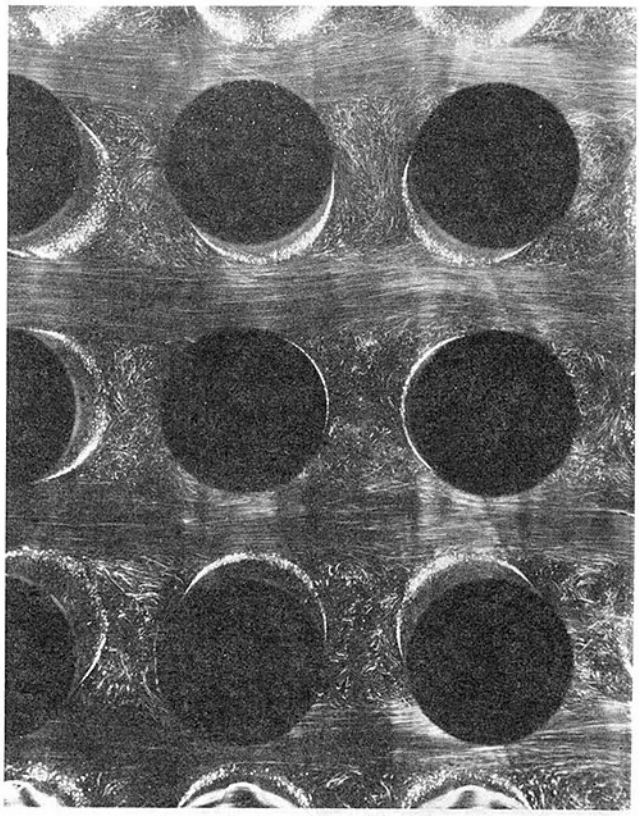

Fig. 5(*c*) $V_u = 0.019$ m/s, ($Re_u = 490$)

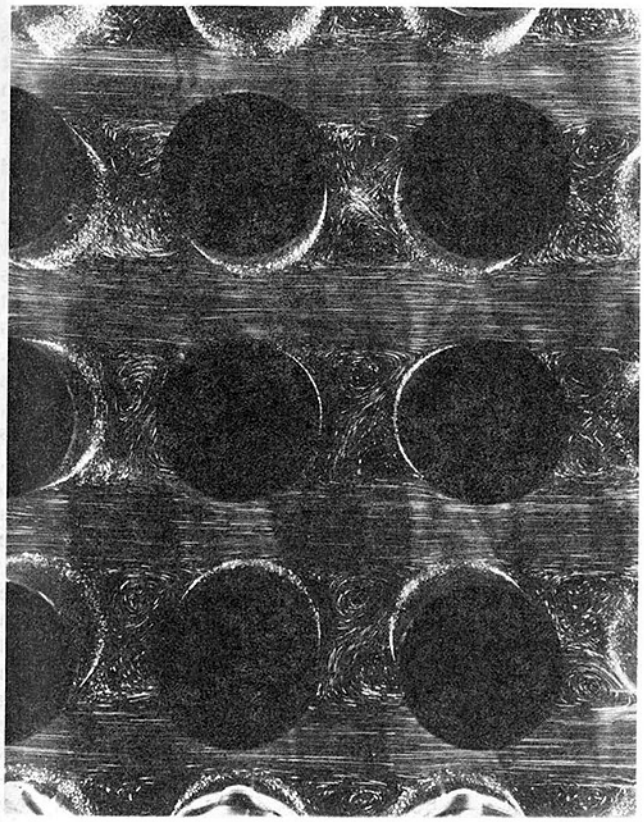

Fig. 5(*b*) $V_u = 0.0059$ m/s, ($Re_u = 150$)

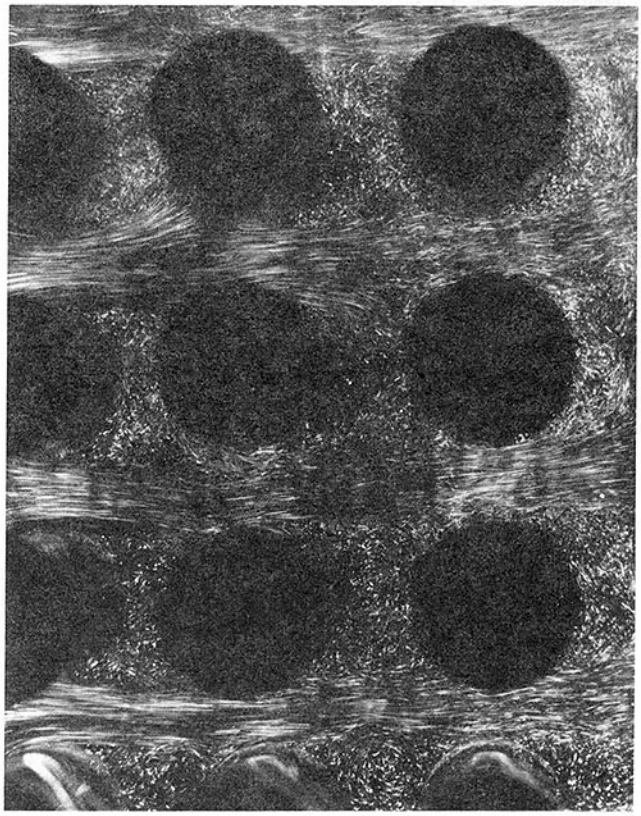

Fig. 5(*d*) $V_u = 0.12$ m/s, ($Re_u = 3.1 \times 10^3$)

Fig. 5 Flow development in tube bundle (uncertainty in V_u, ± 5 percent for $V_u < 0.07$ m/s, ± 0.005 m/s for $V_u > 0.07$ m/s)

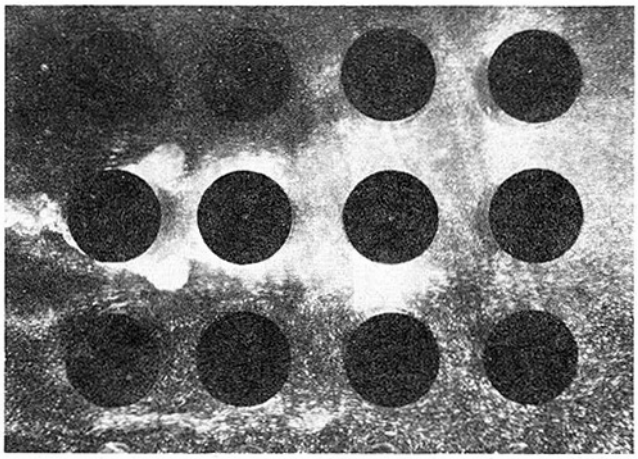

Fig. 6(a)

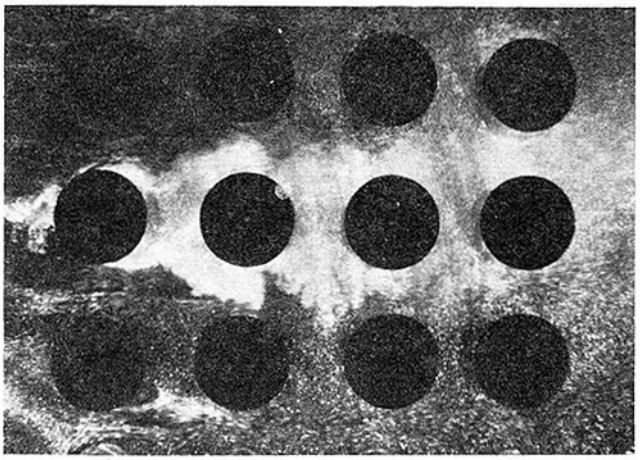

Fig. 6(b)

Fig. 6 Cine film shots of symmetric vortex shedding V_u = 0.25 m/s, $Re_u = 6.5 \times 10^3$ (uncertainty in V_u, ± 0.005 m/s)

those flow velocities at which flow visualization might provide insights into excitation mechanisms. These velocities were established in the test section and numerous still photographs and cine films taken of the flow patterns.

Experimental Results

The rms response in the transverse and streamwise directions of the monitored tubes in the second and third rows are shown in Figs. 2 and 3, respectively, While there are some differences in detail, the responses for the two tubes are seen to be essentially the same. The rms response amplitudes are very small up to an upstream flow velocity of about 0.15 m/s. Beyond this velocity, there is an abrupt increase in amplitude with the predominant response being in the streamwise direction. This response peaks in the neighborhood of 0.30 m/s and falls off sharply to a trough at about 0. 35 m/s. Beyond this velocity, the amplitudes rise again in a whirling mode in which the streamwise and transverse amplitudes are of the same order. It should be stated, however, that in this high velocity range, $V_u > 0.37$ m/s, the responses are highly modulated and the relative modes are unsteady. At times, the response is seen to be primarily transverse with all tubes in a tube column in phase with one another and about 180° out of phase with the tubes in adjacent tube columns. However, this relative mode pattern does not persist and gives way to more apparently random mode patterns. Each such relative mode pattern will be associated with a slightly different frequency. This is why the time-averaged frequency spectra generally show several fluid coupled frequencies, especially at very high flow velocities.

Typical frequency spectra are shown in Fig. 4 for the second row tube. Figure 4(*a*) at V_u = 0.15 m/s shows a turbulence response with the cluster of fluid coupled natural frequencies in the range from about 15–21 Hz. The predominantly streamwise response at V_u = 0.19 m/s is seen in Fig. 4(*b*). Note the absence of other frequencies in the response, this being a much purer response than normally observed for tube arrays in water. The trough in the response curves is characterized by a much less well organized behavior as indicated by the response spectra of Fig. 4(*c*) at V_u = 0.35 m/s. By a flow velocity of V_u = 0.37 m/s, the response is better organized again as shown in the spectra Fig. 4(*d*).

These response curves and spectra suggest that there are three different regions of flow-induced response, characterized by distinct behavior and probably caused by different excitation mechanisms. These ranges are approximately $0 < V_u \leq 0.15$ m/s, $0.15 < V_u \leq 0.35$ m/s and $V_u > 0.35$ m/s. Therefore, the flow visualization experiments were designed to provide insights into the flow behavior in these ranges and the changes which occurred from one range to another

Flow Visualization

The details of the flow were studied using both still photographs and cine films. The examples given in this section have been selected to illustrate the various flow regimes. The corresponding flow velocities and Reynolds numbers are based on conditions upstream of the tube bundle, V_u, but could just as easily have been based on pitch velocity, V_p. This velocity is related to the upstream velocity through the simple relationship $V_p = [p/(p-d)]\ V_u$ or $V_p = 3V_u$ in this case. For this pattern of tube array, the pitch velocity is physically equal to the average flow velocity between adjacent tubes in a transverse tube row.

The flow development in the range $0 < V_u < 0.15$ m/s is illustrated in Fig. 5. In each photograph the flow is from left to right and the tubes seen at the extreme left of each photograph are the upstream tubes (1st tube row). At the lowest flow velocities achievable, V_u = 0.001 m/s or Re_u = 30, the wake regions between tubes in a tube column appeared essentially stagnant, at least, no coherent wake flow pattern was visible. However, it must be stated that it was very difficult to obtain good visualization photographs at such low flow rates. As the Reynolds number is increased, the wakes are seen to consist of two stable vortices with clear straight flow lanes between tube columns. This behavior continues until a Reynolds number of about 150 and is illustrated in Fig. 5(*a*) for a Reynolds number of Re_u = 110. At a Reynolds number of about 150, these vortices begin to become unstable, with flow crossing the wake region and the vortices periodically being swept into the mainstream flows. However, there is no evidence at this point that these mainstream flows are much affected by the developing turbulence in the wakes as seen in Fig. 5(*b*). Note the asymmetry developing in the wakes.

By a Reynolds number of about 400, the wake regions have become fully turbulent. Figure 5(*c*), corresponding to a Reynolds number of Re_u = 490, shows the lack of coherent wake phenomena and the influence of the turbulent wakes in perturbing the mainstream flows. Also visible is the increasing turbulence as the flow progresses through the bundle. The latter is obvious in Fig. 5(*d*) which corresponds to a Reynolds number of 3×10^3 or V_u = 0.12 m/s. In this case, the turbulence is essentially fully developed by the third tube row although mainstream flows between tube columns through the bundle are still visible. It is also clear that the flow pattern surrounding the first row tubes is very different from that seen by the second row or third row tubes.

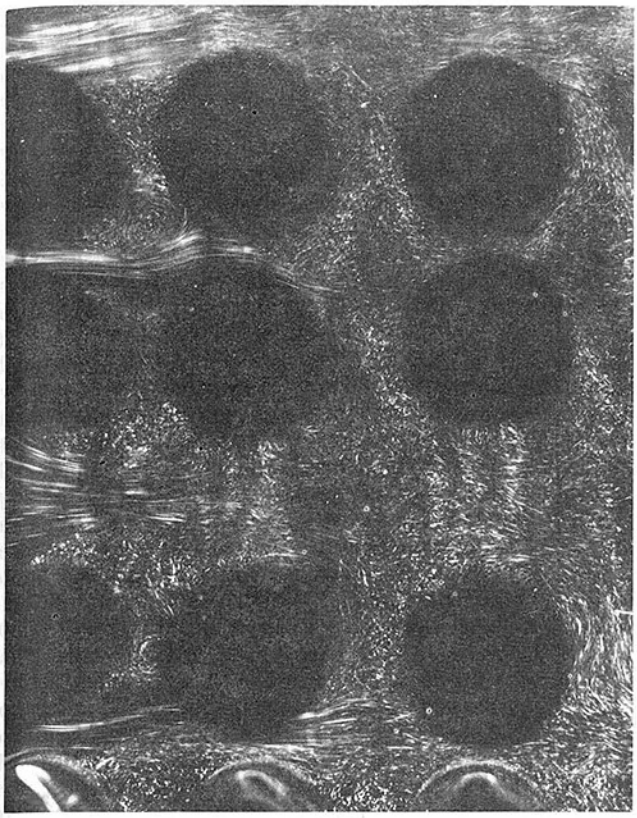

Fig. 7(*a*) Transverse mode

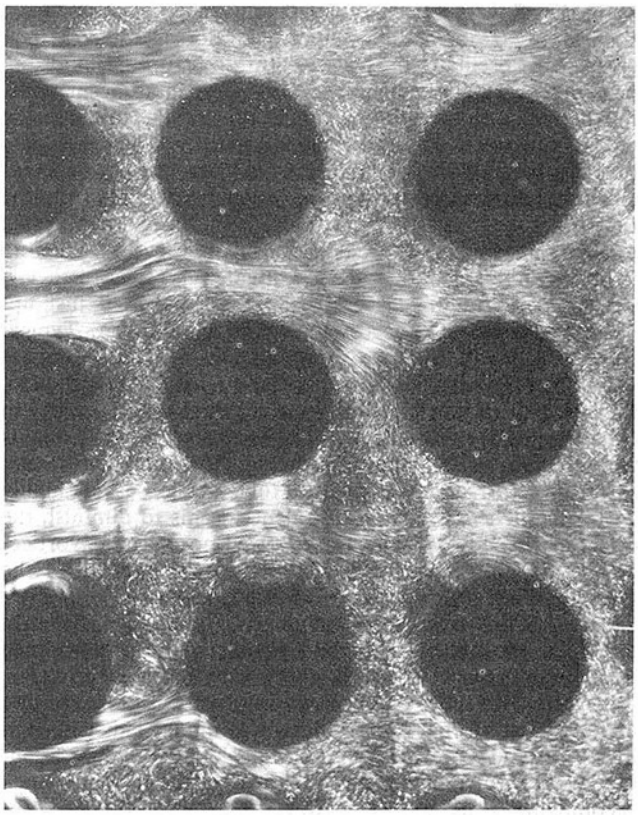

Fig. 7(*c*) Whirling mode

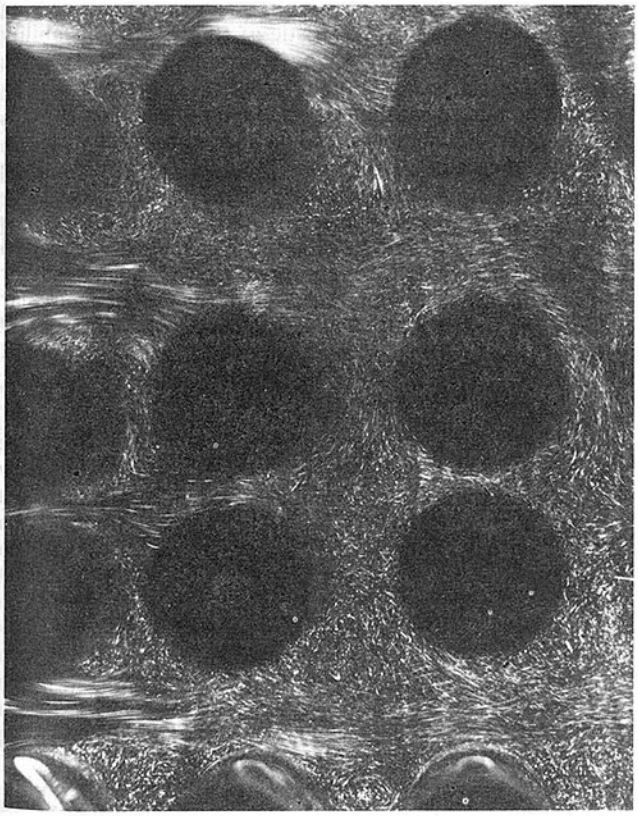

Fig. 7(*b*) Transverse mode

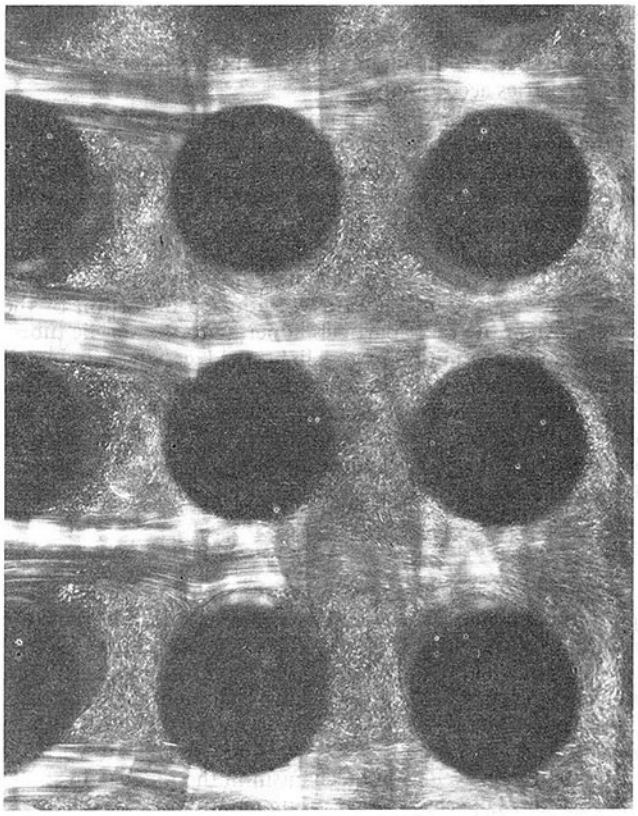

Fig. 7(*d*) Rigid bundle

Fig. 7 V_u = 0.44 m/s, Re_u = 1.1 × 10^4 (all photos) (uncertainty in V_u, ± 0.005 m/s)

In the flow velocity range $0.15 < V_u \leq 0.35$ m/s, significant streamwise oscillations develop. All tubes in a given row oscillate in phase with one another and approximately 180° out of phase with tubes in adjacent rows. Furthermore, the oscillation amplitudes of the tubes in the second row were the largest, reaching nearly 6 percent of a tube diameter. Flow visualization photographs showed that coherent vortices were being shed in symmetric pairs from the first row tubes with all vortex pairs being in phase with one another. The latter is expected as all the tubes were oscillating in phase with one another. To investigate this effect further, a stream of aluminum tracer particles was released just upstream of the first tube row and cine films taken. Typical frames from this film are shown in Fig. 6. The symmetric vortex pair is clearly visible. Even more remarkable is the fact that the pair of vortices shed from the first row tube remain coherent past the second row. This flow phenomenon explains why the observed response behavior is so regular (recall spectrum 4(*b*)) and the relative tube motion is so highly correlated. The developing turbulence seems to diminish the effect as the flow visualization showed no coherent vortices behind the third row tubes in this velocity range and the response of the fourth row tubes was quite small.

Above a flow velocity of about $V_u = 0.35$ m/s, the tube bundle is unstable and highly modulated large amplitude oscillations occur. At times, the tube motion is primarily transverse with tubes in a column in phase with one another and 180° out of phase with adjacent columns. This is seen in Figs. 7(*a*) and (*b*). These photographs leave no doubt about the relative tube mode and the flow redistribution which accompanies this motion. However, the oscillation amplitudes are modulated as just noted, and at times, the relative mode pattern changes entirely. Accompanying this is usually a shift in the dominant fluid coupled natural frequency. The flow visualization photograph in Figure 7(*c*) illustrates such a circumstance. Taken at the same velocity as Figs. 7(*a*) and (*b*), $V_u = 0.44$ m/s, the tubes are whirling in a less regular relative mode pattern and the interstitial flow between tube rows and column varies accordingly.

Finally, for comparison purposes a photograph was taken of the flow through the tube bundle at this same flow velocity, $V_u = 0.44$ m/s, when all the tubes were locked up rigidly, Fig. 7(*d*). This shows clear flow lanes between tube columns with some disturbances due to the highly turbulent wakes. Essentially, the flow behavior is identical to that observed for $V_u = 0.12$ m/s in Fig. 5(*d*). Note that the vertical bands of light and shadows in Fig. 7(*d*) are due to distortion of the sheet of light by tracer particles adhering to the acrylic tubes. These nonuniformities in the light field can be eliminated largely by proper placement of the light source lamps. However, as an experiment progresses, the gradual accumulation of tracer particles to the tubes causes this type of distortion of the light field and ultimately requires dismantling and cleaning of the test section.

Discussion

Careful study of the tube response and flow visualization photogrpahs and films leads to the conclusion that the response in the three different flow velocity ranges selected are indeed due to different excitation mechanisms; turbulence, vorticity shedding and fluid-elastic instability. Turbulence is responsible for the very small amplitude response in the range $0 < V_u \leq 0.15$ m/s. That vorticity shedding is the excitation mechanism in the range $0.15 < V_u \leq 0.35$ m/s is perhaps more argumentative. However, there are a number of compelling observations which support this contention. First, the tube motion is predominantly streamwise which has been found theoretically to be stable from fluid-elastic excitation [9] and supported experimentally

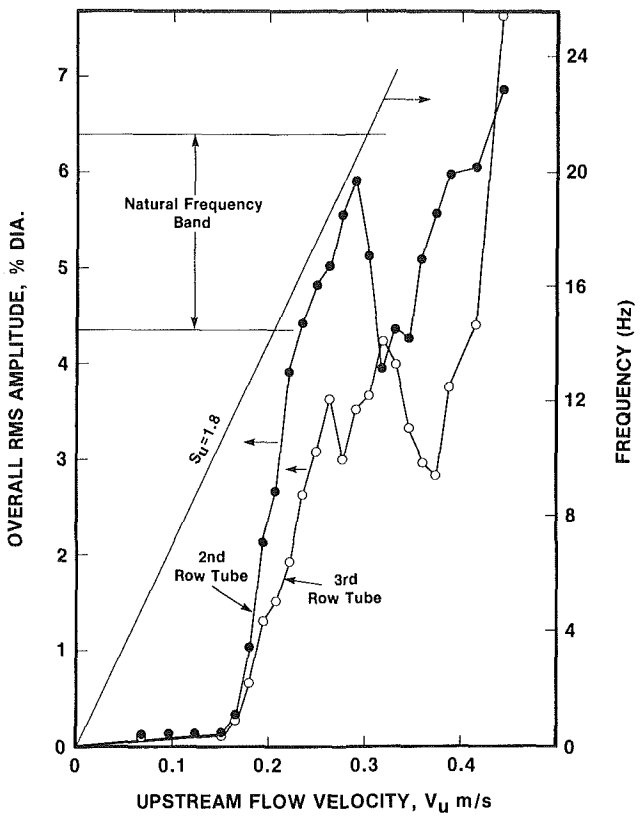

Fig. 8 Overall rms response of 2nd and 3rd row tubes (uncertainty in amplitude, ± 0.1 percent dia, in V_u, ± 0.005 m/s)

for a similar array [17]. Second, the motion is very regular at a single frequency rather than modulated with changing relative mode shapes characteristic of fluid-elastic instability [14, 15]. Third, as pointed out by Weaver and Yeung [18], the onset of the large amplitude response corresponds to a Strouhal number twice that expected from the literature [4, 5, 19]. This Strouhal number based on upstream velocity is $S_u = 1.8$, twice the value of 0.9 from the noted references. (The value quoted in the literature is $S_g = 0.3$ based on the transverse gap flow velocity where $S_u = 3S_g$ for this array.) The factor of 2 could be due to excitation from each vortex and thus lead to the streamwise response observed. Such behavior would be consistent with that found for isolated circular cylinders in water [20]. The coincidence of the constant Strouhal line with the band of fluid coupled natural frequencies is shown in Fig. 8. Finally, while no coherent vortex shedding was observed at flow velocities below 0.15 m/s, the flow visualization photographs show unequivocally that pairs of symmetric vortices are shed in the range $0.15 < V_u \leq 0.35$ m/s.

It is interesting to speculate about the extent to which the longitudinal tube spacing determines the symmetric vortex shedding amplification and large amplitude response. It may be that tube arrays with significantly different pitch ratios will behave quite differently because of the lack of synchronization. It is certainly true that the normal square tube pattern permits synchronization of adjacent tube wakes and, for this reason, may be the worst choice from the point of view of vortex shedding resonance. All staggered arrays have a tube between the wakes of tubes in adjacent rows and hence should not be as susceptible to such global flow organization. This speculation is confirmed for a rotated square array which showed clear vorticity phenomena but no vorticity resonance [18].

There is no question that the tube array has become unstable for $V_u > 0.35$ m/s. The problem is to determine as far

as possible the precise velocity at which fluid-elastic instability occurs, V_{cr}. The ambiguity is clear in Fig. 8 which gives the overall rms response of both tubes calculated as the square root of the sum of squares of the streamwise and transverse response from Figs. 2 and 3. The reasons for the difficulty are threefold. First, the multiplicity of fluid coupled modes and hence, closely spaced natural frequencies, of tube arrays in water create an irregular response as the array shifts from one mode to another [15]. Second, no consistent definition for the stability threshold, V_{cr}, exists in the literature as discussed in reference [18] and the value of V_{cr} depends on the definition employed. Third, the near coincidence of vorticity shedding resonance with the fluid-elastic threshold may influence the latter and, at the very least, makes it difficult to determine when the fluid-elastic mechanism becomes dominant. The rms tube tip amplitudes are 3 to 4 percent of a tube diameter in the flow velocity range around 0.35 m/s. These amplitudes are large enough to produce nonlinear fluid coupling of tubes and possibly to induce early transition to instability. At about 0.35 m/s the transverse motion of the second row tube increases sharply (Fig. 2) as does the overall rms amplitude (Fig. 8). The dominant frequency in the response spectrum, Fig. 4(*c*), is 16.9 Hz and therefore the critical reduced velocity V_{cr}/fd = 0.82. Based on the mean gap velocity between adjacent tubes in a transverse row, this corresponds to a critical reduced velocity of V_{gcr} = 2.45. This agrees well with value of 2.38 quoted in reference [18], for an identical pattern of 12.5-mm-dia aluminum tubes. The critical velocity could be taken as low as 0.32 m/s for the second row tube or as high as 0.37 m/s for the third row tube but, given the change in dominant response frequency over this range, the effect on critical reduced velocity varies only from −6 percent to +3 percent. Thus V_{gcr} = 2.45 is taken as a reasonable estimate of the critical reduced velocity.

The mass ratio, m/pd^2, for the present array is 1.9, where m is the mass per unit length of the tube including fluid added mass and p is the fluid density. Using this and the logarithmic decrement of damping in water, δ = 0.37, the reduced damping parameter, $m\delta/pd^2$, has a value of 0.07. The theory of Lever and Weaver [21] gives a critical reduced velocity for this array, V_{gcr} = 2.3, which agrees quite well with the experimental results reported here. It must be stated, however, that while the theory seems to give reasonable predictions for parallel triangular and square in-line arrays, it does not do so well for other array geometries.

Conclusions

A flow visualization technique has been developed to investigate flow phenomena in heat exchanger tube bundles. The method was used to study flow development in a normal square tube array with a pitch ratio of 1.5. The array tested was only four rows deep and hence the results are indicative of the upstream tube rows of a heat exchanger tube bank. This choice was purposeful as it was desired to observe the flow development both as a function of Reynolds number and as a function of row depth. Also, it is usually the early tube rows of heat exchangers where tube failures due to excessive vibrations occur. The addition of more tube rows downstream of the present array would not be expected to alter the observations made in this study. The principal conclusions drawn are expected to be valid for in-line tube arrays with pitch ratios close to 1.5 and are as follows:

1 For Reynolds numbers below about Re_u = 150 based on upstream velocity, straight laminar flow lanes exist between streamwise tube columns with trapped stable symmetric vortices in the tube wakes.

2 At a Reynolds number based on upstream flow velocity of about Re_u = 150, the wake regions of the tubes become unstable. This transition to turbulence is complete by about Re_u = 400 beyond which no coherent wake phenomena are visible in the absence of tube motion.

3 The flow visualization shows that the flow pattern around first and second row tubes is not typical of that around third and subsequent rows. This is due to the development of turbulence and implies one and two tube row models are not representative of full heat exchanger tube arrays.

4 Vorticity shedding resonance produces large streamwise amplitude response (about 6 percent of a tube diameter) for normal square arrays with a pitch ratio of 1.5 in water. This phenomenon is seen to be associated with the shedding of symmetric vortex pairs from the first tube row and these persist up to at least the third tube row. The second tube row response is largest. Such behavior may not occur for pitch ratios significantly different from 1.5 and is not expected for other array geometries. Furthermore, this behavior is not expected deep inside a similar tube array.

5 Fluid-elastic instability occurs with the development of significant transverse tube motions and occurs approximately at a reduced critical velocity based on gap velocity of 2.45. The flow visualization showed significant flow redistribution as expected but no quantitative measurement of phase lag was possible. The observed fluid-elastic stability behavior is expected to be typical of that deep inside a geometrically similar tube bundle.

The flow visualization technique presented here is being used to study flow development in other array pitches and patterns. The results obtained so far for a staggered array show some quite different phenomena than observed for the square array.

Acknowledgment

The authors gratefully acknowledge the financial support of the Natural Sciences and Engineering Research Council of Canada.

References

1 Paidoussis, M. P., "A Review of Flow-Induced Vibrations in Reactors and Reactor Components," *Nuclear Engineering and Design*, Vol. 74(1), 1983, pp. 31–60.

2 Grotz, B. J., and Arnold, F. R., "Flow-Induced Vibrations in Heat Exchangers," Stanford University, Department of Mechanical Engineering, Technical Report No. 31, 1956.

3 Livesey, J. L., and Dye, R. C. F., "Vortex Excited Vibration of a Heat Exchanger Tube Row," *Journal of Mechanical Engineering Science*, Vol. 4(4), 1962, pp. 349–352.

4 Chen, Y. N., "Flow-Induced Vibration and Noise in Tube-Bank Heat Exchangers Due to von Karman Streets," ASME *Journal of Engineering for Industry*, Vol. 90, 1968, pp. 134–146.

5 Owen, P. R., "Buffeting Excitation of Boiler Tube Vibration," *Journal of Mechanical Engineering Science*, Vol. 7(4), 1965, pp. 431–439.

6 Connors, H. J., "Fluid-Elastic Vibration of Tube Arrays Excited by Crossflow," ASME Symposium on Flow-Induced Vibration in Heat Exchangers, D. D. Reiff, ed., 1970, pp. 42–56.

7 Chen, S. S., "Instability Mechanisms and Stability Criteria of a Group of Circular Cylinders Subjected to Crossflow, Part 1: Theory," ASME *Journal of Vibration, Acoustics, Stress, and Reliability in Design*, Vol. 105(1), 1983, pp. 51–59.

8 Chen, S. S., "Instability Mechanisms and Stability Criteria of a Group of Circular Cylinders Subjected to Crossflow, Part 2: Numerical Results and Discussions," ASME *Journal of Vibration, Acoustics, Stress and Reliability in Design*, Vol. 150(2), 1983, pp. 253–260.

9 Lever, J. H., and Weaver, D. S., "A Theoretical Model for Fluid-Elastic Instability in Heat Exchanger Tube Bundle," ASME *Journal of Pressure Vessel Technology*, Vol. 104, 1982, pp. 147–158.

10 Chen, Y. N., "The Sensitive Tube Spacing Region of Tube Bank Heat Exchangers for Fluid-Elastic Coupling in Cross Flow," ASME Symposium, Fluid-Structure Interaction Phenomena in Pressure Vessel and Piping Systems, Au-Yang, M. K., and Brown, S. J., editors, 1977, pp. 1–18.

11 Zdravkovich, M. M., and Namork, J. E., "Flow Structure Within Both Stationary and Vibrating Tube Banks With Triangular Pitch," *Proceedings of Vibration in Nuclear Plant*, Keswick, U.K., paper 2:5, 1978.

12 Zdravkovich, M. M., and Namork, J. E., "Structures of Interstitial Flow

Between Closely Spaced Tubes in Staggered Array," ASME Symposium on Flow Induced Vibrations, Chen, S. S., and Bernstein, M. D., editors, 1979, pp. 41–46.

13 Heinecke, E., "Stationary and Instationary Flow Phenonema in and Behind Staggered and In-Line Tube Banks," International Symposium on Vibration Problems in Industry, Keswick, U.K., 1973, Paper No. 412.

14 Weaver, D. S., and Grover, L. K., "Crossflow Induced Vibrations in a Tube Bank-Turbulent Buffeting and Fluid Elastic Instability," *J. Sound and Vibration*, Vol. 59, 1978, pp. 277–294.

15 Weaver, D. S., and Koroyannakis, D., "The Crossflow Response of a Tube Array in Water—A Comparison With the Same Array in Air," ASME *Journal of Pressure Vessel Technology*, Vol. 104, 1982, pp. 139–146.

16 Harris, R. E., Dokainish, M. A., and Weaver, D. S., "A Simplified Finite Element for Added Mass and Inertial Coupling in Arrays of Cylinders," ASME Winter Annual Meeting, 1984, to appear.

17 Tanaka, H., and Takahara, S., "Unsteady Fluid Dynamic Force on Tube Bundle and Its Dynamic Effect on Vibration," ASME Symposium Flow-Induced Vibration of Power Plant Components, Au Yang, M. K., ed., 1980, pp. 77–92.

18 Weaver, D. S., and Yeung, H. C., "Approach Flow Direction Effects on the Crossflow Induced Vibrations of a Square Array of Tubes," *J. Sound and Vibration*, Vol. 87(3), 1983, pp. 469–482.

19 Zukauskas, A., and Katinas, V., "Flow Induced Vibration in Heat Exchanger Tube Banks," *Proceedings, IUTAM-IAHR Symposium on Practical Experiences With Flow-Induced Vibrations*, Karlsruhe, 1979, Naudascher, E., and Rockwell, D., editors, Springer-Verlag, Berlin, 1980, pp. 188–196.

20 King, R., and Johns, D. J., "Wake Interaction Experiments With Two Flexible Circular Cylinders in Flowing Water," *J. Sound and Vibration*, Vol. 45(2), 1976, pp. 259–283.

21 Lever, J. H., Weaver, D. S., "On the Stability Behavior of Heat Exchanger Tube Bundles, Part I—Modified Theoretical Model," ASME WAM Symposium on Flow-Induced Vibrations, Vol. 2, pp. 83–98, New Orleans, 1984, editors, Paidoussis, M. P., Au-Yang, M. K., Chen, S. S., "On the Stability Behavior of Heat Exchanger Tube Bundles, Part II—Numerical Results and Comparison With Experiments," ASME WAM Symposium on Flow-Induced Vibrations, Vol. 2, pp. 99–116, New Orleans, 1984, editors, Paidoussis, M. P., Au-Yang, M. K., Chen, S. S.

Between Closely Spaced Tubes in Staggered Array," ASME Symposium on Flow Induced Vibrations, Chen, S. S., and Bernstein, M. D., editors, 1979, pp. 41-46.

13 Heinecke, E., "Stationary and Instationary Flow Phenonema in and Behind Staggered and In-Line Tube Banks," International Symposium on Vibration Problems in Industry, Keswick, U.K., 1973, Paper No. 412.

14 Weaver, D. S., and Grover, L. K., "Crossflow Induced Vibrations in a Tube Bank-Turbulent Buffeting and Fluid Elastic Instability," *J. Sound and Vibration*, Vol. 59, 1978, pp. 277-294.

15 Weaver, D. S., and Koroyannakis, D., "The Crossflow Response of a Tube Array in Water—A Comparison With the Same Array in Air," ASME *Journal of Pressure Vessel Technology*, Vol. 104, 1982, pp. 139-146.

16 Harris, R. E., Dokainish, M. A., and Weaver, D. S., "A Simplified Finite Element for Added Mass and Inertial Coupling in Arrays of Cylinders," ASME Winter Annual Meeting, 1984, to appear.

17 Tanaka, H., and Takahara, S., "Unsteady Fluid Dynamic Force on Tube Bundle and Its Dynamic Effect on Vibration," ASME Symposium Flow-Induced Vibration of Power Plant Components, Au Yang, M. K., ed., 1980, pp. 77-92.

18 Weaver, D. S., and Yeung, H. C., "Approach Flow Direction Effects on the Crossflow Induced Vibrations of a Square Array of Tubes," *J. Sound and Vibration*, Vol. 87(3), 1983, pp. 469-482.

19 Zukauskas, A., and Katinas, V., "Flow Induced Vibration in Heat Exchanger Tube Banks," *Proceedings, IUTAM-IAHR Symposium on Practical Experiences With Flow-Induced Vibrations*, Karlsruhe, 1979, Naudascher, E., and Rockwell, D., editors, Springer-Verlag, Berlin, 1980, pp. 188-196.

20 King, R., and Johns, D. J., "Wake Interaction Experiments With Two Flexible Circular Cylinders in Flowing Water," *J. Sound and Vibration*, Vol. 45(2), 1976, pp. 259-283.

21 Lever, J. H., Weaver, D. S., "On the Stability Behavior of Heat Exchanger Tube Bundles, Part I—Modified Theoretical Model," ASME WAM Symposium on Flow-Induced Vibrations, Vol. 2, pp. 83-98, New Orleans, 1984, editors, Paidoussis, M. P., Au-Yang, M. K., Chen, S. S., "On the Stability Behavior of Heat Exchanger Tube Bundles, Part II—Numerical Results and Comparison With Experiments," ASME WAM Symposium on Flow-Induced Vibrations, Vol. 2, pp. 99-116, New Orleans, 1984, editors, Paidoussis, M. P., Au-Yang, M. K., Chen, S. S.

DISCUSSION

M. M. Zdravkovich[1]

The McMaster's school of Flow Induced Vibration founded by Professor Weaver should be congratulated for yet another revealing study. The study deals with flow visualization, a powerful but often neglected tool in Fluid Mechanics. A significant advancement of our understanding was achieved by the visualization of the interstitial flow in one tube array.

The most interesting was a discovery of symmetric vortex shedding behind tubes oscillating in the streamwise direction. This puzzling phenomenon was first noted in a tidal flow at the estuary of the river Humber near Immingham in England [22]. Subsequent full scale [22] and laboratory simulations by Hardwick and Wootton [23] revealed the mechanism of excitation.

Figure 9 is reproduced from [23] and shows one cycle of oscillation. The initial displacement of the cylinder in the upstream direction induces a formation of a symmetric vortex pair. The increased drag force reverses the displacement in the downstream direction while the growth of symmetric vortices continues until a maximum amplitude in the downstream direction is reached. At that point in the cycle a *forced* shedding of fully grown symmetric vortices is executed and a new vortex pair begins to grow again. The excessive drag force during the downstream stroke of the cylinder maintains the oscillation. The forced symmetric vortex shedding is always synchronized with the displacement of the cylinder. Thus the phenomenon is triggered and governed by the displacement of the elastic cylinder and clearly belongs to the fluid-elastic type of excitation. Moreover the phenomenom is also a self-limiting one because beyond the reduced velocity of about 2.5 the symmetric growth of large vortices cannot be maintained and alternate vortex shedding takes over. This has been verified by King et al. [24] and Dickens [25].

My first question is related to this intrinsic link between streamwise oscillations of the cylinder and symmetric vortex shedding. Have the authors observed the latter when the tubes were stationary?

The interference by a downstream tube placed in the wake of the upstream oscillating tube depended on the size of the gap between them. King and Johns [20] found that forced symmetric shedding behind the upstream oscillating cylinder excited the downstream one to oscillate in an out-of-phase mode but only if the gap was less than 1.75 diameters. Similar out-of-phase oscillations were observed by the authors in the first and second row. However, the authors presented the amplitude of oscillations only for the tubes in the second row. Will it be possible to have a similar but presumably larger amplitude variation for the tube in the first row as well?

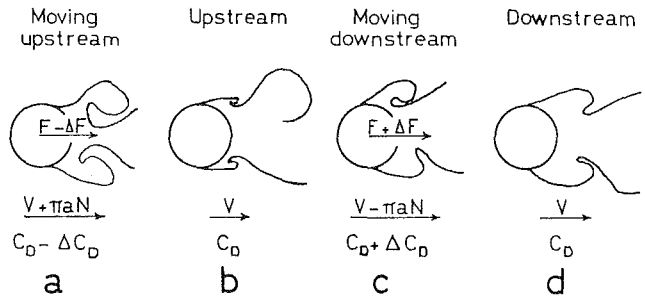

Fig. 9 Formation and forced symmetric shedding of vortex pair

A final comment is related to the in-phase oscillations of all tubes located in the first row. The destructive oscillation of trash racks [26] in water seems to have been caused by synchronized symmetric vortex shedding. The reduced velocity at which excitation was first observed was around 1.2 for all three natural frequencies of the tubes [27]. It might be interesting to ask whether the present authors observed synchronized symmetric vortex shedding behind all tubes in the first row and what was the effect of the side walls on this synchronization?

Additional References

22 Wootton, L. R., Warner, M. H., and Cooper, D. H., *Some Aspects of Oscillations of Full Scale Piles, in Flow Induced Structural Vibrations*, ed., E. Naudascher, Springer Verlag, Berlin, 1974, pp. 587-601.

23 Hardwick, J. D., and Wootton, L. R., "The Use of Model and Full-Scale Investigations on Marine Structures," in *Proceedings of International Symposium of Vibration, Problems in Industry*, ed., J. Wakefield, UKAEA, 1973, paper 127.

24 King R., Prosser, M. J., and Johns, D. J., "On Votrex Excitation of Model Piles in Water," *Journal Sound and Vibration*, Vol. 29, No. 2, 1973, pp. 169-188.

25 Dickens, N. R., "The Self-Induced Vibration of Cylindrical Structures in Fluid Flow," *Proceeding Institution of Civil Engineers*, Vol. 67, 1979, pp. 13-30.

26 March, P. A., and Vigander, S., "Some T V A Experiences with Flow Induced Vibrations," in *Practical Experience with Flow Induced Vibrations*, ed., E. Naudascher and D. Rockwell, Springer Verlag, Berlin, 1980, pp. 228-236.

27 Crandall, S., Vigander, S., and March, P., "Destructive Vibration of Trashracks due to Fluid-structure. Interaction," ASME *Journal of Engineering for Industry*, 1975, pp. 1359-1365.

Authors' Closure

The authors are grateful to Dr. Zdravkovich for his kind

[1] Mechanical Engineering, University of Salford, Salford, England.

remarks and interesting comments on their paper. Dr. Zdravkovich quite correctly points out that there is an intrinsic link between streamwise oscillations of the tubes and symmetric vortex shedding. In the absence of such streamwise cylinder motions, no symmetric vortex shedding was observed. This was easily seen in our experiments as the bundle was made up of both rigid and flexibly mounted tubes.

Synchronized streamwise motions of the tubes were observed primarily in the 3 upstream tube rows, the amplitudes being the largest in the second row. The first and third row tube amplitudes were significant but about 30 percent less than those for the second row. The oscillation amplitudes of the fourth row tubes were relatively small.

As one would expect from the synchronized response of the tubes, the symmetric vortices shed from each tube in a row where precisely in phase with one another. This was especially clear in the still photographs of vortex pairs behind the first row tubes. At a given instant of time, the wakes of the first row flexible tubes were essentially identical. There was no observable side wall effects as the flexible tubes were bounded on each side by rigid cylinders which did not shed symmetric vortices.

As pointed out by Dr. Zdravkovich, the similarities between the symmetric vortex shedding observed in our tube arrays and that observed for tandem tubes and tube rows are remarkable. However, important questions regarding the nature of the excitation mechanisms exist. It is not clear why the reduced velocity for streamwise oscillations of tandem tubes or single tube rows should be about one quarter of that expected for synchronization of alternate vortex shedding. Furthermore, alternate vortex shedding was not observed in the tube array and the reduced velocity associated with symmetric vortex shedding was one half of that expected from Strouhal data in the literature. These observations further serve to emphasize the fact that streamwise oscillations of cylinders associated with symmetric vortex shedding are fluid-elastic in nature and not simply forced vibrations associated with "normal" alternate shedding of vortices.

Node Selection for Two-Point Boundary-Value Problems

C. M. Ablow

S. Schechter

SRI International,
Menlo Park, Calif. 94025

W. H. Zwisler

ATAC Corporation,
Mountain View, Calif. 94041

The solutions of two-point boundary-value problems often have boundary layers, narrow regions of sharp variation, that can occur in any part of the interval between the points. A finite difference method of numerical solution will generally require more closely spaced nodes in the boundary layers than elsewhere. An automatic method is needed for achieving the irregular spacing when the location of the boundary layer is not known in advance. Several automatic node-insertion or node-movement methods have been proposed. A new node-movement method is presented that is optimal under the criterion of producing the least sum of squares of the truncation errors at the nodes. For the Keller box scheme applied to a system of N coupled first-order differential equations this truncation-error minimizing (TEM) method increases the system size to N+6 equations. The campylotropic coordinate transformation method and other published methods based on heuristically derived monitor functions are node-movement methods that involve systems of only N+1 or N+2 first order equations. A comparison is made of the accuracies of several such methods and the TEM method in the solution of a standard problem.

Introduction

The truncation error of a given difference approximation to a differential system is decreased by mesh uniformity and by mesh refinement in the boundary layers, narrow regions where the solution has sharp variation. Both mesh uniformity and local mesh refinement can be obtained by using a transformed coordinate system that expands the scale in the boundary layers. The regions of sharp variation are evident in the magnitude of derivatives and in the shape of the integral curve or surface representing the solution. Thus transformations to coordinates normalizing the derivatives or to intrinsic coordinates defined by the geometry of the integral surface are indicated.

For two-point boundary-value problems it has been shown [1] that distance along the integral curve, augmented with a proper multiple of the curvature, is an effective coordinate for increasing the accuracy of a given low-order difference approximation to differential equations of boundary-layer type. This campylotropic coordinate takes on equally spaced values at the adjusted nodal points. It is therefore a particular case of the monitor functions defined by White [2]. A monitor function with the effect of normalizing the derivatives can also be defined. White showed that an iterative solution of the Keller box difference equations [3] in a properly defined monitor coordinate would converge under weak conditions.

Two criticisms of solution methods based on the change to a monitor coordinate are that the methods are neither optimal nor automatic. Conditions for an optimal monitor that minimizes the truncation error in the least squares sense have been reduced below to a differential equation and boundary conditions. Appending this equation to the given system permits automatic determination of the optimal monitor along with the solution. Because the equation is of the fifth order, lower order, suboptimal, heuristically developed monitor functions remain attractive. They are automatic if any free parameters are chosen to minimize a computable approximation to the truncation error.

Several authors [4–6] have investigated node addition methods recently, a long time after the pioneering work of Pearson [7]. In these methods the tolerable error may be specified in advance of solution, but the number of mesh modes, i.e., the cost, may not. In node movement methods the error is reduced as much as possible for a given cost.

Monitor Functions

The differential equations to be solved are organized here as a first-order system solved for the derivatives. With x the scalar independent variable and y the N-dimensional vector dependent variable, the system is:

$$y' = f(x,y)$$

where the prime denotes differentiation with respect to x and f is an N-dimensional vector-valued function. Boundary conditions are given at the ends of the interval $a \le x \le b$ for which the solution is sought.

Change of the independent variable from x to t is conveniently accomplished through definition of the derivative u

$$\dot{x} = u \text{ or } t' = u^{-1}$$

where the dot denotes differentiation with respect to t. The coordinate transformation is well-defined with a unique inverse if functions u and u^{-1} are bounded, continuous, and of constant sign. The coordinate change yields the $(N+1)$-dimensional system:

Contributed by the Fluids Engineering Division and presented at the Fluids Engineering Conference, Houston, Texas, June 20–22, 1983. Manuscript received by the Fluids Engineering Division, June 27, 1983.

$$\dot{Y} = F(Y)$$

where $Y = (x, y^T)^T$, $F = u(1, f^T)^T$, and T denotes the vector transpose operation.

Coordinate t is chosen to be a monitor function of x, a function that takes equal steps between finite difference nodes adjusted to give accurate solution of the equations. Since a general cause of inaccuracy of a difference method is large variation of the components of y between nodes, transformation to a monitor coordinate that bounds $\dot{x}$ and the $\dot{y}_i$ or that decreases bounds on the $\dot{y}_i$ below those on the y_i' should improve the accuracy of the method.

In many cases the first component y_1 of y has a special significance. For these cases arc length s_1 along the solution curve $y_1 = y_1(x)$ is a useful monitor function because, with $t = s_1$, both $\dot{x}$ and $\dot{y}_1$ are bounded by unity:

$$\dot{x}^2 + \dot{y}_1^2 = 1.$$

Monitor function s_1 also reduces the bounds on all the components of $\dot{y}$ because

$$\dot{y}_i = \dot{x} y_i' = y_i'/[1 + (y_1')^2]^{1/2}$$

so that, if b_i is a bound for $|y_i'|$, a bound on $|\dot{y}_i|$ is the generally smaller quantity

$$b_i/[1 + \min(y_1')^2]^{1/2}.$$

The campylotropic coordinate [1]

$$t = s_1 + C\int |d\Theta_1|$$

where C is a nonnegative constant and Θ_1 is the angle of inclination,

$$\Theta_1 = \arctan y_1',$$

provides for an influence of the curvature κ_1 on the transformation,

$$\kappa_1 = \frac{d\Theta_1}{ds_1} = y_1''/[1 + (y_1')^2]^{3/2}.$$

The bounds on $\dot{x}$ and the $\dot{y}_i$ are obtained from

$$\dot{x}^2 + \dot{y}_1^2 = 1/(1 + C|\kappa_1|)^2$$

and

$$|\dot{y}_n| = |y_n'|/\{(1 + C|\kappa_1|)[1 + (y_1')^2]^{1/2}\}$$
$$n = 1,2, \ldots, N.$$

The bounds will be generally lower for this coordinate than for simple arc length where the same formulas apply but with $C = 0$.

An improved bound on $|\dot{y}_2|$ can be derived in the common case that $y_2 = y_1'$. For then $y_1'' = y_2'$ so that κ_1 and therefore $|\dot{y}_2|$ become functions of $|y_2'|$ and y_2. To derive the bound, one allows these two variables to be independent. Then, by partial differentiation holding $|y_2'|$ fixed, one sees that $|\dot{y}_2|$ is a maximum where

$$1 + y_2^2 = (2C|y_2'|)^{2/3}.$$

The maximum value of $|\dot{y}_2|$ at this point is

$$(4|y_2'|^2/27C)^{1/3}.$$

Thus, if b_2 is an upper bound for $|y_2'|$, the corresponding upper bound on $|\dot{y}_2|$,

$$|\dot{y}_2| \le [4(b_2)^2/27C]^{1/3},$$

will be less than b_2 if C is chosen to be greater than $(4/27b_2)$.

The arc length s_N along the solution curve $[x = x(t), y = y(t)]$ in $(N+1)$-dimensional Euclidean space is a useful generalization of the above monitor functions because, with $t = s_N$

$$\dot{x}^2 + \sum_{n=1}^{N} \dot{y}_n^2 = 1$$

so that the derivative of every variable is bounded by unity.

Table 1 Monitor functions

Coordinate Function t	Derivative t'
Uniform	$(1/L)$
Arc length	$(1/L)[1 + (y_1')^2]^{1/2}$
Campylotropic coordinate	$(1/L)[1 + (y_1')^2]^{1/2}(1 + C\|\kappa_1\|)$
Phase space arc length or normalizing coordinate	$(1/L)\left[1 + \sum_{n=1}^{N} (y_n')^2\right]^{1/2}$
Weighted normalizing coordinate	$(1/L)\left[1 + \sum_{n=1}^{N} C_n (y_n')^2\right]^{1/2}$

A more flexible monitor function with properties similar to those of s_N is defined by

$$\dot{x}^2 + \sum_{n=1}^{N} C_n \dot{y}_n^2 = 1$$

where the weights C_n are positive constants. One obtains

$$|\dot{x}| \le 1, |\dot{y}_n| \le C_n^{-1/2}. n = 1,2, \ldots N.$$

The monitor functions t that are considered here as candidates for the coordinate transformations are presented in Table 1 in terms of their derivatives. The monitor function itself is the integral of its derivative:

$$t = \int_a^x t'\, dx.$$

Since t and any constant multiple of t have equally spaced values at the same nodal points, the definitions contain a free parameter L. The uniform monitor function provides only a change of scale.

Accuracy Criterion

The differential system with t as independent variable is approximated by the finite difference expressions obtained by use of the trapezoidal rule on a uniform mesh of width Δt containing $J+1$ nodes. With the argument j denoting evaluation at $t = (j-1)\Delta t$, one has

$$Y(j+1) - Y(j) = (\Delta t/2)[(F(j+1) + F(j))], j = 1,2 \ldots, J.$$

The truncation error of this approximation has lowest-order term

$$[(\Delta t)^2/12]\ddot{F}(j + 1/2).$$

The coordinate change is best in the least squares sense if unknown function u has been chosen so that the sum of the squares of the local truncation errors T_j,

$$T_j = \{[(\Delta t)^4/144][\ddot{F}(j + 1/2)]^2\}^{1/2},$$

is a minimum. In the expression for T_j the indicated square is the inner product of the vector $\ddot{F}$ with itself.

Repeated application of the trapezoidal rule provides the approximation $\ddot{F}(j + 1/2) = \dddot{Y}(j + 1/2) \doteq (4/3)[Y(j+2) - 3Y(j+1) + 3Y(j) - Y(j-1)]/\Delta t^3$. The resulting approximation to T_j is a computable measure of the local accuracy of the computation that has been used [5-7] in schemes for local mesh adjustment. Here $\bar{S}$, the root mean square value of the T_j,

$$\bar{S} = (J/9)\{[1/(N+1)(J-2)]$$
$$\sum_{j=2}^{J-1} \sum_{m=1}^{N+1} [Y_m(j+2) - 3Y_m(j+1) + 3Y_m(j) - Y_m(j-1)]^2\}^{1/2},$$

has been used to compare the efficacies of the transformations to different monitor functions t. In the formula, $J+1$ is the number of nodes, the interval in t is $0 \le t \le 1$ so that $\Delta t = 1/J$, the dimension of Y is $N+1$, and $Y_m(j)$ is the mth component of Y evaluated at $t = (j-1)\Delta t$.

Truncation Error Minimizing (TEM) Transformation

The analytical determination of a transformation that minimizes the sum of the squares of the truncation errors is simplified if the sum is approximated by the integral S_I,

$$S_I = \int_0^1 \ddot{F}^2 dt$$

Since the given interval $a \le x \le b$ between boundary points has been transformed into $0 \le t \le 1$, $L = b - a$,

$$\int_0^1 u dt = b - a, u = 1/t'.$$

A change of the variable of integration from t to x gives

$$S_I = \int_a^b [u(uF')']^2 (1/u) dx, \int_a^b (1/u) dx = 1,$$

where u appears explicitly.

Finding u as a function of x to minimize S_I while satisfying the side condition is a straightforward problem of the calculus of variations. After combining the integrals with Lagrange multiplier λ, here a constant, one obtains the Euler equation and boundary equations to be satisfied by u. The expressions have a simple appearance after transformation back to the t coordinate:

$$\ddot{F}^2 - 2\dot{F}F^{(3)} + 2FF^{(4)} = \lambda$$

$$F\ddot{F} = 2\dot{F}\ddot{F} - FF^{(3)} = 0 \text{ at } t = 0,1.$$

where the differentiations are all with respect to t. Another differentiation eliminates λ and reduces the Euler equation to:

$$FF^{(5)} = 0.$$

Since F is proportional to u, one may cancel the factor u to obtain a differential equation linear and homogeneous in u. The coefficient of $u^{(5)}$, the highest derivative of the unknown function u, is $(1 + f^2)$ so that the equation is regular over the interval of integration if the solution of the differential system is. An initial value problem for this differential equation would then be well set, with final values continuous functions of the initial ones. A shooting method should then find the solution u if there is one. However, further analysis is needed to show under what conditions the boundary value problem for u has a solution.

Coordinate transformations for fluid dynamics problems have appeared [8–9] that are similar in implementation to the TEM transformation. A time-dependent coordinate system is determined along with the flow by simultaneously satisfying the dynamic equation for minimizing a heuristically chosen functional.

Program SRI2PT

The subroutine program SRI2PT has been written to solve the difference equations for the $Y(j)$ by Newton's method using a block tridiagonal matrix solver [10]. Input to the subroutine are functions defining the given differential system, the boundary conditions, and the monitor function for the transformation. For Newton's method the partial derivatives of each of these functions with respect to the dependent variables, x and the components y_i of vector y, are also needed. Normalization parameter L is included as a dependent variable satisfying the differential equation $\dot{L} = 0$.

The subroutine sets up the solution of the autonomous system. Each iteration of Newton's method provides linear equations for the corrections $\delta(j)$ to initial values $Y(j)$ at node j such that $Y(j) + \delta(j)$ is, under proper conditions, a closer approximation than $Y(j)$ to the solution of the difference equations. When the iterations coverage, a solution to the difference equations has been found.

The equations for the nodes appear in the order of the nodes on the interval. For an initial value problem there is a full complement of boundary functions at $j = 1$. The Jacobian matrix of coefficients of the $\delta(j)$ is then block lower triangular, and the difference scheme is a two-term recursion. For two-point boundary value problems, there are fewer boundary functions at $j = 1$. The first row of submatrix blocks is therefore made up partly of coefficients computed from the boundary functions and partly of ones from the difference formulas. A three term recursion and block tridiagonal coefficient matrix results. Since the block tridiagonal solver begins by inverting the first main diagonal block, the difference equations need to be ordered so that at least this block is nonsingular. A permutation vector giving a proper ordering is also input by the user of the subroutine.

The block matrices are stored by column. The subdiagonal blocks are stored one after the other as are the diagonal and superdiagonal blocks. This organization of the storage gives the non-vanishing blocks of the coefficient matrix the appearance of three long vectors. This is advantageous with current FORTRAN compilers because after an initial dimensional statement, vectors can be passed from one subroutine to another without redimensioning, while multidimensional arrays cannot.

Exponential Example

The example to which the several transformations have been applied is the system:

$$y_1' = py_2$$

$$y_2' = py_1$$

$$y_1(0) = 0, y_1(1) = 1,$$

where p is a parameter. This has the solution

$$y_1 = (\sinh px)/\sinh p,$$

$$y_2 = (\cosh px)/\sinh p.$$

The integral curve runs in the (x, y_1) plane with positive slope from the origin to the point (1,1) and lies closer to the corner at (1,0) for larger p. This is the "exponential example" considered in reference [1].

For the transformed system

$$Y = (x, y_1, y_2, L)^T.$$

Equations of the difference system are

$$Y_1(1) = 0$$

$$Y_2(1) = 0$$

followed by the trapezoidal difference equations for $\dot{Y}_3$, $\dot{Y}_4$, $\dot{Y}_1$, and $\dot{Y}_2$ centered at $j = 3/2$, then those for $j = 5/2$, etc. The last set, for $j = J + 1/2$, is followed by the boundary equations

$$Y_1(J+1) = 1$$

$$Y_2(J+1) = 1.$$

The order was chosen because, in the limit as Δt tends to zero, the diagonal block matrix coefficient of $\delta(1)$ becomes a matrix with 1 or -1 for each main diagonal entry and zeros elsewhere, a nonsingular-matrix as required.

Transformation to the TEM coordinate t requires solution of the system

$$\dot{x} = u$$

$$\dot{y}_1 = puy_2$$

$$\dot{y}_2 = puy_1$$

$$u^{(5)} + p^2[y_1(uy_1)^{(5)} + y_2(uy_2)^{(5)}] = 0$$

A first order system may be obtained in the simplest way by defining new dependent variables u_i, $i = 1, \ldots, 4$. Then the system becomes

$$\dot{x} = u$$

$$\dot{u} = u_1$$

$$\dot{u}_1 = u_2$$

$$\dot{u}_2 = u_3$$

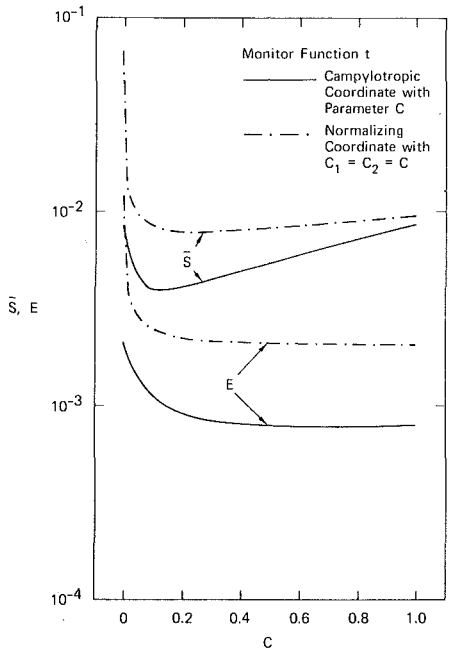

Fig. 1 Root mean square truncation error $\bar{S}$ and maximum actual error E for exponential example ($p = 20$) on a difference mesh with 32 intervals plotted against parameter C

$$\dot{u}_3 = u_4$$

$$\dot{u}_4 = -p^2[y_1(uy_1)^{(5)} + y_2(uy_2)^{(5)} - (y_1^2 + y_2^2)u^{(5)}] / [1 + p^2(y_1^2 + y_2^2)]$$

$$\dot{y}_1 = puy_2$$

$$\dot{y}_2 = puy_1$$

Subroutine SRI2PT solves this system under the uniform monitor function with $L = 1$ if t is considered to be an added dependent variable with derivative 1. Then

$$Y = (t, x, u, u_1, u_2, u_3, u_4, y_1, y_2)^T$$

$$F = (1, Y_3, Y_4, Y_5, Y_6, Y_7, F_7, pY_3Y_9, pY_3Y_8)^T$$

where, after an expansion,

$$F_7 = -p^2[(Y_8^2 + Y_9^2)P_1 + 2Y_8Y_0P_2] / [1 + p^2(Y_8^2 + Y_9^2)],$$

$$P_1 = 15p^4Y_3^4Y_4 + 60p^2Y_3Y_4Y_5 + 15_p2_{Y_3}2_{Y_6} + 15p^2Y_4^3,$$

$$P_2 = p^5Y_3^6 + 20p^3Y_3^3Y_5 + 45p^3Y_3^2Y_4^2 + 15pY_4Y_6 + 10pY_5^2 + 6pY_3Y_7.$$

Functions that are zero at the $j = 1$ boundary are

$$Y_1, Y_2, Y_8, B_1, \text{ and } B_2$$

while those that vanish at $j = J + 1$ are

$$Y_2 - 1, Y_8 - 1, B_1, \text{ and } B_2$$

where

$$B_1 = Y_5[1 + p^2(Y_8^2 + Y_9^2)] + 6p^3Y_3Y_4Y_8Y_9 + p^4(Y_8^2 + Y_9^2)Y_3^2$$

and

$$B_2 = (2Y_4Y_5 - Y_3Y_6)[1 + p^2(Y_8^2 + Y_9^2)] + 2p^4Y_3^3Y_4(Y_8^2 + Y_9^2) + 2p^3Y_8Y_9(3Y_3Y_4^2 - 2Y_3^2Y_5 + p^2Y_3^5).$$

An order of the difference equations that provides for small enough Δt a nonsingular main diagonal block coefficient of $\delta(1)$ is

Table 2 Results for exponential example with $p = 20$, $J = 33$

Monitor function t	Maximum error[a] $E \times 10^3$	rms truncation[b] error $\bar{S} \times 10^3$
Uniform	12.1	67.2
Arc length	2.11	8.38
Campylotropic coordinate $C = 0.1$	1.12	3.94
Normalizing coordinate $C_1 = C_2 = 1.0$	2.12	9.10
$C_1 = C_2 = 0.20$	2.22	7.99
TEM coordinate	0.919	3.56

[a] $E = \max |y_1(j) - (\sinh px_j / \sinh p)|, j = 1, 2, \ldots, J+1$.
[b] This is the error for the given differential equations in the transformed coordinate.

$$(3,4,7,9,1,2,5,6,8).$$

No difficulty was encountered using the equations in this order.

Numerical Results for Parameter C

The root mean square truncation error approximation $\bar{S}$ and the maximum actual error E, the maximum absolute value of the difference between computed and analytic solutions at the grid points, are plotted in Fig. 1 for computations using the campylotropic transformation with parameter C and the weighted normalizing coordinate with equal parameters, $C_1 = C_2 = C$. (The parameters were taken equal because the functions they multiply are nearly equal over most of the domain of integration.) One sees from the figure that a proper positive value for C gives much more accurate solutions than the uniform or arc length transformations obtained with $C = 0$.

In the limit, as the number of mesh intervals increases and their width decreases, $\bar{S}$ then lies where E is also a minimum. One sees in Fig. 1 that, with just 32 intervals, the minima of $\bar{S}$ and E occur at quite different values of C. However, using the value of C that makes $\bar{S}$ a minimum is an automatic way of selecting C that gives an E not too far from its minimum, at least on this example.

The insensitivity of E to variations in C for $C > 0.2$ is due to oscillations (ringing) where the solution functions y_1 and y_2 are very small. The computer points fall alternatively above and below the exact solution with an oscillation amplitude of the order of the truncation error and independent of C. The campylotropic monitor was set up for this example in reference [1] and solved as a second order system. In this calculation the oscillations are suppressed, and error E passes through a sharp minimum as C varies. This sensitivity of E makes the second order method less suitable than the present first order ones for calculations with an approximate C.

Comparison of the Monitor Functions

The monitor functions listed in Table 1 were applied to solve the example problem. The maximum actual errors E and the root mean square approximate truncation errors $\bar{S}$ are shown in Table 2 along with results from the transformation to the TEM coordinate. One sees that the errors are smallest for the campylotropic and TEM schemes. The approximate truncation error $\bar{S}$ is only y_1 and y_2 as shown for the TEM scheme in Table 2 to allow reasonable comparisons among the monitor functions. The value of $\bar{S}$ for all the TEM variables is 6080, a value reflecting the inaccuracy of the computations of the higher derivatives of y_1. Values of $\bar{S}$ are not used in a TEM calculation but could, for example, help decide on the need for more nodes.

The various monitor functions are plotted in Fig. 2. All the nonuniform monitor functions rise less steeply in that part of the x interval where the solution curve is nearly the straight

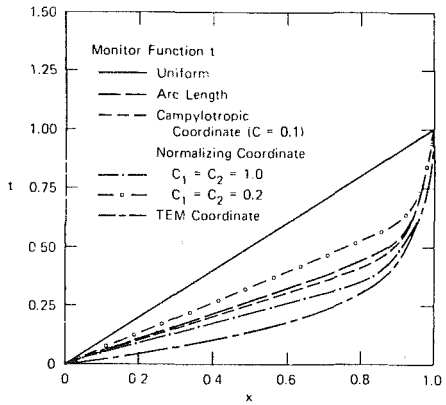

Fig. 2 Monitor functions for exponential example ($p = 20$)

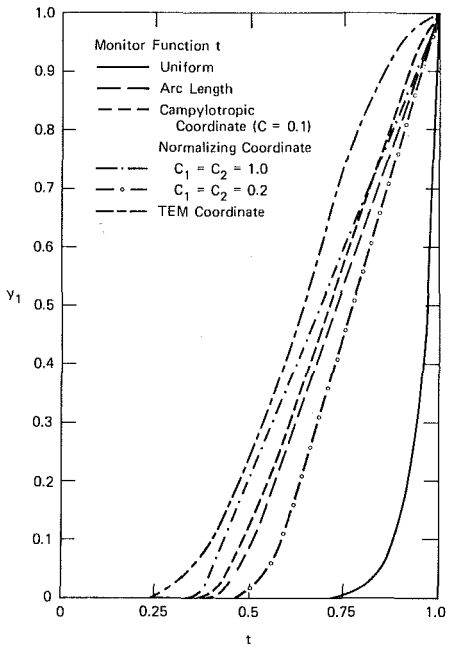

Fig. 3 Solution functions for exponential example ($p = 20$)

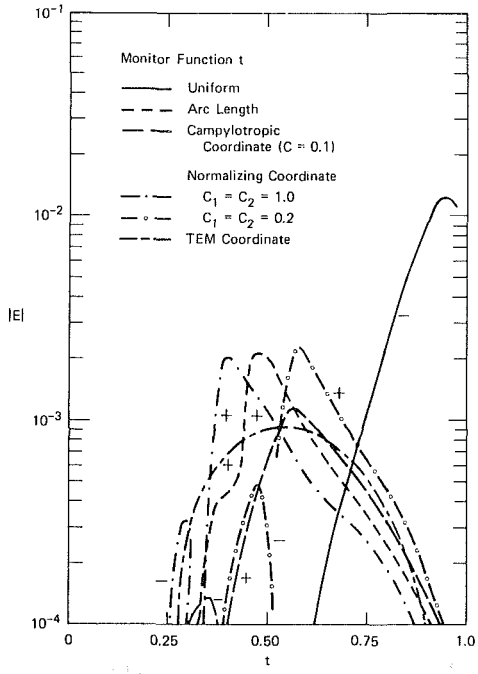

Fig. 4 Local error E with indicated sign for exponential example ($p = 20$)

line $y = 0$ than they do where the solution bends. The corresponding difference meshes are coarser on the straight section than on the curved as desired. The TEM monitor curve is seen to be near the others and have the most uniformly curved shape. The camplyotropic monitor is the next most uniformly curved. It may be that this uniformity produces the accuracy of these two monitors.

In Fig. 3 solution function y_1 is plotted against the several monitor coordinates. For the uniform monitor, $t = x$, the solution curve has its usual appearance. All of the other monitor functions have larger intervals in t over which y_1 is appreciably greater than zero, so that more mesh points are devoted to this region than in the uniform case. The TEM and campylotropic coordinate curves rise above all the others to give a greater density of nodal points near $y_1 = 1$ than the other coordinates do. This is where derivatives of y_1 are large so that the mesh refinement is needed.

The local error E, the difference between the computed and analytic solutions for y_1, is plotted for the different monitor functions in Fig. 4. One sees that the uniform monitor is least accurate where the solution curve rises steeply. The arc length monitor is least accurate and the campylotropic monitor is best where the solution graph is most curved. The TEM coordinate provides a more uniform distribution of the error than the other monitors.

Both normalizing coordinates and the campylotropic coordinate have error segments with different signs. These are evidences of the oscillations referred to earlier.

Conclusions

The objective of the present work was to compare the efficacies of several monitor functions for reducing the error of finite difference computation of a typical problem of boundary layer type. The monitor functions are defined and any free parameters determined without knowledge of the location of the boundary layer. The monitor functions were derived by consideration of the intrinsic geometry of the given system (arc-length and campylotropic coordinates), the algebra of the system (normalizing and weighted normalizing coordinates), and an error analysis of the difference method (TEM coordinate).

Numerical experimentation with the free parameters in the coordinate definitions showed that the actual error at the minimum of a computable approximation to the truncation error is close to the minimum actual error attainable with the coordinate and that application of truncation error minimization to a monitor function with free parameters gives a coordinate close to the unrestricted best one, the TEM coordinate. A method for simultaneously computing the TEM coordinate and the solution to the system has been given.

Since the TEM method complicates the computation of the solution, use of a suboptimal monitor with a few free parameters chosen to reduce truncation remains attractive. Monitors of this kind in Table 1 are the campylotropic coordinate and the weighted normalizing coordinate. The latter has an immediate generalization to systems of higher order.

Acknowledgment

Partial support by the U.S. Air Force Office of Scientific Research under Contract F-49620-77-C-0114 is gratefully acknowledged.

References

1 Ablow, C. M., and Schechter, S., "Campylotropic Coordinates," *J. Computational Physics*, Vol. 27, 1978, pp. 351–362.

2 White, A. B., Jr., "On Selection of Equidistributing Meshes for Two-Point Boundary-Value Problems," *SIAM J. Numerical Analysis*, Vol. 16, 1979, pp. 472–502.

3 Keller, H. B., "Numerical Solution of Two-Point Boundary Value Problems," *Regional Conference Series in Applied Mathematics, SIAM*, Vol. 24, 1976, Philadelphia.

4 Kreiss, H. O., and Nichols, N., "Numerical Methods for Singular Perturbation Problems," *Stanford University Seminars*, 1979.

5 Pereyra, V., and Sewell, E. G., "Mesh Selection for Discrete Solution of Boundary Problems in Ordinary Differential Equations," *Numerische Mathematic*, Vol. 23, 1975, pp. 261–268.

6 Lentini, M., and Pereyra, V., "An Adaptive Finite Difference Solver for Nonlinear Two-Point Boundary Problems with Mild Boundary Layers," *SIAM J. Numerical Analysis*, Vol. 14, 1977, pp. 91–111.

7 Pearson, C. E., "On Nonlinear Ordinary Differential Equations of Boundary Layer Type," *J. of Mathematics and Physics*, Vol. 47, 1968, pp. 351–358.

8 Yanenko, N. N., Kroshko, E. A., Liseikin, V. V., Fomin, V. M., Shapeev, V. P., and Shirov, Yu A., "Methods for the Construction of Moving Grids for Problems of Fluid Dynamics with Big Deformations," *Proc. 5th Intl. Conf. Numerical Methods in Fluid Dynamics*, Belgium, 1976, Springer, *Lecture Notes* in Physics, Vol. 59, 1978, pp. 454.

9 Saltzman, J., "A Variational Method for Generating Multidimensional Adaptive Grids," Department of Energy Report DOE/ER/03077-174, Courant Mathematics and Computing Laboratory, New York University, New York, 1982.

10 Schechter, S., "Quasi-Tridiagonal Matrices and Type-Insensitive Difference Equations," *Quarterly App. Math*, Vol. 18, 1960, pp. 285–295.

N. K. Madavan
Graduate Assistant,
Department of Mechanical Engineering.

C. L. Merkle
Professor,
Department of Mechanical Engineering.

S. Deutsch
Associate Professor,
Applied Research Laboratory.

The Pennsylvania State University,
Univeristy Park, PA 16802

Numerical Investigations Into the Mechanisms of Microbubble Drag Reduction

Computational results of an initial attempt to model the phenomenon of skin-friction reduction by microbubble injection are presented. A well-tested boundary-layer code employing a simple mixing length model for the turbulence is used. The action of the bubbles is simulated by allowing the viscosity and density to vary locally as a function of a prescribed bubble concentration profile. Parametric studies of bubble location in the boundary layer, peak concentration and mixture viscosity model are performed. The order of magnitude and trends of the experimental skin-friction reduction are reproduced quite well by this simple model.

Introduction

A number of experimental studies [1-6] have been reported during the past several years concerning the effects of a high concentration of very small bubbles on the characteristics of a liquid turbulent boundary layer. In general, the overall conclusions of these experiments has been that the introduction of "microbubbles" reduces the skin friction on a flat plate [1-5] or the drag on a towed vehicle [6]. Consequently, this phenomenon is of interest as a potential drag reduction technique. Because of the complexity of this two-phase, turbulent flow, the precise mechanisms whereby this skin-friction reduction is achieved are unclear. The aforementioned references contain some speculations as to mechanisms, but a complete analysis of the effects of microbubbles has yet to be reported. The present paper represents an initial attempt in this direction.

The approach chosen is to devise a simple phenomenological model of the effects of the microbubbles on the flow and to test it in a standard, numerical boundary layer code. The goal is to identify the dominant features of this complex flow and to assess its sensitivity to various parameters. Quantitative comparisons with experiment cannot be expected, but the model does give a reasonable qualitative description of the observed phenomena. The predictions are restricted to the flow over a flat plate.

In the following sections, we begin with a brief review of the experimental findings and the physics of the flow of interest. This is followed by an outline of the analytical model and its incorporation in the boundary-layer code. The results of a parametric series of calculations are discussed next followed by a summary and conclusions section.

Summary of Experimental Findings and Physics of Flow

In the initial experimental study of the effect of microbubbles on a turbulent boundary layer [6], the bubbles were produced by electrolysis by passing current through wires wrapped around the hull of a towed body. This investigation was followed by a series of experiments by Bogdevich, Evseev and co-workers [1-4] in which a simpler flat plate geometry was used. In their experiments the bubbles were produced by injecting air through a porous section of the surface. The most recent experimental studies have been reported by the present authors [5], again using a flat plate with a porous section. In references [1-5], a series of diagnostic measurements was made downstream of the porous section, and it is upon these measurements that the following description of the flow is based. It is noted that the presence of a high concentration of bubbles makes experimental diagnostics, as well as analytical modeling, difficult. In particular, optical access is restricted by the high bubble concentrations so that current optical techniques (such as laser Doppler velocimetry and optical particle sizing) are of marginal use.

An example of the effects of the introduction of microbubbles on the integrated skin friction downstream of the porous section is given in Fig. 1, which is a replot in dimensionless form of data presented in reference [5]. These results were obtained from a 250 × 100 mm force balance immediately downstream of the porous section, and are representative of the magnitudes and trends noted in all the experiments. Note in particular that the integrated skin friction can be reduced by as much as 80 percent from its undisturbed value and that the amount of reduction observed increases as the air flow rate is increased. (In some cases an optimum air flow rate is observed above which the skin friction again begins to increase.) The increased effectiveness of a given air flow rate at the lower free-stream speeds occurs because of the higher volumetric concentration of bubbles at these low speeds.

Local skin-friction measurements [1-4] demonstrate trends and magnitudes which are analogous to those indicated in Fig. 1, and in addition, they contain one further feature of importance. Local measurements show that the maximum C_f

Contributed by the Fluids Engineering Division of THE AMERICAN SOCIETY OF MECHANICAL ENGINEERS and presented at the Symposium on Laminar-Turbulent Boundary Layers, ETCE Conference, New Orleans, LA, February, 1984. Manuscript received by the Fluids Engineering Division, December 8, 1983.

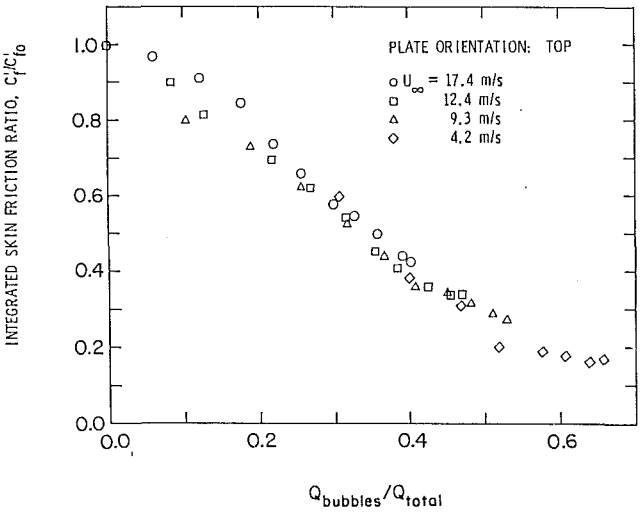

Fig. 1 Experimental results of the effect of microbubbles on the integrated skin friction; replot of experimental data of reference [5]

reduction occurs near the trailing edge of the porous section and then gradually relaxes back toward its undisturbed value. The reason for this diminution appears to be tied to bubble dynamics: Once the bubbles are introduced into the flow, their trajectories are controlled by viscous lift and drag, buoyancy and bubble interactions. The effects of buoyancy have been documented in reference [5] and confirm that the location of the bubbles in the boundary layer is important. The present numerical calculations support this conclusion.

Measurements of the cross-stream variation of the bubble volumetric concentration at various locations along the surface verify that the bubbles drift away from the wall [4]. Downstream of the porous section, the bubble concentration starts from zero near the wall, increases rapidly to a peak value which may be as high as 0.6 or 0.8, and then falls off gradually again to zero in the free stream. Observations from the authors' experiments [5] also suggest that the bubble concentration vanishes at the wall. The reason for this absence of bubbles is not clear although it could be related to viscous lift forces arising because of "ground effect," or because the bubbles are formed away from the surface as the result of instability of an air jet. The calculations presented herein indicate that the absence of bubbles in the near wall region is important in obtaining reductions in the local skin friction.

A final item of importance in the microbubble boundary layer is bubble size. Measurements of air injection through a single pore [7, 8] show that bubble size is nearly independent of pore size. This suggests that bubble size is controlled by a balance between fluid dynamic and surface tension forces. Skin-friction measurements behind porous sections of various pore sizes [3, 9] confirm that the pore size remains of secondary importance in the present application. Accurate estimates of bubble size are difficult to obtain, but it appears that nominal bubble diameters are in the 50 μm range [4].

Analytical Model

There are at least two potential paths by which microbubbles can affect the structure of a turbulent boundary layer. First of all, the microbubbles can alter the local, effective viscosity and density of the fluid, thus changing the local turbulent Reynolds number. This effect can be approximated by treating the microbubble-water mixture as a homogeneous fluid with spatially varying properties. Second, the bubbles can affect the turbulence directly. Accounting for this would require modification of the turbulence model. Although we anticipate that both phenomena act simultaneously, in the present study we consider only the former effect. This allows the global sensitivity to the presence of microbubbles to be studied without the added intricacies of turbulence modeling. A similar approach was used in early attempts to model polymer drag reduction phenomena [10, 11].

Effects of Bubbles on Mean-Flow Properties. The presence of microbubbles in a turbulent fluid can be expected to alter both the density and the viscosity. The simulation of their effect on density is quite straightforward. If the volumetric concentration of air, ϕ, at a given point is known, the local density becomes

$$\rho = \rho_l(1-\phi) + \rho_g\phi \tag{1}$$

where ρ_l and ρ_g represent the density of the liquid and the gas, respectively. It is generally permissible to neglect the gas density term.

Nomenclature

A^+ = constant in Van Driest damping factor
C_f' = integrated skin-friction coefficient in presence of microbubbles
C_{f0}' = integrated skin-friction coefficient in absence of microbubbles
C_f = local skin friction coefficient
D = Van Driest damping factor
H = shape factor, δ^*/θ
k_1, k_2 = numerical constants
l = mixing length
Q = volumetric air flow rate
$Q_{bubbles}$ = volumetric concentration of microbubbles per unit width of boundary layer
Q_{total} = total volumetric concentration (liquid and bubbles) per unit width of boundary layer
$Re_x, Re_{\delta^*}, Re_\theta$ = Reynolds number based on free-stream velocity, liquid viscosity, and streamwise distance, displacement thickness or momentum thickness, respectively
u = streamwise velocity
u^+ = streamwise velocity in inner variables
U_∞ = free-stream velocity
x, y = Cartesian coordinates in streamwise and cross-stream direction, respectively
y^+ = distance form the wall in inner variables, $y\sqrt{\tau_w\rho_l}/\mu_l$
δ = boundary-layer thickness
δ^* = boundary-layer displacement thickness, $\int_0^\delta \left(1-\frac{\rho u}{\rho_l U_\infty}\right)dy$
θ = boundary-layer momentum thickness, $\int_0^\delta \frac{\rho u}{\rho_l U_\infty}\left(1-\frac{u}{U_\infty}\right)dy$
μ = molecular viscosity of liquid and microbubble mixture
μ_e = effective viscosity (laminar and turbulent) of mixture
μ_l = molecular viscosity of liquid
ρ = density of liquid and microbubble mixture
ρ_g = density of gas (air)
ρ_l = density of liquid (water)
τ_w = local wall shear stress
ϕ = bubble concentration in boundary layer
ϕ_{max} = maximum bubble concentration in boundary layer

The effect of the bubbles on the viscosity is considerably more complicated. Numerous data and analyses show that the introduction of a distributed phase into a liquid causes its viscosity to increase. The simplest of these anlayses is that given by Einstein [12] whose results indicate that the viscosity of such a mixture is

$$\mu = \mu_l (1 + 2.5\phi) \tag{2}$$

where μ and μ_l are the viscosities of the mixture and the liquid. Although this analysis is strictly valid only for small concentrations of the distributed phase (less than approximately 2 percent) it has been used successfully at much higher concentrations [13].

Several other analyses and empirical correlations exist [14] in which a quadratic term is added to equation (2), or it is expanded in a power series in ϕ:

$$\mu = \mu_l (1 + 2.5\phi + k_1\phi^2 + k_2\phi^3 + \ldots) \tag{3}$$

where k_1, k_2 . . . are constants chosen to fit selected sets of data. The variety of fits which are available is quite diverse, and depends upon the specific liquid/distributed-phase mixture, the range of volumetric concentration, and the size and shape of the individual elements in the distributed phase. In general these modified formulas have been developed for higher volumetric concentrations than Einstein's, but the variety of coefficients and their uncertain range of applicability make it difficult to choose the most appropriate formula with confidence. We do, however, note that in nearly all cases these formulas suggest that the Einstein relation is conservative, i.e., that the change in viscosity at higher concentrations is underpredicted by Einstein's relation.

In addition to these results for a distributed phase suspended in a liquid, Sibree [15] measured the viscosity of froths and reported his results empirically as

$$\mu = \mu_l / (1 - 1.09\phi^{1/3}). \tag{4}$$

This formula was developed for gas concentrations around 0.3 to 0.6 and gives a result which is larger than those of equations (2) and (3). This concentration range is simlar to the maximum values observed in the present application.

Because of the uncertainty in the effect of bubbles on viscosity, we have chosen to use two models which hopefully bound the effect from above and below. Calculations are presented based upon both Sibree's and Einstein's relations. The Einstein relation is used as a conservative estimate of the effect of microbubbles on viscosity, while Sibree's is used as an optimistic estimate. Comparisons between cases with these two models should give an idea of the sensitivity of the final results to the type of viscosity model used.

For completeness, we also present some calculations in which only the viscosity is changed from its no-air value while the density is left unchanged. These calculations illustrate the relative importance of the density and viscosity changes on the predictions.

Eddy Viscosity Formulation. As just indicated, the present analysis examines the impact on a turbulent boundary layer of viscosity and density changes induced by microbubbles. The turbulence was modeled by a mixing length formulation whose functional form was left unchanged.

The effective viscosity, μ_e, is given by

$$\mu_e = \mu + \rho l^2 \left| \frac{\partial u}{\partial y} \right| \tag{5}$$

where the first term on the right represents the laminar viscosity and the second the contribution from the Reynolds stresses. The mixing length in equation (5) is defined [17] as a function of the nondimensional distance from the wall, y/δ, and a van Driest damping factor, D, as

$$l/\delta = D f(y/\delta) \tag{6}$$

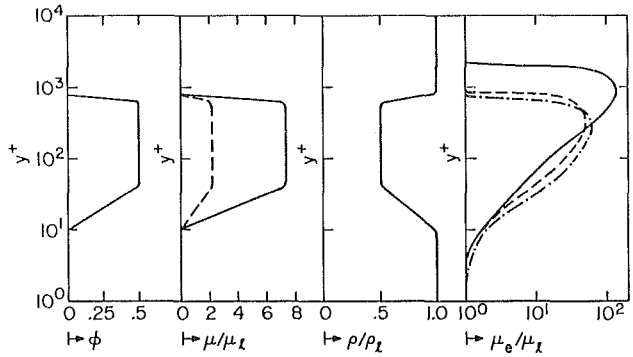

Fig. 2 Variation of viscosity, density and effective viscosity in the boundary layer for a typical trapezoidal air concentration distribution: _·_·_·_·, no air case; ____, Sibree model; _ _ _, Einstein model

where

$$f(y/\delta) = k_2 \tanh (k_1 y/k_2\delta). \tag{7}$$

The values of k_1 and k_2 are chosen as 0.4 and 0.108, respectively. The damping coefficient, based on local properties, is given as

$$D = 1 - \exp\left(- \frac{y^+}{A^+} \frac{\mu_l}{\mu} \sqrt{\frac{\rho}{\rho_l}} \right) \tag{8}$$

where y^+ is defined in terms of wall properties,

$$y^+ = y\sqrt{\tau_w \rho_l}/\mu_l \tag{9}$$

and the constant $A^+ = 26$. The choice of liquid properties at the wall is made because the air content specified there (in concert with the experimental findings cited earlier) was always taken to be zero.

Both the viscosity and density changes caused by the injection of bubbles alter the local effective viscosity as described by equations (5), (6), and (8). In the buffer region their presence in the exponential in equation (8) dominates, resulting in a net decrease in the local value of μ_e in the buffer region. The physical significance of the presence of increased viscosity in the buffer region is that both the turbulent Reynolds number and momentum transfer are decreased. The numerical results indicate that these changes have a sizeable effect on skin friction as is shown in the following section. This mechanism is similar to the one proposed for the effects of polymers on skin friction [10].

Specification of Bubble Concentration Distribution. In an experimental situation the bubble concentration distribution is determined by the collective bubble dynamics and depends upon buoyancy, viscous forces on the bubbles, and virtual mass effects. No attempt has been made to simulate these dynamics in the present calculations. Instead, the concentration has been specified as a function of y^+ throughout the entire boundary layer. This specification effectively provides an equation of state for the density. The omission of bubble dynamics allows emphasis to be placed on identifying the sensitivity of the boundary layer to the presence of microbubbles.

Since the concentration of air in a given element of fluid varies as the element moves along the plate, a compressible flow analysis must be used. Mathematically, this is expressed as

$$\rho = \rho(\phi) \tag{10}$$

where

$$\phi = \phi(x,y). \tag{11}$$

The viscosity is similarly expressed as a function of bubble concentration

$$\mu = \mu(\phi). \tag{12}$$

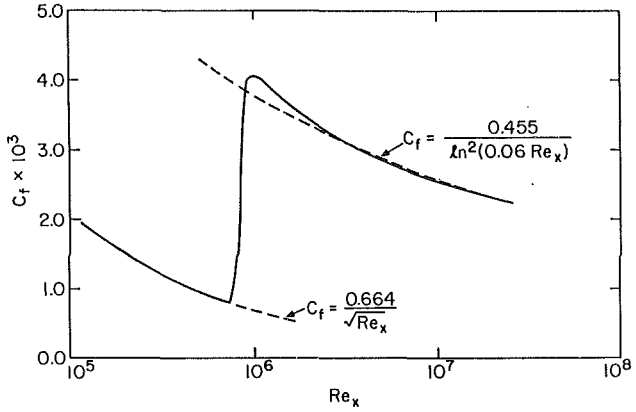

Fig. 3 Comparison of the undisturbed boundary-layer skin friction with classical turbulent boundary-layer correlations (taken from reference [20])

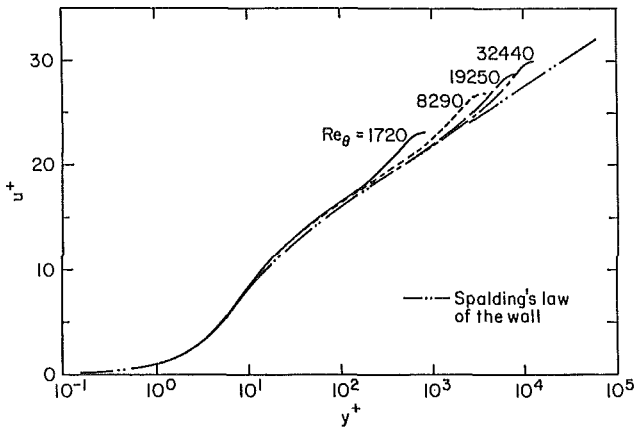

Fig. 4 Comparison of the undisturbed boundary-layer velocity profiles with Spalding's law of the wall

The cross-stream distribution of bubble concentration was specified in terms of a general trapezoidal shape as shown in Fig. 2. This shape was chosen to allow simple parametric variations of concentration distributions and to provide a reasonable representation of observed experimental facts [4]. The density and viscosity variations corresponding to the concentration distribution are also shown in Fig. 2. Finally, the effective viscosity distribution at a specific x-location is also included and compared with the distribution in the absence of bubbles. This comparison demonstrates the manner in which the increased viscosity leads to a decrease in the effective viscosity.

Calculation of the Boundary-Layer Characteristics. The analysis of the effects of the microbubbles on the boundary-layer characteristics was carried out by inserting the modified property variations just described into a numerical boundary-layer code [17–19]. The code solves the complete partial differential equations of the boundary layer for a compressible fluid with an arbitrary equation of state. The numerical solution is computed in a transformed plane by means of a second-order accurate marching procedure. Since the present problem involves no heat transfer, and since neither the density nor viscosity variations are dependent upon the local temperature, it was not necessary to solve the energy equation.

Results and Discussion

In the calculations the boundary layer was started from zero thickness at the leading edge of a flat plate and was allowed to progress through laminar, transitional, and turbulent regimes. All calculations were done at a free-stream velocity of $U = 9.2$ m/s using the properties of water at 300K. This corresponds to a free-stream unit Reynolds number of 9.4×10^6/m.

Transition was simulated by a switch which allowed the turbulence model to be "turned on" gradually. The transitional process was initiated at $x = 0.08$m ($Re_x = 0.7 \times 10^6$) and reached completion at $x = 0.1$m ($Re_x = 0.94 \times 10^6$). Bubbles were not "injected" until a fully turbulent boundary layer had been reached ($x = 0.12$m; $Re_x = 1.15 \times 10^6$). A base case, in which the effects of bubbles were absent, was also computed. All calculations were continued to $x = 2.8$m ($Re_x = 26.5 \times 10^6$).

Characteristics of Undisturbed Boundary Layer. The characteristics of the undisturbed boundary layer in the absence of bubbles are given in Figs. 3 and 4. Figure 3 shows the skin-friction distribution as a function of Reynolds number for this base case. For comparison, the classical C_f variation is also included [20]. As can be seen, the code gives a reasonable $C_f - Re_x$ distribution.

Velocity profiles at several streamwise locations are given in Fig. 4 in inner variables and compared with Spalding's composite profile [20]. Again the profiles constitute reasonable representations of classical boundary-layer data. This curve also shows that the deviation of the $u^+ - y^+$ curve from the log-law distribution at the outer edge of the boundary layer is in qualitative agreement with experiment at the various Re_θ's. Thus we conclude that the mixing length model gives an acceptable description of the mean flow properties of a turbulent boundary layer.

Effect of Changing the Location of Bubbles. Figures 5–8 present the results of a series of calculations which demonstrate the sensitivity of skin friction to the location of bubbles. As indicated in Fig. 2, the concentration distribution was taken as trapezoidal in shape. In this series of computations, the location of the inner leg of the trapezoid was first varied (Figs. 5 and 6) and then the outer leg was varied (Figs. 7 and 8). These cases are distinguished by specifying the vertices of the trapezoid. These vertices were kept at fixed values of y^+ (based on wall values) as the calculations proceeded downstream. The maximum concentration was set at 0.5 at the injection location, but downstream of this station this maximum was varied so as to conserve the volumetric flux of bubbles. In general, the peak concentration drifted by a few percent over the length of the calculation. Although the volumetric flux of bubbles was conserved, the percentage of air in the boundary layer decreased because of entrainment. Finally, we note that to preserve numerical accuracy (as well as to simulate typical experiments), the bubbles were injected over a finite distance (90 mm) instead of at a point. This region is noted on the figures.

The effect of varying the location of the inner leg of the trapezoidal distribution is shown in Figs. 5 and 6. Results are shown for the inner leg between $y^+ = 0$ and 10, 10 and 20, 30 and 40, 50 and 60, and 200 and 300 so that the total air content in the boundary layer was diminished as the inner leg was moved outward. For all these cases the outer leg was positioned between $y^+ = 500$ and 600. The results on Fig. 5 are based on Sibree's viscosity model and show that the minimum skin friction is observed when the inner leg is placed between $y^+ = 10$ and 20. Nevertheless, as long as the inner leg is in the vicinity of the buffer layer the bubbles are quite effective. Skin-friction reductions of as much as 50 percent are predicted immediately downstream of the injection station. This percentage reduction decreases as the Reynolds number increases because entrainment reduces the overall fraction of air in the boundary layer. When the inner leg is

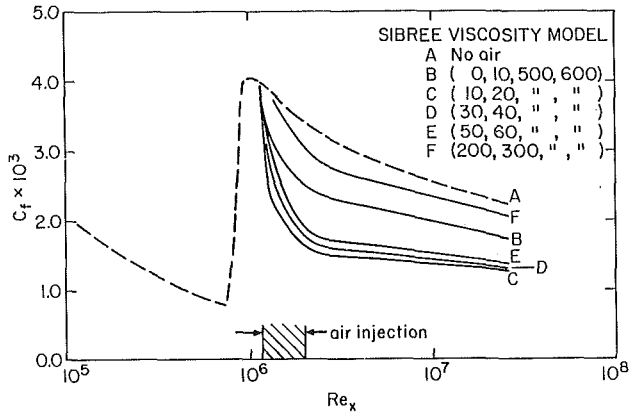

Fig. 5 Effect of the location of the inner leg of the trapezoidal concentration distribution on the skin friction; peak air concentrations = 0.5 (Sibree viscosity model)

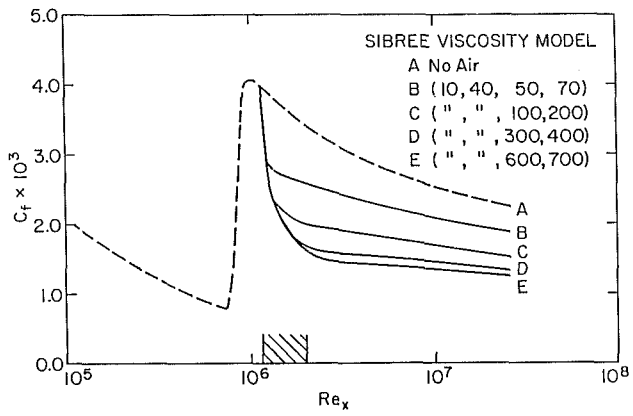

Fig. 7 Effect of the location of the outer leg of the trapezoidal concentration distribution on the skin friction; peak air concentration = 0.5 (Sibree viscosity model)

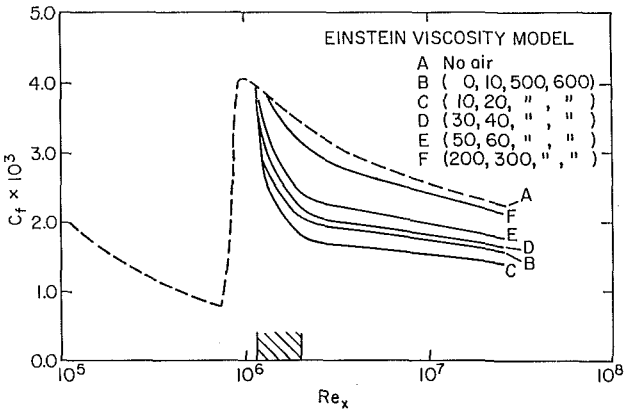

Fig. 6 Effect of the location of the inner leg of the trapezoidal concentration distribution on the skin friction; peak air concentration = 0.5 (Einstein viscosity model)

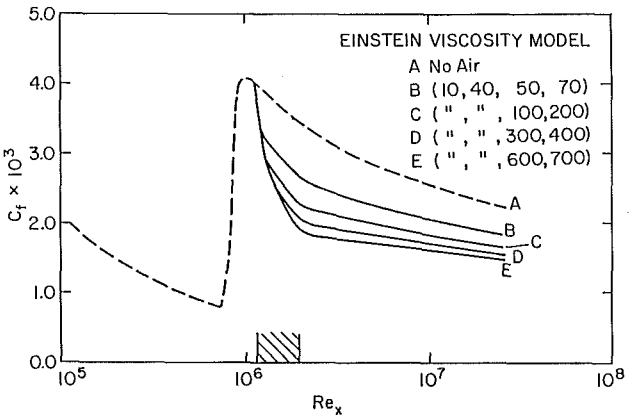

Fig. 8 Effect of the location of the outer leg of the trapezoidal concentration distribution on the skin friction; peak air concentration = 0.5 (Einstein viscosity model)

moved to the outer layer ($y^+ = 200$ to 300) or inside the sublayer ($y^+ = 0$ to 10) the bubbles become less effective.

Analogous results are shown in Fig. 6 for a viscosity variation based upon Einstein's model. Here the weaker variation of viscosity with concentration produces an increased sensitivity to the location of the inner leg of the distribution. Nearly the same maximum skin-friction reduction is predicted when the inner leg is between $y^+ = 10$ and 20, but the effectiveness of the bubbles is reduced more quickly as the bubble concentration is moved away from the wall.

The effects of varying the position of the outer leg of the trapezoidal concentration distribution while the location of the inner leg is held fixed are shown in Figs. 7 and 8. Figure 7 is based on Sibree's viscosity model and shows that the addition of bubbles, farther and farther from the wall continues to reduce the skin friction, but by smaller and smaller amounts. Thus, with the inner leg fixed between $y^+ = 10$ and 40, a modest skin-friction reduction is obtained if the outer leg is placed between $y^+ = 50$ and 70. Moving the outer leg to $y^+ = 100$ to 200 (which corresponds to approximately a factor of five increase in the number of bubbles) nearly doubles the predicted C_f reduction. Extending it further to $y^+ = 300$ to 400 and then to $y^+ = 600$ to 700 gives successively smaller increments of skin-friction reduction even though these two conditions correspond to three and six times the number of bubbles as the 100–200 case. Predictions based upon Einstein's viscosity model (see Fig. 8) are again qualitatively similar, but the maximum skin-friction reduction is smaller than was observed with Sibree's model.

To isolate the relative contribution of the viscosity and density changes, two of the cases described in Fig. 7 have been repeated with only the viscosity changes included and are shown in Fig. 9. These calculations show that both the density and the viscosity changes contribute to the C_f reduction.

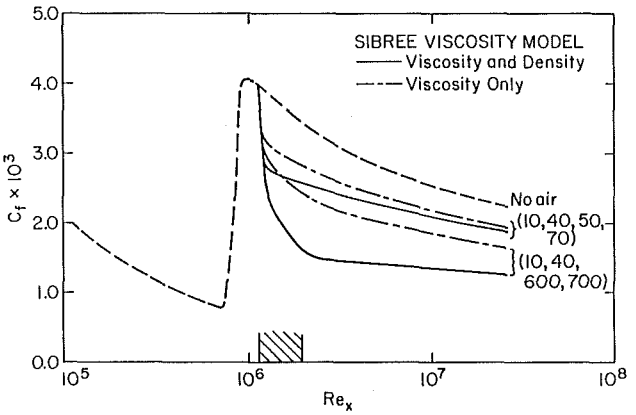

Fig. 9 Comparison of calculations with both the viscosity and the density varying and the viscosity only varying; peak air concentration = 0.5

Effects of Variations in the Peak Concentration. The previous results all corresponded to an initial peak bubble concentration, ϕ_{max}, of 0.50. Figure 10 shows the effects of varying this peak from zero to 0.50. Here the bubble volumetric content is proportionate to ϕ_{max}. These results are based on Sibree's viscosity model and indicate that the sensitivity of the C_f reduction to the presence of bubbles decreases slowly as the peak concentration increases. For example, the incremental reduction in skin friction between the $\phi_{max} = 0$ and 0.05 cases is about the same as that between

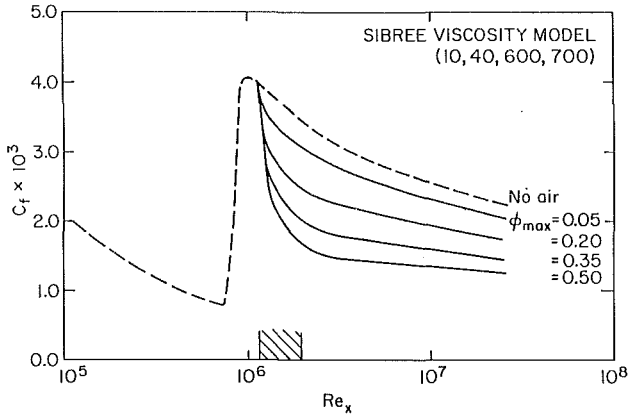

Fig. 10 Effect of variation in peak air concentration

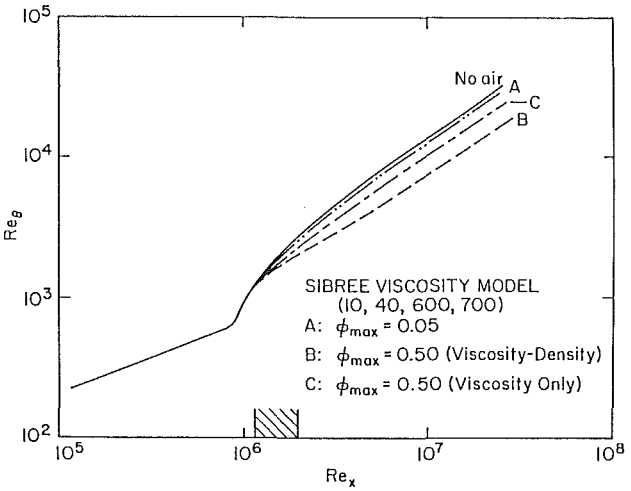

Fig. 11 Effect of microbubbles on the boundary-layer momentum thickness

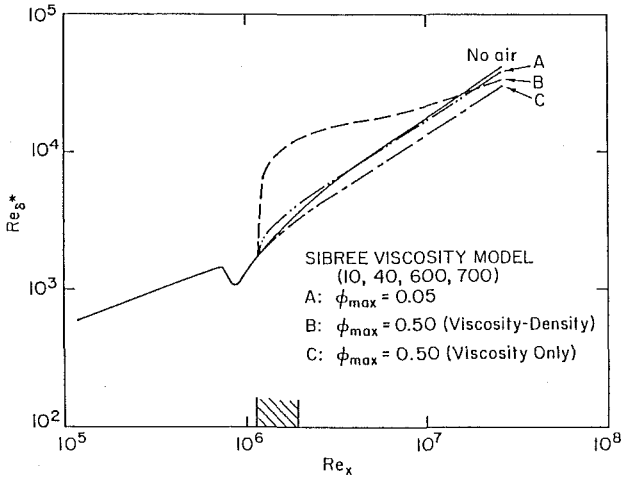

Fig. 12 Effect of microbubbles on the boundary-layer displacement-layer thickness

the ϕ_{max} = 0.35 and 0.50 cases. The calculations presented in Fig. 10 are for a trapezoidal concentration distribution with the inner leg between y^+ = 10 and 40, and the outer leg between y^+ = 700 and 800.

Effects of Microbubbles on Boundary-Layer Integral Parameters. In addition to predicting skin friction, the numerical boundary-layer calculation also provides complete information on the velocity profiles from which the integral parameters of the boundary layer can be obtained. An indication of the manner in which these integral parameters vary when microbubbles are introduced is given in Figs. 11–14. The results of some calculations in which only the viscosity was varied are again included. Similar comparisons for the velocity profiles at one streamwise location are given in Fig. 15. The calculations in these four figures are all for a trapezoidal concentration distribution with vertices at y^+ = 10, 40, 600 and 700.

Figure 11 shows the growth of Re_θ as a function of Re_x. As can be seen, the slope of the $Re_\theta - Re_x$ curve decreases when bubbles are introduced. This change of slope corresponds to the decrease in C_f noted earlier. Some distance downstream, the two curves become nearly parallel. This suggests that one of the effects of introducing microbubbles is to reduce the

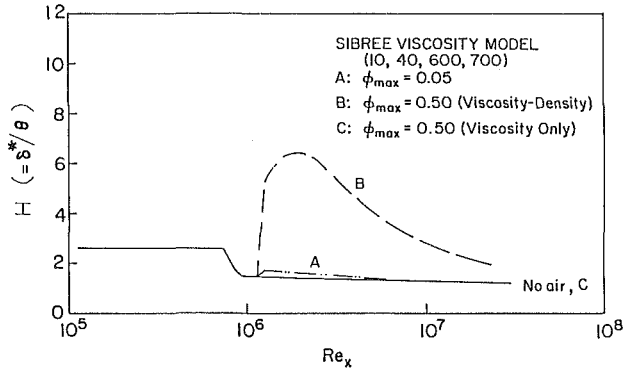

Fig. 13 Effect of microbubbles on the boundary-layer shape factor

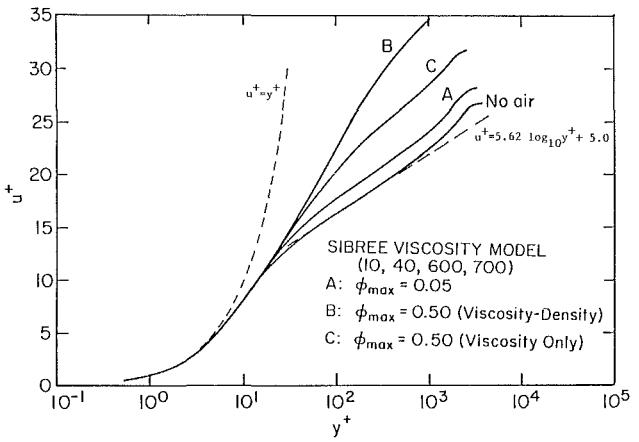

Fig. 14 Effect of microbubbles on the boundary-layer velocity profiles; $Re_x = 4 \times 10^6$

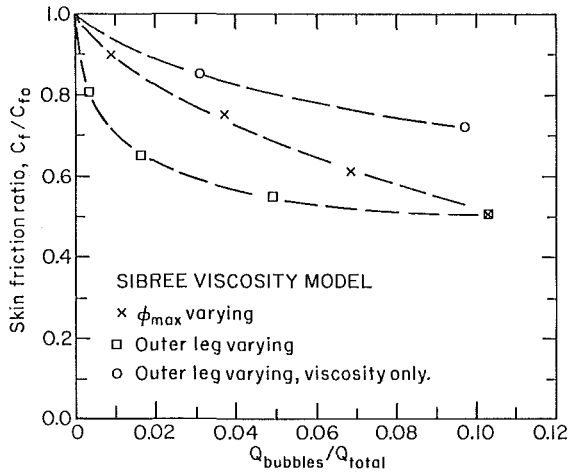

Fig. 15 Variation in the dimensionless skin friction with percent bubble concentration in the boundary layer at $Re_x = 4 \times 10^6$

effective Reynolds number of the boundary layer. The net decrease in θ in the absence of any streamwise pressure gradient also indicates that microbubbles reduce the overall drag. The effect of variations in viscosity only is qualitatively the same as that for variations in both viscosity and density, but exhibits a smaller overall change.

The variations of δ^* which are shown in Fig. 12 are somewhat more dramatic. This figure shows the same cases which were presented in Fig. 11, but here, the density changes cause the value of δ^* to increase rapidly when bubbles are injected. (In the limit, when bubbles are injected at a point, δ^* jumps discontinuously.) This rapid increase is a consequence of the relative densities of air and water. In addition, the calculations show that the increase in δ^* is much larger than the increase in δ. The sensitivity of δ^* to density changes is verified by the viscosity-only calculation. In this case, δ^* is continuous and decreases slightly when bubbles are injected.

The data in Figs. 11 and 12 are replotted again in Fig. 13 as the shape factor, H. This figure shows that the introduction of bubbles increases H locally because of the density change. The shape factor is unchanged for the viscosity only case.

Figure 14 shows the velocity profiles for these cases at one specific x-location ($\mathrm{Re}_x = 4 \times 10^6$). The no-air case, which was presented earlier in Fig. 4 has already been noted to be in agreement with classical data. For low bubble concentrations ($\phi_{\max} = 0.05$), the buffer region grows in thickness. A log-law region is retained but is displaced further away from the wall. As the bubble concentration is increased (to $\phi_{\max} = 0.5$), the thickness of the buffer layer continues to increase and the log region begins to deviate more and more from classical. (Note that both u^+ and y^+ in this figure are based on conditions at the wall, not local conditions.) Similar qualitative observations of increased buffer layer thickness and shifted log law regions have been made for polymer drag reduction based on both experimental and analytical results [10].

Variation of Skin Friction With Fraction of Air in Boundary Layer. The results described earlier have shown how the skin friction and integral properties of the boundary layer are changed by the presence of microbubbles. These results are summarized in Fig. 15 in a format which is analogous to that used by experimenters [1–5]. In this figure, the results of variations in the location of the outer leg of the trapezoidal distribution for the viscosity-density and the viscosity-only cases as well as the maximum concentration variations are shown in terms of the normalized local skin friction versus the fraction of air in the boundary layer. These results are for a Reynolds number of 4×10^6. The four points in the "outer leg varying" curve correspond to the four cases shown in Fig. 7; those for the "$\phi_{\max}$ varying" curve correspond to the four cases in Fig. 10; and those for the "outer leg varying, viscosity only" are from Fig. 9.

Comparison of the outer leg varying with the $\phi_{\max}$ varying curve clearly shows that the location of the bubbles is as important, or more so, than the total volume of bubbles. The effect of increasing air volume by placing air farther and farther out in the outer region of the boundary layer is only minor, as evidenced by both the outer leg varying curves, and supports the statements made earlier that the boundary layer is most sensitive to the presence of bubbles in the inner buffer region. The curve which is most analogous to experimental results (such as those shown in Fig. 1) is the one corresponding to placing the bubbles at fixed location in the boundary layer and varying the peak concentration. This curve indicates that the effect of additional bubbles decreases as the fraction of bubbles in the boundary layer increases. This result is in qualitative agreement with experiment. Note that quantitative comparison with experiment is not currently possible mainly because bubble trajectories are not known. Experiments show, in particular, that many of the injected bubbles do not remain in the boundary layer as they are constrained to do in the computational case.

Finally, we note that Fig. 15 also specifies the volumetric fractions of air of interest. As can be seen, the air content required to attain maximum C_f reduction is nearly 12 percent of the boundary layer, but one-half the maximum reduction can be attained with about one-tenth this amount. These relative changes in air content are again in qualitative agreement with experiment, although as noted earlier the absolute quantity of air which must be added to the experimental boundary layer is considerably higher.

Summary and Conclusions

A model for the effect of microbubbles on the characteristics of a turbulent boundary layer has been formulated and a series of parametric calculations has been presented. Since these represent the first predictions of their kind, emphasis has been placed on maintaining the simplest possible model which remains consistent with the physics. Accordingly, a simple mixing-length eddy-viscosity formulation, whose functional form is unchanged by the presence of bubbles, has been used. The impact of the bubbles on the boundary-layer characteristics arises through changes in the local time-averaged density and viscosity. More sophisticated models can certainly be developed, but the present model is considered appropriate for investigating global effects of the presence of bubbles.

The results of the model show that substantial skin-friction reductions can be obtained when microbubbles are present, thus supporting the idea that microbubbles can act not only as an agent to reduce skin friction, but also as an agent to reduce overall drag. The predictions indicate that skin-friction reductions of as much as 50 percent can be realized. The order of magnitude of this reduction is in keeping with experimental results (where reductions of as much as 80 percent have been noted). Calculations based on two distinct viscosity concentration models result in predictions which are qualitatively similar.

The predictions indicate that the magnitude of skin-friction reduction depends upon the volumetric concentration of the bubbles, and upon their location and distribution in the boundary layer. The bubbles are most effective when they are in the buffer layer. Adding bubbles in the outer region continues to reduce C_f, but large volumes of bubbles are required to obtain small reductions. The presence of bubbles in the sublayer or the absence of bubbles in the buffer layer appears to make the bubbles less effective.

The calculations show that, if a fixed volume flux of bubbles is retained in the boundary layer, the reductions in skin friction can be maintained over long distances. The percent reduction relative to the no-air case, however, continues to decrease with streamwise distance because the entrainment of water at the edge of the boundary layer reduces the volumetric air content to a smaller and smaller fraction.

Since the bubble distribution was specified in the present calculations, the effect of bubbles drifting out of the boundary layer could not be investigated. Further, the influence of bubble size, a phenomenon which is considered to be of importance in experiments, could not be studied. This omission of bubble dynamics is considered to be the most significant shortcoming of the present model.

Acknowledgment

This work was supported by the Office of Naval Research under Grant N00014-81-K-0481.

References

1 Migirenko, G. S., and Evseev, A. R., "Turbulent Boundary Layer With

Gas Saturation," *Problems of Thermophysics and Physical Hydrodynamics* (in Russian), Novosibirsk, Nauka, 1974.

2 Dubnischev, Yu. N., Evseev, E. R., Sobolev, V. S., and Utkin, E. H., "Study of Gas-Saturated Turbulent Streams Using a Laser-Doppler Velocimeter," *J. Appl. Mech. Tech. Phys.*, Vol. 16, No. 1, 1975, p. 114.

3 Bogdevich, V. G., and Malyuga, A. G., "The Distribution of Skin Friction in a Turbulent Boundary Layer in Water Beyond the Location of Gas Injection," in *Investigations of Boundary Layer Control* (in Russian), edited by S. S. Kutateladze and G. S. Migirenko, Thermophysics Institute Publishing House, 1976, p. 62.

4 Bogdevich, V. G., and Evseev, A. R., "Effect of Gas Saturation on Wall Turbulent," in *Investigation of Boundary Layer Control* (in Russian), edited by S. S. Kutateladze and G. S. Migirenko, Thermophysics Institute Publishing House, 1976, p. 49.

5 Madavan, N. K., Deutsch, S., and Merkle, C. L., "Reduction of Turbulent Skin Friction by Microbubbles," *Physics of Fluids*, Vol. 27, No. 2, 1984, pp. 356–363.

6 McCormick, M. E., and Bhattacharyya, R., "Drag Reduction of a Submersible Hull by Electrolysis," *Naval Engineers Journal*, Vol. 85, 1973, pp. 11–16.

7 Silberman, E., "Production of Bubbles by the Disintegration of Gas Jets in Liquid," *Proceedings of the 5th Midwestern Conference on Fluid Mechanics*, University of Michigan, 1957, pp. 263–283.

8 Hughes, N. H., Reischman, M. M., and Holzmann, J. M., "Digital Image Analysis of Two Phase Flow Data," presented at 6th Biennial Symposium on Turbulence, University of Missouri, Rolla, MO, 1979, p. 263.

9 Madavan, N. K., Deutsch, S., and Merkle, C. L., "The Effects of Porous Material on Microbubble Skin Friction Reduction," AIAA-84-0348, AIAA 22nd Aerospace Sciences Meeting, Reno, NE, Jan. 1984.

10 Lumley, J. L., "Drag Reduction in Turbulent Flow by Polymer Additives," *Journal of Polymer Sci.: Macromolecular Reviews*, Vol. 7, 1973, pp. 263–290.

11 Spalding, D. B., "A Model and Calculation Procedure for the Friction and Heat Transfer Behavior of Dilute Polymer Solutions in Turbulent Flow," *Progress in Heat and Mass Transfer*, Vol. 5, 1970, pp. 275–284.

12 Happel, J., and Brenner, H., *Low Reynolds Number Hydrodynamics*, Prentice Hall, Inc., Englewood Cliffs, NJ, 1965, pp. 438–443.

13 Jones, R. T., "Blood Flow," *Annual Review of Fluid Mechanics*, Vol. 1, 1969, pp. 223–243.

14 Happel, J., and Brenner, H., *Low Reynolds Number Hydrodynamics*, Prentie Hall, Inc., Englewood Cliffs, NJ, 1965, pp. 443–471.

15 Sibree, J. O., "The Viscosity of Froth," *Transactions of the Faraday Society*, Vol. 30, Pt. II, 1934, pp. 325–331.

16 McDonald, H., and Camarata, F. J., "An Extended Mixing Length Approach for Computing the Turbulent Boundary Layer Development," *Computation of Turbulent Boundary Layers—1968 AFOSR-IFP—Stanford Conference*, Vol. 1, S. J. Kline, M. V. Morkovin, G. Sovran and D. J. Cockrell, editors, Stanford University Press, 1969, pp. 83–98.

17 Price, J. M., and Harris, J. E., "Computer Program for Solving Compressible Boundary Layer Equations of a Perfect Gas," NASA TM X-2458, Apr. 1972.

18 Merkle, C. L., "Stability and Transition in Boundary Layers," *Flow Research Report 71*, Flow Research, Inc., Kent, WA, June 1976.

19 Merkle, C. L., Tzou, K. T-S, and Kobota, T., "An Analytical Study of the Effect of Surface Roughness on Boundary-Layer Stability," *Dynamics Technology Report DT-7606-4*, Dynamics Technology Inc., Torrance, CA, Oct. 1977.

20 White, F. M., *Viscous Fluid Flow*, McGraw-Hill, Inc., New York, NY, 1974, pp. 468–505.

Wake Flow Stabilization by the Action of Base Bleed

H. Y. Wong
Reader,
Department of Aeronautics and Fluid Mechanics,
University of Glasgow,
Glasgow G128QQ, Scotland

Experimental investigation into the effects of base bleed on wake stabilization for the suppression of flow-induced oscillation has shown that when the bleed flow rate is increased, the initial vortices are formed downstream, thus constituting the main cause of the removal of vortex excitation from the body which has produced them. Base ejections, if unsuitably placed, however, could aggravate oscillation. In wake buffeting, the situation can be greatly improved if base bleed is introduced from the downstream body but not from the upstream body.

Introduction

The flow of fluid around a bluff body is essentially dominated by the generation of vortices resulting in a periodic wake and a number of undesirable consequences such as high form drag, vortex-induced oscillation and wake buffeting. Slender structures with bluff sectional shapes are particularly sensitive to these types of adverse effect. For the purpose of suppressing vortex-induced oscillation, various aerodynamic damping devices have been developed among which the one known as the "slat device" has been found effective by experiment and under working conditions in air as well as in water [1–6]. This device consists of a number of slats which are placed longitudinally around the periphery of the structure. They are fixed at a predetermined distance from the body surface and have regular openings between them through which fluid flow takes place. One of the features influential in reducing drag and in suppressing vortex-induced oscillation was found to be the ejection of fluid between the slats at the rear part of the body [7]. The discovery of a large drag reduction by means of ejecting fluid at small flow rate into the wake region of the base of the body, known as "base bleed," has inspired studies on the subject of drag reduction on blunt-based bodies at transonic and supersonic speeds [8–9] and at low subsonic speeds [10, 11]. However, very little publication has been cited on any investigation into the effects of base bleed on wake stabilization for suppressing vortex-induced oscillation and on wake buffeting. The present experimental study has, therefore, been conducted along this line of inquiry using circular cylinder models in a water channel and a wind tunnel. The preliminary findings were reported at a Euromech meeting in Berlin [12].

Experiment

Experiment using a water channel—the purpose of this experiment was to study the effects of base bleed on the oscillatory behavior of an isolated cylinder model and on the buffeting phenomena of a cylinder model placed directly downstream of another identical model. The water channel, 5.5-m long, 14-cm deep and 14-cm wide, had a closed circuit pumping system, a reservoir at one end, and a dumping tank at the other end. The mean stream velocity, measured with a current flow meter at the furthest quarter of the tank, was controlled by the pumping speed of the motor and by a sluice at the exit of the tank. At the inlet, the channel was attached to a three-dimensional flow guide extending into the reservoir with a contraction ratio of about 16 to 1. An additional aid to smoothing out the flow was provided by a section of honeycomb, 15-cm long, made of wax impregnated paper inserted at the inlet of the channel. No attempt was made to measure the turbulence level of the flow.

At the working section halfway along the channel, the test model, a hollow circular cylinder of 1.9-cm dia and made of brass, was suspended vertically downward on gimbals with its lower end just clear of the channel floor. In operation, only three-quarter of the model's length was immersed in the water giving a working length-to-diameter ratio of about 6 with a 15 percent blockage. Along the rear central line of the model a slit of 0.2 mm in width was provided for base ejection, and in this case, water was used and it was supplied by gravity from a separate water tank. An orifice flow meter was incorporated for measuring the flow rate of ejection. During testing, the model was allowed to oscillate freely or to oscillate against the constraint of springs which were selected to simulate different natural frequencies for the oscillation system. Measurement of crossflow amplitude of oscillation was by means of a capacitance-type of displacement transducer through a vibration meter and a potentiometric recorder. Facilities were provided with highly sensitive load cells for measuring the transient forces (lift and drag components) to be carried out at a later date.

The use of water as a flow medium is also convenient for flow visualization. In the present experiment, dyes of two different colors were used, one being injected into the undisturbed stream ahead of the model and the other into the bleed fluid prior to its entering into the model.

For wake buffeting study, two identical models of dimensions described earlier, were used in a tandem arrangement. The downstream model was allowed to oscillate while the upstream model was held stationary. Base bleed was applied to one or the other of the models but not to both

Contributed by the Fluids Engineering Division for publication in the JOURNAL OF FLUIDS ENGINEERING. Manuscript received by the Fluids Engineering Division, December 15, 1983; final revision, March 1985.

simultaneously. Measurements of the oscillation amplitude were taken from the downstream body only for various spacings between the two models at different base-bleed rates.

In all cases, the stream velocity was gradually increased until the amplitude of oscillation of the test model had attained its maximum magnitude before base bleed was applied. Thereafter the stream velocity was held constant while the bleed flow rate was being changed. The stream Reynolds number for maximum oscillation with zero base bleed varied beween Re = 2000 and Re = 3000.

Experiment Using a Wind Tunnel. The purpose of this experiment was to observe the effects of the base bleed location on the oscillation behavior of an isolated cylinder model. The wind tunnel used has a working section of width 1.14 m and height 0.84 m and it has a maximum flow speed of about 30 m/s. The test model was the model originally used to study the effects of the slat device on vortex suppression [3] which consisted of a basic cylinder of diameter d = 7.6 cm surrounded by 28 longitudinal slats evenly disposed at a distance of 1.1 cm from the surface of the cylinder. By blocking off the openings between the slats and by allowing two such openings at the rear part of the model to remain open and by removing some slats at the front part of the original model, airflow during test could be admitted through a larger frontal opening to flow round the basic cylinder and emerge as base bleed from the two smaller openings at the rear. The cross section of the modified model, as shown in Fig. 1, had a frontal opening angle of either $\theta_1 = 15°$ (Model I) or $\theta_1 = 30°$ (Model II) and the rear opening angle each of $\theta_2 = 5°$. The location of the symmetrically placed rear openings is designated by the angle β so that at $\beta = 0$, the two rear openings are combined into one opening with $\theta_2 = 5°$. This model, tested to linear-mode oscillation, was mounted vertically in the wind tunnel with gimbals at its base. It had a length-to-diameter ratio of about 8, giving a 7.4 percent blockage. Its motion was restrained by four springs of equal stiffness, at right angles to each other. The amplitudes of oscillation were measured in the crossflow direction. The rate of base bleed was self-regulating according to the stream velocity and the size of the frontal opening on which the dynamic pressure acted. Thus it may be supposed that a stronger bleed rate can result from a larger frontal opening. The test stream Reynolds number at which the model attained its maximum amplitude of oscillation varied between Re = 10^4 and Re = 2.5×10^4.

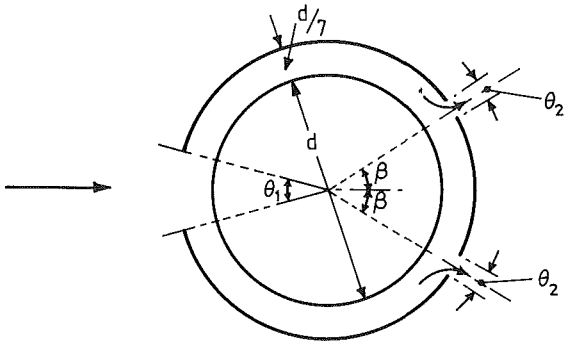

Fig. 1 Cross section of test model used in wind tunnel, d = 7.6 cm, D = (1 + 1/7)d, $\theta_2 = 5°$

Results

The experimental results are grouped into three categories, namely, oscillation of a single cylinder tested in water (Figs. 2, 3), wake buffeting of a downstream cylinder tested in water (Figs. 4, 5) and oscillation of a single cylinder tested in air (Fig. 6). In the first two items, the oscillation behavior of the cylinder model was examined with respect to the bleed rate whereas in the third item, the degree of aerodynamic instability of the model was observed according to the location of the base-bleed openings.

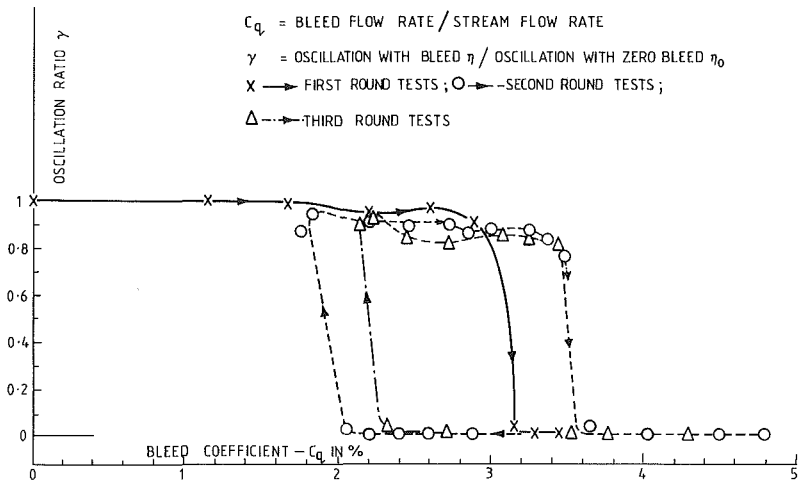

Fig. 2 Variation of oscillation with base bleed at Re = 2650

Nomenclature

A_f = projected frotal area of cylinder model = Dl
C_q = bleed coefficient = Q_b/Q_s
D = overall diameter of model
l = length of model immersed in fluid stream
L = length of splitter plate
N = oscillating frequency of model
Q_b = bleed flow rate
Q_s = stream flow rate = $A_f V$
Re = Reynolds number = VD/ν
V = free-stream mean velocity
V_r = reduced velocity = V/ND
ν = kinematic viscosity of fluid
θ_1 = angle representing the size of model frontal opening
θ_2 = angle representing the size of bleed fluid opening
β = angle marking the location of bleed ejection
η = model tip amplitude of oscillation divided by model diameter D with base bleed
η_0 = model tip amplitude of oscillation divided by model diameter D with zero base bleed
$\gamma = \eta/\eta_0$

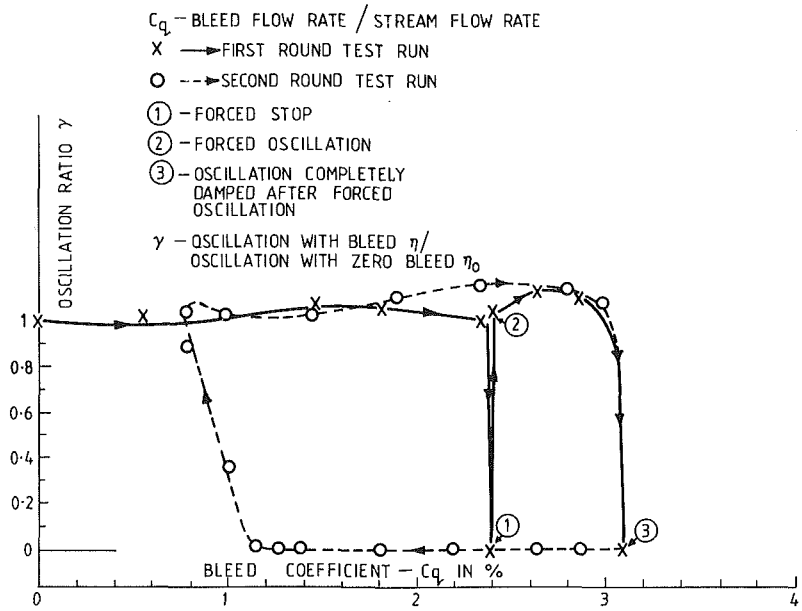

Fig. 3 Variation of oscillation with base bleed with forced stop and forced oscillation at Re = 2790

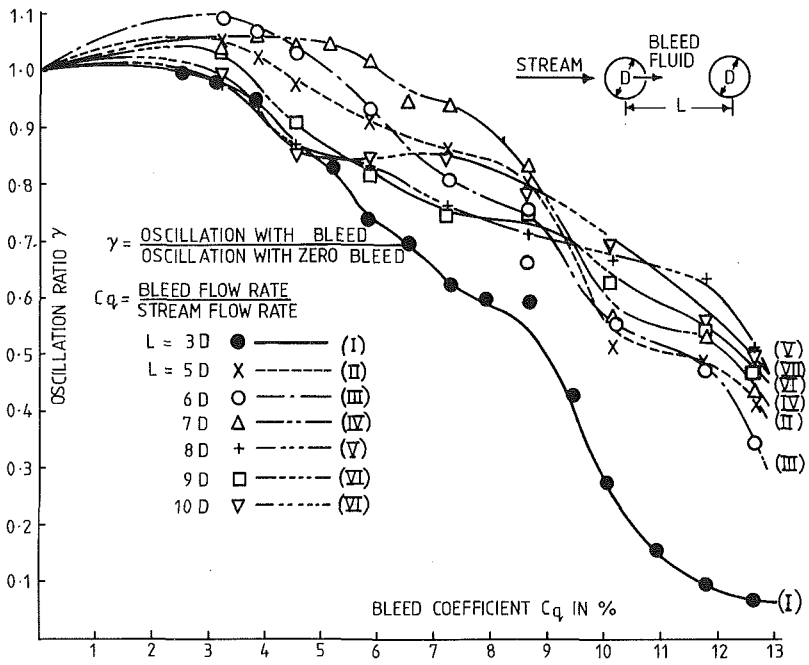

Fig. 4 Effect of base bleed issued from upstream body on wake buffeting at Re ≃ 2100

In these experiments, the certainty of the results is influenced by many factors. For example, models tested in water are affected by the added mass, by the hydrodynamic viscous damping and by the depth of the model's immersion in the water; models tested in air are affected by the model's end effects and its dimensions regarding the exact size, shape and location of the bleed fluid openings. Furthermore, the level of turbulence in the stream and the model surface roughness as well as the blockage effects may play some part in influencing the results. In order to avoid the complication of assessing the inherent damping in each model system and the difficulty of obtaining a reliable blockage correction for a surface piercing bluff body in order to judge the absolute values of each case, it was decided to present the results on a comparative basis to show the essential physical trends of the effects of base bleed. Thus the oscillatory behavior of the model is represented by a tip oscillation ratio $\gamma = \eta/\eta_0$ where η is the nondimensional oscillation amplitude with base bleed and η_0 without base bleed. The uncertainty estimate is ± 5 percent on the tip oscillation ratio, and ± 12 percent on bleed coefficients.

The oscillation behavior of a single cylinder model in water flow is shown against the bleed coefficient C_q defined as the bleed flow rate Q_b divided by the stream flow rate Q_s. The influence of this parameter on the wake flow has been found to be consistent irrespective of the stream velocity by a power spectral analysis of flow velocity measurements using a hot-wire anemometer [13]. In Fig. 2, three rounds of tests were made showing an upper limit value of C_q above which no oscillation can occur and a lower limit value below which base

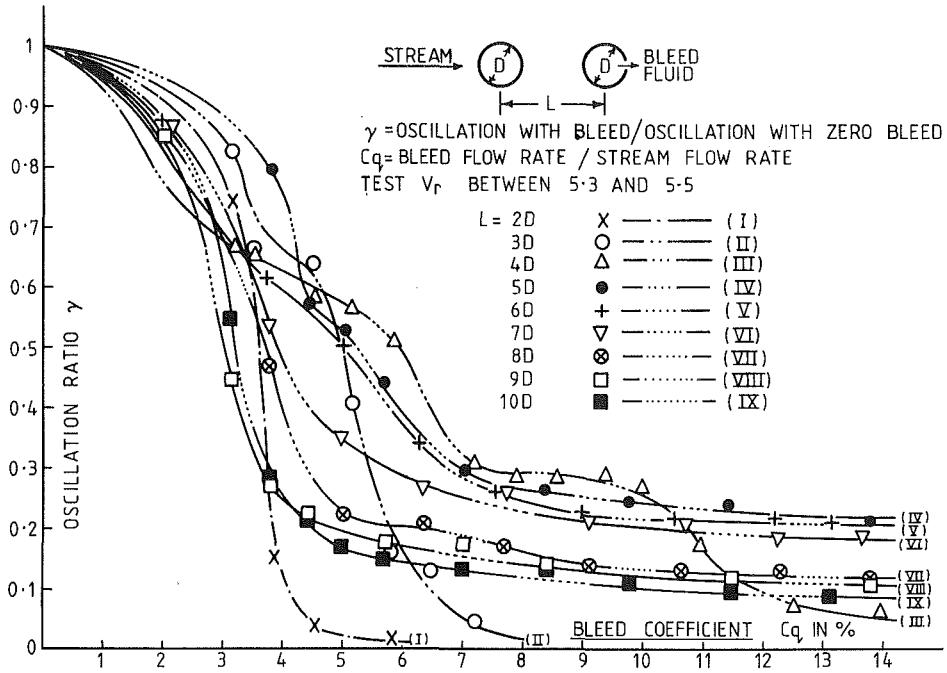

Fig. 5 Effect of base bleed issued from downstream body on wake buffeting at Re ≃ 2200

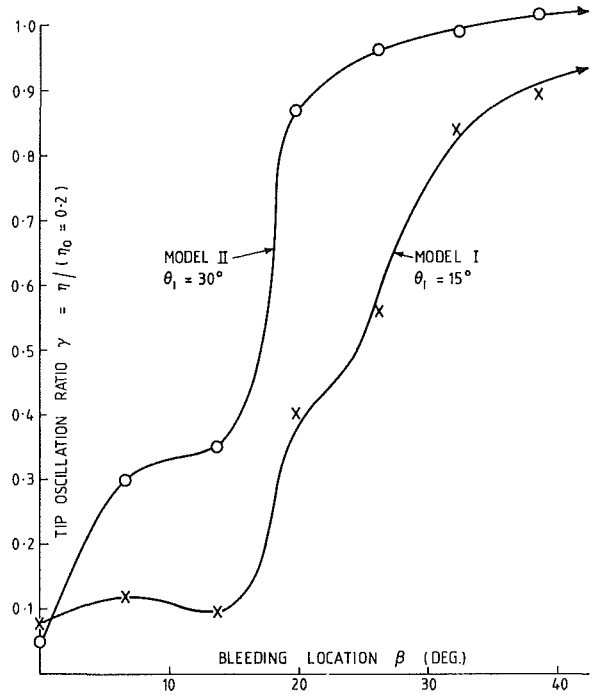

Fig. 6 Effect of base-bleed location on oscillation of model tested in wind tunnel at Re range between 10^4 and 2.5×10^4

bleed becomes ineffective. Between these two limits there lies a region with strong hysteresis effects which prohibits any rational relationship to be observed between the oscillation amplitude and the quantity representing the base-bleed rate. It will be seen in Fig. 3 that within this region the oscillating model if forced to stop oscillating will remain stationary even if the applied force is removed. But once disturbed, it will resume its oscillating motion again. After many test runs, it has been possible to observe that when an upper value of the base-bleed coefficient C_q is reached, the suppression of oscillation is fully effective. This interesting phenomenon will be discussed later.

In Fig. 4, the oscillation of the downstream model due to wake buffeting is plotted against the bleed coefficient C_q for various spacings between the two models when the base-bleed fluid issues from the upstream model. The oscillation amplitude of the downstream model appears to be aggravated by fluid ejection from the upstream model for small C_q-values. Not until the C_q-value has reached a certain quantity (about $C_q = 5$ percent in the present case) can oscillation improvement become to emerge. Even so, a base-bleed rate of as high as $C_q = 12$ percent was required to achieve a 50 percent improvement. With the base-bleed fluid being ejected from the downstream model, however, a noticeable improvement occurred at relativley small values of C_q (Fig. 5). Buffeting was found to improve rapidly at a C_q-value of about 4.5 percent. But the rate of improvement became quite insignificant when the value of C_q was increased beyond 8 percent.

The effects of the base-bleed location are shown in Fig. 6. The tip oscillation ratio γ is the nondimensional amplitude η divided by a reference value of $\eta_0 = 0.2$. From the results, it can be seen that oscillation of the model is increased with the increasing value of β (see Fig. 1). For $\beta = 0$, Model II (for $\theta_1 = 30°$) appeared to have experienced less oscillation than Model I for $\theta_1 = 15°$), indicating that a stronger bleed, which may be beneficial if issuing from the central base line, can cause greater instability. The rapid increase of oscillation with increasing β in both models may suggest that, with a greater bleed velocity component normal to the free-stream direction when the bleed location is moved toward the sides of the cylinder, early flow separation may result and stronger vortices may be encouraged to form close to the body.

Flow Visualization

The flow visualization was applied only to the oscillation experiment using one cylinder model in the water channel. Dye of two colors was used. Photographic pictures of the wake flow at various bleed flow rates were taken with the model being held stationary. These pictures, though not very detailed, have revealed the change of the wake flow structure in relation to the oscillatory behavior of the model. The black and white pictures shown in Fig. 7 were reproduced from

some of the original color pictures. Although the camera used was unable to capture the continuous process of the flows, these pictures do show how the wake flow was modified by the presence of the bleed fluid. As the bleed flow rate was increased, the vortex formation length, defined as the distance from the body at which initial vortices are formed, increased also so that at bleed coefficient of $C_q \simeq 5$ percent in the present case, the stabilized area was extended to almost 6 dia downstream. Any further increase of the bleed rate increased the length only slightly. The oscillation tests have shown that complete suppression of vibration could be achieved when the C_q-value reaches an upper limit, which wsas about 3.4–4 percent in the present experiment (may be less if the blockage correction for stream velocity were taken into account). At this value, the stabilized wake was observed to have extended to 3 dia downstream. A wake study in a wind tunnel by means of a hot-wire anemometer has confirmed that the narrow-band frequency peaks of the power spectrum were removed from the wake close to the body when an upper critical value of the bleed coefficient was reached as reported in reference [13].

Discussion

As the base bleed can reduce the drag of a bluff body by raising the base pressure brought about by delaying the formation of vortices further downstream, the same flow mechanism is expected to be responsible for the suppression

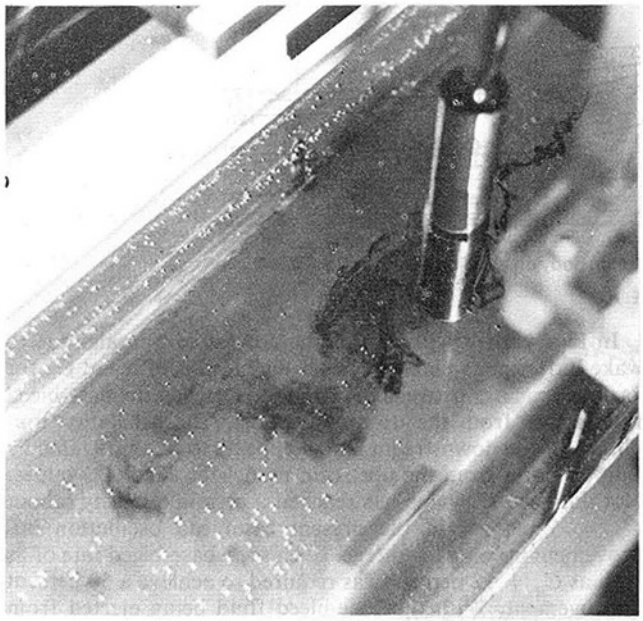

(a) $C_q = 0$

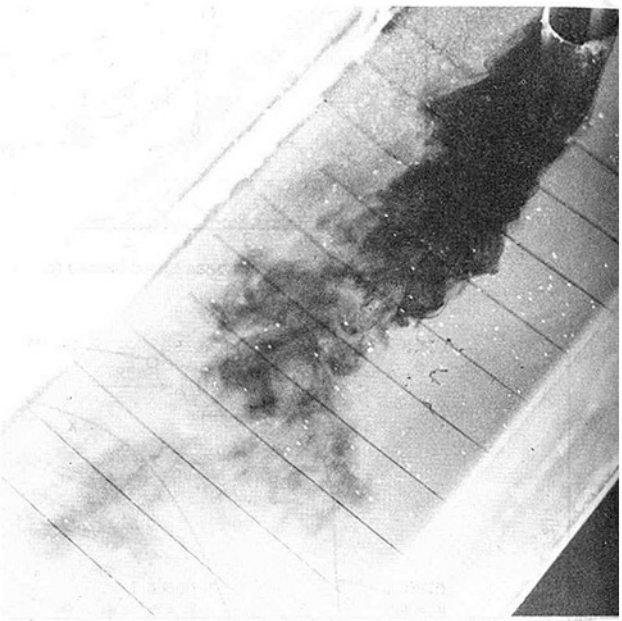

(c) $C_q = 2.5\%$

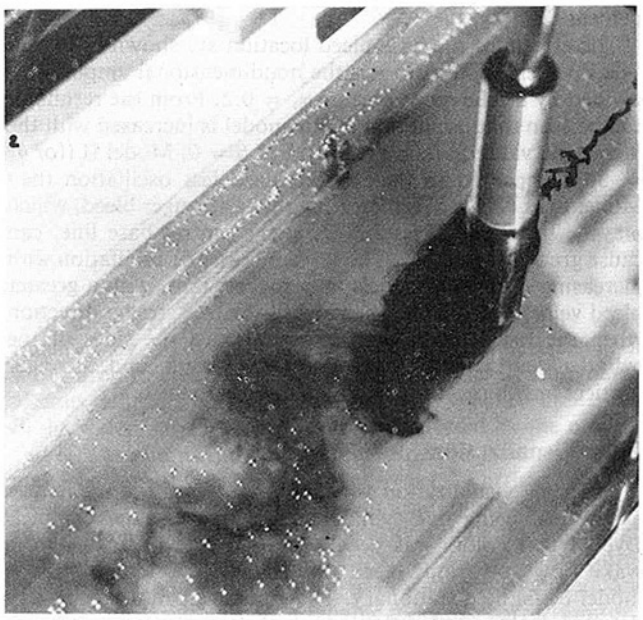

(b) $C_q = 1.5\%$

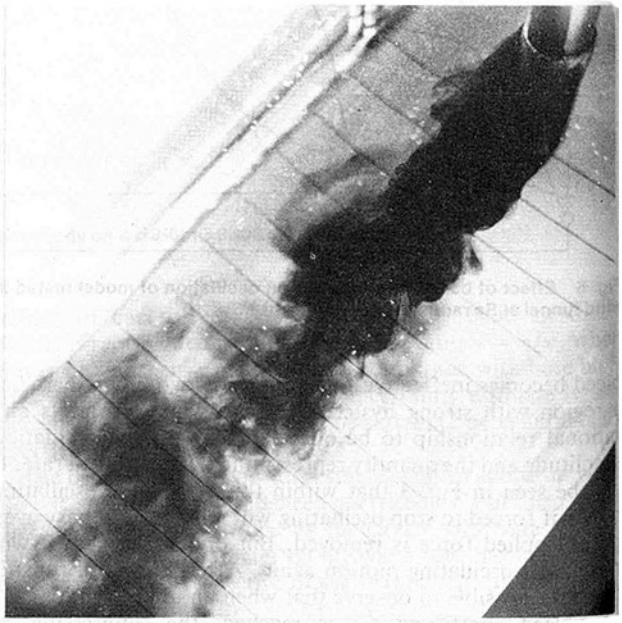

(d) $C_q = 3\%$

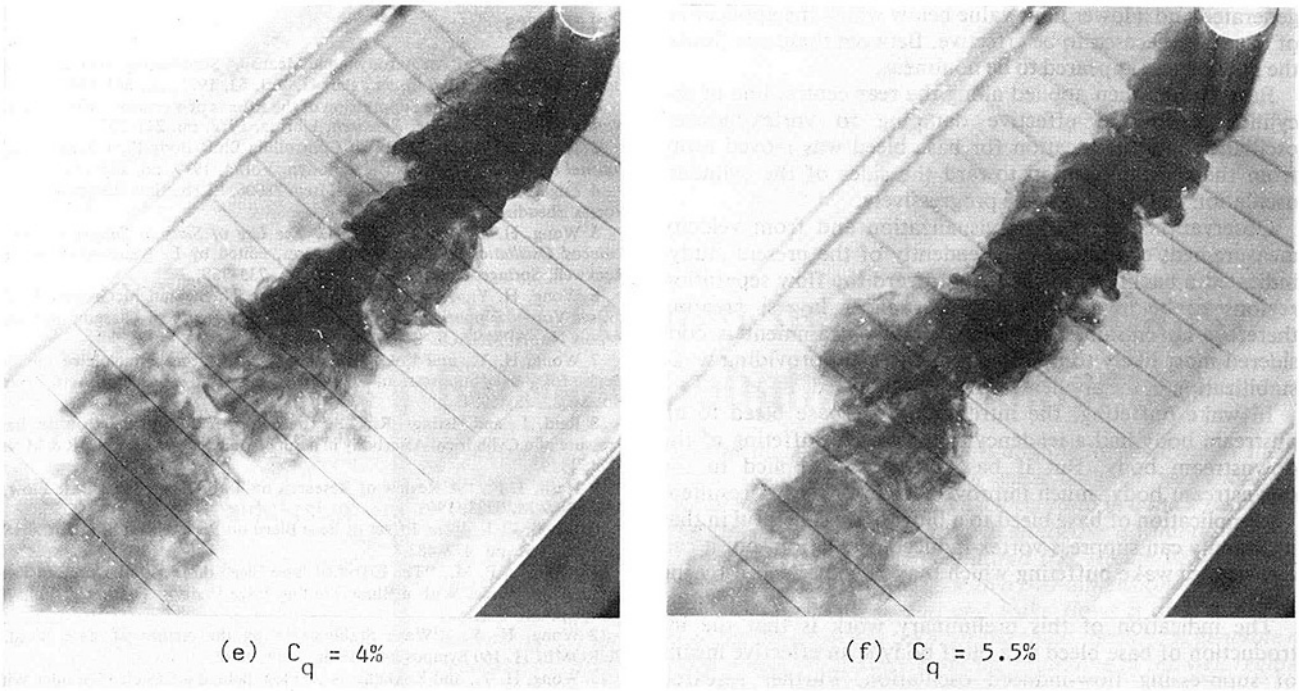

Fig. 7 Photographic pictures of wake flow at various bleed flow rates, at Re = 1800

of vortex-induced oscillation. The interference of the base-bleed fluid with the periodic wake can be deemed to be the cause of wake stabilization through flow entrainment. Observation, from flow visualization and from velocity measurements [13], has revealed that the bleed fluid after emerging from the bleed slot is drawn forward toward the separation region to be mixed with the free shear layers, supplying therefore the necessary fluid for the growth of the vortices. This being so with adequate fluid entrainment in action, there is seemingly no longer the need for one shear layer to interact with another across the wake at least in this near-wake region. However, the shear layers are basically unstable and they have the tendency to roll up into vortices at some distance downstream. When this happens, as shown in Fig. 7, the wake takes on an oscillatory movement with, perhaps, slightly greater vigor on account of the added energy from the base-bleed fluid. This may explain the increased severity of wake buffeting when base bleed is applied to the upstream body only and when the downsteam body is situated beyond the stabilized wake region (Fig. 4). On the other hand, steady wake if formed from a downstream body can help toward the reduction of buffeting, even though the oncoming flow may be from an oscillating wake generated by an upstream body (Fig. 5). The situation may be quite different if the upstream body is allowed to oscillate. This aspect of the problem is presently under investigation.

If fluid entrainment plays a part of primary importance in stabilizing an oscillating wake, it may be considered that the required entraining fluid is more likely to be associated with the fluid mass introduced at the base of the body than with the ejecting velocity. If it were the reverse, gradual damping out of oscillation would be expected to take place with increasing bleed velocity. The power spectrum measurement reported in reference [13] showed that the formation of the peak values usually associated with narrow-band energy concentrations was not, as expected, delayed in terms of distance from the cylinder model by base ejection. Their intensities over the whole near-wake, however, were reduced gradually by the increase of the bleed rate. When a certain minimum bleed rate was reached (C_q = 2–3 percent in the present case), the spectral peaks disappeared altogether.

The action of base bleed for suppressing vortex formation may appear to be like that of a splitter plate placed behind a bluff body with the critical bleed rate in the base-bleed case comparable to the length-to-diameter ratio of $L/D = 5$ in the case of a cylinder with a splitter plate [14]. Though the end results of both cases are similar, the flow controlling mechanisms need not be the same. With the splitter plate, the crossflow tendency in the wake is prevented by the physical intervention of the plate itself which if long enough can also promote flow reattachment, resulting in the bluff body being modified into a somewhat streamlined body. In the base-bleed scheme, however, the flow field in the near-wake is fluid-dynamically modified by the bleed fluid, the consequence of which is to remove the tendency of the shear layers to react with each other across the wake. Unlike the splitter plate, base bleed does not seem to provide a streamlining effect to the cylinder. Even with the applied bleed rate greater than the critical minimum rate for total suppression of vortex-induced oscillation, a well-developed vortex street was found to form 6–7 dia downstream from the cylinder model. The results of the buffeting tests (Fig. 4) in some way lent support to this observation. As base bleed can effectively modify the flow field around the body base, it follows that this is also a more effective means of reducing the pressure drag of a bluff body than a splitter plate. The force measurements which are presently in progress will be able to verify this point. As the use of a long splitter plate is in many ways impracticable, the application of base ejection would appear to offer an attractive proposition.

Conclusions

The effects of base bleed on flow-induced oscillation have been investigated. The test results indicated that a small quantity of bleed flow rate was sufficient to suppress the oscillation completely. There was an upper limit value of the bleed coefficient above which no oscillation could be

generated and a lower limit value below which the application of base bleed ceased to be effective. Between these two limits, the phenomena appeared to be nonlinear.

Base bleed, when applied along the rear central line of the cylinder, provided effective damping to vortex-induced oscillation. As the location for base bleed was moved away from the central position toward the sides of the cylinder, oscillation tended to increase progressively.

Observations, from flow visualization and from velocity measurement conducted independently of the present study, indicated a backflow of the fluid toward the flow separation regions to be mixed with the free shear layers, creating therefore an entrainment action. Fluid entrainment is considered most likely to be the major factor in providing wake stabilization in the application of the base bleed.

In wake buffeting, the introduction of base bleed to an upstream body had a tendency to aggravate buffeting of the downstream body. But if base bleed was applied to the downstream body, much improvement in buffeting resulted. The application of base bleed to a bluff body is helpful in that it not only can suppress vortex-induced oscillation, but it can also reduce wake buffeting which may be experienced by the body itself.

The indication of this preliminary work is that the introduction of base bleed to a bluff body is an effective means of suppressing flow-induced oscillation. Further research work may be profitably conducted to investigate its fundamental mechanism in separated flow control and in wake stabilization so that appropriate systems can be developed for application to external as well as internal flows.

References

1 Wong, H. Y., "An Aerodynamic Means of Suppressing Vortex-Induced Oscillation," *Proc. Civil Engrs.*, Part II, Vol. 63, 1977, pp. 693–699.

2 Wong, H. Y., "The Suppression of the Effects of Vortices," *Proc. 3rd US National Conf. Wind Eng. Research*, Florida, 1978, pp. 241–252.

3 Wong, H. Y., "A Means of Controlling Bluff-Body Flow Separation," *Journal of Wind Eng*, Industrial Aerodyn. Vol. 4, 1979, pp. 183–201.

4 Engineering Science Data Unit, Item 78006, "Crossflow Response Due to Vortex Shedding," 1978.

5 Wong, H. Y., and Cox, R. N., *The Use of Slats to Suppress Vortex-Induced Oscillation of Slender Structures*, edited by E. Naudascher and D. Rockwell, Springer-Verlag, N.Y., 1980, pp. 735–738.

6 Wong, H. Y., Ferguson, A. M., Miller, N. S., and McGregor, R. C., "Riser Vortex Suppression by Slat Device," University of Glasgow Research Report No. AFMNAOE-BGC-7901, May 1979.

7 Wong, H. Y., and Kokkalis, A., "The Operating Principle of the Slat Device for Vortex Suppression," University of Glasgow Reaearch Aero Report No. 8402, May 1984.

8 Reid, J., and Hstings, R. C., "The Effect of a Central Jet on the Base Pressure of a Cylindrical Afterbody in a Supersonic Stream," ARC, R & M No. 3224, 1959.

9 Nash, J. F., "A Review of Research on Two-Dimensional Base Flow," ARC, R & M, 3323, 1963.

10 Wood, C. J., "The Effect of Base Bleed on Periodic Wake," *J.R.Ae.S.*, Vol. 68, 1964, pp. 477–482.

11 Bearman, P. M., "The Effect of Base Bleed on the Flow Behind a Two-Dimensional Model With a Blunt Trailing Edge," *Aero. Quarterly*, Vol. 18, 1967, pp. 207–244.

12 Wong, H. Y., "Wake Stabilization by the Action of Base Bleed," EUROMECH. 160 Symposium, Berlin, Sept. 1982.

13 Wong, H. Y., and Kokkalis, A., "Flow Behind a Circular Cylinder With Base Bleed," University of Glasgow Aero Report No. 8403, June 1984.

14 Apelt, C. J., West, G. S., and Szewczk, A., "The Effects of Wake Splitter Plates on the Flow Past a Circular Cylinder in the Range of $10^4 < Re < 5 \times 10^4$, Part I," *Journal of Fluid Mechanics*, Vol. 61, 1973, pp. 187–198; Part II, *Journal of Fluid Mechanics*, Vol. 71, 1975, pp. 145–160.

Earl Logan

Shu Ho Lin

Obaidul Islam

Mechanical and Aerospace Engineering Department,
Arizona State University,
Tempe, AZ 85287

Flow Formed by Spanwise Gaps Between Roughness Elements

Measurements of the three mean velocity components and the three Reynolds shear stresses were made in the region downstream of gaps between wall-mounted roughness elements of square cross section and high aspect ratio in a thick turbulent boundary layer. The effect of small and large gaps was studied in a wind tunnel at a Reynolds number of 3600, based on obstacle height and free-stream velocity. The small gap produces retardation of the gap flow as with a two-dimensional roughness element, but a definite interaction between gap and wake flows is observed. The interaction is more intense for the large gap than for the small. Both gaps generate a secondary crossflow which moves fluid away from the centerline in the wall region and toward the centerline in the outer ($y > 1.5H$) region.

Introduction

The present work is an experimental study of the effect of the removal of a small portion of a two-dimensional rib-type roughness element on the resulting wake flow behind the two remaining parts of the roughness element and the gap formed by the removal. The laboratory wakes thus studied simulate those formed in the space between two long (high aspect ratio) buildings arranged transversely in the wind or between two transverse ribs mounted on a plane or curved surface and used as artificial roughness elements for the enhancement of turbulent mixing in a flow. Surface-obstacle wakes are of interest in wind engineering, wind-energy-system siting and aviation flight safety. Roughness elements in heat exchangers and combustors are used to promote increased rates of gradient heat and mass transfer and of large-eddy mixing of nonhomogeneous fluids. Knowledge of fluid motion around such elements is vital to an understanding of these transport processes.

The effect of a gap in a roughness element on the centerline flow behind the gap has been reported by Schofield, Barber, and Logan [1]. Centerline skin-friction coefficients were found to dip to very small values downstream of the gap, but no separation zone was observed. Although flow acceleration in the gap itself occurred in gaps of all sizes, the downstream position of the ensuing deceleration depended on the gap width, i.e., the process occurred farther downstream for the larger gaps. Correspondingly, the downstream location in the wake of turbulence-intensity rise depended strongly on gap width. The rise occurred in the gap for the smallest gap size ($0.5H$) and several element heights downstream for the larger gaps. The present work has for its objective an elucidation of the nature of the interaction between the wakes at the two sides of the gap flow and the central portion of the flow downstream of the gap itself.

To accomplish the objective previously given, measurements were made at three off-centerline positions as well as at positions on the centerline. To gain insight into the interaction between the wakes, it was necessary to measure transverse and lateral components of the mean velocity as well as the longitudinal component. To quantify the interaction between the wakes it was also necessary to measure all of the Reynolds shear stresses. Surface flow visualization was used to delineate the boundaries of the separated flow regions and to locate the critical points on the surface in the interaction region.

Investigations of two and three-dimensional wakes behind surface-mounted obstacles have been reported by Hunt [2], Bradshaw and Wong [3], Counihan, Hunt, and Jackson [4], Castro [5] and Schofield, Lin, and Logan [6]. The results of surface flow visualization on and around surface-mounted obstacles and the characteristics of critical points observed by flow visualization are presented by Hunt, et al. [7] and by Castro and Dianat [8].

Experimental Work

Measurements of mean velocity components and Reynolds shear stresses were made in the region downstream of a gap formed between two wall-mounted, bar-type roughness

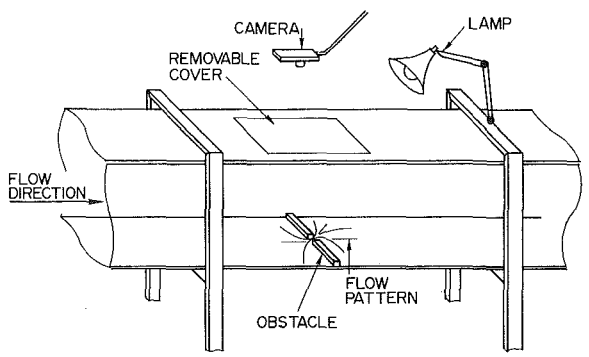

Fig. 1 Flow visualization arrangement

Contributed by the Fluids Engineering Division for publication in the JOURNAL OF FLUIDS ENGINEERING. Manuscript received by the Fluids Engineering Division, May 29, 1984; final revision, April 1985.

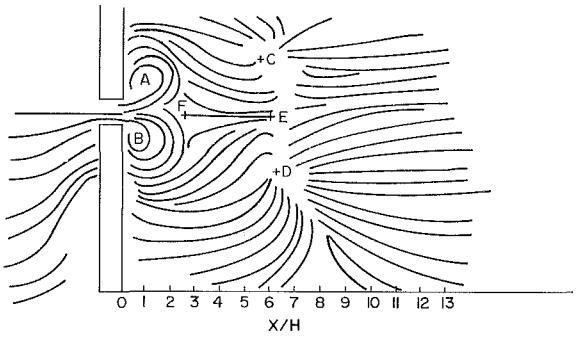

Fig. 2(*a*)

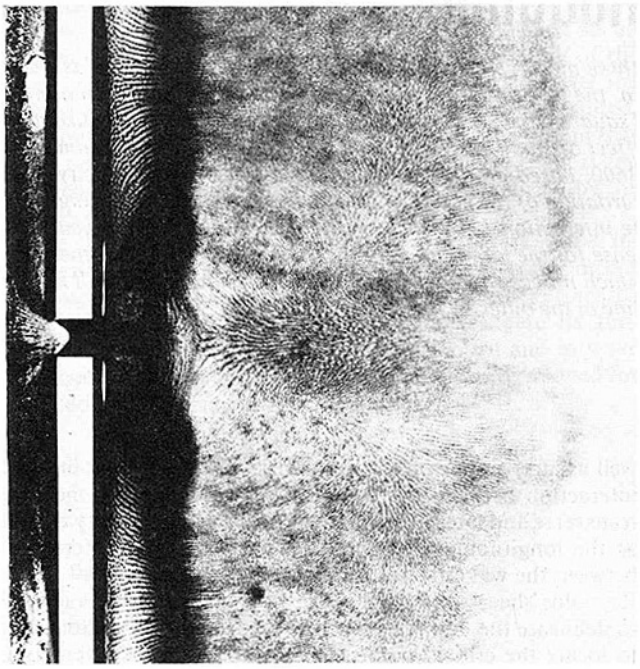

Fig. 2(*b*)

Fig. 2 Surface flow patterns for gap = 1.0*H*

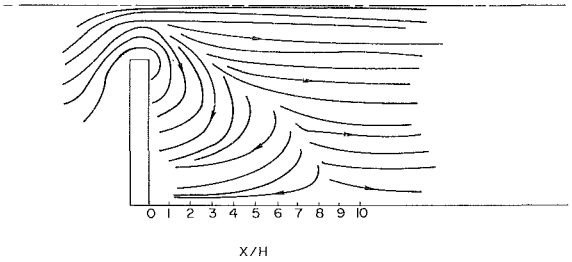

Fig. 3(*a*)

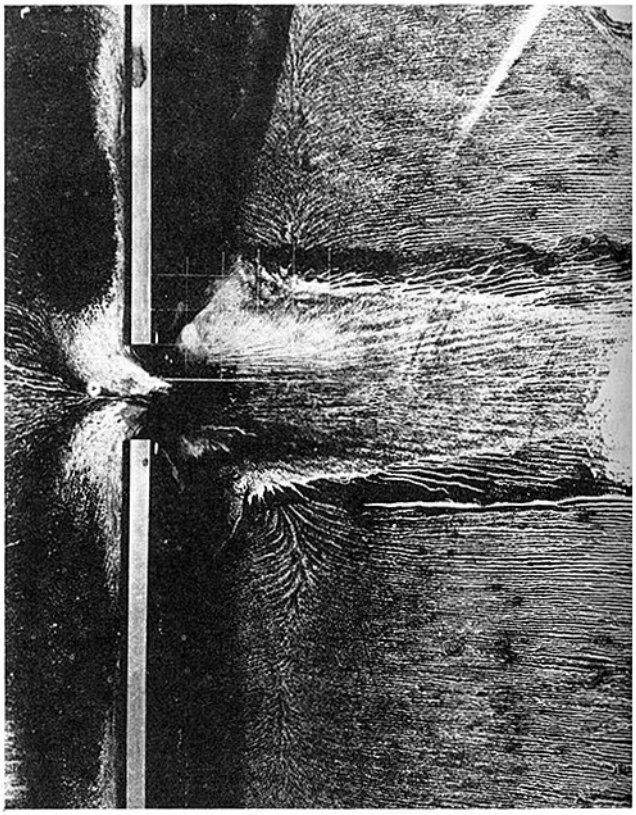

Fig. 3(*b*)

Fig. 3 Surface flow patterns for gap = 5.0*H*

elements of rectangular cross section located in a thick ($\delta \approx 10$ H) turbulent boundary layer. The height H and width W of the roughness elements were 8.38 mm, and the two elements were mounted transversely to the air flow on the floor of a wind tunnel. The wind tunnel is of rectangular cross section and has a width of 56 cm and an average height (constant pressure) of about 25 cm. The longitudinal distance from the inlet to the models is 4.88 m, and the Reynolds number, based on element height H and free-stream velocity U_1, was approximately 3600 for all runs.

A schematic drawing of a portion of the wind tunnel used in the present investigation is shown in Fig. 1. Room air was drawn through the tunnel over the roughness elements in the test section by means of a centrifugal fan. Tunnel walls and roof were transparent, which enabled the photographing of surface flow patterns. Details of the wind tunnel used in the present work have been reported by Logan and Barber [9].

An enlarged view of the gap formed on the floor of the wind tunnel and the coordinate system used are shown in Fig. 13. A mixture of alcohol and graphite powder were spread in and around the gap formed between the ends of the aluminum bars (roughness elements). The streaks on the floor, formed

Nomenclature

C_f = skin friction coefficient
H = height of roughness element
U = longitudinal mean velocity
U_2 = free-stream mean velocity
U_r = reference velocity, 6 m/s ($U_r \approx U_1$)
u_τ = friction velocity
u_{τ_0} = friction velocity for undisturbed flow
u = longitudinal turbulent velocity fluctuation
u' = rms value of the longitudinal turbulent velocity fluctuation
v = vertical turbulent velocity fluctuation
w = lateral turbulent velocity fluctuation
$\overline{uv}, \overline{uw}, \overline{vw}$ = components of kinematic Reynolds shear stresses
V = vertical component of mean velocity
W = lateral component of mean velocity
x = longitudinal coordinate ($x=0$ on back side of roughness element)
y = vertical coordinate
z = lateral coordinate
ξ, η, ζ, = vorticity components
ν = kinematic viscosity

Table 1 Estimates of uncertainty

Quantity	Percent uncertainty	Restrictions
U	10.0	none
V, W	15.0	$V, W < 0.02U$
$\overline{uv}$	20.0	$y/H < 0.5$

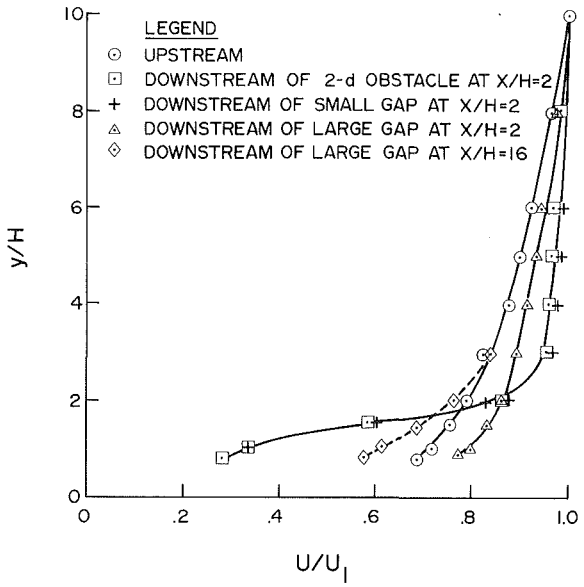

Fig. 4 Comparison of centerline-velocity profiles at $X/H = 2$

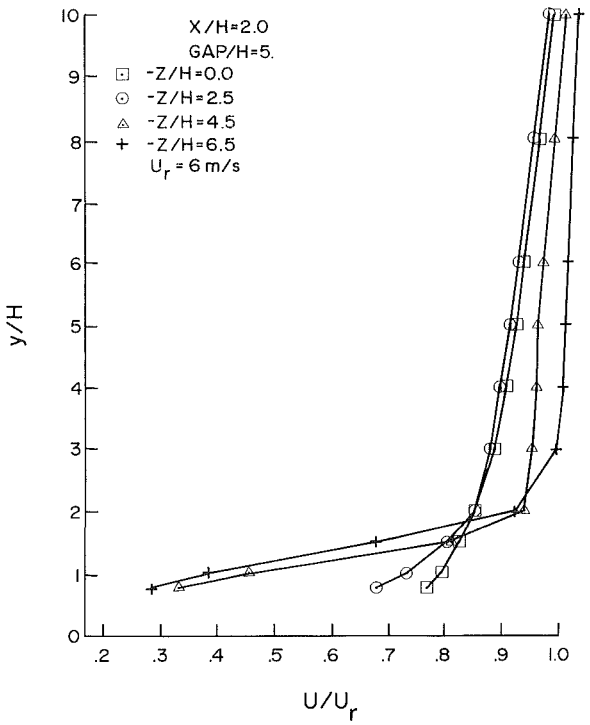

Fig. 5 Mean velocity profiles at off-centerline stations at $X/H = 2$

during wind-tunnel operation, were photographed after each run. Photographs of streak patterns were obtaioned for gap sizes of $0.5H$, $1.H$, $2.H$, $5.H$ and $10\ H$ as well as for the zero-gap condition, i.e., the two-dimensional case.

Gap sizes of $1H$ and $5H$ were chosen for further investigation, because the surface patterns (Figs. 2 and 3) showed significant differences, and these gap sizes were representative of small and large gaps. Measuring stations were established on the centerline and at distances of $2.5H$, $4.5H$ and $6.5H$ away from the centerline. Vertical profiles of data were taken at the four stations at $x/H = 2$, 4, 6, 10, 16 and 28. The objective of this coverage was to obtain sufficient data with which the flow in the interaction region could be described.

The raw data were obtained with a DISA constant-temperature hot-wire anemometer using a linearizer and digital voltmeter. A single-wire probe (DISA 55P12) with the wire (5 micron dia by 1.25 mm long) inclined at 45 deg was supported in the wind tunnel so that its axis was parallel to the main flow and was rotated by means of a ball-bearing mechanism (approximately 13 mm o.d.) through six angular positions at each measuring point. The six probe readings were used to solve the equations of Acrivlellis [10] simultaneously to yield the three velocity components and the three Reynolds shear stresses. Logan and Lin [11] have presented a complete tabulation of the calculated results together with a discussion of the theory and methodology used in their determination.

The size of the mechanism used to rotate the probe limited the closest approach of the wire sensor to the wall to approximately 6.45 mm. Estimates of uncertainty in the absolute inclined-wire measurements are indicated in Table 1.

Results

The photographic results are presented in Figs. 2 and 3. The letters A, B, C, D, E and F are used in a schematic representation in Fig. 2 to indicate critical points. Using the designations of Hunt, et al. [7] the points A and B are nodal points which are foci, while C and D are nodal points which are attachment points. Point E appears to be a saddle point which is an attachment point, and point F is a saddle point which is a separation point. Half-saddle points (not indicated) are at the leading edges of the gap and on the back sides of the bars at a point somewhat remote to the gap where the recirculating flow becomes two-dimensional. The region between F and E could be a very low-lying separation bubble. The present measurements are inadequate to confirm this conjecture. Such an extensive region of reversed flow does not appear in the pattern of Fig. 3. Foci will be present, as in Fig. 2, and these are bounded by reattachment lines which appear to curve toward the two-dimensional reattachment position of approximately $9H$ (see reference [1]).

In Fig. 4 centerline profiles of longitudinal mean velocity U taken behind a surface-mounted two-dimensional obstacle are compared with centerline velocity profiles taken at the same downstream station behind small and large gaps. The response of the flow to the two-dimensional obstacle is observed to include the acceleration of fluid above the approximate height of $2H$ and the deceleration of fluid below that height. It is noted from Fig. 4 that points measured behind the small gap are virtually coincident with those behind the two-dimensional obstacle.

The region of flow retardation ($y/H < 2$) is characterized by high velocity gradients (dU/dy) and associated high levels of turbulence energy and shear. The properties of this region are propagated outward from the wall, and the extent of the region (in the y-direction) grows with downstream distance x. The spread of mean flow momentum and turbulence energy effects a reduction in mean velocity gradient in the affected region.

The gap width appears to affect the amount of flow retardation in the zone near the wall. Zero gap produces maximum retardation. As the gap is sufficiently enlarged the gap flow is accelerated (rather than decelerated) in the region near the wall. The flow behavior following the small gap more nearly resembles the no-gap case. Farther downstream the size of the gap makes only a small difference in the velocity profiles.

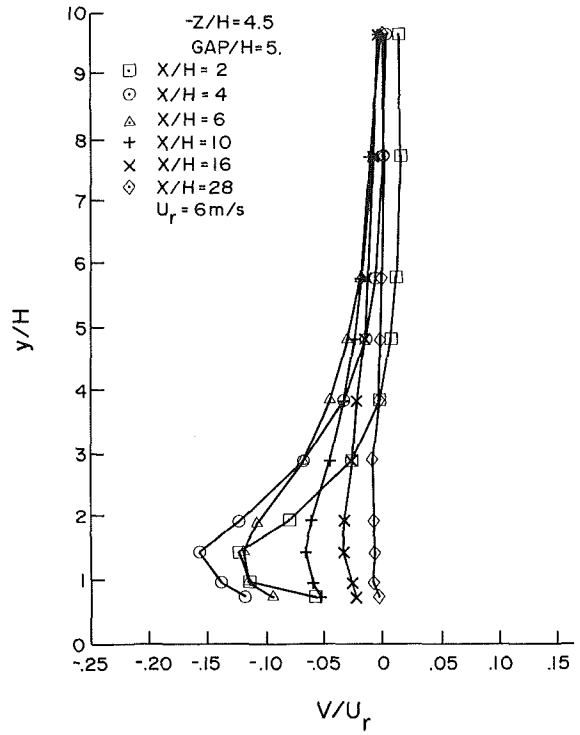

Fig. 6 Profiles of vertical component of mean velocity for large gap $-Z/H = 4.5$

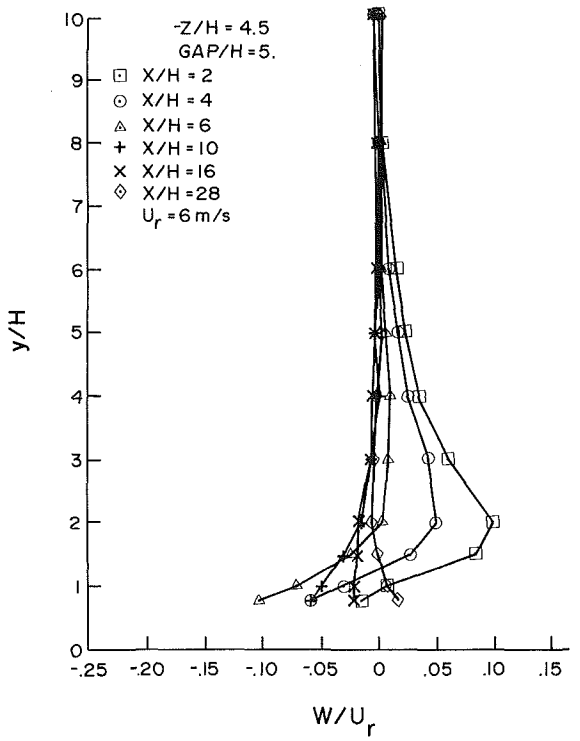

Fig. 7 Lateral components of mean velocity for large gap at $Z = -4.5H$

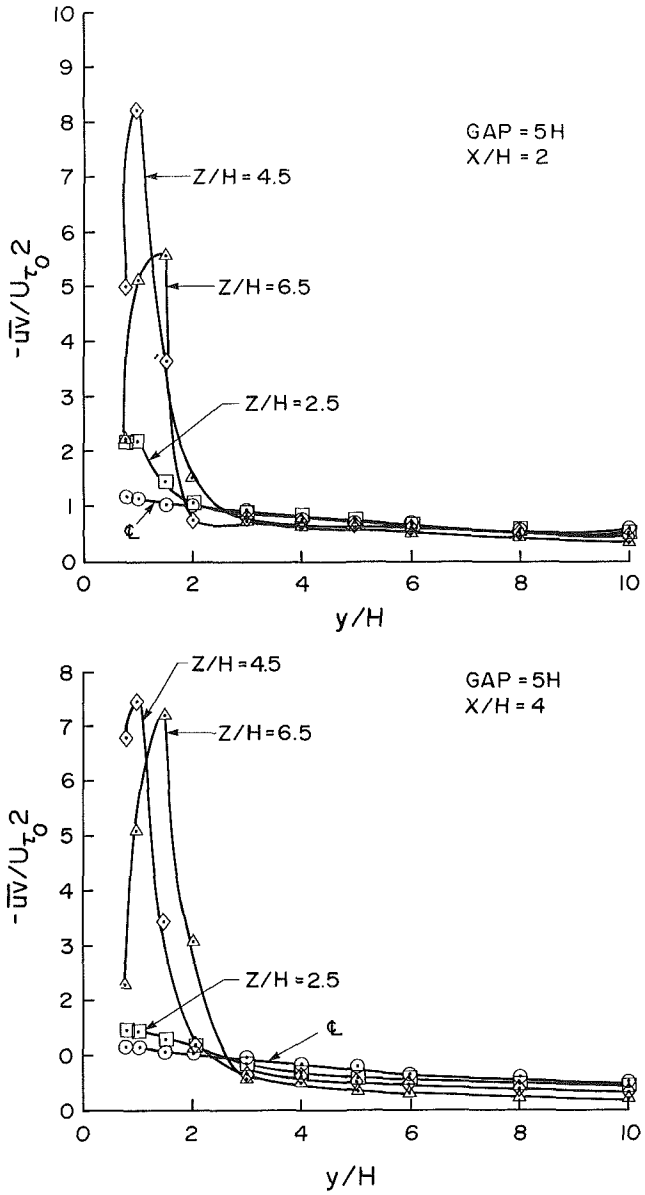

Fig. 8 Reynolds stresses behind large gap at $X/H = 2$ and 4

Figure 5 shows profiles in the line with the end of the obstacle ($-Z/H = 2.5$) at the side of the large gap and behind the obstacle on lines $2H$ and $4H$ distant from the gap boundary. In this comparison of centerline and off-centerline profiles a gradual change from acceleration in the gap to retardation behind the obstacle is seen. Such differences necessitate gradients of U with z and cross currents (W-component of velocity) as well as vertical currents (V-component of velocity).

Figure 6 shows the magnitude of the vertical component of mean velocity V in the wake region near the gap boundary. The flow is downward (toward the wall) in the wake region. The near-wake in this zone exhibits strong secondary currents which are partly stimulated by the gap. Values of V/U_r at $y/H = 1.5$ are 0.1645 for the large gap (see Fig. 6), 0.1132 for the small gap at the same proximity to the gap boundary and 0.0955 for the no-gap case. Thus it appears that the gap produces an enhancement of the vertical component V.

The effect of the gap on the horizontal component W (at the same positions shown in Fig. 6) is shown in Fig. 7. Values of W/U_r for the large-gap, small-gap and no-gap cases are compared below at the same wall distance ($y/H = 2$) and downstream position ($x/H = 2$). These values are 0.104 (see Fig. 7), 0.037 and 0.0195, respectively. The ratio of the first value to the last is 5.33 and is a measure of the enhancement of crossflow by the gap. Pletcher and McManus [12] indicate that the maximum crossflow may have a magnitude of around one percent of the main velocity. Thus it is concluded that any gap creates crossflows in the interaction region near the wall,

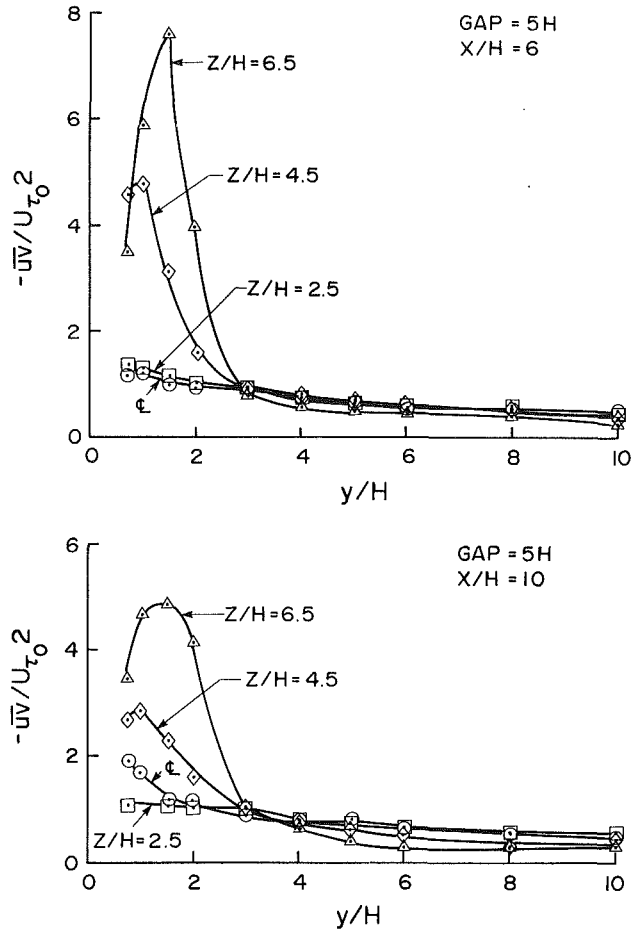

Fig. 9 Reynolds stresses behind large gap at $X/H = 6$ and 10

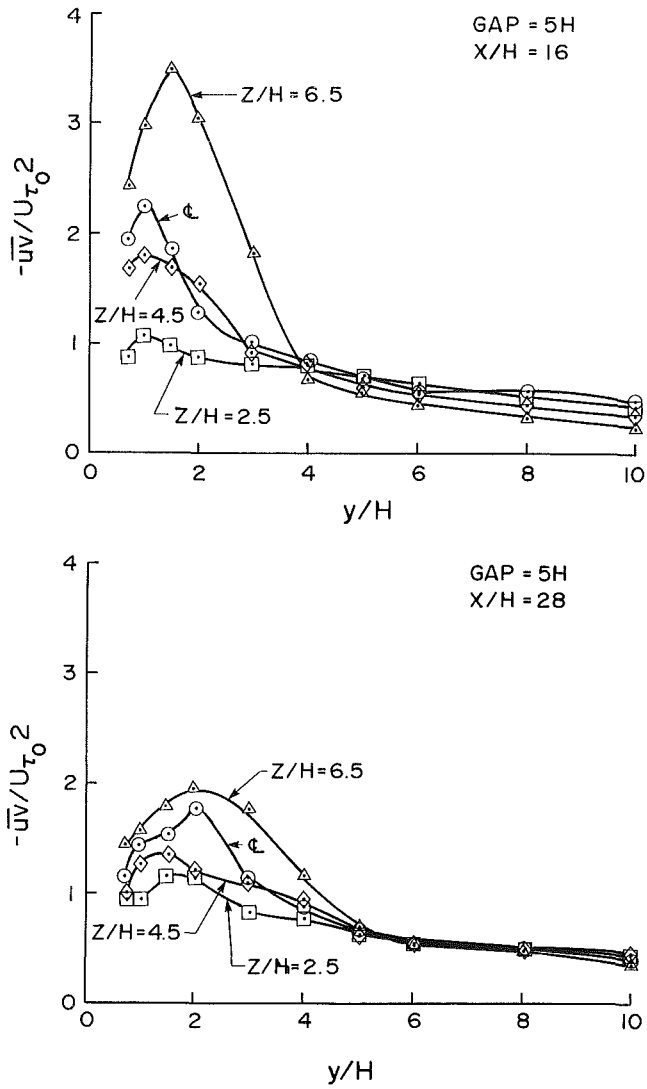

Fig. 10 Reynolds stressed behind large gap at $X/H = 16$ and 28

and that the magnitude of W increases with gap size. The greater mass flow through larger gaps implies a larger mass of fluid available for diversion into the lower pressure region behind the obstacle at either side of the gap.

Three components of Reynolds shear stresses are found to exist downstream of the gap. The predominant stresses are the $\overline{uv}$ stresses, and measurements of these downstream of the large gap are shown in Figs. 8–10. The data nearest the gap, shown in Fig. 8, indicate a sudden rise in $\overline{uv}$ values behind the rib but little disturbance behind the gap itself. In the interaction region $\overline{uv}$ is raised over no-gap values at some wall distances (see Fig. 12). Thus there is considerable enhancement of $\overline{uv}$ stresses in the interaction region.

The $\overline{uw}$ stresses are not shown in Fig. 8. These are much smaller as would be expected with smaller velocity gradients of U in the z-direction. $\overline{vw}$ stresses are also not shown in these figures, but they exceed $\overline{uw}$ stresses and are associated with gradients of W in the y-direction. $\overline{uw}$ and $\overline{vw}$ diminish quickly, as do the cross currents (W) and cross-stream gradients.

In Fig. 9 the stresses begin to diminish somewhat. The stress near the gap boundary ($Z/H = 2.5$) is distributed very nearly as in the undisturbed layer. At $X/H = 10$ stresses at the centerline begin to increase, while those at $Z/H = 2.5$ do not. The trend continues, as is shown in Fig. 10, with peaking occurring at $X/H = 16$ and an eventual return to equilibrium is indicated at $X/H = 28$. Figure 10 indicates widening of the disturbed layer at downstream stations as in the two-dimensional case.

Near-wall data were not taken in the present work because of the probe configuration; however, some pertinent data were available from the near-wall data of Logan and Barber

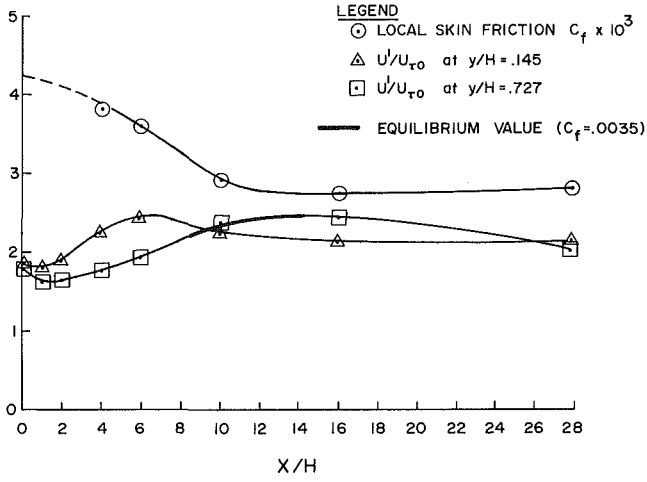

Fig. 11 Skin friction and turbulence intensity on centerline behind large gap

[9]. These data are shown in Fig. 11 and indicate an overshooting of the equilibrium (undisturbed) value of C_f by the centerline flow. The elevated C_f occurs between $X/H = 0$ and $X/H = 6$. The variation of turbulence intensity near the wall ($y/H = 0.145$) is also shown, and it climbs steadily above the

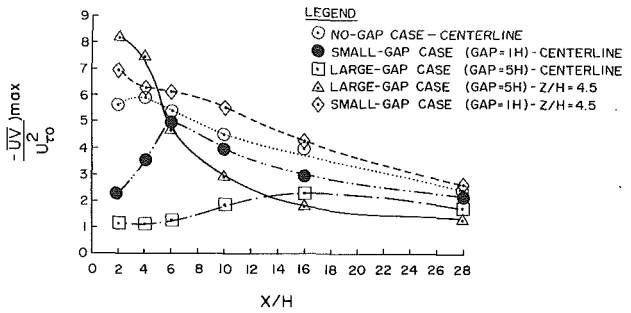

Fig. 12 Longitudinal distribution of maximum Reynolds stresses for three gaps

upstream value (see reference [1]) between $X/H=3$ and $X/H=12$. Turbulence intensity at $y/H=0.727$ is also shown, since this distance is close to the minimum wall distance used in the present work. Here the turbulence intensity, which is representative of the square root of turbulence energy, also exceeds its upstream value from $X/H=8$ to $X/H=24$ with a maximum at about $X/H=14$. Assuming an approximate similarity in turbulence structure, one would expect coincident peaking of turbulence energy and Reynolds stresses in a shear layer. This is the case for the present data. One can speculate that no such peaking of C_f or u' occurs in the wake region behind the end of the roughness element ($Z/H=2.5$).

Figure 12 shows the longitudinal variation of maxima of Reynolds stress for the three gap geometries considered in the present work. Both centerline and off-centerline distributions are shown. The maximum value of $\overline{uv}$ on the centerline depends on gap size for both magnitude and longitudinal position. The smaller the gap, the greater the magnitude and the nearer the roughness element the position of the maximum occurs. At off-centerline positions ($Z/H=4.5$) the maxima of $\overline{uv}$ are notably higher than those encountered behind the continuous (two-dimensional) element. The decay of turbulence stress observed behind the small gap is closest to the $\overline{uv}$ decay for the zero-gap case. The decay of $\overline{uv}$ is much more rapid for the large gap case but attains the higher initial value.

Plots of $\overline{uw}$ and $\overline{vw}$ are not presented in the present paper but tabulations of these quantities are available in reference [11]. These values are high in the interaction region ($z/H=4.5$) immediately downstream of the obstacle. Here the maximum of $\overline{uw}$ is approximately 0.3 of the maximum of $\overline{uv}$, and the maximum of $\overline{vw}$ is roughly twice that of $\overline{uw}$.

Flow Model

It is clear that the effect of the gap is to provide a variable wall resistance in the lateral direction. Higher longitudinal velocity components appear in the wake of the gap at low elevations than occur directly behind the roughness element. The lateral distribution of the U component leads to crosswise velocity gradients and corresponding shear stresses, nonexistent in two-dimensional flows.

Secondary flows are known to arise in association with the lateral variation of longitudinal velocity or of turbulence energy (see Hinze [13]). Near the wall the flow region downstream of the gap contains unretarded fluid. The wake regions behind the roughness element contain retarded fluid which is recirculated by fluid passing above the separation zone. Fluid enters the wake region behind the roughness element from the gap flow via crosscurrents. The crosscurrents reduce lateral velocity gradients and the associated turbulence shear stresses. Close to the wall the secondary flow is directed away from the centerline, as may be observed from the surface flow (Fig. 3) and from the profiles of the lateral component W (Fig. 7). Figure 7 also shows a crossflow toward the centerline beginning at

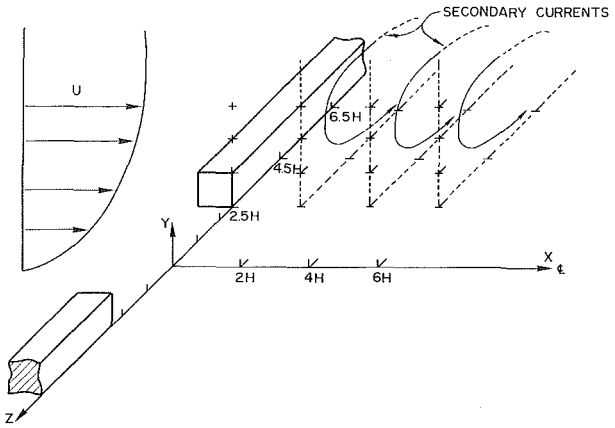

Fig. 13 Schematic of secondary flow behind the large gap

elevations in the range $1<Y/H<2$. Thus counter-rotating secondary cells are observed in the wake on the two sides of the gap as depicted schematically in Fig. 13.

The approaching boundary layer contains vortex lines which are parallel to the z-axis. Fluid particles passing over the roughness element are accelerated more than particles in the gap. Thus transverse vortex lines are rotated so that streamwise vorticity is enhanced in the interaction region of the wake. The sense of the new vorticity is such that low-level fluid flows away from the centerline. Quantification of the rate of vorticity change from turning of vortex lines can be obtained by evaluation of the last term on the left-hand side of the vorticity equation (1).

$$U\frac{\partial\xi}{\partial x}+V\frac{\partial\xi}{\partial y}+W\frac{\partial\xi}{\partial z}-\nu\nabla^2\xi-\xi\frac{\partial U}{\partial x}-\eta\frac{\partial U}{\partial y}-\xi\frac{\partial U}{\partial y}$$

$$=\frac{\partial}{\partial x}\left(\frac{\partial\overline{uv}}{\partial y}-\frac{\partial\overline{uw}}{\partial y}\right)+\frac{\partial^2}{\partial y\partial z}(\overline{v^2}-\overline{w^2})+\left(\frac{\partial^2}{\partial z^2}-\frac{\partial^2}{\partial y^2}\right)\overline{vw} \quad (1)$$

The secondary flow created by vortex line turning is effective in reducing spanwise gradients, which contribute to $U(\partial\xi/\partial x)$ through terms such as $\zeta(\partial U/\partial Z)$ and $(\partial/\partial x)/(\partial\overline{uv}/\partial z)$. Direct action of $-\rho\overline{uw}$ contributes to reduction of $\partial U/\partial z$, and direct action of $-\rho\overline{vw}$ helps abolish $\partial W/\partial y$. Secondary flows disappear rapidly as may be observed in Figs. 6 and 7. These motions virtually disappear after $x=10H$.

Conclusions

The following conclusions were drawn from the data presented:

1 Centerline velocity profiles behind the small gap are similar to profiles behind a two-dimensional obstacle.

2 A strong secondary flow is generated in the zone of interaction, i.e., the region near the gap between the recirculating flow and the unimpeded gap flow.

3 The strength of the secondary currents as reflected by the magnitudes of V and W, increases with gap size because more fluid mass is available.

4 The secondary currents move fluid away from the central region at positions near the wall and toward the central region at positions away from the wall.

5 Combined action of secondary currents and momentum transport by the shear stresses result in the rapid disappearance of spanwise gradients.

6 The three components of Reynolds stress are present behind the gap. $\overline{uv}$ stresses exceed those created by a two-dimensional element.

7 Reynolds stresses on the centerline reach higher maximum values for smaller gaps, and these maxima are

attained nearer to the roughness element for smaller than for larger gaps.

8 Reynolds stresses generated behind the elements and near the gap boundary are higher for the larger gaps than for the smaller, but the rate of decay of $\overline{uv}$ is higher for the large gaps.

Acknowledgments

This work was sponsored in part by Marshall Space Flight Center, National Aeronautics and Space Administration. The authors are grateful for several suggestions provided by Dr. W. H. Schofield, Aeronautical Research Laboratories, Melbourne.

References

1 Schofield, W. H., Barber, D. S., and Logan, E., "Turbulent Boundary Layer Flow Through a Gap in a Wall Mounted Roughness Element," ASME JOURNAL OF FLUIDS ENGINEERING, Vol. 103, pp. 97–103.

2 Hunt, J. C. R., "A Theory of Turbulent Flow Around Two-Dimensional Bluff Bodies," *Journal of Fluid Mechanics*, Vol. 61, 1973, pp. 625–706.

3 Bradshaw, P., and Wong, F. Y. F., "The Reattachment and Relaxation of a Turbulent Shear Layer," *Journal of Fluid Mechanics*, Vol. 52, 1972, pp. 113–135.

4 Counihan, J., Hunt, J. C. R., and Jackson, P. S., "Wakes Behind Two-Dimensional Surface Obstacles in Turbulent Boundary Layers," *Journal of Fluid Mechanics*, Vol. 64, 1974, pp. 529–563.

5 Castro, I. P., "Measurements in Shear Layers Separating From Surface-Mounted Bluff Bodies," *Journal of Wind Engrg. and Ind. Aero.*, Vol. 7, 1981, pp. 253–272.

6 Schofield, W. H., Lin, S., and Logan, E., "Turbulent Sheared Flow Around Surface-Mounted Prisms," Eighth Australasian Fluid Mechanics Conference, University of Newcastle, Sec. 11A, 1983, pp. 9–12.

7 Hunt, J. C. R., Abell, C. J., Peterka, J. A., and Woo, H., "Kinematical Studies of the Flows Around Free or Surface-Mounted Obstacles; Applying Topology to Flow Visualization," *Journal of Fluid Mechanics*, Vol. 86, 1978, pp. 179–200.

8 Castro, I. P., and Dianat, M., "Surface Flow Patterns on Rectangular Bodies in Thick Boundary Layers," Fifth Colliquium on Industrial Aerodynamics, Aachen, 1982.

9 Logan, E., and Barber, D. S., "Effect of Lateral Spacing on Wake Characteristics of Buildings," NASA-CR 3337, Marshall Space Flight Center, Nov. 1980.

10 Acrivlellis, M., "An Improved Method for Determining the Flow Field of Multidimensional Flows of any Turbulence Intensity," *DISA Information*, No. 23, 1978, pp. 11–16.

11 Logan, E., and Lin, S. H., "Wind Tunnel Measurements of Three-Dimensional Wakes of Buildings," NASA-CR 3565, Marshall Space Flight Center, June 1982.

12 Pletcher, R. H., and McManus, H. N., "Secondary Flow in the Entrance Section of a Straight Rectangular Duct," in S. Ostrach and R. H. Scanlan, Ed., *Developments in Mechanics*, Vol. 2, Pergamon, New York, 1965, pp. 269–291.

13 Hinze, J. O., "Experimental Investigation on Secondary Currents in the Turbulent Flow Through a Straight Conduit," *Applied Scientific Research*, Vol. 28, 1973, pp. 453–465.

Masataka Shirakashi
Associate Professor.
Engineering Division,
Technological University of Nagaoka,
Kamitomioka-cho 1603-1, Nagaoka,
Niigata Prefecture, 949–54 Japan

Yasuhiro Ishida
Engineer,
Vending Machine Division,
Tokyo Sanyo Electric Co., Ltd.,
Maesuna 160-1, Fukiage-cho,
Kitaadachi-gun,
Saitama Prefecture, 369-01 Japan

Shoichi Wakiya
Professor
Engineering Division,
Technological University of Nagaoka,
Kamitomioka-cho 1603-1, Nagaoka,
Niigata Prefecture, 949-54 Japan

Higher Velocity Resonance of Circular Cylinder in Crossflow

This report concerns the oscillation of an elastically supported circular cylinder in a uniform crossflow. Several investigators have observed an unexpected subharmonic-like resonance at $f_v/f_n = 3$ in addition to the normal one at $f_v/f_n = 1$, where f_v is the Kármán vortex shedding frequency and f_n is the natural frequency for the cylinder oscillation. Durgin, et al., proposed an explanation of the mechanism for the abnormal resonance at a higher velocity, which he called the Lower Mode Response. In this work comprehensive experiments on the higher velocity resonance were carried out and two alternative mechanisms are proposed for the phenomenon. It is concluded that, as long as the amplitude of the cylinder oscillation is not too large, the description of Durgin, et al., cannot be applied, and that the end effect at the side wall of the measuring channel or the rotation mode oscillation can be attributed to the local maximum amplitude at a higher velocity.

1 Introduction

The flow-induced oscillation of a cylindrical structure is found in many engineering applications. Numerous investigations concern the oscillation of an elastically supported circular cylinder in a uniform flow [1] and experimental results have confirmed that a resonance occurs when the frequency of the Kármán vortex shedding is equal to the natural frequency of the cylinder oscillation. Under certain conditions, the vortex shedding frequency coincides with that of the cylinder oscillation over some velocity region [2] and this is called a lock-in phenomenon. In addition to this usual resonance, Penzien [3] observed another resonance phenomenon, that is, as the velocity of the flow increased, the amplitude of the oscillation attained a secondary maximum value when the vortex shedding frequency was around three times the natural frequency of the cylinder oscillation. Durgin, et al. [4] called the usual resonance a Fundamental Mode Response and the second a Lower Mode Response. For the latter, he suggested a model to explain the mechanism based on the vortex shedding.

All of the foregoing reports exclusively treated the oscillation of a cylinder held parallel at all time, assuming that the motion is purely translational. Shirakashi, et al. [5] found that a rotational mode oscillation could be induced for a cylinder elastically supported at both ends due to the inherent random phase shift of Kármán vortex shedding along the cylinder axis.

In this investigation, a cylinder was supported at both ends by plate springs normal to the free flow to confine the displacements at the supporting points normal to the free flow and the cylinder axis. The displacements at each end of the cylinder and the velocity fluctuation at a point in the wake were measured simultaneously. Then, influences of the condition at the cylinder ends on the oscillation and the vortex shedding were examined.

2 Experimental Apparatus

An outline of the apparatus used is indicated in Fig. 1. The wind tunnel was a blowdown type with a nozzle section of 350 mm × 350 mm with a maximum velocity of 40 m/s. The measuring channel was 320 mm × 320 mm in cross section and 1000 mm in length. The deviation of the velocity distribution of the free flow from uniformity was ±0.1 percent with the turbulence intensity of 0.3 percent at the velocity $U = 10$ m/s. The side walls of the measuring channel had an open slot 50 mm in height and 42 mm in length through which the cylinder passed. A circular cylinder was set horizontally in the central plane of the measuring channel. Two plate springs with equal spring constants supported the cylinder outside the side walls so as to confine the displacements at the supported points only in the vertical direction as shown in Fig. 1.

The velocity of the free flow was measured by a Pitot tube. A hot-wire probe was set to detect u, the x-component of the velocity fluctuation, at the point $x = 3d$ and $Z = 2d$, where the wave corresponding to the Kármán vortex shedding was most clearly observed in u-signal. The vertical displacements at both ends of the cylinder, Z_R and Z_L, were measured using noncontacting sensors. Measurement errors are indicated by symbol Δ's for all the quantities as indicated in the Nomenclature or in Tables 1 and 2. The frequency range effective for the signal processing of Z_R, Z_L and u was 0 ~ 10

Contributed by the Fluids Engineering Division for publication in the JOURNAL OF FLUIDS ENGINEERING. Manuscript received by the Fluids Engineering Division, July 20, 1984.

Table 1 Experimental conditions for oscillating cylinders

Test number	Diameter mm	virtual mass per unit length 10^{-2}kg/m	virtual spring constant per unit length 10^2N/m^2	for translation mode: natural frequency f_{nz} Hz	for translation mode: damping factor* 10^{-3}	for rotation mode: natural frequency $f_{n\theta}$ Hz	for rotation mode: damping factor* 10^{-3}	$f_{n\theta}/f_{nz}$	end condition
1	25.2	14.4	36.8	25.4	1.92	56.0	-	2.20	
2	25.0	26.6	7.93	8.7	1.66	28.0	-	3.22	without blocking plates
3	26.5	11.9	6.52	11.8	1.37	33.6	-	2.85	
4	32.6	24.3	23.3	15.6	2.02	45.6	6.10	2.92	
5**	32.6	34.4	33.0	15.6	1.94	46.4	4.36	2.97	
6	26.5	21.3	39.2	21.6	3.79	67.0	-	3.10	
7	26.5	23.6	20.4	14.8	3.69	43.0	-	2.91	with blocking plates
8	32.6	28.2	41.0	19.2	2.67	76.0	12.0	3.96	
9	32.6	26.2	21.4	14.4	2.59	50.0	10.4	3.47	
Error	±0.05mm	±2.3%	±3%	±1.1%	±8%	±1.1%	±8%	±2.2%	

* A damping factor ζ was obtained by

$$\zeta = \frac{1}{2\pi}\cdot\frac{1}{n}\ln\frac{a_n}{a_0}$$

where a_n/a_0 was the ratio of the amplitudes of n-cycle apart waves in a free damping oscillation.

** Only for Test 5 the width of the measuring channel was 226 mm.

Table 2 Errors of variables in figures

mean velocity (m/s) U	ΔU	frequency	displacement of cylinder	Reynolds number and Strouhal number for d=32.6mm* R_e (10^4)	$\lvert\Delta R_e/R_e\rvert$, $\lvert\Delta S_t/S_t\rvert$
1	0.29	$\lvert\Delta f/f\rvert$ =	$\lvert\Delta z\rvert$= 4 μm	0.3	16 %
2	0.16			1	1.6%
3	0.11	0.4%	$\lvert\Delta\theta/\theta\rvert$=0.3%	1.3∿	less than 1%
5	0.07			* $\lvert\Delta R_e/R_e\rvert$ and $\lvert\Delta S_t/S_t\rvert$ decrease nearly inversely with d	
6∿	less than 1%				

kHz. Experiments on elastically supported cylinders were conducted for two end conditions; (1) a cylinder without blocking plates, (2) a cylinder with blocking plates (see Fig. 1). For comparison, measurements of vortex shedding from fixed cylinders with these two end conditions were carried out.

The experimental conditions for oscillating cylinders are summarized in Table 1. Values of the logarithmic damping factors for the translation-mode and the rotation-mode oscillations obtained from a free oscillation in stationary air are presented and noted to be small.

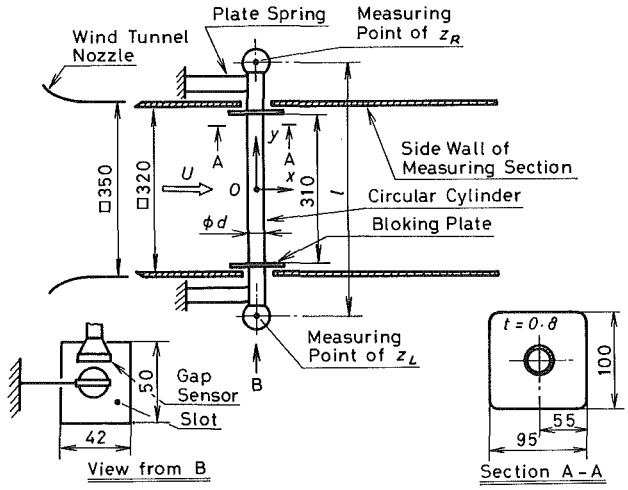

Fig. 1 Outline of apparatus (mm)

3 Results and Discussion

3.1 The Oscillation of a Cylinder Through Open Slots. For the end condition (1), that is, a cylinder which passed through the slots on the side walls of the measuring channel, measurement of the displacement of the cylinder at one end showed that the amplitude of the oscillation contained three local maximum values with increasing free flow velocity. Figures 2 and 3 illustrate the fluctuation signals and their spectra at the second and the third resonance peaks for Test 1. In part (*a*) of each figure are shown the velocity fluctuation u and the displacements at both ends of the cylinder as measured simultaneously. The oscillogram indicated by symbol $Z_R \wedge Z_L$ in (*a*) is obtained by superposing these two displacement signals. S_u and S_{zL} in (*b*) and (*c*) are the spectral densities of u and Z_L, respectively, which were calculated from 128 series of signals. The curve "Average" expresses the average value over the 128 series and the curve "Peak Hold" was obtained by holding the maximum value of

Nomenclature

d = diameter of cylinder, $\Delta d = 0.05$ mm
f = frequency
f_{nz} = natural frequency for the translation mode oscillation of cylinder
$f_{n\theta}$ = natural frequency for the rotation mode oscillation of cylinder
f_v = Kármán vortex shedding frequency
f_z = peak frequency of S_z
f_θ = peak frequency of S_θ
l = virtual length of cylinder, Fig. 1, $\Delta l = 0.5$ mm
R_e = Reynolds number, $= Ud/\nu$
S_t = Strouhal number, $= f_v d/U$
$S_u, S_z, S_{zL}, S_\theta$ = power spectral densities of u, Z_A, Z_L and θ
$S_{zp}, S_{\theta p}$ = peak values of S_z and S_θ
U = free flow velocity
u = x-component of the velocity fluctuation
$O-x,y,z$ = coordinates, Fig. 1, $\Delta x = \Delta y = 0.5$ mm, $\Delta z = 0.02$ mm
Z_A = translational displacement of cylinder, $= (Z_L + Z_R)/2$
Z_L, Z_R = displacements at the ends of cylinder, Fig. 1
θ = angular displacement of cylinder, $= (Z_R - Z_L)/l$
ν = kinematic viscosity of air

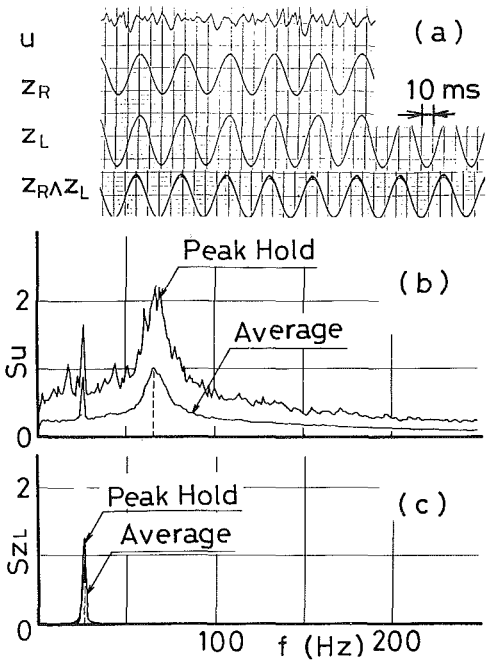

Fig. 2 Fluctuation signals and their spectra at the second resonance for Test 1 ($U = 10.2$ m/s)

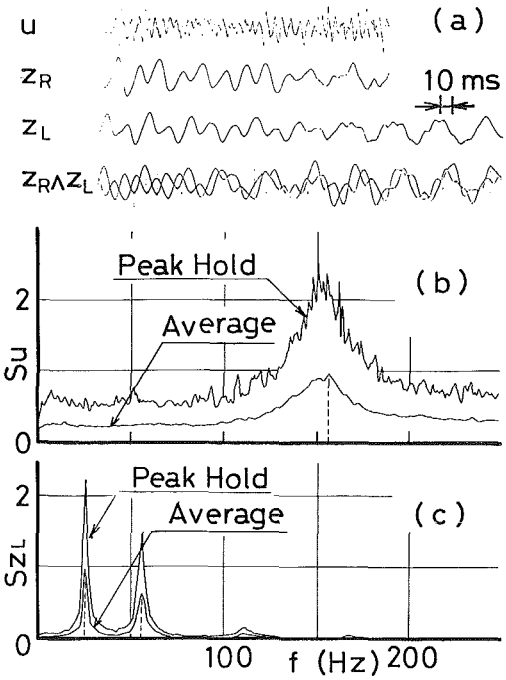

Fig. 3 Fluctuation signals and their spectra at the third resonance for Test 1 ($U = 23.8$ m/s)

the 128 series. Both curves are normalized by the peak value of the average spectrum.

For Test 1, the first resonance peak was observed at $U = 3.7$ m/s and it was accompanied by the lock-in phenomenon. In such cases, a regular Kármán vortex shedding component was dominant in the u-signal and its frequency f_v was exactly equal to that of the cylinder oscillation. Moreover, Z_R and Z_L were almost sinusoidal and their amplitudes and phases coincided with each other, showing that the motion was purely translational at any instant. These features of the signals resulted in spectra similar to the delta function with a slight discrepancy between the peak hold and the average spectra. In addition, the peak frequency of S_{zL} was confirmed to be identical with the natural frequency f_{nz} of the translation-mode oscillation of the cylinder.

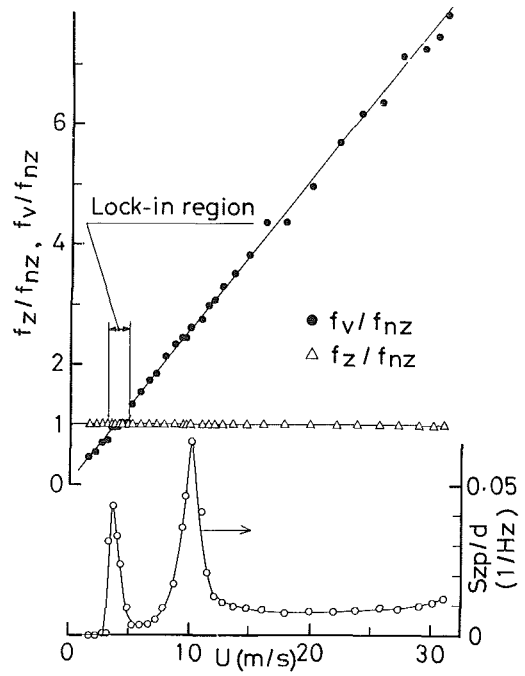

Fig. 4 Feature of the translation-mode oscillation for Test 1

The second resonance peak for Test 1 was observed at $f_v/f_{nz} \simeq 2.6$ (Fig. 2). In this case, the feature of the cylinder oscillation was similar to that at the first peak, that is, the cylinder oscillated almost sinusoidally in a translation mode with its natural frequency. However, the u-signal was not so regular as in the case of the first resonance and then its spectrum S_u was widely distributed as shown in Fig. 2(b). The highest peak of S_u appeared at the usual Kármán vortex shedding frequency and another was observed at the cylinder oscillation frequency, as seen in Fig. 2(b).

When the free flow velocity, U, was low (for example, $U \leqq 10$ m/s for Test 1), only one peak appeared in S_{zL}. In this case Z_R and Z_L coincided with each other whether or not in resonance, showing that the motion of the cylinder was translational at any instant.

When U increased, a higher frequency component was added to the displacement signals. This increased with U until the third local maximum peak of oscillation amplitude was attained. At this resonance, two dominant frequency components were definitely discerned in the displacement signals. These two components appeared alternately or simultaneously as shown in Fig. 3(a). As clearly observed in the oscillogram $Z_R \wedge Z_L$, the phases of the lower frequency components of Z_R and Z_L coincided with each other, while those of the higher frequency components were shifted 180° from each other.

From the spectrum S_{ZL}, it was shown that the lower peak frequency was equal to the natural frequency f_{nz} for the translation-mode oscillation of the cylinder and the higher peak frequency to that for the rotation mode $f_{n\theta}$. These two modes of an oscillation were confirmed to be separated definitely as follows. The translation-mode oscillation of a cylinder was represented by the mean value of the displacements at both ends of the cylinder, that is, $Z_A = (Z_R + Z_L)/2$, and the rotation mode by $\theta = (Z_R - Z_L)/l$. As an example, the features of the translation-mode oscillation for Test 1 is illustrated in Fig. 4. In Fig. 4, the peak value of S_z, the normalized peak frequency of S_z and the normalized vortex shedding frequency are plotted against the free flow velocity U. A similar plot for the rotation-mode oscillation showed that $S_{\theta p} - U$ curve had only one peak around $f_\theta/f_{n\theta} = 3$ in contrast to Fig. 4.

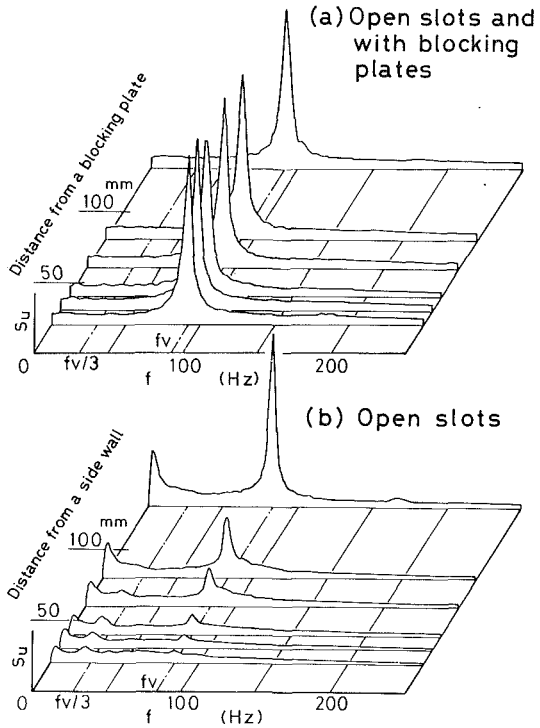

Fig. 5 Effect of blocking plates on velocity spectra for a fixed cylinder ($d = 32.6$ mm, $U = 16.0$ m/s)

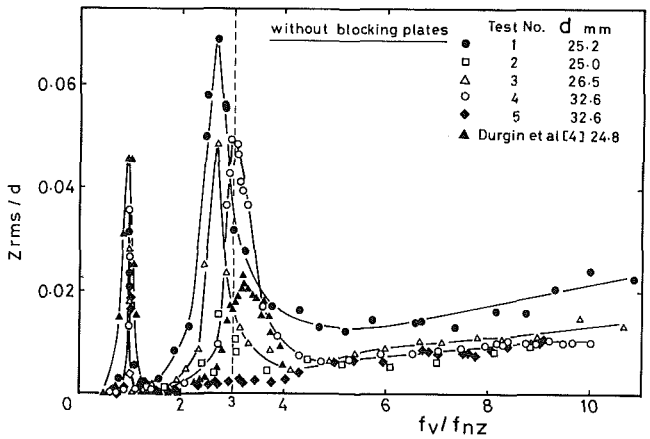

Fig. 6 Translation-mode oscillations of cylinders without blocking plates (z_{rms}/d values of Durgin, et al.'s results are reduced by a factor about 1/10)

Summarizing the aforementioned results, one notes that the oscillating behavior of an elastically supported cylinder whose natural frequency $f_{n\theta}$ for the rotation-mode oscillation is several times higher than that for the translation mode f_{nz} can be illustrated as follows: When the free flow velocity U is low, a translation-mode oscillation occurs at a frequency $f=f_{nz}$. With increasing U, its amplitude attains a maximum peak when the vortex shedding frequency f_v is equal to f_{nz}. With increasing U, a second maximum amplitude occurs when the ratio f_v/f_{nz} is around three, the motion remaining purely translational. As U becomes still higher, a rotation-mode oscillation is superposed also with its natural frequency $f_{n\theta}$, which gives a third maximum amplitude peak in the displacement at an end of a cylinder when $f_v/f_{n\theta}$ is also around three.

3.2 The Effect of the End Condition on Vortex Shedding. The velocity fluctuation u at points with various y was measured to determine the effect of the end condition on the vortex shedding from oscillating cylinders. For large diameter

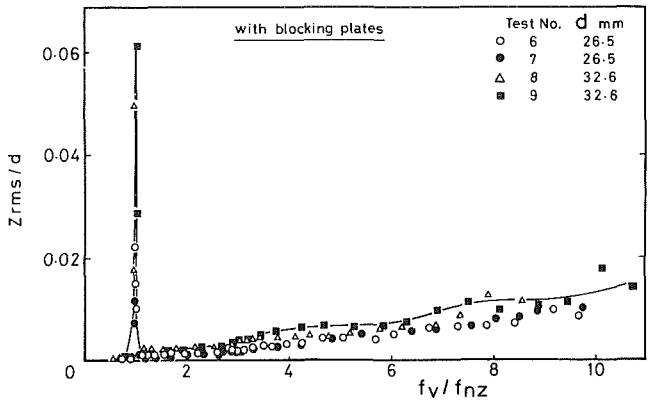

Fig. 7 Translation-mode oscillations of cylinders with blocking plates

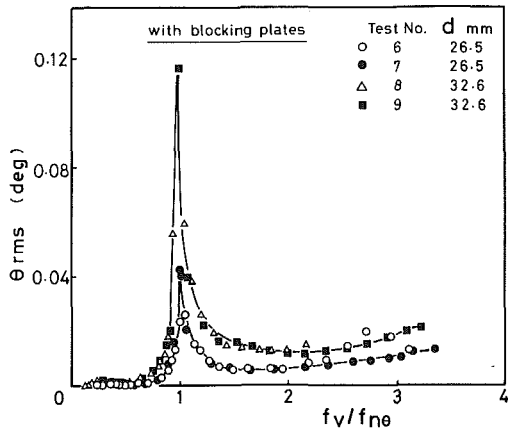

Fig. 8 Rotation-mode oscillations of cylinders with blocking plates

cylinders (that is, $d \geqq 25$ mm), the vortex shedding frequency was 15 ~ 20 percent lower for end condition (1) (without blocking plates) than that for (2) (with blocking plates) even at the center of the measuring section. It was also found that the vortex shedding was irregular for the condition (1). It is worth noting here that for the condition (1) an additional peak was found in the spectrum S_u at a frequency nearly one-third of the usual Kármán vortex shedding frequency when the probe was set at a point near to the side wall.

These effects of open slots on the vortex shedding were also observed for a fixed cylinders as shown in Fig. 5(*b*), which confirmed that the additional peak of S_u at $f \cong f_v/3$ was not induced by the cylinder oscillation. When the blocking plates were attached to the cylinder, all foregoing effects of the slots were completely erased as shown in Fig. 5(*a*) both for fixed cylinders and oscillating cylinders. However, sealing the whole equipment supporting the cylinder outside the side walls from the external room environment by air tight boxes, as conducted by Durgin, et al., could not depress the effects of the slots. This is because the boxes formed bypass routes for airflow from the high pressure zone near the upstream stagnation point of the cylinder to the downstream low pressure wake, the effect of which is virtually equivalent to the open slots.

3.3 The Effect of Blocking Plates on the Cylinder Oscillation. The effects of the blocking plates on the oscillating behavior of a cylinder are clearly revealed from Figs. 6 and 7. In Fig. 6, the translation-mode oscillation of a cylinder without blocking plates has two resonant amplitude peaks at $f_v/f_{nz} = 1$ and $f_v/f_{nz} \cong 3$, the latter of which is considered to be caused by the additional peak of S_u at $f \cong (1/3)f_v$ near the side walls. By attaching the blocking plates, the higher velocity peaks in Fig. 6 were completely removed and the lower velocity peaks became more sharp as seen in Fig. 7.

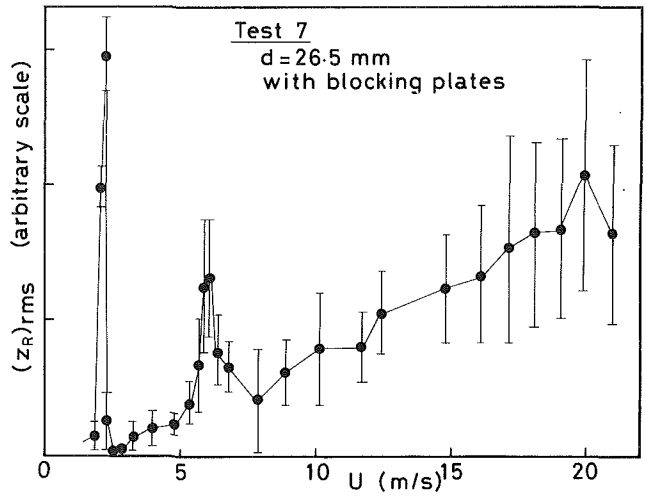

Fig. 9 Amplitude of displacement at an end of a cylinder with blocking plates; Test 7; $d = 26.5$ mm, $f_{nz} = 14.8$ Hz, $f_{n\theta} = 43$ Hz

For the rotation-mode oscillation, only one resonant peak appeared in a $\theta_{\text{rms}} \sim f_v/f_{n\theta}$ curve at $f_v/f_{n\theta}$ around three without blocking plates. This resonance peak may also be attributable to the additional peak in S_u. For this mode, as shown in Fig. 8, the blocking plates generated a basic resonance peak at $f_v/f_{n\theta} = 1$ and removed the higher velocity peak.

The whole oscillating behavior of a cylinder with blocking plates expressed by the root-mean-square value of the displacement at one end is shown in Fig. 9. Two peaks appear in the $z_{\text{rms}} \sim U$ curve; the lower velocity peak corresponds to the resonance for the translation-mode oscillation and the higher velocity peak corresponds to the rotation-mode oscillation of the cylinder.

4 Concluding Remarks

Although the model of Durgin, et al., for the Lower Mode Response on the oscillation of an elastically supported cylinder in a uniform flow is acceptable, the experimental results presented here offer an alternative and different explanation. At this stage, it is more rational to consider that the locally maximum amplitude peak of the oscillation at a higher velocity is caused by the end effect at the side wall where the cylinder passes through. Another possibility is that the lower velocity peak is caused by resonance for the translation-mode oscillation and the higher velocity peak for the rotation-mode oscillation. The ratio of the natural frequencies for these two modes is around one-third for the dimensions of the cylinders used here or by Durgin, et al.

In investigating a cylinder oscillation induced by Kármán vortex shedding in a wind tunnel, much care should be taken to avoid flow through the slots on the tunnel walls and to distinguish the two modes included in an oscillation of the cylinder.

References

1 Griffin, O. M., "Vortex-Excited Crossflow Vibration of a Single Cylinder Tube," ASME *Journal of Pressure Vessel Technology*, Vol. 12, 1980, pp. 158–166.

2 Scruton, C., National Physical Lab. Symposium on Wind Effects on Buildings and Structures, Paper 16, 1963.

3 Penzien, J., "Wind Induced Vibration of Cylinder Structures," *J. M. ASCE*, Paper 1141, 1957, pp. 1–17.

4 Durgin, W. W., March, P. A., and Lefebvre, P. J., "Lower Mode Response of Circular Cylinders in Crossflow," ASME JOURNAL OF FLUIDS ENGINEERING, Vol. 102, 1980, pp. 183–190.

5 Shirakashi, M., Ueno, S., Ishida, Y., and Wakiya, S., "Vortex-Excited Oscillation of a Circular Cylinder in a Uniform Flow," *Bull. JSME*, Vol. 27, No. 228, 1984, pp. 1120–1126.

M. Samimy
Assistant Professor,
Department of Mechanical Engineering,
The Ohio State University,
Columbus, Ohio 43210
Assoc. Mem. ASME

A. L. Addy
Professor and Associate Head,
Department of Mechanical and
Industrial Engineering,
University of Illinois at
Urbana-Champaign,
Urbana, Illinois 61801
Fellow ASME

The Fluid Dynamics of Safety Valve Vent Stacks

The flow through a safety valve vent stack system has been modeled and analyzed theoretically and experimentally. The theoretical analysis is based on the well known Chapman-Korst base flow theory. The base flow model is augmented with an empirically determined recompression factor to improve agreement between the theoretical analysis and experimental results. A computer program has been developed to solve the equations and provide necessary information to designers.

Introduction

Large quantities of high-pressure, high-temperature steam are often released by safety valves in steam power plants under faulty conditions. This steam is vented from the power plant through an elbow-type pipe connected to the safety valve which is referred to as the valve pipe and a long vent line which is referred to as the vent pipe.

There are two general types of valve pipe and vent pipe arrangements as shown in Fig. 1; they are the umbrella type and the direct-connected type. The direct-connected type has a continuous connection between the vent pipe and the valve pipe. This type of connection prevents back flow into the power plant but introduces reaction forces on the safety valve. The umbrella type, which is more common, will be discussed here. In the umbrella type arrangement shown in Fig. 2, the vent pipe can have one of the three configurations: a straight pipe, a converging pipe, or a diverging pipe followed by a straight pipe. Because of adequate clearance between the vent pipe and the valve pipe in this type, there are less reaction forces on the vent pipe. The back flow of steam from an umbrella type safety valve vent stack can occur and if it does, the back flow represents a serious safety hazard. However, with the proper design of the safety valve and vent stack, a minimum possible vent pipe diameter can be established so that steam back flow does not occur from the clearance between the vent pipe and the valve pipe.

Early designers applied "rule-of-thumb" methods to the design of safety valve vent stack systems. In the 1940s Benjamin [1, 2] presented a new design method which was mostly based on his experience in the field and some flow considerations. Recently investigators [3, 4] have used one-dimensional flow analyses to investigate and design safety valve vent stack systems. In general, for very low safety valve release pressure, one-dimensional theory could give reasonable results, but for moderate to high safety valve release pressure, one-dimensional theory could predict a negative absolute pressure within the flow after expanding from the valve pipe exit. Therefore, these methods could underestimate the vent stack size for moderate to high safety

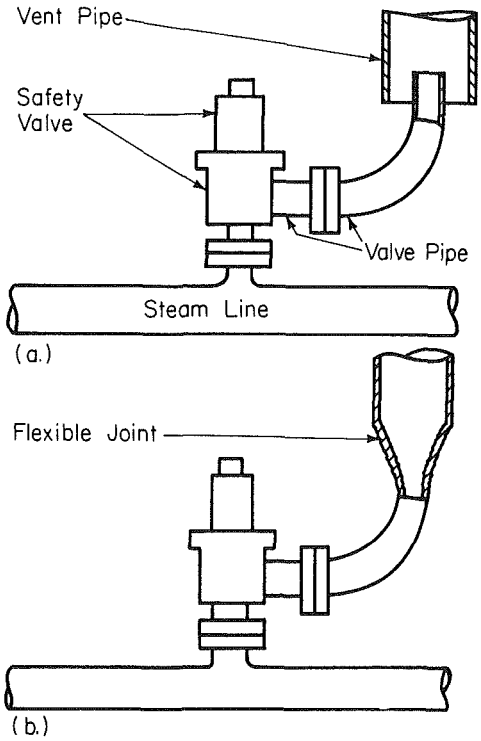

Fig. 1 Safety valve vent-stack arrangements: (*a*) umbrella type and (*b*) direct-connected type

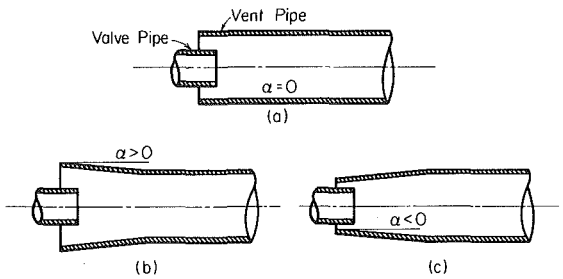

Fig. 2 Vent pipe configurations: (*a*) straight vent pipe, (*b*) converging vent pipe, and (*c*) divergent vent pipe

Contributed by the Fluids Engineering Division and presented at the Winter Annual Meeting, Boston, Mass., November 13–18, 1983, of THE AMERICAN SOCIETY OF MECHANICAL ENGINEERS.

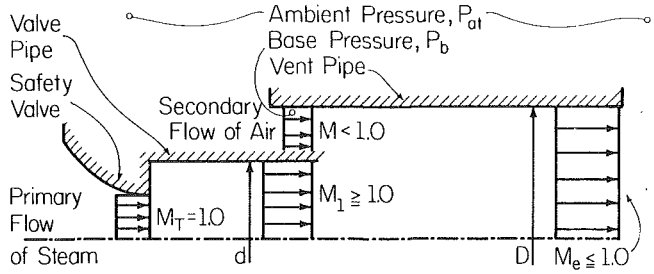

Fig. 3 Idealized flow model for the safety valve vent stack

valve release pressures. The goals of this investigation were to develop and test an analysis of the safety valve vent stack flow which would be useful as a design tool and to show the significant effects of different configurations of the vent pipe on steam back flow.

Flow Description

A simplified schematic figure of an umbrella-type valve system is shown in Fig. 1(*a*). When the pressue of the steam in a line increases to the release pressure, the safety valve system then automatically opens the valve and the steam discharges to the atmosphere through the valve and vent pipes. The transient effects due to the safety valve opening are assumed to be small. The steam flow is choked at the safety valve orifice under steady-state flow conditions. Due to the short passage between the steam line and the valve orifice and subsonic velocities upstream of the orifice, the flow from the steam line to the orifice is assumed to be nearly isentropic. The flow expands into the safety valve after passing through the valve orifice and becomes supersonic. A complex system of interacting expansion/shock waves forms as the supersonic flow changes direction to follow the valve wall contours. Due to the short length of the valve body downstream of the orifice, the flow always exits the safety valve supersonically. This supersonic flow expands further as it enters the valve pipe and passes through the elbow. The supersonic flow through the elbow of the valve pipe creates large reaction forces which in turn apply a large moment to the safety valve. This moment is directly proportional to the moment arm, which is the length of the valve pipe from the safety valve to the turning point. Since this moment arm is kept as short as possible, the flow is very likely to have a supersonic or a sonic velocity at the valve pipe exit. The supersonic or sonic flow at the valve pipe exit expands as it enters the vent pipe. Depending upon operating conditions, i.e., the steam line release pressure, the vent pipe length, and diameter, there may be (1) an induced secondary flow of air with the primary flow of steam, (2) no induced secondary flow of air with the primary flow of steam, or (3) back flow of steam between the vent pipe and the valve pipe. It is possible for the flow to be

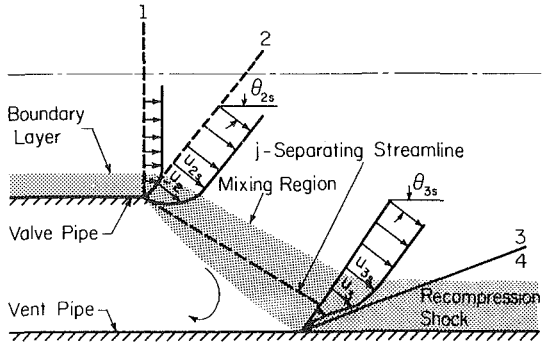

Fig. 4 Flow model for zero secondary flow

supersonic, sonic, or subsonic at the vent pipe exit. However, the vent pipes, in typical power plants, are sufficiently long so that sonic or subsonic flow occurs at the vent pipe exit under usual operating conditions.

Flow Model

A simple flow model was formulated which describes the flowfield discussed above and is mathematically tractable [5]. The theoretical analysis is based on the overall flow model and notation which are shown in Fig. 3. The flow passage up to the safety valve orifice, the safety valve orifice, and piping that may be located downstream of the valve are approximated, for simplicity, by an equivalent converging nozzle discharging into a sudden enlargement of constant diameter. The valve and vent pipes are considered together as a constant-area, supersonic-subsonic ejector. The goal of the present work was to obtain results for the design of the vent stacks without back flow. Consequently, the limiting case of the zero secondary flow regime of an ejector was studied. The special case of a zero secondary flow ejector is a well-known problem; it is also equivalent to the "base-flow" problem. There have been many investigations and publications concerning ejector and base flow problems; since a comprehensive review is not intended here, interested readers are referred to the literature [6–16].

The Chapman-Korst base flow model, which has been used extensively over the past 30 years, separates individual flow components, analyzes, and combines them into a comprehensive model. The components interact, each providing boundary or initial conditions for the others.

The flow model which is based on the Chapman-Korst component model [5–7] is shown in Fig. 4. The basic concepts underlying this flow model are: (1) steam flow separation at the exit plane of the valve pipe, (2) turbulent mixing between the freestream steam and the air entrained within the base region, and (3) the recompression process at the end of the mixing region.

Nomenclature

C = mass fraction
C_p = specific heat at constant pressure
d = valve pipe diameter
D = vent pipe diameter
G = mass flowrate
h = specific enthalpy
H = total enthalpy
k = ratio of specific heats
Le = Lewis number
M = Mach number
N = recompression factor
P = pressure
Pr = Prandtl number
T = absolute temperture
u = velocity component in x-direction
v = velocity component in y-direction
ϵ_v = eddy coefficient of viscosity
η = dimensionless coordinate
ρ = density
σ = jet spread parameter
ϕ = dimensionless velocity
$[\ ]_b$ = average of the quantity in the brackets in the base

Subscripts

0 = stagnation state
1,2,3,4 = system locations
a = air
at = atmosphere
b = conditions in the base
d = conditions along the discriminating streamline
i = floating index
j = conditions along the jet-boundary streamline
R = refers to a streamline within freestream flow
s = steam
t = turbulent

Due to the complexity of the recompression process, there is no theoretical solution of this component. But many efforts have been undertaken to find correlations and empirical information for this component. The recompression of the "discriminating-streamline" which divides the recirculated flow from the freestream steam is expressed by Korst [7] as:

$$\frac{P_{0d}}{P_3} = N\frac{P_4}{P_3}$$

where N is the recompression factor.

Korst et al. [6–8], and other investigators [9] assumed $N = 1$; however, experimental evidence suggests that the value of N is less than one [9–12]. Nash [10], Tanner [11], Carriere [12], and Page [14] have proposed other reattachment criteria. All these criteria are based on empirical coefficients obtained from experimental results. Since these experiments [12, 14] were conducted at low pressures which are not typical of the high pressures encountered in safety valve vent stack system, therefore, the Korst criterion was selected in this investigation and a recompression factor was determined by a series of high pressure experiments.

The freestream steam flow separates at the exit plane of the valve pipe. The separated flow forms a free shear layer which attaches to the valve pipe wall. It has been shown experimentally [12] that the wall geometry at the reattachment region, but not upstream and downstream of the reattachment region, has significant effects on the recompression process. Therefore, the addition of a converging or diverging section to the vent stack, as shown in Fig. 2, can change the base pressure if the shear layer reattaches to this section. The vent pipe entrance configurations were investigated and the results are reported here.

Conservation Equations for the Turbulent Mixing Layer

The conservation of momentum, species, and energy were obtained by assuming the eddy viscosity as a function of x, $\epsilon_v = \epsilon_v(x)$, and the turbulent Lewis and Prandtl numbers were assumed equal to unity [5, 7, 15]:

$$\rho u\frac{\partial u}{\partial x} + \rho v\frac{\partial u}{\partial y} = \epsilon_v\frac{\partial^2 u}{\partial y^2} \tag{1}$$

$$\rho u\frac{\partial C_i}{\partial x} + \rho v\frac{\partial C_i}{\partial y} = \epsilon_v\frac{\partial^2 C_i}{\partial y^2} \tag{2}$$

$$\rho u\frac{\partial H}{\partial x} + \rho v\frac{\partial H}{\partial y} = \epsilon_v\frac{\partial^2 H}{\partial y^2}. \tag{3}$$

Comparing equations (1), (2), and (3), it is seen that the mass fractions of species, C_i, and the total enthalpy, H, are linearly related to the velocity. Defining $\phi = u/u_{2s}$ and applying boundary conditions for ϕ, $\phi = 0$ in the base and $\phi = 1$ in the freestream, the results are:

$$C_s = \{1 - [C_s]_b\}\phi + [C_s]_b \tag{4}$$

$$C_a = (1-\phi)[C_a]_b \tag{5}$$

$$\frac{1}{H_{2s}}\sum_{i=1}^{2}\int_0^T C_i C_{p_i}\,dT = \phi + \frac{[H]_b}{H_{2s}} - \frac{(u_{2s}\phi)^2}{2H_{2s}}. \tag{6}$$

The specific heats of steam and air cannot be assumed constant because of the large range of temperature variation encountered in practice. For the present work, empirical equations for the specific heats were used [17].

The fully developed mixing velocity profile employed in this work is an error function-type profile. This velocity profile was derived for negligible approach boundary layer thickness [6]. There are methods available [16] to account for an appreciable approaching boundary layer thickness; since there is a lack of data for approaching boundary layer in the valve pipe, the error function-type profile was selected as a first approximation.

The conservation of mass and energy in the base may be written as:

$$\left[G_a + \frac{\rho_{2s}u_{2s}x}{\sigma}\int_{\eta_{Ra}}^{\eta_d}\frac{\rho}{\rho_{2s}}\phi d\eta\right][C_a]_b = G_a + \frac{\rho_{2s}u_{2s}x}{\sigma}\int_{\eta_{Ra}}^{\eta_d} C_a\frac{\rho}{\rho_{2s}}\phi d\eta \tag{7}$$

$$\left[G_a + \frac{\rho_{2s}u_{2s}x}{\sigma}\int_{\eta_{Ra}}^{\eta_d}\frac{\rho}{\rho_{2s}}\phi d\eta\right][H]_b = G_a H_a + \frac{\rho_{2s}u_{2s}x}{\sigma}\int_{\eta_{Ra}}^{\eta_d}\frac{\rho}{\rho_{2s}}\phi H d\eta \tag{8}$$

where

$$[H]_b = \sum_{i=1}^{2}\int_0^{T_b} C_i C_{pi}\,dT$$

and

$$G_a = \frac{\rho_{2s}u_{2s}x}{\sigma}\left[\int_{\eta_{Ra}}^{\eta_d}\frac{\rho}{\rho_{2s}}\phi d\eta - \int_{\eta_{Ra}}^{\eta_j}\frac{\rho}{\rho_{2s}}\phi d\eta\right],$$

where G_a is the mass flowrate between the jet-boundary and the discriminating streamlines. The jet-boundary streamline, η_j, separates the steam flow originally in the jet from the air flow entrained due to mixing, see Fig. 4. The discriminating streamline is located above the jet-boundary streamline, j-streamline, with secondary flow of air, on the j-streamline with no secondary flow of air, and blew the j-streamline with steam blowback. The streamline Ra is a streamline within the freestream flow. η is a dimensionless coordinate and defined as $\sigma y/x$, where σ is the jet spread parameter and function of Reynolds and Mach numbers [18, 19]

To complete the set of equations, there are two more equations for the d and j streamlines.

$$\int_{\eta_{Ra}}^{\eta_j}\frac{\rho}{\rho_{2s}}\phi d\eta = \int_{\eta_{Ra}}^{\eta_{Rs}}\frac{\rho}{\rho_{2s}}\phi(1-\phi)d\eta, \tag{9}$$

and

$$\frac{P_{0d}}{P_b} = N\frac{P_4}{P_b} = \left[1 + \frac{k_{2s}(k_1-1)}{2k_d}\frac{\rho_d}{\rho_{2s}}(\mathrm{M}_{2s}\phi)^2\right]^{k_d/(k_d-1)} \tag{10}$$

where

$$k_d = \frac{\sum_{i=1}^{2} C_i C_{p_i}}{\sum_{i=1}^{2} C_i C_{v_i}}.$$

Equations (4) through (10) are a complete set and can be solved for zero secondary flow, $G_a = 0$ or $\eta_j = \eta_d$. The only unknown in this set is the recompression factor, N, which must be determined experimentally.

Even though the original mixing layer analysis was developed for two-dimensional flowfield [6, 8], it has extensively been used in axisymmetric mixing layers. Superimposition of the two-dimensional mixing region on the corresponding axisymmetric inviscid flowfield proved to be very successful [9, 20, 21].

Experimental Program

In a typical power plant, the steam temperature is of the

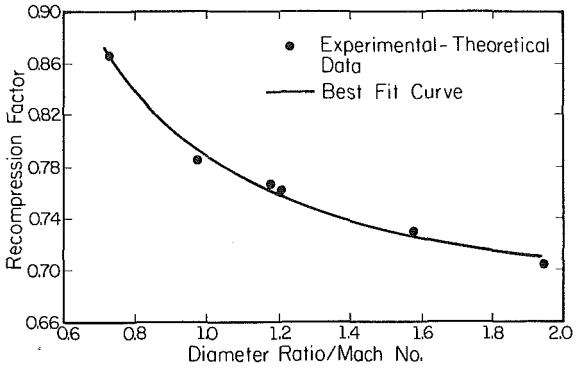

Fig. 5 Empirically determined base flow recompression factor versus diameter ratio/Mach number, $(D/d)/M_1$. (Uncertainty in recompression factor = ± 5 percent, in $(D/d)/M_1$ = ± 2 percent.)

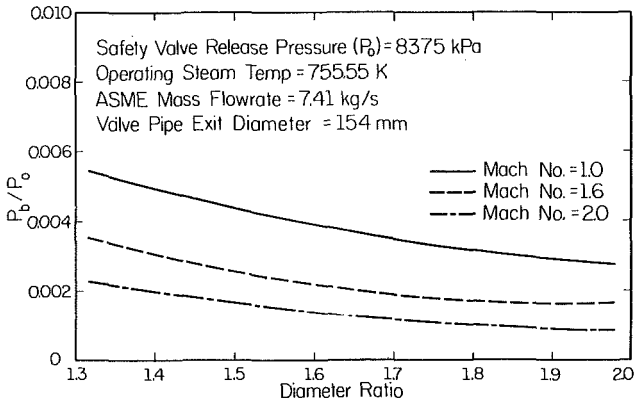

Fig. 6 Theoretical base-to-safety valve release pressure ratio versus the vent-to-valve pipe diameter ratio, D/d. ($P_{at}/P_0 = 0.012 > P_b/P_0$ in the given range of diameter ratio; thus back flow does not occur.)

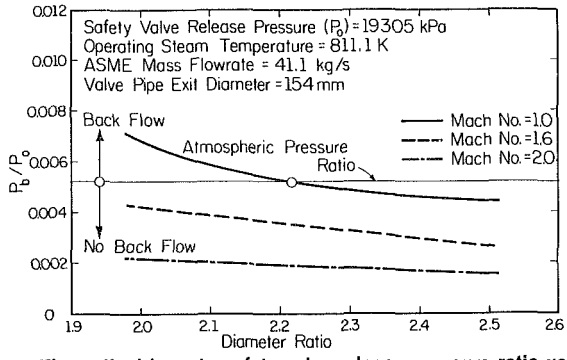

Fig. 7 Theoretical base-to-safety valve release pressure ratio versus the vent-to-value pipe diameter ratio, D/d. (For a diameter ratio less than 2.2, there would be back flow since $P_{at}/P_0 = 0.00525$ is less than P_b/P_0.)

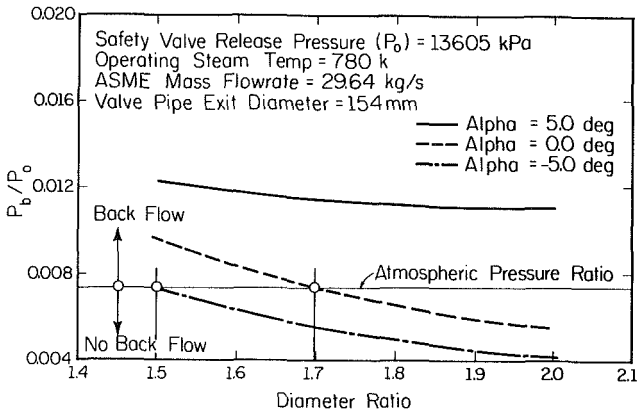

Fig. 8 Theoretical base-to-safety valve release pressure ratio versus the vent-to-value pipe diameter ratio, D/d, for three configurations of the vent pipe

order of 500°C and highly superheated. Since the length of the valve pipe is short, the flow through the valve pipe is approximately adiabatic and the total temperature in the region of concern stays high even though the velocity of the steam after exiting from the valve pipe could be 1000 m/s with a local temperature of approximately 160°C. For these conditions, the steam is still superheated. Therefore, in the flowfield, steam can be treated as an ideal gas; in our experiments, we modeled the flow with air. A series of high pressure air experiments were conducted to obtain experimental results for comparison with the theoretical analysis and to determine an empirical relationship for the recompression factor, N. Dry air was supplied from bottles of compressed air at a maximum pressure level of 1.75×10^4 kPa, at an ambient temperature of 25°C and a total maximum volume of 55 m^3. Steady-state operation was possible for one minute with a stagnation pressure level of 3.62×10^3 kPa and a nozzle throat diameter of 10 mm. The flow exited the stagnation chamber through a smooth elliptical converging nozzle with throat diameter of 10 mm and expanded through a Mach 2 nozzle, a Mach 1.5 nozzle, or a sudden enlargement tube which had a 21.5 mm long section of 15 mm inside diameter. The exit plane diameters of the M = 2 and M = 1.5 nozzles were 13.3 mm and 10.9, respectively. Both nozzle throat diameters were 10 mm. Three 762 mm long tubes with inside diameters of 19.05 mm, 25.4 mm, and 31.75 mm were used as vent stacks. In all combinations of nozzles and tubes, the stagnation and base pressures were measured.

Results

For a negligible approach boundary layer, the Mach number at the exit plane of the valve pipe, M_1, and the vent-to-valve pipe diameter ratio, D/d, have a significant effect on the base pressure and the recompression factor. A correlation between the recompression factor, N, and $(D/d)/M_1$ was achieved by determining an N that produced the same theoretical base pressure as was obtained experimentally at given values of $(D/d)/M_1$. Then, as shown in Fig. 5, a curve was fitted to these data.

In order to compare the results of the present work with previous work, input conditions to equations (4) through (10) were taken from the work of Liao [3] and Brandmaier [4]. Using two different vent pipe diameters, namely 202.7 mm and 254.5 mm, Liao has shown that both pipes satisfy all his criteria for the vent pipe design but the smaller pipe, 202.7 mm, fails to satisfy his momentum criterion. The momentum criterion imposed by Liao is, in our opinion, questionable. If this limit is removed from Liao's one-dimensional analysis, his results are in agreement with the results of the present paper. Figure 6 shows the base-to-stagnation pressure ratio versus the vent-to-valve pipe diameter ratio for various Mech numbers at the exit plane of the valve pipe. Since there is no available experimental data for the valve pipe exit in the vent-stack system, a conservative estimate of the back flow potential can be made by assuming $M_1 = 1$. Even with this conservative choked flow assumption at the valve pipe exit, both vent pipes satisfy the design condition for a vent pipe. As a result, Liao's analysis overestimates the vent pipe size. Brandmaier [4] has examined three different vent sizes, namely 304.8 mm, 336.5 mm, and 387.3 mm diameters. He found that 336.5 mm diameter vent pipe was the smallest one with no back flow. For the conservative $M_1 = 1$ assumption, Fig. 7 shows that the base pressure predicted for this vent pipe is 112.8 kPa which is somewhat greater than atmospheric pressure and back flow is likely. The base pressure for the vent pipe with a diameter of 387.3 mm is 84.67 kPa which is well below atmospheric pressure, thus, this vent pipe is a

better choice. Therefore, Brandmaier's analysis underestimates the vent pipe size according to the results of the current analysis.

Figure 8 illustrates the effect of different geometries of the vent pipe entrance section on steam back flow. For the five degree converging configuration, back flow occurs for the entire calculated range shown in Fig. 8. For the straight and five degree diverging configurations, back flow occurs if the vent pipe-to-valve pipe diameter ratios are less than 1.7 and 1.5, respectively.

Conclusions and Recommendations

As a result of this theoretical and experimental investigation of the safety valve and vent stack problem, the following conclusions can be drawn:

(1) The flow nonuniformity after exiting from the valve pipe is significant. Therefore, the two-dimensional axisymmetric analysis is a realistic approach to modeling the flow and gives consistent results in all ranges of the safety valve release pressure. In contrast, a one-dimensional analysis could underestimate or overestimate the base pressure in different ranges of the safety valve release pressure.

(2) The proposed theoretical analysis with experimentally determined recompression factor together with the computer program provides a useful tool for the design of a safety valve vent stack system even though the boundary layer and Mach number data is not available at the exit of the valve pipe. Assuming a negligible boundary layer gives a lower base pressure while assuming a sonic flow instead of a supersonic flow at the valve pipe exit gives a higher base pressure. Due to the short length of the valve pipe, the boundary layer thickness would not be significant and the flow could be supersonic, therefore, assuming a thin boundary layer and a sonic flow is a conservative approach.

(3) This investigation showed that the vent pipe with a diverging entrance section is the best configuration for the safety vent stack system.

For further improvement of this design approach, it is recommended that the safety valve manufacturers should provide static and stagnation pressure data and boundary layer information at the valve pipe exit. These data could be obtained during experiments of the safety valve to determine its mass flowrate characteristics.

References

1 Benjamin, M. W., "Sizing Vent Piping for Safety Valves," *Heating, Piping, and Air Conditioning*, Oct. 1941, pp. 615–619.

2 Benjamin, M. W., "How to Design Safety Valve Vent Piping of the Umbrella Type," *Heating, Piping, and Air Conditioning*, Dec. 1943, pp. 655–659.

3 Liao, G. S., "Analysis of Power Plant Safety and Relief Valve Vent Stacks," ASME *Journal of Engineering for Power*, Oct. 1975, pp. 484–494.

4 Brandmaier, H. E., and Knebel, M. E., "Steam Flow Through Safety Valve Vent Pipes," ASME JOURNAL OF FLUIDS ENGINEERING, June 1976, pp. 199–207.

5 Samimy, M., "An Experimental and Theoretical Investigation of the Fluid Dynamics of Safety Vent-Stacks," M.S. thesis, Department of Mechanical and Industrial Engineering, University of Illinois at Urbana-Champaign, Urbana, IL 61801.

6 Korst, H. H., Page, R. H., and Childs, M. E., "A Theory for Base Pressure in Transonic and Supersonic Flow," University of Illinois ME Technical Note 392-2, Mar. 1955.

7 Korst, H. H., "A Theory for Base Pressures in Transonic and Supersonic Flow," ASME *Journal of Applied Mechanics*, Dec. 1956, pp. 593–600.

8 Korst, H. H., Chow, W. L., and Zumwalt, G. W., "Research on Transonic and Supersonic Flow of a Real Fluid at Abrupt Increases in Cross Section," University of Illinois ME Technical Report 392-5, Dec. 1959.

9 Page, R. H., "A Review of Component Analysis of Base Pressure for Supersonic Turbulent Flow," *Proc. 10th International Symposium on Space Technology and Science*, Tokyo, Japan, 1973.

10 Nash, J. F., "An Analysis of Two Dimensional Turbulent Base Flow, Including the Effect of the Approaching Boundary Layer," R. and M. No. 3344, Her Majesty's Stationary Office, London, England, 1963.

11 Tanner, M., "Two Different Theoretical Approaches to the Base Pressure Problem in Two-Dimensional Super-sonic Flow," *Aeronautical Quarterly*, Vol. 29, May 1978, pp. 114–130.

12 Carriere, P., Sirieix, M., and Delery, J., "Methodes de Calcul des Ecoulements Turbulents Decolles en Supersonique," *Prog. Aerospace Sci.*, Vol. 16, No. 4, 1975, pp. 385–429.

13 Chow, W. L. and Addy, A. L., "Interactions Between Primary and Secondary Streams of Supersonic Ejector Systems and Their Performance Characteristics," *AIAA Journal*, Vol. 2, No. 4, Apr. 1964, pp. 686–695.

14 Page, R. H., Hill, W. G., Jr., and Kessler, T. J., "Reattachment of Two-Dimensional Supersonic Turbulent Flows," 1967 ASME Paper No. 67-FE-20.

15 Vasiliu, T., "Turbulent Mixing of a Rocket Exhaust Jet with a Supersonic Stream Including Chemical Reactions," *Journal of the Aerospace Science*, Jan. 1962, pp. 19–28.

16 Kirk, F. N., "An Approximate Theory of Base Pressure in Two-Dimensional Flow at Supersonic Speeds," RAE TN, AER02377, 1959.

17 Van Wylen, G. J. and Sonntag, R. E., *Fundamentals of Classical Thermodynamics, SI Version, Second Edition*, Wiley, 1978.

18 Channapragada, R. S., "Compressible Jet Spread Parameter for Mixing Zone Analyses," *AIAA Journal*, Vol. 1, No. 9, 1963, pp. 2188–2190.

19 Bauer, R. C., "Another Estimate of the Similarity Parameter for Turbulent Mixing," *AIAA Journal*, Vol. 6, No. 5, 1968, pp. 925–927.

20 Wagner, B. and White, R. A., "Supersonic Base Flow Problem in Presence of an Exhaust Jet," *AIAA Journal*, Vol. 18, No. 8, 1980, pp. 876–882.

21 Hong, Y. S., "Base Flow Environment Analysis of a Single Engine Booster," *Journal of Spacecraft*, Vol. 9, No. 7, 1972, pp. 481–482.

D. C. Wiggert
Department of Civil and Sanitary Engineering,
Michigan State University,
East Lansing, Mich. 48824

R. S. Otwell
McNamee, Porter and Seeley,
Ann Arbor, Mich.

F. J. Hatfield
Department of Civil and Sanitary Engineering,
Michigan State University,
East Lansing, Mich. 48824

The Effect of Elbow Restraint on Pressure Transients

Transient pressure in piped liquid is a function of structural restraint at elbows. If supported rigidly, an elbow causes no appreciable alteration of the pressure transient generated by rapid valve closure. However, if the support is relaxed, significant alteration is observed. Motion of the elbow, driven by axial stresses in the pipe and by the liquid pressure, causes the alteration. Experimental data are presented to support these contentions. Two mechanisms are proposed as causes of the observed interaction of transient pressure and pipe motion. Verification that the mechanisms have been identified correctly is given by comparison of the experimental data to predictions of an analytical model that incorporates the mechanisms.

Introduction

Problem Description. Piping systems used for transfer of pressurized liquids operate under time-varying conditions imposed by pump and valve operation. Traditionally, to analyze the unsteady behavior of the liquid, the equations of motion and continuity of the liquid are solved without regard to motion of the piping. The transients propagate at the acoustic velocity, or wavespeed, of the liquid in the pipe. The diameter, wall thickness, and elastic modulus of the piping are used in computing the wavespeed, after which the liquid is assumed to be flowing through a straight, rigid pipe.

Recently there has been concern that the transient behavior of liquid in a piping system that is neither rigid nor straight may differ from that predicted by a traditional rigid pipe analysis. It is reasoned that the dynamic forces exerted by the liquid at fittings where flow direction or area changes (elbows, tees, valves, and reducers) can set the pipe in motion and that such motion can alter the liquid transient. Some investigators have suggested that this alteration is either negligible or that rigid pipe analysis provides a conservative estimate of the transient pressure because of the transfer of energy out of the liquid and into the structure. However, experiments have shown that in some systems the elasticity of the piping amplifies transient pressure in the liquid to a significant degree.

Motion of piping is caused by dynamic forces in the liquid and the pipe wall. The amplitude and frequency of the pipe motion also are functions of the mechanical properties and support conditions of the piping. Accurate analysis of pressure transients in piping requires formulation of the mechanisms by which liquid and piping are coupled, and incorporation of parameters describing the pipe structure.

Background. In the late 1800s Joukowsky [1] determined that the wavespeed of liquid in a pipe, and hence the speed at which liquid discontinuities propagate, is related to the relative circumferential stiffness of the pipe. He assumed that pressure is uniform across any cross-section and neglected the radial inertia of the liquid, mass of the pipe wall, and axial and bending stresses in the wall.

There are several other ways in which pipe properties affect the dynamic response of contained liquid. The following discussion explores two such mechanisms that appear to be significant but are neglected in contemporary engineering practice.

Strain-Related Coupling. Strain-related, or Poisson, coupling results from the transformation of circumferential strain caused by internal pressure to axial strain:

$$\epsilon_x = -\nu\epsilon_\theta \tag{1}$$

Skalak [2] extended Joukowsky's formulation to include Poisson effects. The extension consisted of treating the pipe wall as an elastic membrane to include the axial stresses and axial inertia of the pipe. For sudden valve closure, a tension wave was found to propagate in the pipe wall at a wavespeed near that of the pipe material; hence, a "precursor" wave travels ahead of the main pressure wave in the liquid. The axial tension is a Poisson effect in response to pipe dilation caused by the pressure transient. An increase in liquid pressure due to the tension wave was identified, but this increase was small because it was caused by the small contraction in pipe diameter due to the tension wave; it is a second-order Poisson effect. Thorley [3] completed a study similar to Skalak's, including experimental validation of the theory. Williams [4] also conducted a similar study and found that longitudinal and flexural motion of piping caused damping that was greater than the viscous damping in the liquid.

Walker and Phillips [5] formulated a one-dimensional, axisymmetric system of six equations that included the radial and axial equations of motion of the pipe wall, two constitutive equations for the pipe wall, and the equations of motion and continuity for the liquid. They reported that the method "retains much of the rigor of the axisymmetric, two-dimensional approach" of Lin and Morgan [6]. They found their method ideal for transients where the generation of the pressure pulse occurs in several microseceonds, and that the

Contributed by the Fluids Engineering Division for publication in the JOURNAL OF FLUIDS ENGINEERING. Manuscript received by the Fluids Engineering Division, May 17, 1984.

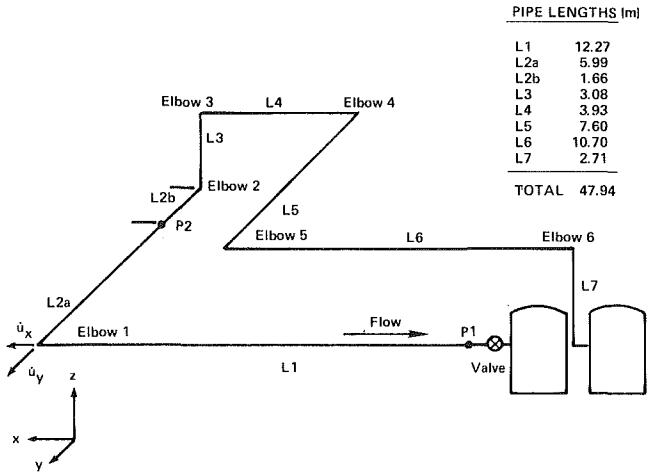

Fig. 1 Experimental setup

classical waterhammer equations are adequate for longer pulses.

None of these studies considered the possiblity that a fitting, such as an ellow, might move in response to the precursor wave and alter the transient response of the liquid.

Pressure Resultant Coupling. At fittings where the pipe area or direction changes, pressure exerts a localized force on the pipe. Hatfield et al. [7] developed a general solution procedure for this type of fluid-pipe interaction with harmonic loadings. Coupling took place at fittings only, hence the Poisson effect was not considered. Wood [8] studied the effect of pipe motion on liquid behavior as a function of structural parameters and valve closure rate. He concluded that pipe motion could significantly alter pressures. Wood and Chao [9] set up an experimental apparatus that included an elbow between two lengths of pipe. With the elbow unrestrained, there was alteration of the response in the form of an oscillation about the pressure observed for the restrained elbow case. This alteration was thought to be caused by motion of the elbow driven first by a stress wave in the pipe and then by the pressure wave. An analytical method was devised that used the measured structural velocities from the experiment as input into flow conservation relationships at the elbow in the liquid model. Favorable comparisons were shown between this analysis and the experiment.

Ellis [10] developed an analytical procedure to couple liquid equations with the equations for axial motion of piping. Coupling took place at fittings such as valves, elbows and tees, and mass and stiffness were lumped at the fittings. The Poisson effect was not incorporated in the analysis. Schwirian and Karabin [11], Giesecke [12], Otwell [13], and Wiggert and Hatfield [14] all developed general analytical techniques to couple liquid and pipe equations in order to study the dynamics of general piping systems driven by non-periodic excitation; coupling was imposed only at fittings.

In all of the above studies, the effect of support and piping stiffness was shown to be significant. In contrast, Swaffield [15] completed a study which concluded that an elbow's influence was solely dependent on its geometry and not on its restraint. However, it was reported subsequently that the restraints had not been sufficient to prevent elbow motion [16].

Objective. Although there is much evidence suggesting that the dynamic behavior of liquid can be influenced by the piping system that contains it, the actual mechanisms are not fully understood. Two types of coupling have been identified but their significance and their relationship to each other have not been quantified. Little experimental validation has been attempted.

One objective of this study was to conduct an experiment that isolated the mechanisms of liquid-pipe interaction. Structural restraint of an elbow was the independent variable. Additionally, a numerical model was developed that incorporates structural parameters necessary to represent the coupling mechanisms.

Experiment

The experiment enables observation of the alteration of a pressure transient for varied structural restraint at an elbow. Thus the pipe parameters influencing the alteration could be determined. One extreme was to fix the elbow rigidly to determine if geometric aspects of the elbow caused significant alteration of the liquid behavior. Once that was established, the elbow restraint was removed, and alteration of the liquid behavior caused by pipe motion was observed.

Experimental Setup. Figure 1 is a schematic of the pipe setup. It includes 47.9 meters of 26 mm inside diameter copper pipe. The pipe material constants are: ρ_t = 8940 kg/m^3, E = 117 GPa, ν = 0.34, and e = 1.27 mm. The system has a total of six elbows with radius of 20.6 mm. The elbows are standard copper pipe fittings.

The elbow to be studied is elbow 1, and the connecting pipe reaches L1 and L2 are suspended by wires that contribute negligible stiffness, inertia and damping for motion in the plane of the elbow. At the upstream end is a constant pressure tank and at the downstream end is a valve with a closure time of approximately 4 ms. The valve is similar to one used by Wood [9]. The valve body is fastened rigidly to the concrete floor. Water, ρ_f = 998 kg/m^3, is the contained liquid.

Rigid connections to concrete walls or floors are used at elbows 3, 4, and 5, and, as needed, at elbows 1 and 2. Elbow 6 could not be rigidly supported.

Data Acquisition. Flush-mounted quartz pressure transducers (PCB Model 111A26) are used to measure the dynamic pressure at two locations, P1 and P2, as shown in Fig. 1. Quartz accelerometers (PCB Model 302A) are used to measure the movement of elbow 1 in orthogonal directions.

Data are recorded and stored on a DEC 11/02 minicomputer, and the transducer outputs are run through an A/D converter and stored as digital quantities. The accelerometer signals are integrated electronically to record structural velocities.

Nomenclature

a = wavespeed in infinite medium
A = cross-sectional area
C = wavespeed
e = pipe wall thickness
E = Young's modulus of elasticity
E^* = $E/(1-\nu^2)$
K = bulk modulus of liquid
K = stiffness coefficient
p = pressure
r = pipe inside radius
t = time
u = pipe axial displacement
$\dot{u}$ = pipe axial velocity
V = liquid velocity
x = distance along pipe axis
ϵ = strain
λ = characteristic roots
ν = Poisson ratio
ρ = density
σ = axial stress

Subscripts

f = liquid
t = pipe
x = x-direction
y = y-direction
θ = circumferential direction

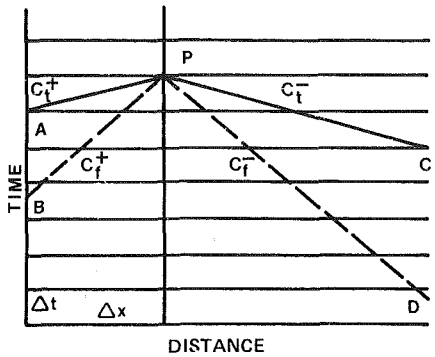

Fig. 2 Characteristics representation

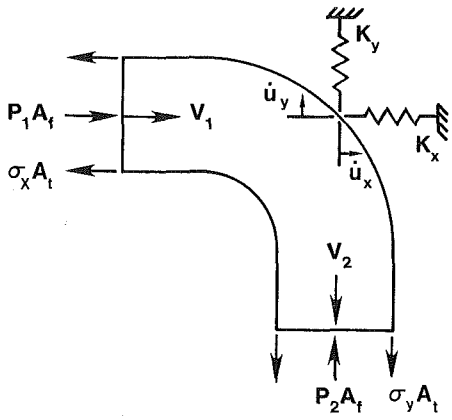

Fig. 3 Elbow

Experimental observations were terminated at the onset of column separation, about 80 ms.

Experimental Uncertainty. For the pressure transducers and accelerometers, the uncertainty is estimated by the manufacturer at ±3 percent full scale, resulting in an accuracy within ±45 kPa for pressure and ±0.015 m/s for velocity. Another possible source of error is the conversion of the analog voltages to digital quantities by the A/D converter. The uncertainty of that process is 0.03 percent.

Analytical Development

To support the hypothesis that the experimental results demonstrate strain-related and pressure resultant coupling, the observations were compared to the predictions of an analytical model incorporating those mechanisms. The model utilizes the following assumptions:

1. Piping is prismatic, round, thin-walled, linearly elastic, homogeneous, and isotropic.
2. Caviation and column separation do not occur.
3. Damping is negligible.
4. A phenomenon may be neglected if its fundamental frequency is two or more orders of magnitude greater than the fundamental frequency of the liquid column. For the experimental piping, this assumption permits neglect of transverse pressure variation, inertia associated with deformation of the pipe cross section, and pressure and density differences along the length of an elbow.
5. Transverse motion of a length of pipe is represented adequately by its first flexural mode.

These simplifying assumptions are valid for the experimental piping but not necessarily for all pipe systems. Therefore, caution is advised in applying the analytical model to other systems.

Four-Equation Model. Internal pressure stresses the pipe circumferentially and axially due to the Poisson effect. A four-equation model has been developed [17] that includes as dependent variables the liquid pressure p, liquid velocity V, axial pipe stress σ, and axial pipe velocity u. The model is based on the work of Walker and Phillips [5] and utilizes their observation that radial inertia is insignificant for pressure rise times in the millisecond range. This simplification permits their six equation model to be reduced to four equations. Following are the axial momentum equations for the liquid and pipe wall, a continuity equation for the liquid, and a constitutive equation for the pipe wall:

$$\rho_f \frac{\partial V}{\partial t} + \frac{\partial p}{\partial x} = 0 \tag{2}$$

$$\frac{\partial \sigma}{\partial x} - \rho_t \frac{\partial \dot{u}}{\partial t} = 0 \tag{3}$$

$$\left(\frac{1}{K} + \frac{2r}{eE^*}\right)\frac{\partial p}{\partial t} - 2\nu \frac{\partial \dot{u}}{\partial x} + \frac{\partial V}{\partial x} = 0 \tag{4}$$

$$\frac{\partial \sigma}{\partial t} - E\frac{\partial \dot{u}}{\partial x} - \frac{r\nu}{e}\frac{\partial p}{\partial t} = 0 \tag{5}$$

Method of Characteristics Representation. Equations (2)–(5) are transformed from partial differential equations into ordinary differential equations by the method of characteristics [18]. The characteristic roots are the wavespeeds in the liquid-pipe system. The first two roots are the liquid wavespeeds:

$$\lambda_{1,2} = \pm C_f = \pm \frac{a_f}{J} Q1 \tag{6}$$

and the second two are the pipe wavespeeds:

$$\lambda_{3,4} = \pm C_t = \pm \frac{a_t}{J} H\, Q2 \tag{7}$$

where

$$a_t = (E/\rho_t)^{1/2},\quad a_f = (K/\rho_f)^{1/2} \tag{8}$$

$$J = \left[1 + \frac{2rK}{eE^*}\right]^{1/2},\quad H = \left[1 + \frac{2rK}{eE}\right]^{1/2} \tag{9}$$

$$Q1 = \left[1 + \frac{\nu^2 2r\,\rho_f}{e\rho_t(1-q)}\right]^{1/2},\quad Q2 = \left[1 - \frac{\nu^2 2r\,\rho_f}{e\rho_t q(1-q)}\right]^{1/2} \tag{10}$$

$$q = (a_t/a_f)^2\left[1 + \frac{2rk}{eE}\right] \tag{11}$$

The compatibility equations are:

$$\frac{dp}{dt} \pm \rho_f C_f \frac{dV}{dt} \pm \rho_t C_f G_f \frac{d\dot{u}}{dt} - G_f \frac{d\sigma}{dt} = 0 \tag{12}$$

which are valid along $\frac{dx}{dt} = \pm C_f$, and:

$$\frac{dp}{dt} \pm \rho_f C_t \frac{dV}{dt} \pm \rho_t C_t G_t \frac{d\dot{u}}{dt} - G_t \frac{d\sigma}{dt} = 0 \tag{13}$$

which are valid along $\frac{dx}{dt} = \pm C_t$

where

$$G_f = \frac{e}{r\nu}(1 - Q1^2),\quad G_t = \frac{e}{r\nu}[1 - (a_t/a_f)^2 H^2 Q2^2] \tag{14}$$

Figure 2 shows the characteristic representation in the x-t plane. Equations (12) and (13) are integrated along their respective characteristic lines; the two lines with positive slope are designated as $C+$ characteristics and the two with negative slopes are $C-$ characteristics. The four resulting finite difference equations are solved simultaneously for

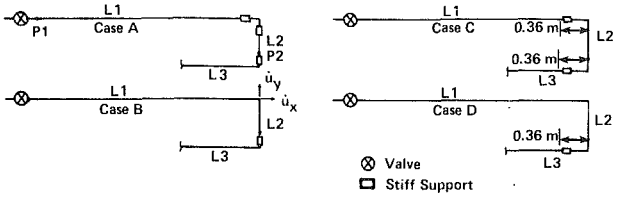

Fig. 4 Structural restraint for four experimental cases

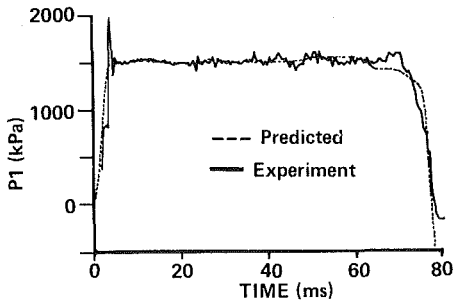

Fig. 5 Comparison of experimental and predicted pressures for Case A

discrete points along the pipe. At an elbow, additional information is necessary.

Elbow Boundary. An elbow is shown schematically in Fig. 3. Only motion in the plane of the elbow is considered since out of plane motion is not coupled to internal pressure. Because of the comparatively short length of the elbow, the variation of pressure and density from point 1 to point 2 is negligible, and flow conservation may be expressed:

$$(V_1 - \dot{u}_x) = (V_2 + \dot{u}_y) \tag{15}$$

Flexural stiffness of the upstream and downstream pipe reaches connected to the elbow are denoted K_y and K_x, respectively. For the support conditions of the experiment, the effective masses associated with flexural displacements were found to be comparatively small and therefore are neglected. The equations of motion of the elbow simplify to:

$$p_1 A_f - \sigma_x A_t = K_x u_x, p_2 A_f - \sigma_y A_t = K_y u_y \tag{16}$$

Equations (15) and (16), the pressure invariance condition, and the compatibility equations (12) and (13) are solved simultaneously to determine pressure, stresses and velocities at an elbow.

Comparison of Experimental and Numerical Results

Four different conditions of structural restraint were investigated, both experimentally and analytically. Figure 4 shows the restraints. The first setup, Case A, has elbows 1 and 2 totally restrained. For the second setup, Case B, the stiff supports were removed at elbow 1 so that it is restrained only by the axial stiffnesses of legs L1 and L2. The third setup, Case C, has two restraints placed 0.36 m from elbows 1 and 2. Axial translation of L2 is restrained by the bending stiffness of the two short lengths. This arrangement is more flexible than Case B because pipes are much stiffer axially than in flexure. The fourth setup, Case D, represents a combination of Case B and Case C.

Responses were predicted by a computer program incorporating the solution described in the preceding section. The flexural stiffness coefficients, K, were calculated by the stiffness method [19]. Flexural stiffnesses of the long lengths (L1 and L2) are comparatively small and were neglected. For Case C, the two 0.36 m lengths each contribute a stiffness of 94800 N/m for translation in the y-direction. For Case D, K was determined to be 88700 N/m for the one short length. Axial stiffness is included in the four-equation model.

Case A: Immobile Elbow. Motion of elbow 1 was restrained by two rigid supports. Figure 5 shows the predicted and experimental pressure responses at the valve. The pressure spike at 4 ms on the experimental trace is from valve flutter and does not affect the subsequent pipe response. The remainder of the trace is essentially flat, with only small amplitude, high frequency oscillations. If the pressure pulse had been reflected at the elbow, it would have arrived at the valve in approximately 20 ms, but this is not apparent. In the 40–60 ms range larger oscillations occur. These are from the upstream elbow that could not be supported as rigidly. Notice the predicted response is not flat as would be predicted by a traditional two-equation model, the variation being caused by the second-order Poisson effect. For the analytical prediction, velocities of the elbow, $\dot{u}_x$ and $\dot{u}_y$, are identically zero.

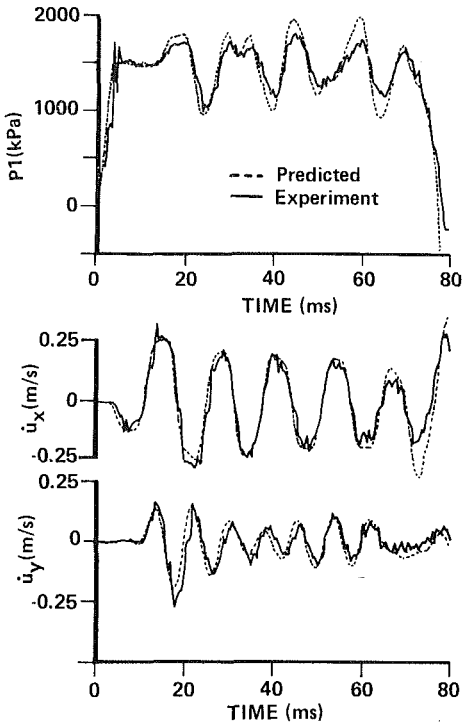

Fig. 6 Comparison of experimental and predicted pressures and elbow velocities for Case B

Case B: Axial Stiffness: The supports on both sides of elbow 1 are now removed, and the elbow is restrained in its plane by the axial stiffness of leg L1 in the x-direction and the axial stiffness of leg L2 in the y direction. An examination of Fig. 6 shows that the pressure response at P1 is significantly different from that of Case A. Elbow motion is initially in the negative x-direction and is driven by the precursor stress wave; this action results in an increase in the liquid pressure. The pressure increase propagates to the valve and is recorded at 13 ms. The elbow motion at 10 ms is the result of the primary pressure pulse driving the elbow in the positive x and y-directions, resulting in a decrease in pressure as shown on the P1 curve at 20 ms. The elbow continues to vibrate at the natural frequencies of the piping, and the pressure response is a combined effect of the resultant velocities. The maximum recorded pressure, occurring at 44 ms, is 22 percent above that which would occur in a system with no elbow motion as in Case A. The maximum elbow velocity recorded is 0.27 m/s and the maximum displacement is approximately 0.5 mm.

Case C: Bending Stiffness. The two elbows and the connecting reach L2 are allowed to translate in the y-direction by the flexibility of the attached piping. Because of the large axial stiffness of these short attached lengths, translation in the x-direction is negligible. As shown in Fig. 7, the frequency of vibration in the y-direction is much lower than that of Case

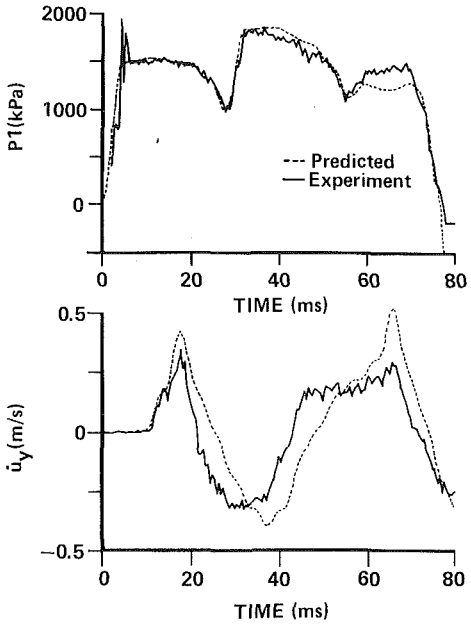

Fig. 7 Comparison of experimental and predicted pressures and elbow velocities for Case C

B. The pressure response also displays the lower frequency. The maximum recorded pressure at P1 is 25 percent above that of Case A. The predicted elbow velocity is slightly out of phase with the experimental data, suggesting that the estimated flexural stiffness K was too small.

Case D: Combined Effects. The support near elbow 1 is now removed so that it is restrained by the axial stiffness of leg L1 in the x-direction and by the flexural stiffness of one 0.36 m length in the y-direction. As shown in Fig. 8, the x-direction velocity is similar to that of Case B, and the y-direction velocity is similar to that of Case C. The pressure response shows the high frequency component of Case B superimposed on the low frequency component Case C. The pressure oscillation is the greatest of all cases, and the maximum pressure at 46 ms is 33 percent greater than that of Case A. The predicted elbow velocities compare well to those observed in the x-direction, but again are slightly out of phase in the y-direction.

Discussion and Conclusions

In the experiment, no pressure reflection from the immobile elbow was observed. However, when the elbow was not fully restrained, alterations of the transient were observed, including a 33 percent increase in maximum pressure. These alterations are related to the direction and amplitude of the motion of the elbow and are dependent on support conditions.

An analytical model that incorporates strain-related and pressure resultant coupling accurately predicted the experimental results. Therefore, the importance of including both those mechanisms in engineering analysis is established. Such procedures also may need to include effects that were not significant for the pipe system used in this study.

Acknowledgment

The support of the National Science Foundation, through Grant No. MEA-82009049, is gratefully acknowledged.

References

1 Joukowsky, N. E., translated by O. Simin as "Water Hammer," *Proceedings*, American Water Works Association, Vol. 24, 1904, pp. 341-424.

2 Skalak, R., "An Extension of the Theory of Water Hammer," TRANS. *ASME*, Vol. 78, No. 1, 1956, pp. 105-116.

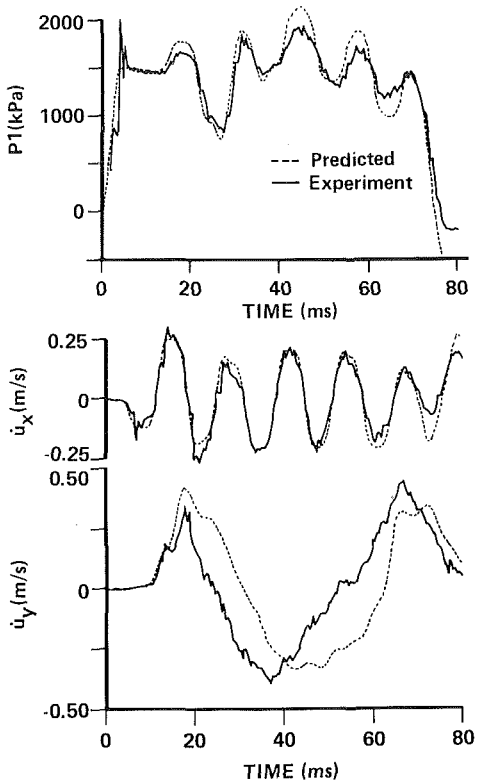

Fig. 8 Comparison of experimental and predicted pressures and elbow velocities for Case D

3 Thorley, A. R. D., "Pressure Transients in Hydraulic Pipelines," ASME *Journal of Basic Engineering*, Vol. 91, Sept. 1969, pp. 453-461.

4 Williams, D. J., "Waterhammer in Non-Rigid Pipes: Precursor Waves and Mechanical Damping," *Journal of Mechanical Engineering Science*, Institute of Mechanical Engineers, Vol. 19, No. 6, 1977, pp. 237-242.

5 Walker, J. S., Phillips, J. W., "Pulse Propagation in Fluid Filled Tubes," ASME *Journal of Applied Mech.*, Mar. 1977, pp. 31-35.

6 Lin, T. C., and Morgan, G. W., "Wave Propagation Through Fluid Contained in a Cylindrical, Elastic Shell," *Journal of Acoustical Society of America*, Vol. 28, No. 6, 1956, pp. 1165-1173.

7 Hatfield, F. J., Wiggert, D. C., and Otwell, R. S., "Fluid Structure Interaction in Piping by Component Synthesis," ASME JOURNAL OF FLUIDS ENGINEERING, Vol. 104, No. 3, Sept. 1982, pp. 318-325.

8 Wood, D. J., "Influence of Line Motion on Waterhammer Pressures," *Journal of Hydraulics Division, Proc. ASCE*, Vol. 95, May 1969, pp. 941-959.

9 Wood, D. J., and Chao, S. ,P., "Effect of Pipeline Junctions on Waterhammer Surges," *Transportation Engineering Journal, Proc. ASCE*, Vol. 97, Aug. 1971, pp. 441-456.

10 Ellis, J., "A Study of Pipe-Liquid Interaction Following Pump Trip and Check-Valve Closure in a Piping Station," *Proc. Third Intl. Conf. on Pressure Surges*, Vol. 1, BHRA Fluid Engr., Canterbury, England, Mar. 1980, pp. 203-220.

11 Schwirian, R. E., and Karabin, M. E., "Use of Spar Elements to Simulate Fluid-Solid Interaction in the Finite Element Analysis of Piping System Dynamics," *Symposium on Fluid Transients and Structural Interactions in Piping Systems*, ASME, June 1981, pp. 1-11.

12 Giesecke, H. D., "Calculations of Piping Response to Fluid Transients Including Effects of Fluid/Structure Interaction,' Sixth International Conference on Structural Mechanics in Reactor Technology, North-Holland Publishing Co., Aug. 1981.

13 Otwell, R. S., "The Effect of Elbow Translations on Pressure Transient Analysis of Piping Systems," *Fluid Transients and Fluid-Structure Interaction*, ASME PVP-Vol. 64, 1982, pp. 127-136.

14 Wiggert, D. C., and Hatfield, F. J., "Time Domain Analysis of Fluid-Structure Interaction in Multi-Degree-of-Freedom Piping System," *Proc. 4th Intl. Conf. on Pressure Surges*, BHRA, Sept. 1983.

15 Swaffield, J. A., "The Influence of Bends on Fluid Transients Propagated in Incompressible Pipe Flow," *Proc. Instn. Mechanical Engrs.*, Vol. 1983, Part 1, No. 29, 1968-1969, pp. 603-614.

16 Wilkinson, D. H., "Dynamic Response of Pipework Systems to Waterhammer," *Proc. Third Intl. Conf. on Pressure Surges*, Vol. 1, BHRA Fluid Engr., Canterbury, England, Mar. 1980, pp. 185-202.

17 Otwell, R. S., "The Effect of Elbow Restraint on Pressure Transients," Ph.D. dissertation, Michigan State University, 1984.

18 Forsythe, G. E., and Wasow, W. R., *Finite Difference Methods for Partial Differential Equations*, Wiley, 1960.

19 White, R. N., Gergly, P., and Sexsmith, R. G., *Structural Engineering*, Wiley, 1976.

Calculation of 1-*D* Unsteady Flows in Pipe Systems of I.C. Engines

T. Bulaty

H. Niessner

Brown Boveri and Co., Ltd.,
Lindenhof 3,
CH-5430 Wettingen, Baden,
Switzerland

*Linear finite-difference methods of higher than first-order accuracy applied to the calculation of 1-*D *unsteady flow inevitably produce numerical overshoot at discontinuities. Several remedies have been proposed in the past; a simple and effective one is flux correction. We propose it in the naive form, which destroys neither the order of accuracy nor the stability of the underlying method. Particular problems arise at the boundaries, where appropriate precautions help to fulfill the conservation laws. Additionally allowing for elasticity of the valve control system, results with acceptable accuracy are obtained in supercharging practice. A comparison of computing time, accuracy and storage requirements confirms the advantages of naive flux correction.*

Unsteady Flow Equations in the Form of Conservation Laws

The 1-*D* unsteady flow in a pipe is described by a system of differential equations for mass, impulse and energy. On the right-hand side this system includes perturbation terms for friction and viscosity, heat transfer and conductivity:

$$\frac{\partial}{\partial \mathfrak{C}}\begin{pmatrix}\rho\\ \rho u\\ \rho\left(e+\frac{u^2}{2}\right)\end{pmatrix}+\frac{\partial}{\partial x}\begin{pmatrix}\rho u\\ \rho u^2+p\\ \rho u\left(e+\frac{u^2}{2}+\frac{p}{\rho}\right)\end{pmatrix}=\begin{pmatrix}0\\ -\frac{\xi}{2d}\,\mathrm{sign}\,(u)\rho u^2+\frac{\partial}{\partial x}\left(\frac{4}{3}\eta\frac{\partial u}{\partial x}\right)\\ \frac{\xi}{2d}\rho/u/c_p(T_w-T)+\frac{\partial}{\partial x}\left(\lambda\frac{\partial T}{\partial x}+\frac{4}{3}\eta u\frac{\partial u}{\partial x}\right)\end{pmatrix} \quad (1)$$

where t = time, x = space, ρ = density, u = velocity, e = internal energy, p = pressure, ξ = friction coefficient, d = diameter, η = viscosity, c_p = specific heat, λ = conductivity, T = gas temperature, T_w = wall temperature. This system is of the form

$$\frac{\partial}{\partial \mathfrak{C}}W+\frac{\partial}{\partial x}F=W_t+F_x=S \quad (2)$$

where W, F, and S are vectors of dimension 3. The elements of $W=W(x,\ t)$ are called dependent, whereas x and t are called independent variables. Since $p=p(\rho,e)$ and ρ, u, e can be expressed by the elements of W, F is a function of W, i.e., $F=F(W)$. With zero right-hand side (i.e., $S=0$) Lax and Wendroff [1] call such a system a system of conservation laws. If all eigenvalues of the matrix $F'=\partial F/\partial W$ are real, which is true for (1), this system is hyperbolic.

The conservation law form of the hyperbolic equations has the favorable property that conservative finite-difference methods, like the method of Lax-Wendroff discussed in the next section, produce solutions automatically satisfying the Rankine-Hugoniot relations across a shock, thereby greatly facilitating accurate shock calculation.

Substituting the variables in (1) by representative mean values from turbocharging practice, we can estimate the importance of each perturbation term. Using SI units, we obtain the following magnitudes:

$$0\{W_t+F_x(W)\}\sim\begin{pmatrix}500\\ 2\cdot10^5\\ 5\cdot10^8\end{pmatrix};\ 0\{S\}\sim\begin{pmatrix}0\\ 1600+0.02\\ 3\cdot10^6+50+2.5\end{pmatrix}$$

Taking into account the magnitude of the left-hand side in the impulse equation (2nd row), the influence of the viscosity on the right-hand side is negligible compared to that of the friction. On the right-hand side of the energy equation (3rd row), the heat convection prevails strongly relative to the viscosity and heat conduction. It is therefore necessary to take into consideration only the first disturbance terms, e.g., friction and heat transfer. Even so, these disturbances are quite small and it is convenient to treat them to one accuracy order lower than the integration of the left-hand side.

Computational Methods for Calculating the Solution

Practical one-dimensional unsteady flow calculations in supercharging of internal combustion engines came into use more than 30 years ago [2]. Soon the time-consuming hand calculations with charts were substituted by computer calculations, and numerical methods gained importance in this field.

The first computer programs were based on the hand calculation using the true method of characteristics: They

Contributed by the Fluids Engineering Division and presented at the Winter Annual Meeting, New Orleans, La., December 5-8, 1984, of The American Society of Mechanical Engineers. Manuscript received by the Fluids Engineering Division, June 25, 1984.

gave accurate solutions [3, 4] by calculating crossing points of the characteristic lines. Problems arise with interpretation since one has to cut the net of characteristics at either constant time or constant position. The commonly used linear interpolation between calculated points lowers the accuracy to 1st order. While tracking a pressure shock is possible with difficulty, two or more shocks are almost impossible to handle because of storage limits. Pursuing the contact discontinuity between layers of different properties requires following their path lines with due attention to the deflection of characteristics at this discontinuity.

To avoid these peculiarities in the presentation of the results, the hybrid method of characteristics in a rectangular grid (the mesh method) was developed [5]. It calculates the characteristic values at the known node points of the grid (at given position and new time level) by determining the foot points of appropriate characteristic lines. These values are mostly calculated by linear interpolation between mesh points of the row at the old time level so that the accuracy also deteriorates to 1st order. Shocks and discontinuities are now smeared because of the low accuracy but beyond that cause no further difficulty.

The next stage of development is represented by finite-difference methods. Most important is the method of Lax-Wendroff. Developing (2) into a Taylor's series with respect to time, and replacing the time derivatives by space derivatives approximated by central differences, the one-step Lax-Wendroff method

$$W_j^{D+1} = W_j^n - \frac{1}{2}\frac{\Delta t}{\Delta x}(F_{j+1}^n - F_{j-1}^n) + \Delta t \cdot S_j^n + \frac{1}{4}\left(\frac{\Delta t}{\Delta x}\right)^2 \cdot \{(F'^{\,n}_{j+1} + F'^{\,n}_{j})(F_{j+1}^n - F_j^n) - (F'^{\,n}_{j} + F'^{\,n}_{j-1})(F_j^n - F_{j-1}^n)\} \quad (3)$$

is obtained, where the subscript j denotes the mesh point and the superscript n or $n+1$ denotes the old or new time level, respectively. Its properties can be considered as a good compromise between simplicity (only three points at the old time level are involved), accuracy (2nd order), speed and a certain robustness in the sense that it produces only a moderate overshoot in the case of discontinuous initial conditions. Although the two-step Lax-Wendroff versions requiring two evaluations of $F(W)$ per gridpoint exist, the one-step method using $F(W)$ and $F'(W)$ for each grid point is more efficient since the computation of $F'(W)$ usually causes very little additional effort.

Overshoot at Discontinuities

The problems connected with the treatment of pressure shocks are commonly known, but real pressure shocks occur quite seldom in supercharging practice. Methods of 1st accuracy order show no problems either with pressure shocks or with temperature discontinuities because they are both smeared out by the method itself. Due to the low accuracy one sometimes even cannot discover the existence or position of such anomalies. Methods of 2nd accuracy order mostly indicate the proper position of the pressure shock but, depending on its strength, produce overshoot before or after the shock front.

We first encountered temperature overshoot in a "Comprex" cell calculation (similar to those in [6, 7]) and subsequently also in the calculation of unsteady flow in the exhaust pipes of supercharged I.C. engines. If the engine has pronounced scavenging, after the exhaust valve opens, the hot gas strikes the cold scavenging air behind the exhaust port. Besides different gas composition (which we usually neglect) the temperature difference between these layers can exceed 1000 K. In the cell calculation just mentioned, the temperature at the discontinuity rose steadily from step to step reaching over 3000 K until the whole calculation failed. To find out what happened, we calculated a comparable shock tube case with similar temperature difference but constant pressure and zero velocity. The same disastrous result was obtained.

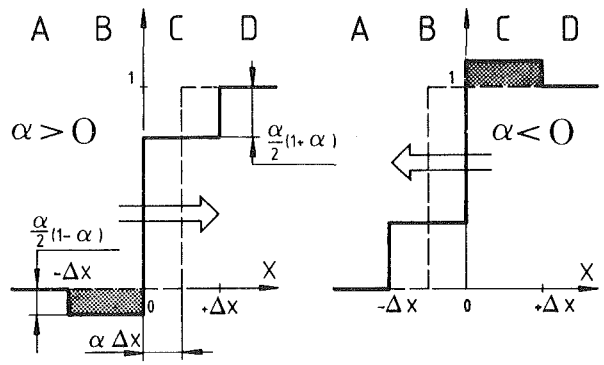

Fig. 1 Numerical (full line) and analytical (dashed line) solutions of unit step transport with overshoot (cross-hatched)

In fact all linear finite-difference methods of higher than first order produce solutions with nonphysical overshoot in the presence of discontinuities. As a consequence time steps permitted by the stability criterion became smaller and the solution completely distorts after a large number of time steps.

Let us analyze what happens during the transport of a shock by the Lax-Wendroff method. Substituting the step function

$$W^n(x) = s(x) = \begin{cases} 0 & \text{if } x < 0 \\ 1 & \text{elsewhere} \end{cases}$$

into (3) we obtain

$$W^{n+1}(x) = -\frac{\alpha}{2}(1-\alpha)\cdot s(x+\Delta x) + (1-\alpha^2)\cdot s(x) + \frac{\alpha}{2}(1+\alpha)\cdot s(x-\Delta x)$$

after one time step, where

$$\alpha = \frac{\Delta t}{\Delta x}\cdot F'$$

is the Courant number. For constant F' it is proportional to the time step. According to the Courant-Friedrichs-Lewy stability criterion its absolute value must not be greater than one. After some reformulation we obtain four different possible values (Fig. 1):

$$W(x) = \begin{cases} 0 & \text{if } x < -\Delta x & \text{(section A)} \\ 0 - \alpha/2(1-\alpha) & \text{if } -\Delta x \le x < 0 & \text{(section B)} \\ 1 - \alpha/2(1+\alpha) & \text{if } 0 \le x < +\Delta x & \text{(section C)} \\ 1 & \text{if } x > +\Delta x & \text{(section D)} \end{cases}$$

According to the sign of α we obtain two patterns of solution and we see that the overshoot occurs always on the backward side of the shock relative to the direction of its movement and vanishes completely for the maximum time step, i.e., with $|\alpha| = 1$. See also figures for different values of α in [8, 9].

Proposals to Reduce the Overshoot

Damping Terms. Some methods amplify the physical viscosity or add artificial viscosity terms similar to those in (1) acting on momentum and energy components only (for a short review see [10]). They act only if W changes with position and do not act on the density. Consequently they do not help in the case of a contact discontinuity with a density step. According to our experience, amplifying the physical viscosity by even 7-orders-of-magnitude distorts only the

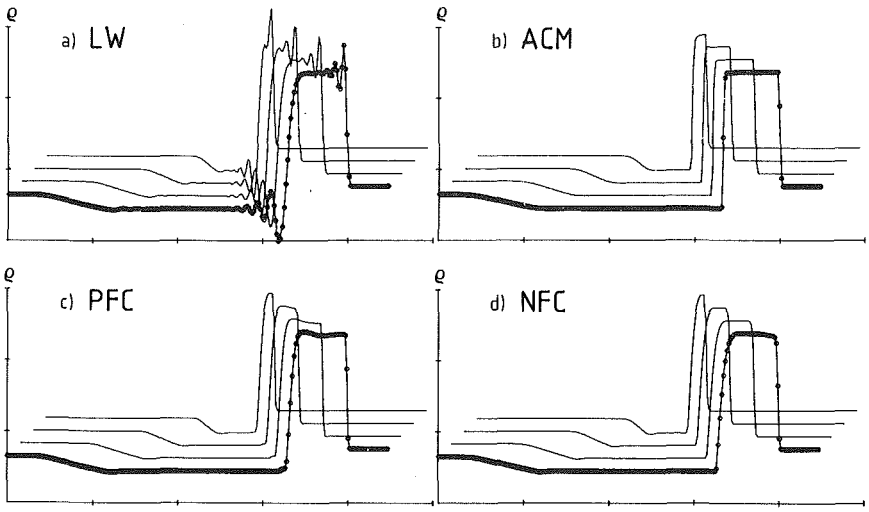

Fig. 2 Development of the numerical solution of the shock tube problem [14]. Density at four equidistant times (shifted for clarity) calculated by the one-step Lax-Wendroff (*a*), artificial compression (*b*), phoenical flux correction (*c*), and naive flux correction (*d*), methods

pressure transient but leaves the temperature overshoot unchanged [8].

Other methods add damping terms acting likewise on all conserved quantities in W. Linear second-order damping terms, if strong enough, are able to remove the overshoot completely but reduce the order of accuracy to one. Nonlinear damping proposed in [1] is effective merely in the neighborhood of a discontinuity and introduces an error of 3rd order only, but is inactive with constant F'. Damping terms generally worsen the stability properties of the undamped method.

Smoothing. In contrast with damping, smoothing the solution after completion of a time step does not deteriorate stability. It reduces the amplitude of higher frequency components only, thus reducing the overshoot considerably without altering phases. For test results with smoothing of 2nd and 4th order, see [8, 9].

The Method of Lerat-Peyret. Since neither damping terms nor smoothing work satisfactorily, one might be tempted to devise a method which suppresses overshoot by itself without requiring the complication of damping terms or smoothing steps. Lerat and Peyret generalized several two-step Lax-Wendroff methods to a two-parameter family and showed how optimal damping with practically no overshoot can be obtained for the shock solution of the Burger equation. Unfortunately even particular adjustment of the parameter to the given problem does not eliminate temperature overshoot at a contact discontinuity [11]. Actually in the case of constant F' this method is identical with the two-step Lax-Wendroff method and produces the same overshoot.

Flux Correction. The method of flux correction comprises two stages [12]. The first stage damps the solution strongly enough to produce no overshoot. Then in the second stage the damping is removed but (with the help of a nonlinear correction) only as far as no overshoot occurs. This method proves to be simple and effective and will be discussed in more detail in the next section (Fig. 2*c*, *d*).

Artificial Compression. The artificial compression method (ACM) proposed in [13, 14] yields excellent results in simple flow situations, like that in a shock tube. Adaptively switching to a first-order scheme in the neighborhood of a discontinuity removes overshoot and retains the second order of accuracy except at the discontinuity. Afterward adaptive artificial compression sharpens the smeared transition in the compression region (Fig. 2*b*). In more complicated practical cases results are disappointing showing numerous nonphysical spikes in temperature transients.

Flux-Corrected Lax-Wendroff Method

After the so-called transport stage, which in our case is a complete time step of the Lax-Wendroff (LW) method, flux correction is applied. It consists of a diffusion and an antidiffusion stage. Several variants of the flux correction method exist [12]. In [15] we discuss a whole family of such methods, but here we only briefly review the phoenical (PFC) and naive (NFC) forms.

Lef us write *the transport stage* (4) with $S=0$ in the form

$$W^{n+1} = W^n + L \cdot W^n \tag{4}$$

thus defining the notation W^n and transport operator L. This stage is accurate to second order in Δx and Δt. Let us define the flux $\Phi(W)$ resulting from W by

$$\Phi_{j+1/2}(W) = \frac{\omega}{4} \cdot (W_{j+1} - W_j) \tag{5}$$

where ω is some positive constant of the order of magnitude 1. Defining also the diffusion operator D by

$$(DW)_j = + \{\Phi_{j+1/2}(W) - \Phi_{j-1/2}(W)\} \tag{6}$$

the diffusion stage for both the phoenical and the naive forms may be written as

$$\tilde{W}^{n+1} - W^{n+1} + D \cdot W^n \tag{7}$$

thus having access only to the values W^n and W^{n+1} available within the current time step. This is simply linear second-order damping which completely eliminates overshoot for $\omega \geq 1/2$ but reduces the stability limit to $|\alpha| \leq \sqrt{1-\omega/2}$ (for $\omega = 1/2$ this becomes $|\alpha| \leq 0.866$).

The purpose of *the antidiffusion stage* is to restore the accuracy of the transport stage without producing overshoot. Necessarily this stage contains a nonlinear operation. Using the positive clipping factor q and the notation

$$(a)_+ = \begin{cases} a & \text{if } a \geq 0 \\ 0 & \text{elsewhere} \end{cases} \tag{8}$$

we define the nonlinear clipping operator $C(\tilde{W})$ as

$$[C(\tilde{W}) \cdot \Phi(W)]_{j+1/2} = q \cdot \Phi_{j+1/2} \cdot \min \left\{ \left(\frac{\tilde{W}_{j+2} - \tilde{W}_{j+1}}{\Phi_{j+1/2}} \right)_+, \frac{1}{q'} \left(\frac{\tilde{W}_j - \tilde{W}_{j-1}}{\Phi_{j+1/2}} \right)_+ \right\} \tag{9}$$

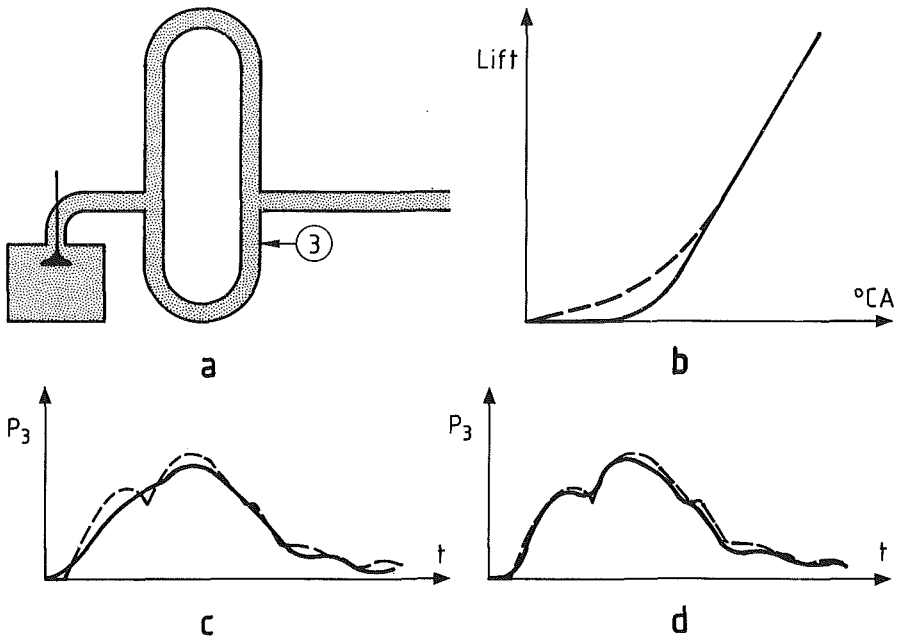

Fig. 3 Configuration of an experimental single cylinder with pipe system (*a*), valve opening curve, (*b*) without (dashed line) and with (full line) elasticity pressure calculated without (*c*) and with (*d*) elasticity (dashed lines show experimental results)

and the nonlinear antidiffusion operator $A(\tilde{W})$ including clipping by

$$(A(\tilde{W})\cdot W)_j = -\{[C(\tilde{W})\cdot\Phi(W)]_{j+1/2} - [(C(\tilde{W})\cdot\Phi(W)]_{j-1/2}\} \quad (10)$$

The phoenical form of the flux correction thus reads

$$\tilde{W}^{n+1} = \tilde{W}^{n+1} + A(\tilde{W}^{n+1})\cdot W^{n+1} \quad (11)$$

So far this form, together with $q=1$, has been considered to be the best one [12], because it has only small phase errors and no diffusion in case of zero velocity (i.e., $L=0$). Incidentally, Ikeda and Nakagawa [16] indicate that by using $q=5/8$, the new extrema which could be created with $q=1$ are avoided. The promotors of the phoenical correction method did not mention that without the nonlinear clipping operation (i.e., with $C=1$) the stability limit is reduced to $|\alpha|\leq\sqrt{1-\omega}$ (i.e., $|\alpha|\leq 0.707$ for $\omega=1/2$). In contrast to [12], numerical evidence shows no essential enhancement of the stability limit with nonlinear clipping.

In order to retain stability we propose the naive form

$$\tilde{W}^{n+1} - \tilde{W}^{n+1} + A(\tilde{W}^{n+1})\cdot W^{n} \quad (12)$$

Without clipping the stability limit of this form is $|\alpha|\leq 1$. With the clipping factor $q=1/2$ the method preserves monotonicity for $|\alpha|\leq 0.866$. We obtained good and stable results [15] computing with $q=5/8$ and $|\alpha|\leq 1$. Because of the higher stability limit the computational costs were less than with the phoenical flux correction.

Conservation Laws and Boundaries

The LW method is claimed to be conservative, e.g., the equations for conservation of mass, impulse and energy are satisfied during the integration from the old to the new time level except for terms at the boundaries. In the case of turbocharging a scavenged engine, this is true for exhaust pipes sufficiently far from the cylinders, but in pipes adjacent to scavenged cylinders the temperature discontinuity builds up. In one representative calculation conservation of mass was violated up to 1.7 percent, and by using the Lax-Wendroff method (LW) with damping term D (which is of 1st accuracy order) this error increased up to 17 percent. In both cases more mass flowed out of the pipes than into it.

Flux correction is also conservative because all corrections cancel each other except at the boundaries. Defining the clipping operator at the boundaries is problematic. A simple solution is to ignore the unavailable clipping terms in (9) at and outside of the boundary; this introduces smaller errors (−1.5 percent), but of opposite sign. Alternatively one could try to bring the balance back to LW level by cancelling the damping of the diffusion stage within the boundary meshes. This can be realized by not clipping in the antidiffusion stage. The mass balance is then positive again, but the pressure and temperature transients show light disturbances. The best results are, however, achieved by combining both possibilities, in particular with 75 percent unclipped and 25 percent clipped antidiffusion flux at boundaries. In the aforementioned calculation the maximum error then becomes 0.4 percent and its sign varies in different pipes.

Using adaptive damping in the diffusion stage of ACM delivers similar results as LW with damping of PFC and NFC. The subsequent adaptive artificial compression of ACM, however, did not restore the original accuracy as did the antidiffusion of NFC and PFC in the foregoing example. With our version of ACM we obtained a maximum error of 15 percent, which is not acceptable in practical applications.

Table 1 Computing time for different methods. Case 1: Shock tube problem [15] with 500 meshes; Case 2: Configuration with 3 pipes (29 meshes), 2 cylinders, 1 turbine and 1 junction. Case 3: Configuration with 7 pipes (38 meshes), 4 cylinders, 1 turbine and 3 junctions.

Method	Computing time in ms						
	case 1	case 2			case 3		
	total	bound.	pipes	total	bound.	pipes	total
FEM	-	-	-	936	-	-	2920
LW1	6312	2788	1159	3947	10980	2470	13450
SM2	5348	2787	1664	4451	-	-	-
SM4	6647	2683	1688	4371	10457	2475	12932
PFC	9837	3555	3156	6711	14197	4668	18865
NFC	6776	2735	2262	4997	10669	3328	13997
ACM	8896	3084	3218	6302	11826	4725	16551

Results of Practical Calculations

Our first application of the methods just discussed was concerned with the propagation of a step function and different Fourier-components by the one-dimensional scalar advection equation, i.e., with $F'=$constant and has been

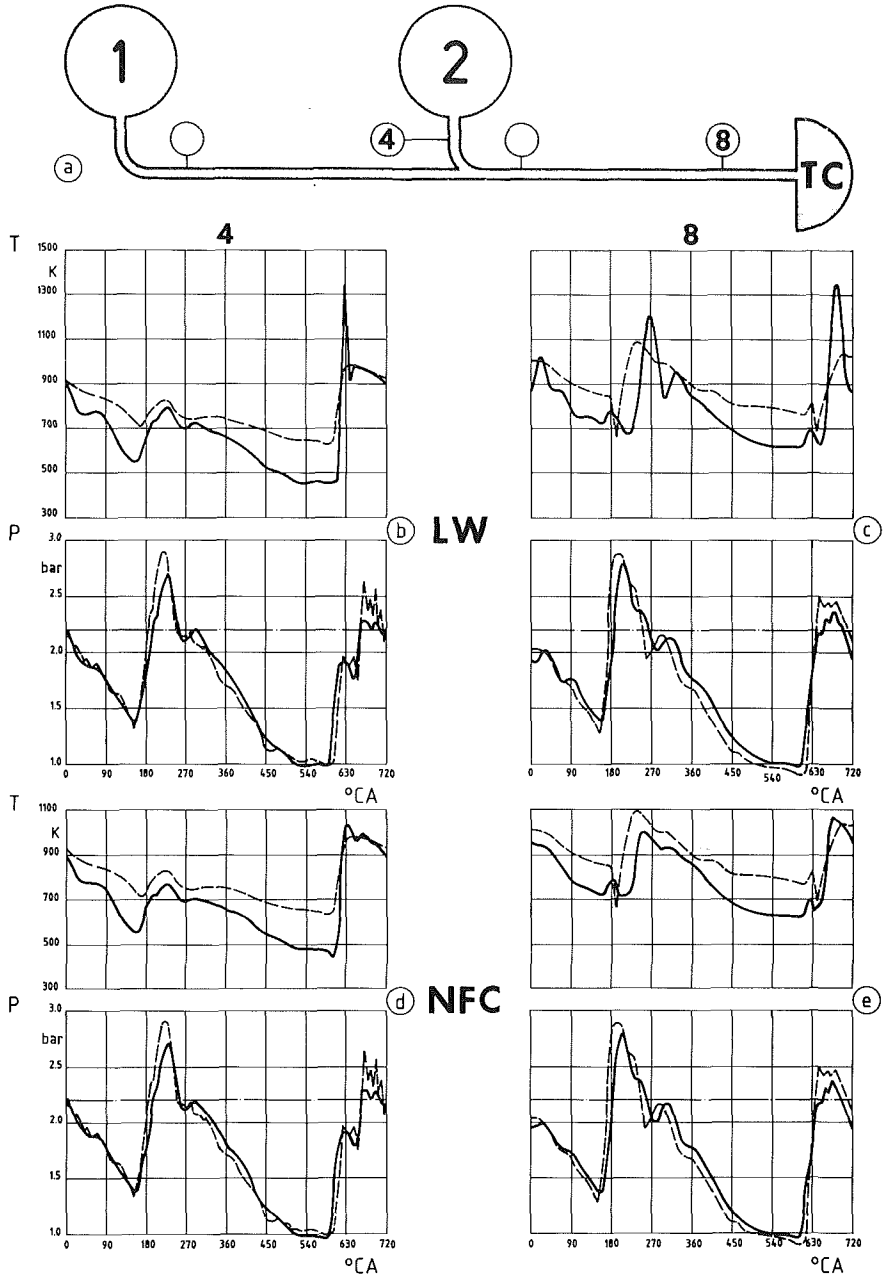

Fig. 4 Two cylinder engine pipe system (*a*) pressure and temperature calculated by Lax-Wendroff method without (*b*, *c*) and with (*d*, *e*) naive flux correction. Calculation: full lines; Measurement: dashed lines.

reported in [8, 9, 15]. A rather more complicated example was the shock tube problem [15] as studied by Harten [14], which has been previously discussed and will be mentioned in the following section as case 1 of Table 1.

Measurements on a single cylinder rig of individual exhaust waves propagating in the adjacent pipe systems have been reported in [17]. We have successfully simulated many of these measurements by our calculations. At high pressure levels particular problems arise as illustrated for the configuration of Fig. 3(*a*). With the geometrical valve opening curves of Fig. 3(*b*) the calculation yielded disappointing results, Fig. 3(*c*). By taking into account the elasticity of the control system, however, i.e., assuming a delay at the start of the valve opening, we obtained results in good agreement with the measurements, Fig. 3(*d*).

We now show a comparison with measured pressure and temperature transients in the exhaust pipes of a supercharged medium-speed diesel engine at the positions shown in Fig. 4(*a*). The measured temperature distribution may be subject to a systematic uncertainty in magnitude, but the form was not significantly affected by the response time of the temperature sensors. Fig. 4(*b*) shows pronounced temperature peak obtained at the cylinder flange by the Lax-Wendroff method. Fig. 4(*c*) in addition demonstrates how overshoots produced by two cylinders interact to give completely distorted temperature results. The naive flux correction employed for Figs. 4(*d*, *e*) successfully copes with overshoot giving results with good agreement in shape.

Computing Time and Storage Requirements

In this section, we summarize information on the relative computing times and storage requirements of various methods.

Quasi-Steady and Unsteady Flow Calculations. The quasi-steady states (i.e., without wave action) in compact pipe systems can be calculated very effectively by the so-called filling and emptying method (FEM). Criteria for the use of

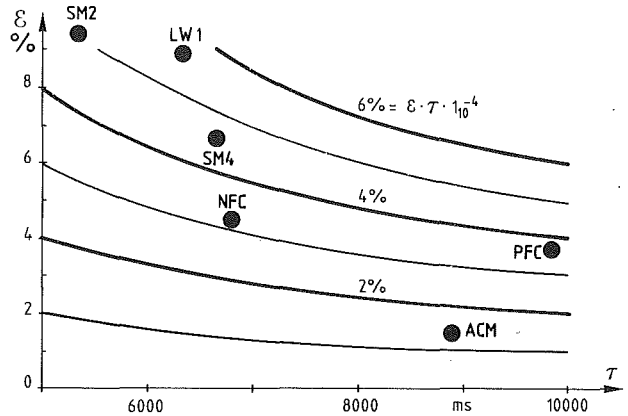

Fig. 5 Comparison of several methods in respect to the time effort τ and error ϵ (at the contact discontinuity) related to the exact solution. SM2 and SM4 are 2nd and 4th order smoothing, respectively (for other abbreviations, see text).

this method, and details of a sophisticated version used to optimize turbocharger applications to I.C. engines are given in [18]. By comparison with the FEM as reported in [19], the unsteady flow calculation (including wave action) by the hybrid characteristic method (HCM) requires 2.6 times as much storage space. The computing time for 3 or 6 cylinders are 3.6 or 5.5 times longer, respectively. Our unsteady flow program, based on a finite-difference method including all variants discussed here, requires only 25 percent more storage and 5.3 times more computing time for a 2 cylinder calculation than our implementation of FEM [18].

Characteristic and Finite-Difference Methods (Including Boundaries). In [20] the true characteristic method (CM), its hybrid form (HCM) and the two-step Lax-Wendroff method (LW2) were compared. With CM results have to be stored at all intersections of the characteristic lines, but with grid methods (HCM, LW2) only at two time levels. The storage ratio was 5:3, and with additional treatment of one shock this ratio increased to 10:3. Reformulation of the flow equations form nondimensional to dimensional form shortened the computing time by 29 percent. In simple cases without shocks CM and HCM required almost the same time effort, being 90 percent slower than LW in the case of 1 pipe with 2 boundaries, or 30 percent slower for 2 pipes with 3 boundaries, respectively. In the former case with one shock, CM needed 4 times more computation time than LW. In [21] the violation of continuity by HCM led to the use of LW2 with 30–60 percent shorter computing time for 9 and 12 cylinder cases, respectively.

Finite-Difference Methods (Without Boundaries). In most cases the calculation of unsteady flow in pipes requires time-consuming treatment at the boundaries. In supercharging practice with cylinders, turbines and junctions this requires a time effort comparable to that for the flow calculation within the pipes. Therefore the most appropriate test case for a comparison of the methods is the shock tube problem with boundaries excluded. Figure 5 compares the performance of several methods for this problem, and shows the relative error obtained as a function of the computing time. The product of these quantities provides a measure of "effectiveness." A choice between two methods on the same curve will depend on the relative importance of accuracy and computing time for a given application. For the shock tube problem, we have observed that all methods show roughly the same error for some time period after bursting the diaphragm. The high accuracy of ACM is achieved later when distinct flow regions have been built up.

Practical Calculations. When comparing the computing effort of practical cases one has to keep in mind the number of pipes, meshes and boundaries. Furthermore the stability limit and overshoot reducing ability of the method determine the number of time steps for an engine cycle and therefore the computing time. The relative importance of the number of internal and boundary points is shown in Table 1, where we see that the more complicated the configuration the less important is the higher computational effort required for flow calculation within the pipes.

Effective methods seem to be ACM and flux corrections. Because ACM seriously violated the conservation laws and sometimes leads to solutions with nonphysical spikes, we recommend flux corrections. The most economical one is the naive form (NFC) since it allows larger time steps.

References

1 Lax, P., and Wendroff, B., "Systems of Conservation Laws," *Comm. Pure Appl. Math.*, Vol. 13, 1960, pp. 217–237.

2 Jenny, E., "Eindimensionale instationäre Strämung unter Berücksichtigung von Reibung, Wärmezufuhr und Querschnittsänderung," *Brown Boveri Mitteilungen*, Vol. 47, No. 11, Nov. 1959, pp. 447–461.

3 Tsai, D. H., "Effect of Size on the Inlet-System Dynamic in Four Stroke, Single-Cylinder Engines," TRANS. ASME, Vol. 78, Jan. 1956, pp. 197–210.

4 Bulaty, T., "The Use of Unsteady Flow in Internal Combustion Engines to Increase Volumetric Efficiency and Output," Motor Car Research Institute publication, Prague 1967.

5 Benson, R. S., Garg, R. D., and Woollatt, D., "A Numerical Solution of Unsteady Flow Problems," *Int. J. Mech. Sci.*, Vol. 6, 1964, pp. 117–144.

6 Zehnder, G., "Calculating Gas Flow in Pressure-Wave Machines," *Brown Boveri Review*, Vol. 58, No. 4/5, 1971, pp. 172–176.

7 Croes, N., "The Principle of Pressure-Wave Machines as Used for Charging Diesel Engines," *Proc. of the 11th Int. Symp. on Shock Tubes and Waves*, University of Washington Press, 1978.

8 Niessner, H., and Bulaty, T., "Comparison of Some Numerical Methods for Solving Hyperbolic Differential Equations With Discontinuous Initial Values," *Proceedings of GAMM 3rd Conference*, Vol. 2, 1979, pp. 221–230.

9 Niessner, H., "Comparison of Different Numerical Methods for Calculating One-Dimensional Unsteady Flows," *Vierteljahresschrift der Naturforschenden Gesellschaft in Zürich*, Vol. 126, No. 2, 1981, pp. 99–127.

10 Roach, P. J., *Computational Fluid Dynamics*, Hermosa Publishers, Albuquerque, 1972, p. 434.

11 Lerat, A., and Peyret, R., "The Problem of Spurious Oscillations in the Numerical Solution of the Equations of Gas Dynamics," *Proc. of 4th Int. Conf. on Num. Math. in Fluid Dyn.*, University of Colorado, June 1974, Springer 1975.

12 Book, D. L., Boris, J. P., and Hain, K., "Flux-Corrected Transport II: Generalization of the Method," *J. Comp. Phys.*, Vol. 18, 1975, pp. 248–283.

13 Harten, A., and Zwas, G., "Self-Adjusting Hybrid Schemes for Shock Computations," *J. Comp. Phys.*, Vol. 9, 1972, pp. 568–583.

14 Harten, A., "The Artificial Compression Method for Computation of Shocks and Contact Discontinuities," *Math. Comp.*, Vol. 32, 1978, pp. 363–389.

15 Niessner, H., and Bulaty, T., "A Family of Flux-Correction Methods to Avoid Overshoot Occurring With Solutions of Unsteady Flow Problems," *Proceedings of GAMM 4th Conf.*, 1981, pp. 241–250.

16 Ikeda, T., and Nakagawa, T., "On the SHASTA FCT Algorithm for Equation $\partial\rho/\partial t + \partial(v(\rho)\rho)/\partial x = 0$," *Math. Comp.*, Vol. 33, 1979, pp. 1157–1169.

17 Mayr, B., "Berechnung des Ladungswechsels an Verbrennungskraftmaschinen mit besonderer Berücksichtigung der instationären Strömung in Rohrleitungen," *Forschungsvereinigung Verbrennungskraftmaschinen*, Forschungsbericht 227/4, 1968.

18 Bulaty, T., "Ein Programmsystem zur Berechnung des Zusammenwirkens von Verbrennungsmotoren und Abgasturboladern," *MTZ*, Vol. 43, 1982, pp. 535–543.

19 Chen, T., "Computer Performance Prediction of a Medium Speed Diesel Engine," *ASME Paper 83-DGP-13*, pp. 1–8.

20 Stark, W., "Stand der Programmierung der Verfahren zur Berechnung instationärer Strömungsvorgänge," *Kolloquium der FVV*, Heft R256, Mai 1959, pp. 85–100.

21 Azuma, T., Yura, T., and Tokunaga, Y., "Some Aspects of Constant Pressure Turbocharged Marine Diesel Engines of Medium and Low Speed," ASME *Journal of Engineering for Power*, Vol. 105, July 1983, pp. 697–711.

Steady and Unsteady Airflow Through the Intake Valve of a Reciprocating Engine

A. F. Bicen
C. Vafidis
J. H. Whitelaw

Imperial College of Science and Technology,
Department of Mechanical Engineering,
Fluids Section,
London SW7 2BX, UK

An experimental investigation of the airflow through various axisymmetric intake ports of a motored reciprocating engine is reported. Detailed velocity field measurements obtained by laser Doppler anemometry and for steady and various unsteady flow conditions are presented together with valve discharge coefficients from steady flow tests. The results showed that over the lift range investigated the valve flow exhibited various regimes indicated by the changes in the flow pattern at the valve exit. With a 45-deg seat angle, four regimes were identified compared to three in the case of a 60-deg valve. The overall behavior of the 45-deg valve, however, was found to be generally better. Rounding of the edges of the 45-deg valve reduced the number of flow regimes to two with marked improvements on discharge coefficient. The flow angle at the valve exit depended less on the flow regimes and more on the cylinder confinement, in the absence of which the transition from one regime to another was delayed. The mean flow pattern at the valve exit was found to be insensitive to flow unsteadiness, piston confinement and valve operation and thus could be predicted with reasonable accuracy from steady flow tests. The in-cylinder flow characteristics were also insensitive to valve operation, but strongly depended on piston interaction, flow unsteadiness and residual effects from the previous cycle.

Introduction

The flow behavior through the intake valve of a reciprocating internal combustion engine plays an important role in the engine performance particularly since it affects its volumetric efficiency. References [1-6], for example, have examined the valve flow behavior by means of discharge coefficient measurements under steady flow conditions. The recently developed multidimensional codes, such as that of reference [7], for predicting the in-cylinder flow in internal combustion engines required detailed information of the valve exit flow as boundary conditions for the solution of the flow equations. However, there is a lack of relevant experimental data probably due to practical difficulties associated with the measurement of the unsteady flow field at the valve exit plane. Some of these difficulties can be alleviated by considering the valve flow to be quasi-steady, as suggested in references [3, 8].

The validity of the quasi-steady assumption has been examined here by comparing LDA measurements of the velocity field at the intake valve exit plane under both steady and unsteady conditions. The results obtained provide detailed information on the flow through the intake valve to minimize the uncertainties associated with the lack of boundary conditions for calculation methods and quantify earlier findings about the influence of geometric and flow parameters on the valve performance.

2 Experimental System

2.1 Flow Configurations. Four flow configurations were considered. The first comprized a steady flow test section, shown in Fig. 1(*a*), mounted on a plenum chamber which was connected to a compressed air supply. The flow through the valve discharged axisymmetrically in an open-ended plexiglass cylinder extending downstream as well as upstream of the cylinder head which was fabricated from a thin transparent sheet of plexiglass. This arrangement allowed axial velocity measurements with laser Doppler anemometry to be performed at the valve exit plane and up to an axial distance of 0.5 mm away from the cylinder head, as described in reference [9].

The second flow configuration consisted of an unsteady

Table 1 Main characteristics of model engine

Engine speed, rpm	200
Bore, mm	75
Stroke, mm	94
Connecting rod length, mm	363.5
Clearance at TDC, mm	14
Compression ratio	7.7
Intake valve opening, deg*	0
Intake valve closure, deg*	210
Maximum valve lift, mm*	9.2

*For operating valve

Contributed by the Fluids Engineering Division and presented at the Forum on Fluids Mechanics, Winter Annual Meeting, New Orleans, LA, December 5-10, 1984, of THE AMERICAN SOCIETY OF MECHANICAL ENGINEERS. Manuscript received by the Fluids Engineering Division, July 25, 1984.

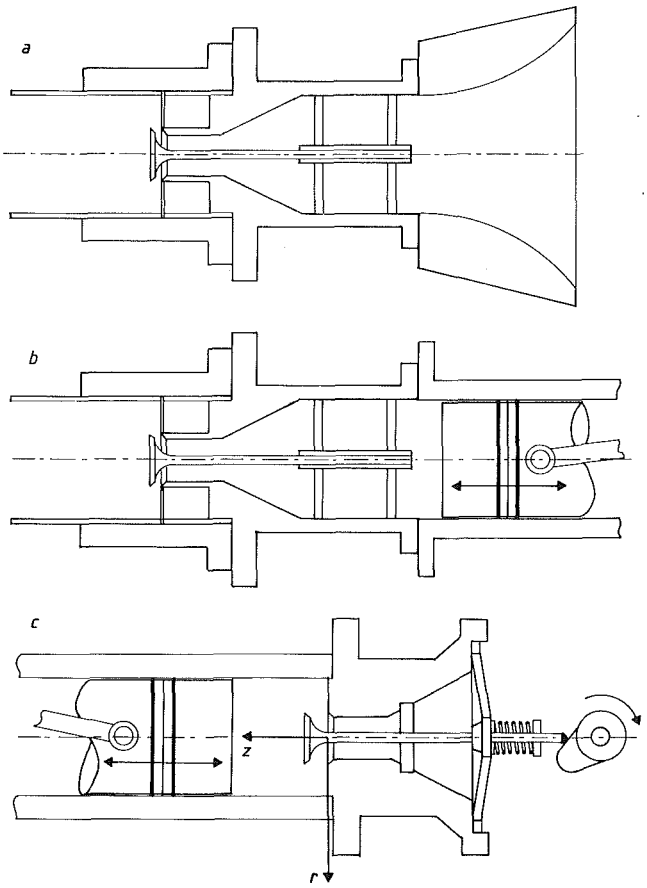

Fig. 1 Schematic of flow configurations. (a) Steady flow rig; (b) Unsteady flow rig with stationary valve and upstream operating piston; (c) Model engine with stationary and operating valves.

flow arrangement shown in Fig. 1(*b*). The test section previously described was, this time, mounted on an engine with the piston reciprocating at 200 rpm inside a cylinder upstream of a stationary valve.

The third and fourth flow configurations were also unsteady and consisted of a model engine with the piston reciprocating downstream of the valve and inside a plexiglass cylinder, as shown in Fig. 1(*c*). For the third flow configuation the model engine was operated with an open stationary valve in the absence of compression, while in the fourth configuration the engine was driven in a four-stroke mode with a cam-operated valve. The main characteristics of the model engine are summarized in Table 1 with more details given in reference [10].

Three valve geometries were examined and are shown in Fig. 2. The first had a 45-deg seat angle and sharp corners and is referred to as valve Type I. The second had a 60-deg seat angle with sharp corners and is referred to as valve Type II. The third valve was identical to Type I with rounded corners

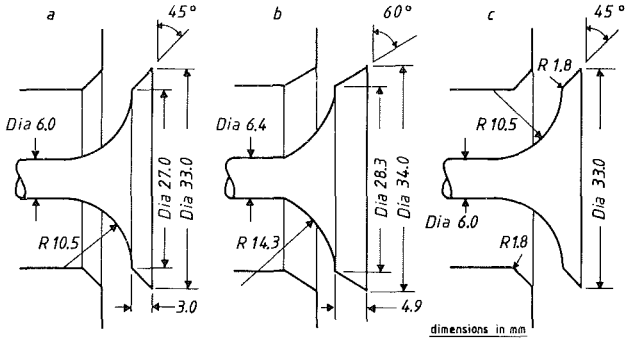

Fig. 2 Details of valve geometries. (a) Type I; ψ = 45 deg with sharp corners; (b) Type II; ψ = 60 deg with sharp corners; (c) Type III; ψ = 45 deg with rounded corners.

Table 2 Optical characteristics of laser Doppler anemometer

Half angle of beam intersection, deg	5.9 or 9.0
Length of probe volume at e^{-2} intensity level, μm	960 or 630
Diameter of problem volume at e^{-2} intensity level, μm	100
Fringe spacing, μm	3.06 or 2.02
Number of fringes	32 or 49

on both sealing faces as shown in Fig. 2(*c*) and will be referred to as Type III.

2.2 Discharge Coefficient Measurements. The blowdown-type steady flow arrangement could provide air mass flow rates up to 100 kg/h. The air flow was controlled by a series of pressure and flow regulators and metered with an orifice meter. The total pressure upstream of the valve, P_0, was taken to be the stagnation pressure in the plenum chamber and the static pressure downstream of the valve, P, was assumed to be atmospheric; wall static pressure measurements in the vicinity of the valve exit gave values very close to the atmospheric pressure, thus justifying this assumption. The pressure drop across the valve, ΔP, was taken as $P_0 - P$. The discharge coefficient (C_l or C_m) was calculated according to the procedure outlined in the Appendix which also includes the definitions of the most commonly used geometric areas. Comments on the choice of geometric areas are made in Section 3.1.

2.3 Velocity Measurements. Lasser Doppler anemometry was used to measure the velocity field at the exit and downstream of the valve with particular emphasis on the flow field at the valve exit plane. The laser Doppler anemometer was operated in the dual-beam forward-scatter mode. It consisted of a 5 mW He-Ne laser and a rotating diffraction grating which split the beam and provided variable frequency shifts between 1–5 MHz. Details of the optical system are given in Table 2. Seeding of the flow was provided by silicone-oil droplets with an average size of around 2μm.

For the steady flow measurements, the signals from the

Nomenclature

A_e = effective flow area
A_l = peripheral valve lift area
A_m = minimum geometric area
C_l = discharge coefficient based on valve lift area
C_m = discharge coefficient based on minimium geometric area
D = diameter of valve head
d = diameter of valve stem
L = valve lift
$\dot{m}$ = mass flow rate
P = static pressure
P_0 = stagnation pressure
R = radius of cylinder
t = valve seat width
U, V = axial and radial velocity components
$\bar{U}, \bar{V}$ = ensemble-averaged mean velocities
$\sqrt{\overline{u^2}}, \sqrt{\overline{v^2}}$ = ensemble-averaged rms velocities
V_p = instantaneous piston speed
$\bar{V}_p$ = mean piston speed
z, r = cylindrical coordinates
γ = specific heat ratio
$\Delta\theta$ = crank angle window
ΔP = pressure drop
θ = crank angle
ρ = air denstiy
ψ = valve seat angle

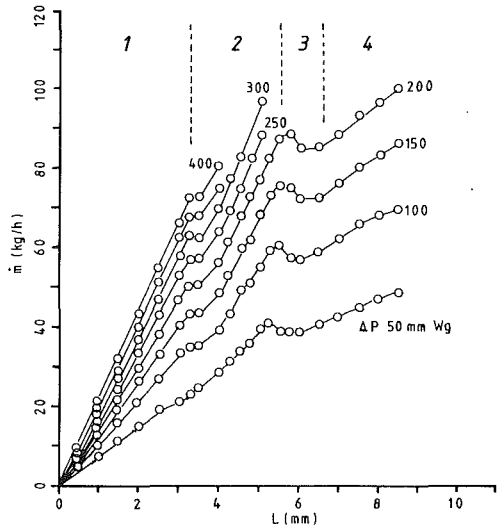

Fig. 3 Variation of mass flow rate with valve lift and pressure drop; Type I with confinement; mm Wg = mm water gauge

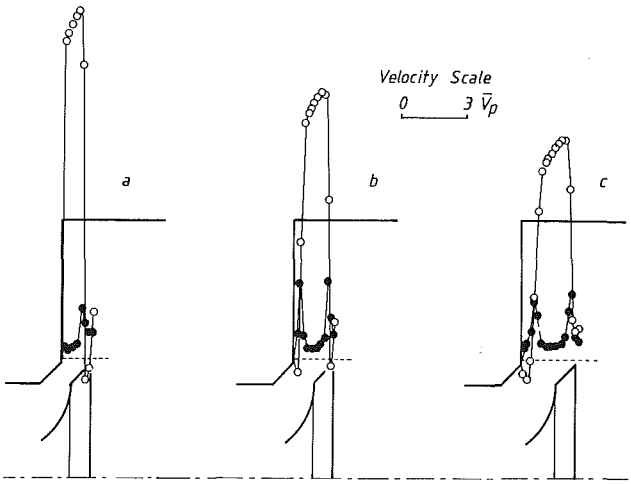

Fig. 4 Radial veolcity profiles at the valve exit; Type I with confinement, ○ = mean velocity, • = rms velocity; $\bar{V}_p$ = 0.63 m/s; (a) L = 4.25 mm; (b) L = 6 mm; (c) L = 8 mm

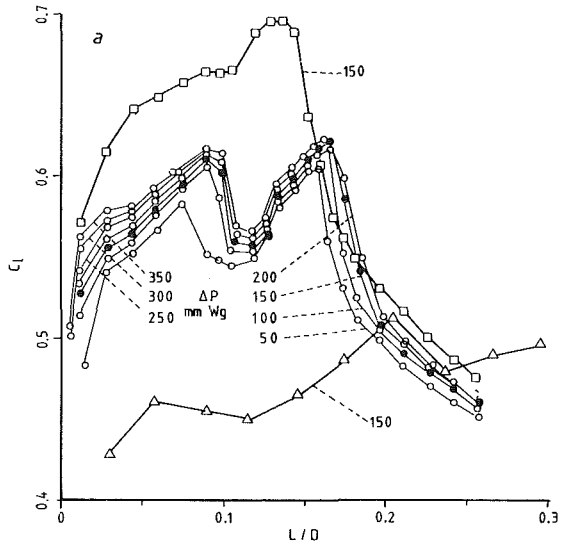

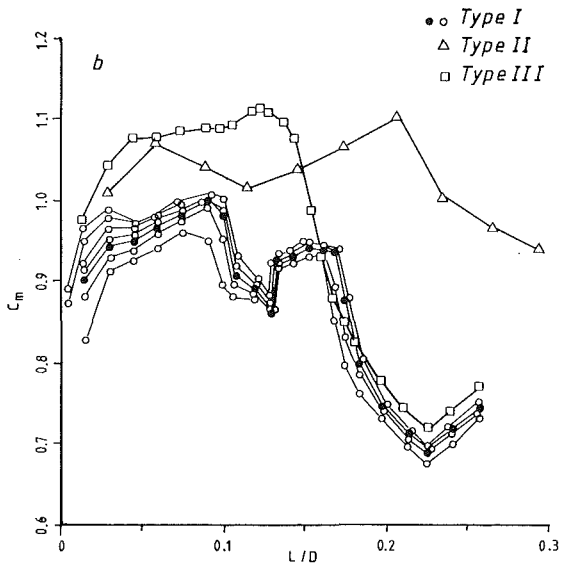

Fig. 5 Variation of discharge coefficient with valve lift for valve Types I, II, and III with confinement; (a) C_l, based on lift area; (b) C_m, based on minimum area

photomultiplier were band-pass filtered, amplified and input to a frequency counter which was interfaced to a microcomputer for data collection and subsequent processing. For the unsteady flow measurements, the window-ensemble technique was used. The same measuring system was employed with the additional feature of a digital shaft encoder mounted on the crank shaft of the piston-cylinder assembly and linked to a gating circuit which enabled the counter to measure only within a preset crank angle window.

2.4 Precision. The flow rate of the steady flow rig was controlled within 0.4 percent, while the large plenum chamber almost eliminated any short term fluctuations incurred in the air supply. The overall error in the discharge coefficient measurements was estimated to be 3 percent (reference [9]).

Velocity gradient broadening was minimized by the small dimensions of the probe volume (see Table 2) and by positioning its long axis parallel to the velocity gradients, where possible. The unsteady flow velocity measurements were obtained with a crank angle window of $\Delta\theta$ = 1.44 deg and, according to reference [11], should be free from crank angle broadening effects. Refraction corrections due to the curved boundaries were applied both for velocity magnitude and measurement position according to the procedure of reference [12]. The overall accuracy of the ensemble-averaged velocity measurements is estimated to be 3 and 5 percent for the mean and rms velocities, respectively, including velocity bias and sample size related errors.

3 Results and Discussion

The mean and rms values of the axial and radial velocity components were measured at the valve exit and a downstream radial plane, z = 15 mm, under steady and unsteady flow conditions. For the steady flow tests the velocity measurements were obtained with a constant mass flow rate of 12 kg/h corresponding to the mean flow rate ($\pi R^2 \rho \bar{V}_p$) of the unsteady flow for an engine speed of 200 rpm. All the velocity values are normalized by the mean piston speed $\bar{V}_p$ (0.63 m/s).

3.1 Steady Valve Flow. *3.1.1 Valve Type I With Confinement.* The curves of mass flow rate versus valve lift for the valve Type I confined axisymmetrically by a cylinder, are shown in Fig. 3 with the pressure drop across the valve as a parameter. It can be seen that the valve flow exhibits four flow regimes indicated by changes in curve slope. The interpretation of these results is similar to that of reference [1] and is supported by the radial velocity measurements at the

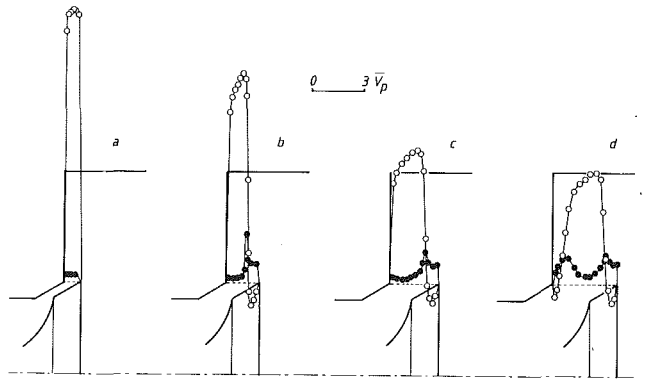

Fig. 6 Radial velocity profiles at the valve exit; Type II with confinement, ○ = mean velocity, • = rms velocity; (*a*) L = 3 mm; (*b*) L = 6 mm; (*c*) L = 9 mm; (*d*) L = 12 mm

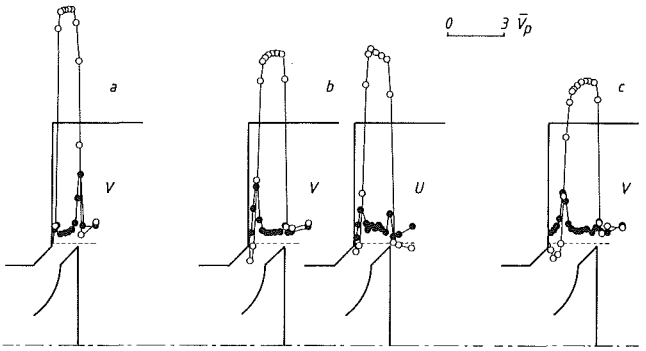

Fig. 7 Radial and axial velocity profiles at the valve exit; Type II with confinement, ○ = mean velocity, • = rms velocity; (*a*) L = 4.25 mm; (*b*) L = 6 mm; (*c*) L = 8 mm

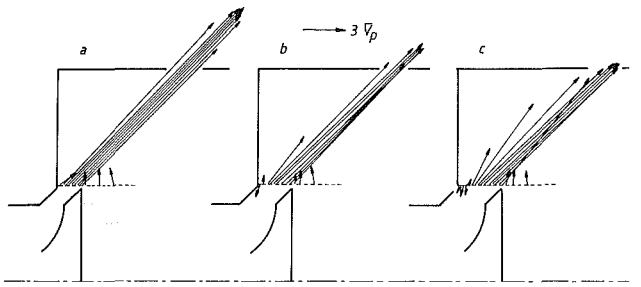

Fig. 8 Velocity vectors at the valve exit; Type III with confinement, (*a*) L = 4.25 mm; (*b*) L = 6 mm; (*c*) L = 8 mm

valve exit plane shown in Fig. 4. At small lifts, the flow is initially attached to the walls of the valve passage and corresponds to the flow regime 1 in Fig. 3. For valve lifts greater than 3 mm the flow detaches from the valve sealing face and effectively reduces the actual flow area and consequently the slope of the curve, corresponding to the flow regime 2. The increase in valve lift to values above 5.5 mm results in flow separation not only at the valve but also at the valve seat as shown in Fig. 4(*b*) and sets on the transition to flow regime 3 of Fig. 3. Although the transition from flow regime 3 to 4 is not clearly evident in the flow curves in Fig. 3, its existence is proved by the velocity measurements in Fig. 4(*c*) which show that for valve lifts higher than 6.5 mm the flow reattaches on the valve but remains detached at the valve seat.

The variation of discharge coefficients C_l and C_m with dimensionless valve lift L/D and pressure drop across the valve are shown in Fig. 5: this figure also includes the discharge coefficients of Type II and III valves which are discussed in the following sections. An increase in pressure drop increases the discharge coefficent and its influence is

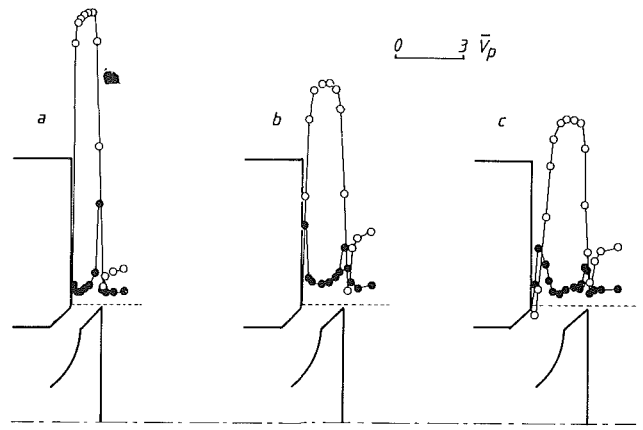

Fig. 9 Radial velocity profiles at the valve exit; Type III with confinement, ○ = mean velocity, • = rms velocity; (*a*) L = 4.25 mm; (*b*) L = 6 mm; (*c*) L = 8 mm

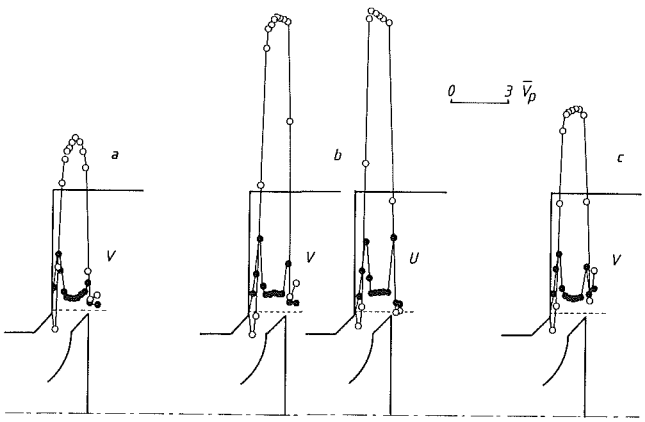

Fig. 10 Radial velocity profiles at the valve exit and with L = 6 mm; Type III, upstream operating piston with stationary valve, ○ = mean velocity, • = rms velocity; (*a*) Early intake; (*b*) Mid intake; (*c*) Late intake

shown to be stronger at small lifts due to pronounced viscous effects at low Reynolds numbers. As the pressure drop increases, and hence the Reynolds number, viscous effects become less important and the discharge coefficient progressively improves collapsing into one curve for values greater than 200 mm Wg. The trends of the aforementioned results agree with those reported in references [3, 4, 8], but show a greater dependence on pressure drop as expected with the lower flow rates.

The curves of discharge coefficent C_m indicate values near or greater than unity and a recovery toward high lifts. There are two points which question the use of C_m. The first concerns the inconvenience of using three equations to describe the minimum geometric area for a lift range of practical importance (see Appendix). The second, and probably more important, is the arbitrary assumption that the static pressure at the throat is equal to the pressure downstream of the valve leading to values of C_m greater than unity.

3.1.2 Valve Type II With Confinement. The radial velocity measurements obtained at the exit plane of valve Type II are shown in Fig. 6, and when compared to those of Fig. 4, quantify the effect of seat angle on valve flow performance. The profiles in Fig. 6 indicate three flow regimes as opposed to four with the valve Type I. At low lifts the flow is attached at both sealing faces corresponding to flow regime 1 as in the case of the 45-deg valve. At L = 6 mm the regime 2 is observed and sustained for a wider range of valve lifts. At L = 12 mm an additional flow separation occurs at the seat face and this final mode corresponds to the flow regime 3.

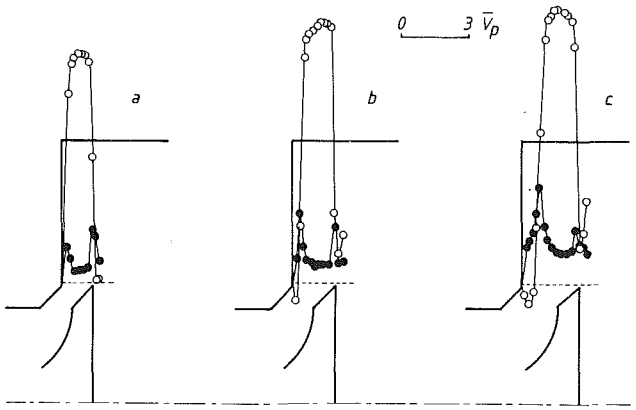

Fig. 11 Radial velocity profiles at the valve exit; Type III, model engine with stationary valve, ○ = mean velocity, ● = rms velocity; (*a*) L = 4.25 mm and at θ = 30 deg; (*b*) L = 6 mm and at θ = 48 deg; (*c*) L = 8 mm and at θ = 68 deg

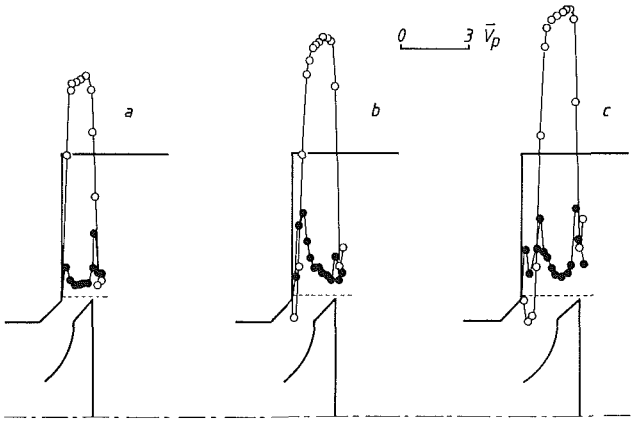

Fig. 12 Radial velocity profiles at the valve exit; Type III, model engine with operating valve, ○ = mean velocity, ● = rms velocity; (*a*) L = 4.25 mm (θ = 30 deg) (*b*) L = 6 mm (θ = 48 deg); (*c*) L = 8 mm (θ = 68 deg)

Although the number of flow regimes in the low-to-medium lift range is less with the 60-deg valve than that with the 45-deg one, the actual flow area is smaller due to the larger flow separation associated with the 60-deg valve. This is reflected on the values of discharge coefficent C_l which indicate differences up to 25 percent between the two valve cases in the low-to-medium lift range, as shown in Fig 5. As the lift increases above L/D = 0.18, the effect of seat angle becomes less pronounced due to smaller differences in the actual flow area of the two cases. The values of C_m, on the other hand, show an opposite trend to that of C_l being larger for the 60-deg valve. This may be attributed to the stronger convergent-divergent effect of the 60-deg valve passage and to the larger minimum geometric area associated with the 45-deg valve at a given lift. The latter effect becomes more apparent at high lifts where larger differences are observed for similar actual flow areas. The foregoing observation again casts doubt on the use of C_m for comparative studies and is in agreement with reference [6] which favors the use of lift area of A_l.

3.1.3 Valve Type III With Confinement. The radial and axial velocity profiles obtained at the exit plane of valve Type III are shown in Fig. 7 and indicate that the rounding of the valve edges reduces the number of flow regimes from four to two in the same lift range. Only the flow regimes 1 and 4 are encountered and the flow regime 1 is sustained up to larger lifts when compared to the valve Type I. As a result of this, significant improvements on the values of discharge coefficient, up to 15 percent or more, are observed at low and medium lifts, as also indicated in Fig. 5.

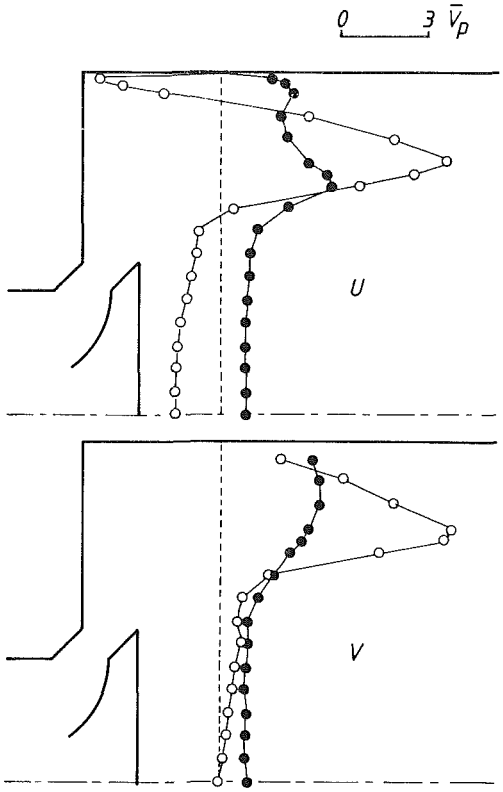

Fig. 13 Axial and radial velocity profiles at z = 15 mm and with L = 6 mm; Type III, steady flow, ○ = mean velocity, ● = rms velocity

The velocity vector plots in Fig. 8 are deduced from the measurements of axial and radial velocity components and indicate that valve III gives a well-defined jet-like flow especially near the valve head, issuing at 45 deg to the axis for nearly all practical lifts. The knowledge of flow direction during the induction stroke is important for flow calculations particularly if the piston comprises a combustion bowl. Existing computational results, such as those of reference [7], underpredict the maximum in-cylinder velocities during the induction stroke. One possible reason for that could be the lower velocities through the valve used as boundary conditions by assuming the whole lift area as effective.

3.1.4 Valve Type III Without Confinement. Measurements of radial velocity component obtained with the valve Type III and in the absence of cylindrical confinement are shown in Fig. 9. Comparison with the profiles in Fig. 7 for the confined valve shows that the separation from the seat face is smaller and occurs at larger lifts for the unconfined valve. Examination of the relative magnitudes of axial (reference [9]) and radial velocity components over the valve lift range, indicated that the flow angle varied with valve lift. The flow initially emerges from the valve gap at 45 deg and later deviates toward the cylinder head. At larger lifts the flow changes direction again and deviates toward the cylinder axis. This observed variation in flow angle is due to the entrainment of surrounding air near the cylinder head which decreases the pressure in this region causing the flow to deviate toward the cylinder head until it separates from the valve seat. This also explains the delay in flow separation observed with the unconfined valve.

These results indicate that is it not advisable to extrapolate information from an unconfined valve to a confined one. This comment emphasizes the observations made in reference [3] which reports changes in the position of the changeover points of the discharge coefficient curve with valve confinement.

3.2 Unsteady Valve Flow. The results presented in this

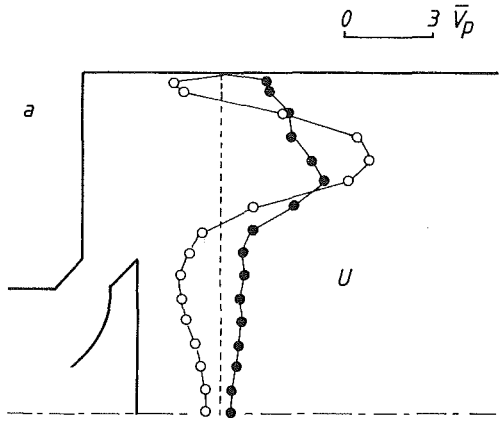

Fig. 14 (*a*) Early intake;

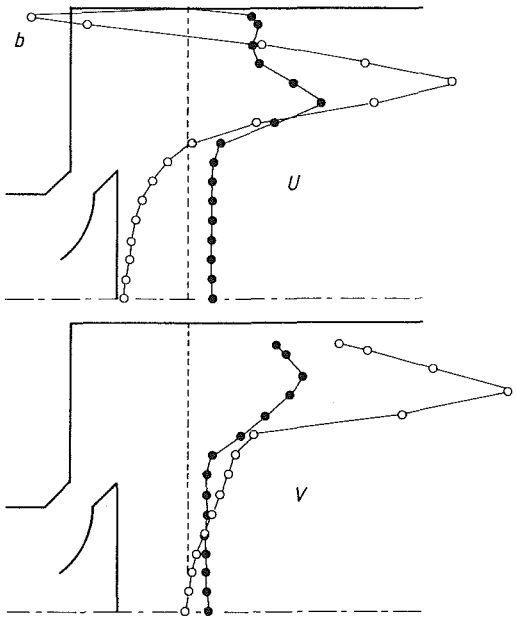

Fig. 14 (*b*) Mid Intake;

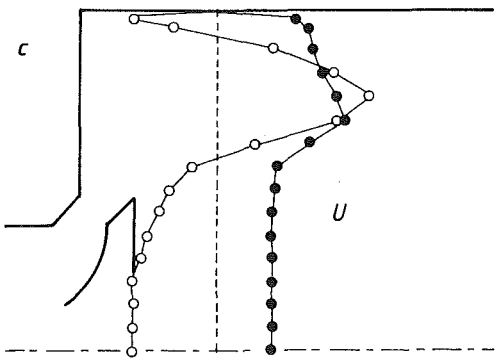

Fig. 14 (*c*) Late intake

Fig. 14 Axial and radial velocity profiles at z = 15 mm and with L = 6 mm; Type III, upstream operating piston with stationary valve, ○ = mean velocity, ● = rms velocity

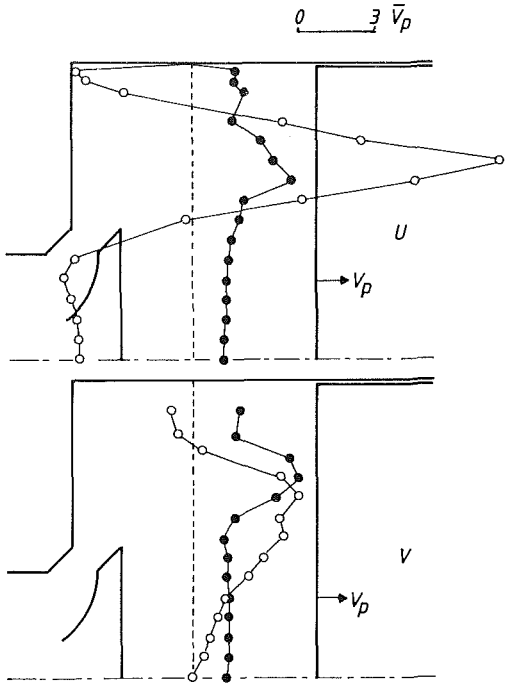

Fig. 15 Axial and radial velocity profiles at z = 15 mm and θ = 48 deg, with L = 6 mm; Type III, model engine with stationary valve, ○ = mean velocity, ● = rms velocity

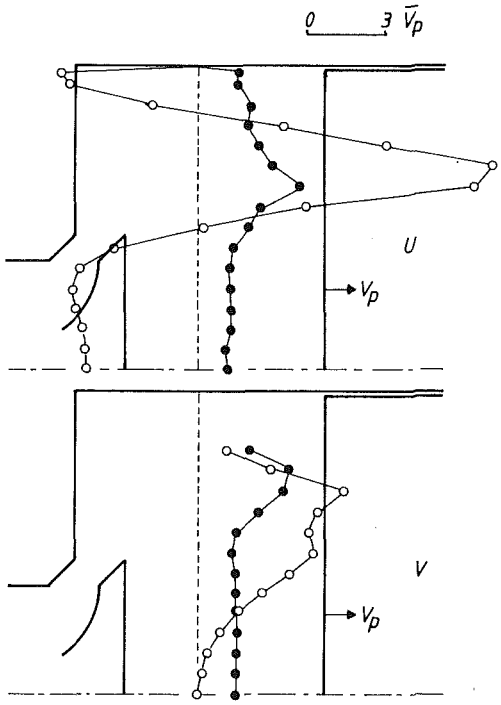

Fig. 16 Axial and radial velocity profiles at z = 15 mm and L = 6 mm (θ = 48 deg); Type III, model engine with operating valve, ○ = mean velcity, ● = mean velocity

section were obtained with valve Type III, but the discussion and conclusions are also valid for valves Type I and II.

The velocity profiles at the exit plane of a stationary valve with an upstream operating piston are shown in Fig. 10 for the valve lift of 6 mm. The results were obtained at three different instants covering the accelerating and decelerating periods of the flow, and are referred to as early, mid and late induction corresponding to the crank angle locations of 225, 276 and 325 deg of the upstream operating piston. Figure 10 shows that the mean flow pattern remains the same throughout the intake process. The rms velocities increase toward mid and late induction due to the gradual development of the flow to fully turbulent. Comparison of the results to those obtained under steady flow conditions and presented in Fig. 7(*b*) shows

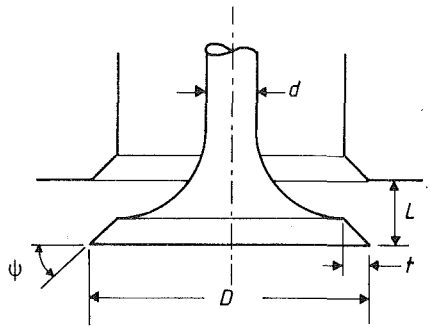

Fig. 17

that the radial and axial mean velocity distributions at the valve exit are similar for both cases. The rms velocities, on the other hand, are almost always higher for the unsteady flow case particulary at late induction, probably due to the enhanced mixing since the beginning of the process as well as the flow deceleration past mid intake.

Radial velocities obtained at the exit plane of a stationary and operating valve in the model engine are shown in Figs. 11 and 12, respectively. With the stationary valve, measurements were obtained at crank angle locations of 30, 48, and 68 deg for valve lifts of 4.25, 6 and 8 mm, respectively. These crank angles were chosen as they correspond to the same lift values under operating conditions. The two mean flows are similar to each other as well as to those obtained both with upstream operating piston (Fig. 10) and under steady flow conditions (Fig. 7), indicating that the main features of the mean flow at the valve exit remain insensitive to flow unsteadiness, piston interaction and valve operation.

In general, these results indicate that the mean velocity distribution at the exit plane of an intake valve can be accurately estimated from steady flow experiments, at least in a low speed engine with a large clearance volume at TDC. Possible resonance and choking effects in the intake port of a high speed engine and valve flow confinement by close piston proximity at TDC may reduce the accuracy of the corresponding steady flow tests.

3.3 In-Cylinder Flow. Axial and radial velocity profiles at a downstream location of $z = 15$ mm are shown in Figs. 13–16 for the four flow configurations considered with the valve Type III and the valve lift of 6 mm. When these results are compared to each other, they quantify the effects of flow unsteadiness, piston interaction, and valve operation on the in-cylinder flow characteristics.

The profiles in all four figures exhibit the jet-like nature of the flow with main production of turbulence taking place in the shear layers and with recirculation regions on either side. Comparison of the steady flow profiles in Fig. 13 to those with unsteady flow in Fig. 14 indicates some similarities with respect to both mean flow and turbulence with the similarity steadily improving at mid and late induction. The differences are attributed mainly to the residual effects from the exhaust stroke and to the developing nature of the unsteady flow. One noteworthy feature of the unsteady flow is the lower levels of turbulence near the axis of the early part of induction which are considered to be due to the small time available for turbulence transport by the mean flow.

Comparison of Figs. 14 and 15 shows the effect of the piston interaction with the unsteady in-cylinder flow. The low pressure region near the piston associated with its movement, alters the jet angle toward the axis with consequent impingement on the piston face, which distributes the turbulence field with less peaky rms profiles as indicated in Fig. 15. The operation of the valve does not alter significantly the aforementioned observed trends, as can be seen through the comparison of the profiles in Figs. 15 and 16. Higher values of radial mean velocities observed with the operating valve indicate a more oblique angle of the jet which can be traced back to the changes in the valve flow pattern associated with varying lift, as discussed in Section 3.1.3.

Overall, it can be stated that although the flow behavior of an intake valve under operating conditions can be predicted with reasonable accuracy from steady flow measurements, the in-cylinder flow characteristics downstream of the valve cannot. The reason for that is mainly the strong interaction of the piston with the in-cylinder flow and partly the residual effects of the previous cycle as well as the developing nature of the unsteady flow.

4 Conclusions

The most important findings of this investigation can be summarized as follows:

1 The velocity measurements at the exit plane of the valve revealed various flow regimes which explain previously observed variations of discharge coefficient with valve lift. Four flow regimes, characterized by the presence and nature of flow separation from the faces of the valve, were encountered with the 45-deg seat angle as opposed to three in the case of the 60-deg valve. The overall behavior of the 45-deg valve was found to be better in the low-to-medium lift range. Rounding of the edges of the 45-deg valve reduced the number of flow regimes to two with improvements in the discharge coefficient of up to 15 percent, while the flow angle at the valve exit was found to depend on cylinder confinement.

2 The close correspondence between the results of the steady and three unsteady configurations examined here indicated that the mean flow pattern at the valve exit was insensitive to flow unsteadiness, piston confinement and valve operation, and thus could be predicted with reasonable accuracy from steady flow tests. In constrast, the in-cylinder flow characteristics were strongly dependent on piston interaction, flow unsteadiness and residual effects, and could not be predicted from steady flow measurements.

Acknowledgements

The financial support provided by the Joint Research Committee of European Engine Manufacturers and the Department of Energy, USA is gratefully acknowledged.

References

1 Tanaka, K., "Air Flow Through Suction Valve of Conical Seat," *Aeronautical Research Institute Report*, Tokyo Imperial University, 1929, Part 1, p. 260; Part 2, p. 361.

2 Wood, G. B., Hunter, D. U., Taylor, E. S., and Taylor, C. F., "Airflow Through Intake Valves," *Transactions of SAE*, Vol. 50, 1942, p. 212.

3 Kastner, L. S., Williams, T. J., and White, J. B., "Poppet Inlet Valve Characteristics and Their Influence on the Induction Process," *Proc. I. Mech. E.*, Vol. 178, 1963, p. 955.

4 Woods, W. A., and Khan, S. R., "An Experimental Study of Flow Through Poppet Valves," *Proc. I. Mech. E.*, Vol. 180, 1965, p. 32.

5 Wallace, W. B., "High-Output Medium-Speed Diesel Engine Air and Exhaust System Flow Losses," *Proc. I. Mech. E.*, Vol. 182, 1967, p. 134.

6 Annand, W. J. D., "Engine Breathing," *Automobile Engineer*, Feb. 1969.

7 Ahmadi-Befrui, B., Acroumanis, C., Bicen, A. F., Gosman, A. D., Jahanbakhsh, A., and Whitelaw, J. H., "Calculations and Measurements of the Flow in a Motored Model Engine and Implications to Open-Chamber Direct-Injection Engines," *Proc. Symposium on Three Dimensional Turbulent Shear Flows*, ASME Spring Meeting, St. Louis, 1982.

8 Fukutani, I., and Watanabe, E., "Air Flow Through Poppet Inlet Valves—Analysis of Static and Dynamic Flow Coefficients," SAE Paper 820154, 1982.

9 Vafidis, C., and Whitelaw, J. H., "Steady and Pulsating Air Flow Through a Stationary Intake Valve of a Reciprocating Engine," Imperial College, Mech. Eng. Dept., Report FS/84/4, 1984.

10 Bicen, A. F., "Air Flow Characteristics of Model Internal-Combustion Engines," PhD thesis, University of London, 1983.

11 Morse, A. P., "The Effect of Crank Angle Broadening on Laser-Doppler Measurements in Reciprocating Engines," Imperial College, Mech. Eng. Dept., Report FS/77/18, 1977.

12 Bicen, A. F., "Refraction Corrections for LDA Measurements in Flows With Curved Optical Boundaries," Imperial College, Mech. Eng. Dept., Report FS/81/17, 1981; also *TSI Quarterly*, April–June 1982, Vol. 8, No. 2.

APPENDIX

Calculation of Discharge Coefficient

The discharge coefficient is defined as the ratio of the effective flow area A_e, which is considered to be the throat area of an ideal nozzle and through which the measured flow passes, to some geometric area representative of the valve configuration. The choice of the geometric area is arbitrary and various reasonable choices exist. Most widely used area are the minimum valve area A_m, reference [3], and the peripheral lift "curtain" area A_l, reference [6], which are both functions of valve lift with the former being also a function of valve seat angle. The corresponding discharge coefficients are

$$C_m = A_e / A_m \tag{1}$$

and

$$C_l = A_e / A_l \tag{2}$$

The effective area may be calculated using the integrated energy and continuity equations together with the assumption of isentropic expansion through the valve and is given for subsonic flow by

$$A_e = \dot{m}\left\{2P_0\rho_0 \frac{\gamma}{\gamma-1}\left(\frac{P}{P_0}\right)^{\frac{2}{\gamma}}\left[1-\left(\frac{P}{P_0}\right)^{\frac{\gamma-1}{\gamma}}\right]\right\}^{-\frac{1}{2}} \tag{3}$$

The area A_l is a function of valve lift and is given by

$$A_l = \pi D L \tag{4}$$

The minimum area A_m is a function of valve and port geometry as well as valve lift (Fig. 17). Three cases may be encountered and are described by the following equations deduced from geometrical considerations; see, for example, reference [3].

Case 1

For $0 < L \leq 2t/\sin 2\psi$, A_m corresponds to the side area of a frustum of a cone with slant height perpendicular to the valve seat face and is given by

$$A_m = \pi L \cos\psi\,[D - 2t + (L/2)\sin 2\psi] \tag{5a}$$

Case 2

For

$$2t/\sin 2\psi < L \leq t\tan\psi + \left(\left[\frac{(D-2t)^2 - d^2}{4(D-t)}\right]^2 - t^2\right)^{1/2},$$

the slant height is no longer perpendicular to the seat face and A_m is given by

$$A_m = \pi(D-t)\,[(L - t\tan\psi)^2 + t^2]^{1/2} \tag{5b}$$

Case 3

For

$$t\tan\psi + \left(\left[\frac{(D-2t)^2 - d^2}{4(D-t)}\right]^2 - t^2\right)^{1/2} < L,$$

A_m corresponds to the passage area in the port and is given by

$$A_m = \frac{\pi}{4}\,[(D-2t)^2 - d^2] \tag{5c}$$

The Unsteady Potential Flow in an Axially Variable Annulus and Its Effect on the Dynamics of the Oscillating Rigid Center-Body

Dan Mateescu
Associate Professor.

Michael P. Paidoussis
Professor and Chairman.
Fellow ASME

Department of Mechanical Engineering,
McGill University,
Montreal, Quebec, Canada H3A 2K6

This paper presents an analytical investigation of the unsteady potential flow in a narrow annular passage formed by a motionless rigid duct and an oscillating rigid center-body, both of axially variable cross section, in order to determine the fluid-dynamic forces exerted on the center-body. Based on this theory, a first-approximation solution as well as a more accurate solution are derived for the unsteady incompressible fluid flow. The stability of the center-body is investigated, in terms of the aerodynamic (or hydrodynamic) coefficients of damping, stiffness and inertia (virtual mass), as determined by this theory. The influence of various system parameters on stability is discussed.

1 Introduction

The dynamics and stability of flexible cylindrical pipes conveying fluid have been studied very extensively, partly as a means to solving real flow-induced vibration problems in industrial installations, and partly because of the inherent interest in the dynamical behavior of this class of fundamental problems in Applied Mechanics [1]. In the first set of studies, a historical review of which may be found in reference [2], the pipe was considered to be a tubular beam. Later, the case of thin-walled pipes, considered to be thin cylindrical shells, was also analyzed; a literature review in this case is given in reference [3].

The dynamics of cylindrical bodies in axial flow has also received considerable attention, e.g., [4–6], the impetus in this case coming from the presence of such systems in nuclear reactors and in aeronautical and underwater applications – vide [7] for a review of this topic.

However, the study of dynamics of coaxial cylindrical bodies, with flow in the annular space in between, has received considerably less attention, despite the fact that such geometries are common in many engineering systems (e.g., in PWR and AGR nuclear reactors, in heat exchangers, certain types of valves, and large jet pumps) and that they have been shown to be particularly prone to a host of vibration-induced problems [1]. Some of the few studies on this topic were limited to cylindrical beams in cylindrical conduits, e.g., [8, 9], utilizing analytical tools not particularly suitable for very narrow annuli (which are of particular interest here), and very recently to coaxial cylindrical shells [3, 10]. The problem of a nonuniform body of revolution in annular flow has been given most attention in the United Kingdom, in conjunction with flow-induced vibration of the fuel stringers of AGR-type nuclear reactors, experienced while refueling [11–15]. The early work by Miller and Kennison [16, 17] and a recent review by Mulcahy [18] also ought to be mentioned.

Hobson [14] considered the problem of a rigid, flexibly mounted cylindrical structure with a rounded leading edge ("nose") in a cylindrical conduit or a diffuser. Based on the assumption of a very narrow annular clearance and neglecting the radial variation of the fluid velocity, interesting solutions for the fluid forces on the center-body were obtained, which were found to be in good accord with experiment. This work [14, 15] is of particular interest, because it attempts to solve a similar type of problem as that addressed in the present paper – although by a completely different approach and method of solution.

The present paper, which is the first part of a larger research program undertaken by the authors in this field, is devoted to the study of flow-induced vibrations of a flexibly mounted rigid body of revolution in a duct or nozzle, where the annular clearance is small and where both center-body and duct have specified axial variations of their cross sections. Despite the assumption of a small annular clearance with respect to the center-body radius, radial variations in the unsteady annular flow are nevertheless taken into account.

In order to determine the generalized unsteady fluid-dynamic (aerodynamic or hydrodynamic) forces, the present analysis of the unsteady annular flow will deal with the case of incompressible and inviscid fluids. A subsequent paper will be devoted to the analysis of the effect of fluid viscosity on the flow-induced vibrations of the center-body. In fact, a preliminary investigation of the influence of viscosity [19] indicates that it is not very important and that its effect on the dynamics of the center-body is stabilizing. Hence, the analysis presented here is a valid first approximation for the problem at hand.

Contributed by the Fluids Engineering Division and presented at the Symposium on Flow Induced Vibrations, Winter Annual Meeting, New Orleans, LA, December 5–10, 1984. Manuscript received by the Fluids Engineering Division, July 19, 1984.

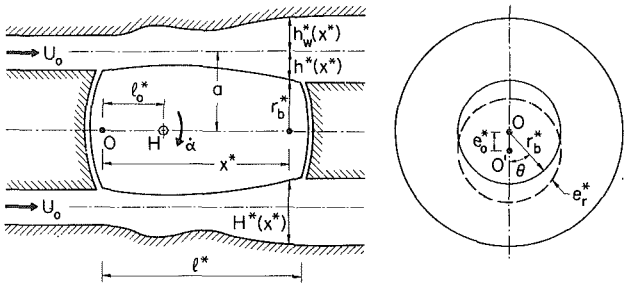

Fig. 1 Geometry of the oscillating body of revolution inside the duct of variable cross section

In the first part of the paper, the equations of unsteady annular flow are considered and solved by a method based on a local linearization scheme to determine the pressures and the fluid-dynamic forces acting on the center-body. This method of solution is applied to the usual case, where the length of the oscillating center-body is larger than, or comparable with, the mean annular radius; however, an extension of the method to the case of smaller center-body length is also presented, in Section 7.

With the fluid-dynamic forces acting on the body determined, the stability of the system is considered next, with the aim of establishing the conditions under which fluid-elastic instabilities are possible. The influence on flow-induced vibration of some geometrical parameters is also investigated, e.g., the effect of the shape of the annular passage (convergent or divergent), the position of the point of support of the body, and so on.

2 Problem Formulation

The system under consideration is shown in Fig. 1. It consists of a rigid center-body of revolution, hinged at point H and lying in a duct, so that it is subjected to an annular flow, as shown. The center-body is considered to perform oscillatory motion about the hinge-point, under the action of motion-dependent fluid forces, and restoring and retarding forces of a rotational spring and a dashpot (not shown). The circular cross sections of both center-body and duct are assumed to be axially variable, such that the annular clearance has a specified axial variation over the length of the center-body.

Two fixed cylindrical bodies are considered to be situated upstream and downstream of the oscillating center-body, and the corresponding annular clearance over these portions is considered to remain constant.

The following notation will be used in formulating the analytical model:

l^* = length of oscillating center-body
l_0^* = length OH, defining the position of the hinge, as shown in Fig. 1
a = mean radius of the annular passage
x^*, r^*, θ = cylindrical coordinate system
$r_b^*(x^*) = a - h^*(x^*)$ = center-body radius at location x^*
$r_w^*(x^*) = a + h_w^*(x^*)$ = duct-wall radius at location x^*
$H^*(x^*) = h^*(x^*) + h_w^*(x^*)$ = overall annular clearance at location x^*
$H_0^* = H^*(0), H_l^* = H^*(l^*)$ = annular clearances upstream and downstream of the oscillating center-body, respectively
$\alpha(t)$ = angle of rotation of center-body axis, in oscillatory motion about hinge-point
$\dot{\alpha}(t) = d\alpha/dt$ = angular velocity of center-body about hinge-point
Ω = circular frequency of center-body oscillation
$e_0^*(x^*,t) = (x^* - l_0^*)\alpha(t)$ = lateral displacement of center-body axis

The starred dimensional quantities have been utilzied here, so that their dimensionless counterparts, which are more widely used, may be defined later in simpler form; e.g., $x = x^*/a$.

At the upstream end of the system, where the annular clearance is constant, the fluid flow is assumed to be uniform and steady, with velocity U_0. Furthermore, assuming incompressible fluid flow, the velocity potential in cylindrical coordinates is

$$\frac{\partial^2\Phi}{\partial x^{*2}} + \frac{\partial^2\Phi}{\partial r^{*2}} + \frac{1}{r^*}\frac{\partial\Phi}{\partial r^*} + \frac{1}{r^{*2}}\frac{\partial^2\Phi}{\partial\theta^2} = 0, \tag{1}$$

subject to the boundary conditions

$$\left.\frac{\partial\Phi}{\partial r^*}\right|_{r^*=r_b^*} = \frac{\partial e_r^*}{\partial t} + \left[\frac{\partial\Phi}{\partial x^*}\right]_{r^*=r_b^*}\left\{\frac{\partial e_r^*}{\partial x^*} - \frac{\partial h^*}{\partial x^*}\right\} + \left[\frac{1}{r^*}\frac{\partial\Phi}{\partial\theta}\right]_{r^*=r_b^*}\frac{1}{r^*}\frac{\partial e_r^*}{\partial\theta} \tag{2a}$$

$$\left.\frac{\partial\Phi}{\partial r^*}\right|_{r^*=r_w^*} = \left[\frac{\partial\Phi}{\partial x^*}\right]_{r^*=r_w^*}\frac{dh_w^*}{dx^*}, \quad \left.\frac{\partial\Phi}{\partial x^*}\right|_{x^*\to-\infty} = U_0, \tag{2b}$$

where $e_r^*(x^*, \theta, t)$ represents the radial displacement of the oscillating center-body surface,

$$e_r^*(x^*,\theta,t) = e_0^*(x^*,t)\cos\theta = (x^* - l_0^*)\alpha(t)\cos\theta \tag{3}$$

in which the oscillatory motion of the center-body may be expressed as follows:

$$\alpha(t) = \alpha_0 \exp(i\Omega t) \tag{4}$$

Introducing the dimensionless quantities

$$x = x^*/a,\ r = r^*/a,\ \tau = U_0 t/a,\ \omega = \Omega a/U_0, \tag{5}$$

$$e_r = e_r^*/a,\ h = h^*/a,\ h_w = h_w^*/a,\ H(x) = h(x) + h_w(x), \tag{6}$$

and separating the fluid flow into a steady axisymmetric component (denoted with the subscript "s") and an unsteady one (without subscript), so that

$$\Phi(x^*, r^*\theta, t) = U_0 a[\phi_s(x,r) + \phi(x,r,\theta,\tau)] \tag{7}$$

equation (1) becomes

$$\frac{\partial^2\phi_s}{\partial x^{*2}} + \frac{\partial^2\phi_s}{\partial r^2} + \frac{1}{r}\frac{\partial\phi_s}{\partial r} = 0 \tag{8}$$

$$\frac{\partial^2\phi}{\partial x^2} + \frac{\partial^2\phi}{\partial r^2} + \frac{1}{r}\frac{\partial\phi}{\partial r} + \frac{1}{r^2}\frac{\partial^2\phi}{\partial\theta^2} = 0 \tag{9}$$

subject to the boundary conditions

$$\left.\frac{\partial\phi_s}{\partial r}\right|_{r=1-h} = -\left[\frac{\partial\phi_s}{\partial x} + \frac{\partial\phi}{\partial x}\right]_{r=1-h}\frac{\partial h}{\partial x}, \tag{10a}$$

$$\left.\frac{\partial\phi_s}{\partial r}\right|_{r=1+h_w} = \left[\frac{\partial\phi_s}{\partial x} + \frac{\partial\phi}{\partial x}\right]_{r=1+h_w}\frac{\partial h_w}{\partial x}, \quad \left.\frac{\partial\phi_s}{\partial x}\right|_{x\to-\infty} = 1, \tag{10b}$$

$$\left.\frac{\partial\phi}{\partial r}\right|_{r=1-h} = \frac{\partial e_r}{\partial\tau} + \left[\frac{\partial\phi_s}{\partial x} + \frac{\partial\phi}{\partial x}\right]_{r=1-h}\frac{\partial e_r}{\partial x} + \left[\frac{1}{r}\frac{\partial\phi}{\partial\theta}\right]_{r=1-h}\frac{1}{r}\frac{\partial e_r}{\partial\theta}, \tag{11a}$$

$$\left.\frac{\partial\phi}{\partial r}\right|_{r=1+h_w} = 0, \quad \left.\frac{\partial\phi}{\partial x}\right|_{x\to-\infty} = 0. \tag{11b}$$

Denoting by $p_s(x, r)$ and $p(x, r, \theta, \tau)$ the perturbation pressures corresponding to the axisymmetric steady fluid flow

and the unsteady fluid motion, respectively, and applying the Bernoulli-Lagrange equation, one obtains

$$p_s(x, r)+p(x,r,\theta,\tau)=-\tfrac{1}{2}\rho U_0^2\left\{2\frac{\partial\phi}{\partial\tau}+(\nabla\phi_s+\nabla\phi)^2-1\right\}. \quad (12)$$

Obviously, the generalized unsteady fluid-dynamic forces acting on the oscillating center-body do not depend on the perturbation pressure $p_s(x, r)$, because it is axially symmetric and time-independent; hence, the axisymmetric steady flow corresponding to the potential $\phi_s(x, r)$ will not be discussed in the subsequent analysis.

3 Linearization Procedure

In order to obtain an analytical solution of the problem, equations (10)–(12) have to be linearized, through the use of the small disturbance assumption.

In this connection, it is noted that the usual procedure of linearization with respect to the undisturbed fluid velocity U_0 (or, in nondimensional form, with respect to $\bar{U}_0 = 1$) is not sufficiently accurate for the case of narrow annuli, because the mean axial velocity $U^*(x^*)$ at location x^* could be substantially different from U_0, i.e.,

$$U^*(x^*)=\frac{1}{\pi(h_w^*+h^*)(2a+h_w^*-h^*)}\int_{a-h^*}^{a+h_w^*}\int_0^{2\pi}\frac{\partial\Phi}{\partial x^*}r^*dr^*d\theta. \quad (13)$$

For this reason, a procedure of local linearization will be used, with respect to the local dimensionless mean axial flow velocity, $U(x) = U^*(x^*)/U_0$, which may be obtained by applying the equation of continuity in integral form, so that

$$U(x)=H_0/H(x) \text{ where } H_0=H(0)=H^*(0)/a. \quad (14)$$

At the same time, defining the nondimensional variable

$$z=(r^*-a)/a=r-1, \quad (15)$$

the assumption of a narrow annular passage ($z << 1$) is introduced in the potential flow equations, (8) and (9).

Taking into consideration the form of boundary conditions (11 *a*, *b*), it is convenient to introduce the reduced motion potentials $\hat{\phi}_0(x, z)$ and $\hat{\phi}_1(x, z)$, defined by the relation

$$\phi(x, z, \theta, \tau)=\left\{\frac{d\alpha}{d\tau}\hat{\phi}_1(x,z)+\alpha(\tau)\hat{\phi}_0(x,z)\right\}\cos\theta, \quad (16)$$

where

$$\alpha(\tau)=\alpha_0\exp(i\omega\tau). \quad (17)$$

In this manner, the problem may be formulated by the following linearized equations:

$$\frac{\partial^2\hat{\phi}_j}{\partial x^2}+\frac{\partial^2\hat{\phi}_j}{\partial z^2}+\frac{\partial\hat{\phi}_j}{\partial z}-\hat{\phi}_j=0, \quad j=0,1, \quad (18)$$

subject to the boundary conditions

$$\left.\frac{\partial\hat{\phi}_0}{\partial z}\right|_{z=-h}=\frac{H_0}{H(x)}, \quad \left.\frac{\partial\hat{\phi}_0}{\partial z}\right|_{z=h_w}=0, \quad (19)$$

$$\left.\frac{\partial\hat{\phi}_1}{\partial z}\right|_{z=-h}=x-l_0, \quad \left.\frac{\partial\hat{\phi}_1}{\partial z}\right|_{z=h_w}=0, \quad (20)$$

where $l = l^*/a$ and $l_0 = l_0^*/a$.

The perturbation pressure equation, in linearized form, now becomes

$$-\frac{1}{\rho U_0^2}p(x,z,\theta,\tau)=\left\{\frac{d^2\alpha}{d\tau^2}\hat{\phi}_1(x,z)+\frac{d\alpha}{d\tau}\left[\hat{\phi}_0(x,z)+U(x)\frac{\partial\hat{\phi}_1}{\partial x}\right]+\alpha(\tau)U(x)\frac{\partial\hat{\phi}_0}{\partial x}\right\}\cos\theta. \quad (21)$$

4 Equation of Motion of the Center-Body

The equation of motion of the oscillating center-body may be written as

$$J_H\ddot{\alpha}+C\dot{\alpha}+K\alpha=M, \quad (22)$$

where J_H is the moment of inertia of the body about the hinge axis, K and C are the mechanical spring stiffness and damping; M represents the moment of pressure forces about the hinge axis,

$$M=-a^3\int_0^l\int_0^{2\pi}(x-l_0)p(x,-h,\theta,\tau)S(x)\cos\theta\,dx\,d\theta. \quad (23)$$

where

$$S(x)=\frac{1-h(x)}{[1+h'^2(x)]^{1/2}}\left\{1-\frac{1-h(x)}{x-l_0}h'(x)\right\}\simeq\frac{1-h(x)}{[1+h'^2(x)]^{1/2}}$$

accounts for the local slope of the body surface; $h(x)$ has been defined in equation (6) and $h'(x) = dh/dx$.

Introducing the dimensionless parameters

$$\sigma=\frac{\pi\rho a^5}{J_H}, \; k_0^2=\frac{K a^2}{J_H U_0^2}, \; k_1=\frac{C a}{J_H U_0}, \quad (24)$$

the foregoing equation of motion may be written in nondimensional form as

$$(1+\sigma q_2)\frac{d^2\alpha}{d\tau^2}+(k_1+\sigma q_1)\frac{d\alpha}{d\tau}+(k_0^2+\sigma q_0)\alpha(\tau)=0, \quad (25)$$

where q_0 and q_1 represent the dimensionless coefficients of the fluid-dynamic stiffness and damping, respectively, and q_2 is the nondimensional added or apparent (virtual) mass; more specifically,

$$q_0=-\int_0^l(x-l_0)S(x)U(x)\frac{\partial\hat{\phi}_0}{\partial x}(x,-h)dx, \quad (26a)$$

$$q_1=-\int_0^l(x-l_0)S(x)\left\{\hat{\phi}_0(x,-h)+U(x)\frac{\partial\hat{\phi}_1}{\partial x}(x,-h)\right\}dx, \quad (26b)$$

$$q_2=-\int_0^l(x-l_0)S(x)\hat{\phi}_1(x,-h)dx. \quad (26c)$$

As previously mentioned, these coefficients, which in fact represent the generalized unsteady fluid-dynamic forces, in nondimensional form and with inverted sign, do not depend on the steady flow potential, $\phi_s(x, r)$, because of the axial symmetry of the flow passage. For this reason, in this analysis, only the reduced motion potentials $\phi_0(x,z)$ and $\hat{\phi}_1(x,z)$, will be examined, wherein are included all unsteady effects.

5 First-Approximation Solution

A further simplification of the problem in the case of smooth axial variation of the narrow annular clearance may be introduced, based on the slender body assumption. In this case, the first term of equation (18) may be neglected, so that it simplifies to

$$\frac{\partial^2\hat{\phi}_j}{\partial z^2}+\frac{\partial\hat{\phi}_j}{\partial z}-\hat{\phi}_j=0, \quad j=0,1. \quad (27)$$

This clearly has a solution of the form

$$\hat{\phi}_j(z;x)=A_j(x)\exp(\beta_1 z)+B_j(x)\exp(\beta_2 z), \quad (28)$$

where

$$\beta_1=\tfrac{1}{2}(\beta-1), \; \beta_2=-\tfrac{1}{2}(\beta+1), \; \beta=\sqrt{5} \quad (29)$$

The coefficients A_j and B_j are smooth functions of x and may be determined from boundary conditions (19) and (20). Thus, for example, in the case of a cylindrical center-body and a variable cross-section duct, i.e., $H(x) = h_w(x)$, the solutions for the reduced potentials $\hat{\phi}_j$ and their axial derivatives $\partial\hat{\phi}_j/\partial x$ on the oscillating center-body may be expressed in the form

$$\hat{\phi}_0(-h;x) = U(x)G(H), \tag{30a}$$

$$\frac{\partial \hat{\phi}_0}{\partial x}(-h;x) = U(x)G'(H) + U'(x)G(H), \tag{30b}$$

$$\hat{\phi}_1(-h;x) = (x-l_0)G(H), \tag{31a}$$

$$\frac{\partial \hat{\phi}_1}{\partial x}(-h;x) = (x-l_0)G'(H) + G(H), \tag{31b}$$

$$G(H) = -\frac{\beta}{\exp(\beta H)-1} - \tfrac{1}{2}(\beta-1),$$

$$G'(H) = \beta^2 \frac{\exp[\beta H]}{[\exp(\beta H)-1]^2}. \tag{32}$$

Introducing these results into equations (26*a–c*), the determination of the nondimensional fluid-dynamic coefficients of stiffness, damping and virtual mass is reduced to simple quadratures. Numerical examples of these solutions will be presented in Section 8.

6 A More Accurate Method of Solution

It is expected that for higher frequency oscillations, the first approximation solution developed in Section 5 is not sufficiently accurate. This is because the virtual mass coefficient and the coefficient of fluid-dynamic damping, which depend on the reduced potential $\hat{\phi}_1$, cannot be accurately reproduced if the slender body approximation is utilized, even for very smooth or null axial variation of the annular clearance.

In this case, the complete form of partial differential equation (18) must be considered. A solution of the following form is substituted therein,

$$\hat{\phi}_j(x,z) = \sum_k f_{jk}(x)F_{jk}(z), \tag{33}$$

which yields the ordinary differential equations

$$f''_{jk}(x) - \gamma_k^2 f_{jk}(x) = 0, \tag{34a}$$

$$F''_{jk}(z) + F'_{jk}(z) - (1-\gamma_k^2)F_{jk}(z) = 0; \tag{34b}$$

these admit the general solutions

$$f_{jk}(x) = A_{jk}\exp(\gamma_k x) + B_{jk}\exp(-\gamma_k x), \tag{35a}$$

$$F_{jk}(z) = a_{jk}\exp(\beta_{1k}z) + b_{jk}\exp(-\beta_{2k}z), \tag{35b}$$

where

$$\beta_{1k} = \tfrac{1}{2}(\beta_k - 1),\ \beta_{2k} = \tfrac{1}{2}(\beta_k + 1),\ \beta_k = \sqrt{5-4\gamma_k^2}. \tag{36}$$

Assuming imaginary values for the constants $\gamma_k(\gamma_k = ic_k)$ the expressions $U(x) = H_0/H(x)$ and $x-l_0$, which appear in boundary conditions (19) and (20), may be expanded in the form of truncated Fourier expansions

$$U(x) = \frac{H_0}{H(x)} = \sum_{k\in N^*} D_{0k}\cos c_k x + \sum_{k\in N} E_{0k}\sin c_k x, \tag{37a}$$

$$x - l_0 = \sum_{k\in N^*} D_{1k}\cos c_k x + \sum_{k\in N} E_{1k}\sin c_k x, \tag{37b}$$

where

$$N = \{1,2,3,\ldots,n,\ldots\},\ N^* = \{0,1,2,\ldots,n,\ldots\}. \tag{38}$$

Introducing these expressions in (19) and (20), for example, in the case of a cylindrical center-body and a variable cross-section duct, i.e., $H(x) = h_w(x)$, the solutions

$$\hat{\phi}_j(x,-h) = \sum_{k\in N^*} D_{jk}G_k(H)\cos c_k x + \sum_{k\in N} E_{jk}G_k(H)\sin c_k x, \tag{39}$$

may be obtained, where

$$G_k(H) = -\frac{4\beta_k}{\beta_k^2-1}\frac{1}{\exp(\beta_k H)-1} - \frac{2}{\beta_k+1},\ \beta_k = \sqrt{5+4c_k^2}. \tag{40}$$

The determination of the nondimensional fluid-dynamic coefficients of stiffness, damping and virtual mass has been thus reduced again to simple quadratures.

A comparison between the solutions obtained with this more accurate method and with the approximate method developed earlier is presented in Section 8.

7 Extension of the Method for the Case of Short Center-Bodies

The foregoing solutions have been derived on the assumption that the length of the oscillating center-body is larger than or comparable with the mean annular radius, and hence that it is much greater than the width of the narrow annular passage. In fact, this is the usual situation in the majority of concrete applications involving narrow annular passages. Under such conditions, small variations in the pressure distribution at the two ends of the center-body (resulting from differences in the upstream and downstream boundary conditions of the unsteady fluid flow) have very little effect on the fluid-dynamic coefficients of stiffness, damping and virtual mass.

Nevertheless, the case where the length of the oscillating body is smaller than its radius, and hence not very large with respect to the narrow annular clearance, can also be treated by the method of Section 6. Special precautions have to be taken in this case, however, in order to obtain solutions satisfying accurately all the boundary conditions.

The boundary conditions (19) and (20) on the oscillating center-body have to be expressed in convenient truncated expansions (with real or imaginary values for the constants γ_k) of the form

$$\left.\frac{\partial \hat{\phi}_0}{\partial z}\right|_{z=-h} = \frac{H_0}{H(x)}\mathcal{H}(x)\mathcal{H}(l-x) = \sum_{k\in N^*}\{D_{0k}\exp(\gamma_k x) + E_{0k}\exp(-\gamma_k x)\}, \tag{41}$$

$$\left.\frac{\partial \hat{\phi}_1}{\partial z}\right|_{z=-h} = (x-l_0)\mathcal{H}(x)\mathcal{H}(l-x) = \sum_{k\in N^*}\{D_{1k}\exp(\gamma_k x) + E_{1k}\exp(-\gamma_k x)\}, \tag{42}$$

where $\mathcal{H}(x)$ denotes the Heaviside generalized function

$$\mathcal{H}(X) = \begin{cases} 0 \text{ for } X<0, \\ 1 \text{ for } X>0. \end{cases} \tag{44}$$

8 Stability of Flow-Induced Vibrations of the Center-Body in a Variable Cross-Section Duct

The dynamics of the oscillating center-body is governed by the equation of motion (25), where the nondimensional coefficients of fluid-dynamic stiffness q_0, damping q_1, and virtual mass q_2, as well as all the other parameters, have been defined in Section 4.

All essential characteristics of vibration of the center-body in the annular flow, e.g., the frequency, amplitude and stability of the vibrations, depend critically on the fluid-dynamic coupling terms (fluid-dynamic stiffness, damping and virtual mass), as well as on the relative magnitude of these terms vis-à-vis the mechanical stiffness and damping

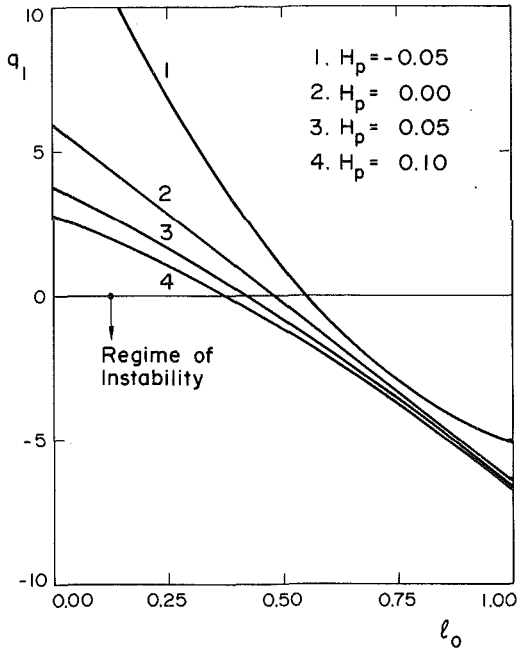

Fig. 2 Typical variation of the nondimensional coefficient of fluid-dynamic damping, by the analysis of Section 6; $H_0 = 0.1$

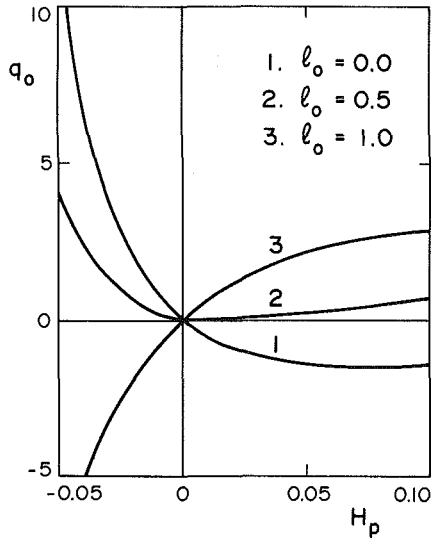

Fig. 3 Typical variation of the nondimensional coefficient of fluid-dynamic stiffness, by the analysis of Section 6; $H_0 = 0.1$

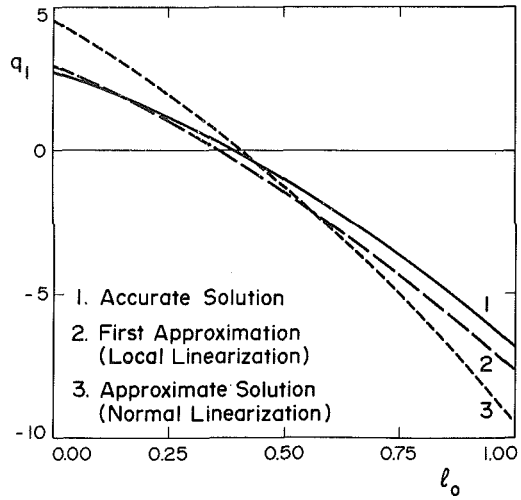

Fig. 4 Nondimensional coefficient of fluid-dynamic damping (H_0 = 0.1. H_p = 0.1); comparison between: 1 Accurate solution (by the analysis of Section 6); 2 First approximation solution based on local linearization (by the analysis of Section 5); 3 Approximate solution based on normal linearization (by an analysis similar to that of Section 5).

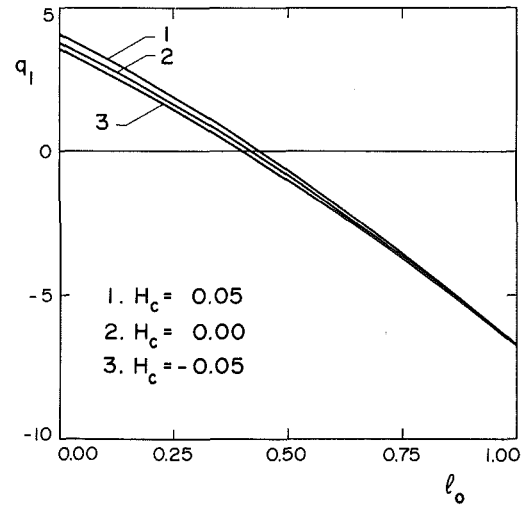

Fig. 5 Influence of the wall curvature parameter H_c on the nondimensional coefficient of aerodynamic damping (H_0 = 0.1; H_p = 0.05)

parameters. A very important role is played by the dimensionless parameter σ, defined by equation (24), and involving the fluid density, the mean radius of the annular passage and the moment of inertia of the oscillating center-body.

For the sake of simplicity – and without any loss of generality – the case of vanishingly small mechanical stiffness and damping coefficients ($k_1 \simeq k_0 \simeq 0$) will be considered first. In this case, amplified (unstable, in the linear sense) vibrations will occur, provided that the fluid-dynamic stiffness coefficient is positive and the corresponding damping coefficient negative (i.e., $q_0 > 0, q_1 < 0$).

The case of negative fluid-dynamic stiffness is of course also possible – which could lead to divergence, if $|\sigma q_0| > k_0{}^2$ – but will not be examined here in great detail, again for simplicity, and because it is considered that, for a real system, the condition $k_0{}^2 + \sigma q_0 > 0$ is likely to be satisfied, in any case.

Of course, the condition of an overall negative damping *must* be satisfied if amplified vibrations are to materialize, so that, generally, the condition $k_1 + \sigma q_1 < 0$ must be satisfied. It is noted that this condition is more restrictive than the one specified in the foregoing for $k_1 \simeq 0$. Nevertheless, if the damping characteristics of a system are known, so that k_1 may be determined, the results to be presented may be used as they stand, simply by linearly shifting the condition of amplified vibrations from $q_1 \leq 0$ to $q_1 \leq -k_1/\sigma$.

There is a great variety of possible geometrical systems which could be analyzed. However, to illustrate the effect of some of the system parameters and to show the type of results which can be obtained by means of the analytical models developed here, calculations are confined to one particular type of system: a cylindrical center-body, hinged at a variable dimensionless distance $l_0 = l_0^*/a$ (see Fig. 1), in a duct of variable cross section; the resulting clearance of the annular passage may be linear or parabolic, as defined by the relationships

$$H(x) = H_0 + H_p x, H_p = (H_1 - H_0)/l, \tag{44}$$

$$H(x) = H_0 + H_p x + H_c x^2, \tag{45}$$

respectively.

The variation of fluid-dynamic damping coefficient q_1, with l_0 is shown in Fig. 2, for four values of H_p, as defined by equation (44). It is seen that in all cases, if l_0 is sufficiently large, i.e., as the hinge-point is moved downstream, q_1 eventually becomes negative, indicating the possibility of amplified vibrations. It is of interest that for $H_p = 0$, i.e., for a cylindrical duct, if the hinge-point is downstream of the mid-length of the center-body, approximately, amplified vibrations are predicted to occur.

It is seen, furthermore, that a linearly divergent (diffuser-shaped) duct, corresponding to $H_p > 0$, destabilizes the system vis-à-vis a cylindrical duct – so that it is necessary to place the hinge-point further upstream to ensure stability. The opposite is true for a convergent duct shape, which has a stabilizing influence on the system.

The dependence of the fluid-dynamic stiffness coefficient, q_0, on H_p is illustrated in Fig. 3 for three values of l_0. It is seen that for $H_p > 0$, i.e., a diffuser-shaped duct, it is possible to have a slightly negative q_0, provided that the hinge-point is located at the foremost end of the body ($l_0 = 0$); however, this does not correspond to an instability, because for this set of parameters $q_1 > 0$. On the other hand, for a convergent duct and $l_0 = 1.0$, q_0 can be strongly negative in a region of $q_1 < 0$, indicating the possibility of divergence.

A comparison between the two variants of the analytical model, i.e., between the first-approximation (slender-body) solution of Section 5 and the more accurate soluton of Section 6, is made in Fig. 4. These two solutions were obtained by the method of local linearization, developed in Section 3; results, based on the normal (as opposed to local) linearization scheme, with respect to the undisturbed flow velocity U_0, are also shown. It is important to note that significant differences in the predicted q_1 arise, specifically if the inferior "normal linearization" scheme were to be employed (curve 3), instead of that based on local linearization; moreover, predictions of instability, based on the former, are nonconservative.

Considering parabolic variations of annular width, as given by equation (45), the results of Fig. 5 indicate that the effect on q_1 is not very strong. Nevertheless, in the case of a divergent annular passage, a concave shape, as viewed from the annulus-side of the system, tends to destabilize the system, as compared to a linear diffuser-shaped one; while the opposite is true for a convex shape.

At this point, it would be useful to present a concrete example, so as to illustrate the utilization of the results of Figs. 2–5 and to discuss stability in terms of the annular flow velocity, U_0. Consider, therefore, a cylindrical center-body of radius $a = 0.05$ m, in a divergent duct defined by $H_0 = 0.10$ and $H_p = 0.05$. Consider further that the center-body is supported at its midpoint ($l_0 = 0.5$), in such manner that its natural frequency is $\omega_n = 60$ rad/s and the mechanical damping factor $\zeta = C/(2\omega_n J_H) = 0.005$. Furthermore, assuming that the fluid is water, let σ, defined in (24), take on the reasonable value of $\sigma = 0.2$ (to which corresponds a certain J_H for given a and ρ).

Now, from Fig. 3 it is seen that the fluid-dynamic stiffness coefficient q_0 is positive (which precludes the possibility of divergence), and from Fig. 2 it is found that the fluid-dynamic damping coefficient is negative, $q_1 = -0.79$, indicating that the system could be susceptible to amplified oscillation. The instability threshold, defined by $k_1 + \sigma q_1 = 0$ in equation (25), may be rewritten in dimensional terms as $U_{0\,cr} = 2\times \zeta\omega_n a/(-q_1\sigma)$. Utilizing the numerical values given previously, it is found that the system develops amplified oscillation for $U_0 \geq 0.19$ m/s, which is a very small flow velocity indeed; of course for $l_0 > 0.5$ the critical U_0 would be lower. On the other hand, if the center-body were located in a convergent duct ($H_0 = 0.10$, $H_p = -0.05$), then $q_1 > 0$ for $l_0 = 0.5$, indicating that the system would be unconditionally stable for all values of U_0 and ζ. In this case, increasing U_0 would generate additional fluid-dynamic damping which will increase the stability of the system.

9 Conclusions

An analytical theory for studying the unsteady potential flow in an axially variable narrow annular passage has been developed in the first part of this paper. Based on a new and more accurate method of local linearization of the problem, this theory has permitted to determine analytically, for the first time, a first-approximation solution, as well as a more accurate one.

To the best of the authors' knowledge, this theory for the unsteady annular flow is original and is presented for the first time in this paper.

The stability of flow-induced vibrations of the center-body has been studied with the aid of the fluid-dynamic forces obtained by means of the foregoing analyses. It was found that the most influential parameter on the stability of flow-induced vibrations is the position of the center-body hinge. Amplification of flow-induced vibrations occurs when the hinge-point is situated toward the downstream end of the center-body, behind a critical position at which the fluid-dynamic damping coefficient vanishes.

The critical position of the hinge axis is substantially influenced by axial variations of the annular clearance. A divergent annular passage will move upstream the critical position of the hinge, having a destabilizing effect, while a convergent annular passage will do the opposite, having a stabilizing effect.

The curvature of the duct wall and the ratio of annular clearance to mean radius of the center-body have smaller effects on the stability of flow-induced vibrations.

Currently, work is under way to extend the theoretical model in order to take into account the influence of viscosity (vide some preliminary results in reference [19]) and to test the theoretical results experimentally.

Acknowledgments

The authors gratefully acknowledge the support given to this research by the Natural Sciences and Engineering Research Council of Canada.

References

1 Paidoussis, M. P., "Flow-Induced Vibrations in Nuclear Reactors and Heat Exchangers: Practical Experiences and State of Knowledge," in *Practical Experiences with Flow Induced Vibrations*, eds., Naudascher, E., and Rockwell, D., Springer-Verlag, Berlin, 1980, pp. 1–81.

2 Paidoussis, M. P., and Issid, N. T., "Dynamic Stability of Pipes Conveying Fluid," *Journal of Sound and Vibration*, Vol. 33, 1974, pp. 267–294.

3 Paidoussis, M. P., Chan, S. P., and Misra, A. K., "Dynamics and Stability of Coaxial Cylindrical Shells Containing Flowing Fluid," *Journal of Sound and Vibration*, Vol. 97, 1984, pp. 201–235.

4 Paidoussis, M. P., "Dynamics of Flexible Slender Cylinders in Axial Flow. Part 1: Theory; Part 2: Experiments," *Journal of Fluid Mechanics*, Vol. 26, 1966, pp. 717-736, 737-751.

5 Paidoussis, M. P., "Dynamics of Cylindrical Structures Subjected to Axial Flow," *Journal of Sound and Vibration*, Vol. 29, 1973, pp. 365–385.

6 Dowell, E. H., and Widnall, S. E., "Generalized Aerodynamic Forces on an Oscillating Cylindrical Shell: Subsonic and Supersonic Flow," *AIAA Journal*, Vol. 4, 1966, pp. 607–610.

7 Paidoussis, M. P., "Fluidelastic Vibration of Cylinder Arrays in Axial and Crossflow: State of the Art," *Journal of Sound and Vibration*, Vol. 76, 1981, pp. 329–360.

8 Paidoussis, M. P., and Pettigrew, M. J., "Dynamics of Flexible Cylinders in Axisymmetrically Confined Flow," ASME *Journal of Applied Mechanics*, Vol. 46, 1979, pp. 37–44.

9 Paidoussis, M. P., and Ostoja-Starzewski, M., "Dynamics of a Flexible Cylinder in Subsonic Axial Flow," *AIAA Journal*, Vol. 19, 1981, pp. 1467–1475.

10 Paidoussis, M. P., Misra, A. K., and Chan, S. P., "Dynamics and Stability of Coaxial Cylindrical Shells Conveying Viscous Fluid," Symposium on

Flow-Induced Vibrations; Vol. 4: Vibration Induced by Axial and Annular Flows, eds., Paidoussis, M. P., and Au-Yang, M. K., pp. 71–86; Dec. 1984, ASME, New York, ASME *Journal of Applied Mechanics*, Vol. 52, 1985, pp. 389–396.

11 Parkin, M. W., "A Review of Basic Studies and Modelling Applied to Annular Flow," *Proceedings UKAEA/NPL International Symposium on Vibration Problems in Industry*, Keswick, U.K., 1973, Paper No. 628.

12 Roberts, G. P., Hallam, M. G., Dean, R. B., and Parkin, M. W., "A Theoretical Study of Hartlepool AGR Stringer Vibration during Refueling at Power," *Proceedings 3rd International Conference in Vibration in Nuclear Plant*, Keswick, U.K., pp. 624–648.

13 Parkin, M. W., France, E. R., and Boley, W. E., "Flow Instability Due to a Diameter Reduction of Limited Length in a Long Annular Passage," ASME *Journal of Vibraiton, Acoustics, Stress, and Reliability in Design*, Vol. 105, 1983, pp. 355–360.

14 Hobson, D. E., "Fluid-Elastic Instabilities Caused by Flow in an Annulus," *Proceedings 3rd Keswick International Conference on Vibration in Nuclear Plant*, Keswick U.K., pp. 440–463.

15 Hobson, D. E., et al., A Series of Confidential C.E.G.B. Memoranda, Marchwood Engineering Laboratories, U.K., 1980–1983, made available to the authors.

16 Miller, D. R., and Kennison, R. G., "Theoretical Analysis of Flow-Induced Vibration of a Blade Suspended in Channel Flow," ASME Paper No. 66-WA/NE-1, 1966.

17 Miller, D. R., "Generation of Positive and Negative Damping With Flow Restrictor in Axial Flow," *Proceedings of the Conference on Flow-Induced Vibrations in Reactor System Components*, Argonne National Laboratory Report ANL-7685, 1970, pp. 304–307.

18 Mulcahy, T. M., "A Review of Leakage-Flow Induced Vibrations of Reactor Components," Argonne National Laboratory Report ANL-83-43, 1983.

19 Mateescu, D., and Paidoussis, M. P., "Annular-Flow-Induced Vibration of an Axially Variable Body of Revolution in a Duct of Variable Cross Section," Symposium on Flow-Induced Vibrations; Vol. 4: Vibration Induced by Axial and Annular Flows, eds., Paidoussis, M. P., and Au-Yang, M. K., Dec. 1984, ASME, New York, p. 53–69.

Journal of Fluids Engineering

Technical Briefs

Roughness Effects in Head's Integral Boundary-Layer Method

G. H. Christoph[1]

Introduction

Most roughness analyses are based on Nikuradse's sand-grain experiments and the law-of-the-wall velocity profiles fit to the data. Several correlations have been proposed relating actual roughness heights, spacings, and shapes to an equivalent sand-grain height so that Nikuradse's results can be used. Examples of such correlations can be found in Dvorak [1], Simpson [2], and Dirling [3]. These correlations are not always reliable, especially for closely spaced roughness elements such as are usually found in practice.

More accurate methods that account for actual roughness effects are those employed by Finson and Clarke [4], Lin and Bywater [5], Christoph and Pletcher [6] and Taylor et al. [7]. These techniques calculate the form-drag contributions of individual roughness elements. The governing boundary layer equations are cast in a form to account for the blockage effects of the roughness elements. The effect of roughness is then described by a sink term (form drag) in the momentum equation.

Based on results of numerous computer runs using the discrete element approach, Finson [8] suggested a correlation relating equivalent sand-grain height to roughness height, spacing, and shape. This correlation was shown by Finson [8] to be accurate for closely packed elements. In this Technical Brief, Finson's correlation is used to generate rough-wall skin friction and thicknesses from Head's entrainment method. Calculations are compared to the data sets of Coleman [9] and Healzer et al. [10].

Approach

The purpose of this study was to implement a simple but accurate roughness methodology using Head's entrainment technique. For a two-dimensional incompressible flow the momentum integral equation is

$$\frac{d\theta}{dx} = \frac{c_f}{2} - \theta\left(\frac{2+H}{u_e}\frac{du_e}{d_x}\right) \tag{1}$$

and the boundary-layer entrainment equation is

$$\frac{dq}{dx} = F(G) - \frac{q}{u_e}\frac{du_e}{dx} \tag{2}$$

where

$$q = G\theta, H = \delta^*/\theta. \tag{3}$$

For a smooth surface, Head's [11] shape factor G and the rate of entrainment function $F(G)$ have been modeled as

$$G = 1.535(H-0.7)^{-2.715} + 3.3 \tag{4}$$

$$F(G) = 0.0306(G-3.0)^{-0.653} \tag{5}$$

For all results presented, the smooth-wall skin-friction coefficient c_{fs} was determined from [8]

$$(2/c_{fs})^{1/2} = \frac{1}{K}\ln \mathrm{Re}_\theta + 5.5, K = 0.41 \tag{6}$$

In the present study it was assumed that roughness effects are accounted for simply by including roughness in the skin-friction model. The momentum thickness θ and the shape factor H are affected by roughness through integration of equations (1) and (2). The process of entrainment is mainly controlled by the velocity defect in the outer part of the boundary layer and therefore the entrainment models should not be very sensitive to surface roughness. In fact, Dvorak [1] shows Head's smooth surface entrainment functions F and G are excellent correlations for the rough plate data of Bettermann. Also, Head [11] states that even for such wall effects as injection or suction, the functions F and G are substantially unaltered. The magnitude of the entrainment variables (G and F) will change, however, due to their dependence on H.

Roughness effects are modeled in c_f through the classical velocity shift, that is,

$$u_r^+ = u_s^+ - \Delta B \tag{7}$$

where

$$u_s^+ = \frac{1}{K}\ln y^+ + 5.5, K = 0.41$$

$$\Delta B = \frac{1}{K}\ln k_{es}^+ - 3 \text{ (fully rough)} \tag{8}$$

The subscripts s and r refer to smooth and rough conditions, respectively. Equation (7) can be written in terms of the rough-wall skin-friction coefficient c_{fr} and the smooth-wall skin-friction friction coefficient c_{fs} as

$$(2/c_{fr})^{1/2} = (2/c_{fs})^{1/2} - \Delta B. \tag{9}$$

If c_{fs} and the equivalent sand-grain height k_{es} are known, then c_{fr} is easily solved from equation (9).

Calculation of Equivalent Sand-Grain Height-Discrete Element Approach

Following the analysis of Finson [8], the wall shear coefficient is given by

$$c_{fr} = c_{fs} + \int_0^k \frac{u^2}{u_e^2} c_D f(y)\frac{D(y)}{L^2}\,dy \tag{10}$$

where

[1]Science Applications International Corp., Annapolis, MD 21401.

Contributed by the Fluids Engineering Division of The American Society of Mechanical Engineers. Manuscript received by the Fluids Engineering Division, September 11, 1984.

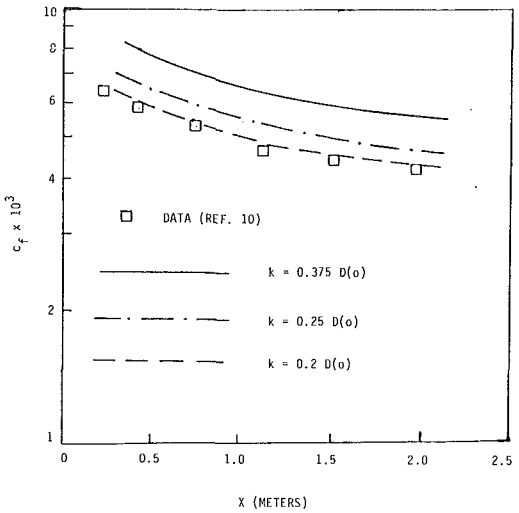

Fig. 1 Rough surface skin friction comparisons to data of Healzer et al. (u = 42.37 m/s)

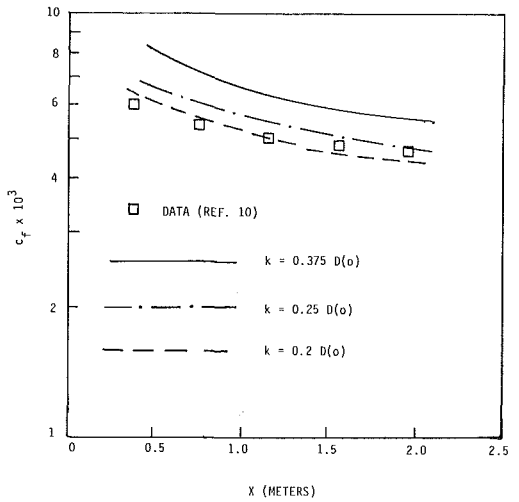

Fig. 2 Rough surface skin friction comparisons to data of Healzer et al. (u = 73.76)

$$f(y) = \frac{1 - D(y)L}{1 - \pi D^2(y)/(4L^2)}, \tag{11}$$

c_D is a form-drag coefficient, k is the actual roughness height, $D(y)$ is the roughness element diameter at height y, and L is the average center-to-center element spacing. Taking $u = u_R$ = constant, c_D = constant and evaluating $f(y)$ at $y = k/2$, equation (10) becomes

$$c_{fr} = c_{fs} + \frac{u_R^2}{u_e^2} c_D f(k/2)/\lambda_k \tag{12}$$

where the parameter

λ_k^{-1} = projected frontal area of the elements per unit surface area.

Based on numerous calculations for a variety of roughness shapes and spacings, Finson [8] correlated u_R/u_e with λ_k. A value of c_D = 0.6 was used. Using this u_R/u_e correlation, along with equations (12) and (6), rearrangement of equation (9) results in an expression for k_{es}. The result is

$$k_{es}/k = \exp[K(8.5 - (2/c_{fr}^*)^{1/2} + \frac{1}{K}\ln(2/c_{fr}^*)^{1/2})]. \tag{13}$$

where

$$c_{fr}^* = 0.00177 + 0.6(0.247 + 0.234 \log_{10}\lambda_k)^2 f(k/2)/\lambda_k. \tag{14}$$

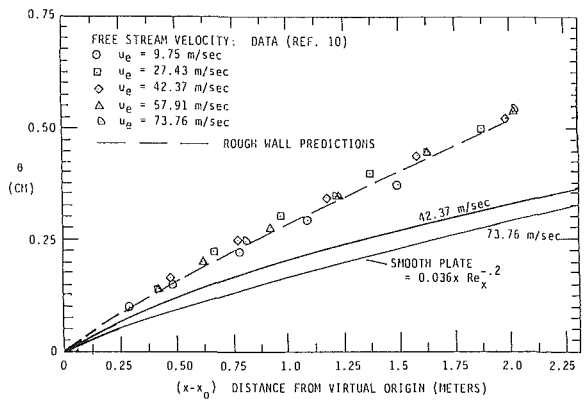

Fig. 3 Rough surface momentum thickness predictions for Healzer et al. data

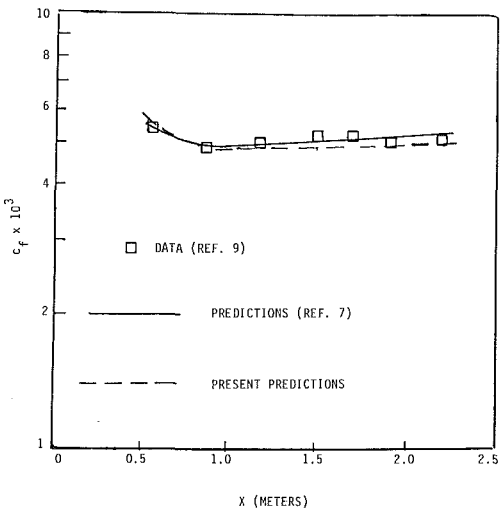

Fig. 4 Comparison of calculations to data of Coleman (K_r = 0.15 × 10^{-3})

Results

The roughness approach described above was validated by comparison to the roughness data of Healzer, et al. [10] and Coleman [9]. First comparisons were made to the fully rough plate data of Healzer et al. [10].

The incompressible flow experiments of Healzer et al. [10] provided data on skin-friction, heat transfer and profiles for rough surfaces with and without blowing. The rough surface consisted of a regular array of tightly packed ($L/D(0)$ = 1) spherical elements, each 0.127 cm in diameter. Tests were run at freestream velocities from 9.75 to 73.76 m/s. Since the roughness elements in these experiments were touching each other, it was necessary to define an effective wall location. Three effective roughness heights were chosen for evaluation: k = 0.2D(0), 0.25D(0), 0.375D(0); where D(0) is the sphere diameter. Taylor et al. [7] found that k = 0.2D(0) gave the best overall results for Schlichting's skin-friction data for most densely packed spheres, and was also the value they successfully used for all Stanford data comparisons. Present calculations for the skin-friction coefficients are shown in Figs. 1 and 2 for free-stream velocities of 42.37 and 73.76 m/sec. As seen from Figs. 1 and 2, excellent agreement is obtained for k = 0.2D(0). Rough-wall predictions for momentum thickness are shown in Fig. 3 for freestream velocities of 42.37 and 73.76 m/s. Results are essentially identical for both velocities. This phenomenon is confirmed by the experimental data.

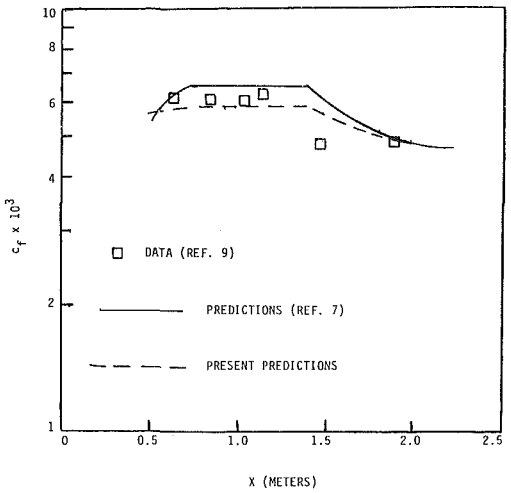

Fig. 5 Comparison of calculations to data of Coleman ($K_r = 0.29 \times 10^{-3}$)

Comparisons were also made to the rough-wall, favorable pressure gradient data of Coleman [9]. The surface roughness characteristics were identical to those of Healzer et al. [10]. Figures 4 and 5 present calculations for $K_r = D(0)/2u_e$ $du_e/dx = 0.15 \times 10^{-3}$ and 0.29×10^{-3}, respectively. Also shown are predictions from Taylor et al. [7]. An effective roughness height $k = 0.2D(0)$ was used.

Closing Remarks

A simple procedure was presented to include surface roughness effects in Head's momentum integral entrainment method. An equivalent sand-grain height correlation, suggested by Finson [8] from his discrete element approach to solving the boundary-layer equations, was employed. This correlation explicitly includes roughness height, spacing and geometric effects. Comparisons were shown for the rough-wall data sets of Coleman [9] and Healzer et al. [10]. In both cases good agreement was obtained.

Acknowledgments

This work was sponsored by the Naval Sea Systems Command General Hydrodynamics Research Program, administered by the David W. Taylor Naval Ship Research and Development Center under the Office of Naval Research Contract #N00014-81-C-0234. The author is grateful to Dr. C. von Kerczek of Science Applications International Corporation for his helpful suggestions.

References

1 Dvorak, F. A., "Calculation of Turbulent Boundary Layers on Rough Surfaces in Pressure Gradient," *AIAA Journal*, Vol. 7, No. 9, Sept. 1969, pp. 1752–1759.

2 Simpson, R. L., "A Generalized Correlation of Roughness Density Effects on the Turbulent Boundary Layer," *AIAA Journal*, Vol. 11, No. 2, Feb. 1973, pp. 242–244.

3 Dirling, R. B., Jr., "A Method for Computing Roughwall Heat Transfer Rates on Re-entry Nosetips," AIAA Paper No. 73-763, presented at the AIAA 8th Thermophysics Conference, Palm Springs, CA, 16–18 July 1973.

4 Finson, M. L., and Clarke, A. S., "The Effect of Surface Roughness Character on Turbulent Re-entry Heating," AIAA Paper No. 80-1459, 1980.

5 Lin, T. C. and Bywater, R. J., "Turbulence Models for High-Speed, Rough-wall Boundary Layers," *AIAA Journal*, Vol. 20, No. 3, Mar. 1982, pp. 325–333.

6 Christoph, G. H. and Pletcher, R. H., "Prediction fo Rough-Wall Skin Friction and Heat Transfer," *AIAA Journal*, Vol. 21, No. 4, Apr. 1983, pp. 509–515.

7 Taylor, R. P., Coleman, H. W., and Hodge, B. K., "A Discrete Element Prediction Approach for Turbulent Flow Over Rough Surfaces," Report TFD-84-1, Mississippi State University, Feb. 1984.

8 Finson, M. L., "A Model for Rough Wall Turbulent Heating and Skin-Friction," AIAA Paper No. 82-0199, presented at AIAA 20th Aerospace Sciences Meeting, Orlando, FL, 11-14 Jan. 1982.

9 Coleman, H. W., "Momentum and Energy Transport in the Accelerated Fully Rough Turbulent Boundary Layer," Stanford University Department of Mechanical Engineering Report HMT-24, 1976.

10 Healzer, J. M., Moffat, R. J., and Kays, W. M., "The Turbulent Boundary Layer on a Porous Rough Plate: Experimental Heat Transfer with Uniform Blowing," AIAA Paper No. 74-680 and ASME Paper No. 74-HT-14, presented at the AIAA/ASME 1974 Thermophysics and Heat Transfer Conference, Boston, MA, 15–17 July 1974.

11 Head, M. R., "Cambridge Work on Entrainment," *Proceedings Computation of Turbulent Boundary Layers*—1968 AFOSR-IFP-Stanford Conference, Stanford University Department of Mechanical Engineering, Stanford, CA.

Boundary Conditions for Flow Over Permeable Surfaces

G. J. Hokenson[1]

Introduction

The subject of this work is viscous flow adjacent to a permeable surface and the boundary conditions appropriate thereto [1]. Our objective is to generalize and extend the analysis in references [2 and 3] from first principles in order to clarify the relationship between the experimental reality of a distribution of discrete nonuniform jets in a crossflow and computations which employ continuous (locally uniform) normal velocity and zero slip boundary conditions. The hypothesis is that some details of the (vortical) flow passing through the boundary and the external (partially slipping [1]) flow along the boundary affect the qualitative structure of the solution.

The analysis presented here is an extension of the work described in reference [4] and is directed at continuum flow phenomena. Although, for most problems of practical importance, we are generally interested in turbulent flow, a laminar flow is considered here to expose the particulars of the premise. Some of the results, therefore, bear directly on current interest in laminar flow control by suction. The role which turbulent flow considerations play shall be discussed subsequently. Finally, the restriction that a boundary layer structure be maintained, forcing limitations on the mass transfer magnitude, shall not be invoked.

Background

Consider first the detailed picture of a porous wall as a distribution of discrete jets. (The case of blowing will be used for purposes of discussion.) By placing a "jump-type" control volume at the exit plane of an individual jet, the results of reference [4] indicate that the external flow "slips" over the jet (i.e., the mass transfer vector tilts) with a velocity determined by:

$$\delta(\rho uv) = \delta\tau, \tag{1}$$

where δ signifies the jump in values of the variables across the control volume. Conventional notation assigns ρ, u, v, and τ to the fluid density, streamwise velocity, normal velocity and shear stress, respectively. Invoking continuity:

$$\delta(\rho v) = 0, \tag{2}$$

[1]Chief Scientist, The Hokenson Company, Los Angeles, Calif., Mem. ASME.

Contributed by the Fluids Engineering Division of THE AMERICAN SOCIETY OF MECHANICAL ENGINEERS. Manuscript received by the Fluids Engineering Division, February 4, 1984.

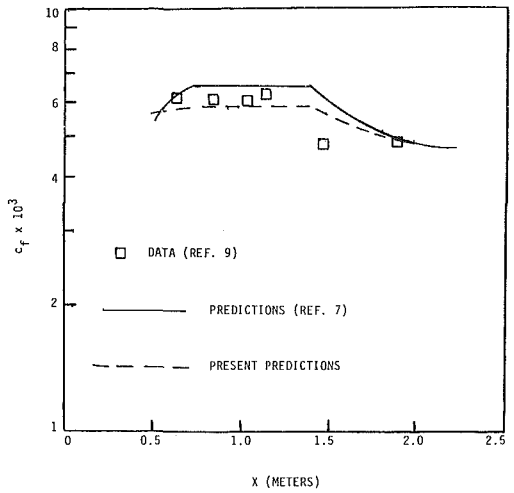

Fig. 5 Comparison of calculations to data of Coleman ($K_r = 0.29 \times 10^{-3}$)

Comparisons were also made to the rough-wall, favorable pressure gradient data of Coleman [9]. The surface roughness characteristics were identical to those of Healzer et al. [10]. Figures 4 and 5 present calculations for $K_r = D(0)/2u_e$ $du_e/dx = 0.15 \times 10^{-3}$ and 0.29×10^{-3}, respectively. Also shown are predictions from Taylor et al. [7]. An effective roughness height $k = 0.2D(0)$ was used.

Closing Remarks

A simple procedure was presented to include surface roughness effects in Head's momentum integral entrainment method. An equivalent sand-grain height correlation, suggested by Finson [8] from his discrete element approach to solving the boundary-layer equations, was employed. This correlation explicitly includes roughness height, spacing and geometric effects. Comparisons were shown for the rough-wall data sets of Coleman [9] and Healzer et al. [10]. In both cases good agreement was obtained.

Acknowledgments

This work was sponsored by the Naval Sea Systems Command General Hydrodynamics Research Program, administered by the David W. Taylor Naval Ship Research and Development Center under the Office of Naval Research Contract #N00014-81-C-0234. The author is grateful to Dr. C. von Kerczek of Science Applications International Corporation for his helpful suggestions.

References

1 Dvorak, F. A., "Calculation of Turbulent Boundary Layers on Rough Surfaces in Pressure Gradient," *AIAA Journal*, Vol. 7, No. 9, Sept. 1969, pp. 1752–1759.

2 Simpson, R. L., "A Generalized Correlation of Roughness Density Effects on the Turbulent Boundary Layer," *AIAA Journal*, Vol. 11, No. 2, Feb. 1973, pp. 242–244.

3 Dirling, R. B., Jr., "A Method for Computing Roughwall Heat Transfer Rates on Re-entry Nosetips," AIAA Paper No. 73-763, presented at the AIAA 8th Thermophysics Conference, Palm Springs, CA, 16–18 July 1973.

4 Finson, M. L., and Clarke, A. S., "The Effect of Surface Roughness Character on Turbulent Re-entry Heating," AIAA Paper No. 80-1459, 1980.

5 Lin, T. C. and Bywater, R. J., "Turbulence Models for High-Speed, Rough-wall Boundary Layers," *AIAA Journal*, Vol. 20, No. 3, Mar. 1982, pp. 325–333.

6 Christoph, G. H. and Pletcher, R. H., "Prediction fo Rough-Wall Skin Friction and Heat Transfer," *AIAA Journal*, Vol. 21, No. 4, Apr. 1983, pp. 509–515.

7 Taylor, R. P., Coleman, H. W., and Hodge, B. K., "A Discrete Element Prediction Approach for Turbulent Flow Over Rough Surfaces," Report TFD-84-1, Mississippi State University, Feb. 1984.

8 Finson, M. L., "A Model for Rough Wall Turbulent Heating and Skin-Friction," AIAA Paper No. 82-0199, presented at AIAA 20th Aerospace Sciences Meeting, Orlando, FL, 11-14 Jan. 1982.

9 Coleman, H. W., "Momentum and Energy Transport in the Accelerated Fully Rough Turbulent Boundary Layer," Stanford University Department of Mechanical Engineering Report HMT-24, 1976.

10 Healzer, J. M., Moffat, R. J., and Kays, W. M., "The Turbulent Boundary Layer on a Porous Rough Plate: Experimental Heat Transfer with Uniform Blowing," AIAA Paper No. 74-680 and ASME Paper No. 74-HT-14, presented at the AIAA/ASME 1974 Thermophysics and Heat Transfer Conference, Boston, MA, 15–17 July 1974.

11 Head, M. R., "Cambridge Work on Entrainment," *Proceedings Computation of Turbulent Boundary Layers*—1968 AFOSR-IFP-Stanford Conference, Stanford University Department of Mechanical Engineering, Stanford, CA.

Boundary Conditions for Flow Over Permeable Surfaces

G. J. Hokenson[1]

Introduction

The subject of this work is viscous flow adjacent to a permeable surface and the boundary conditions appropriate thereto [1]. Our objective is to generalize and extend the analysis in references [2 and 3] from first principles in order to clarify the relationship between the experimental reality of a distribution of discrete nonuniform jets in a crossflow and computations which employ continuous (locally uniform) normal velocity and zero slip boundary conditions. The hypothesis is that some details of the (vortical) flow passing through the boundary and the external (partially slipping [1]) flow along the boundary affect the qualitative structure of the solution.

The analysis presented here is an extension of the work described in reference [4] and is directed at continuum flow phenomena. Although, for most problems of practical importance, we are generally interested in turbulent flow, a laminar flow is considered here to expose the particulars of the premise. Some of the results, therefore, bear directly on current interest in laminar flow control by suction. The role which turbulent flow considerations play shall be discussed subsequently. Finally, the restriction that a boundary layer structure be maintained, forcing limitations on the mass transfer magnitude, shall not be invoked.

Background

Consider first the detailed picture of a porous wall as a distribution of discrete jets. (The case of blowing will be used for purposes of discussion.) By placing a "jump-type" control volume at the exit plane of an individual jet, the results of reference [4] indicate that the external flow "slips" over the jet (i.e., the mass transfer vector tilts) with a velocity determined by:

$$\delta(\rho uv) = \delta\tau, \tag{1}$$

where δ signifies the jump in values of the variables across the control volume. Conventional notation assigns ρ, u, v, and τ to the fluid density, streamwise velocity, normal velocity and shear stress, respectively. Invoking continuity:

$$\delta(\rho v) = 0, \tag{2}$$

[1]Chief Scientist, The Hokenson Company, Los Angeles, Calif., Mem. ASME.

Contributed by the Fluids Engineering Division of THE AMERICAN SOCIETY OF MECHANICAL ENGINEERS. Manuscript received by the Fluids Engineering Division, February 4, 1984.

across the control volume allows us to write equation (1) as:

$$\delta u = \delta\tau/\rho v. \tag{3}$$

This result shall now be generalized to an arbitrarily permeable surface for comparison to the aforementioned zero slip, (locally) constant normal velocity boundary condition theoretical formulation. For cases in which u and τ within the boundary are zero, equation (3) is compatible with the results in [1-3].

Development

Consider the flow along a porous surface composed of a distribution of openings which is specified statistically in terms of size and location. The external flow is assumed to be two-dimensional, however, extension of the results to include three-dimensional effects is straightforward and will be noted. A local averaging process is now invoked [3] in planes parallel to the boundary.[2] The spatial scales of the averaging are large relative to the porosity yet small relative to the streamwise (and span-wise) variations in the mean flow. Each of the variables is decomposed into its local spatial mean plus a perturbation (e.g., $u = \langle u\rangle + u^0$). When this decomposition is applied to the Navier-Stokes equations for constant density flow, the resulting equations may be spatially-averaged to provide the result:

$$\langle u\rangle_x + \langle v\rangle_y = 0 \tag{4}$$

$$\langle u\rangle_t + (\langle u\rangle^2)_x + (\langle u\rangle\langle v\rangle)_y = -\langle p\rangle_x/\rho - \langle u^{0^2}\rangle_x - \langle u^0 v^0\rangle_y + \nu\langle\omega\rangle_{(z)y} \tag{5}$$

$$\langle v\rangle_t + (\langle u\rangle\langle v\rangle)_x + (\langle v\rangle^2)_y = -\langle p\rangle_y/\rho - \langle v^{0^2}\rangle_y - \langle u^0 v^0\rangle_x - \nu\langle\omega\rangle_{(z)x}, \tag{6}$$

where subscripts denote differentiation and subscripts in parentheses denote a vector component.[3] Not surprisingly, this is reminiscent of Reynolds decomposition for turbulent flow. Additional terms required for three-dimensional mean flows are apparent. If we now apply the jump-type control volume to the permeable boundary over the averaging domain, the results analogous to reference [4] are:

$$\delta\langle v\rangle = 0 \tag{7}$$

$$\langle v\rangle\delta\langle u\rangle = -\delta\langle u^0 v^0\rangle + \nu\delta\langle\omega\rangle_{(z)} \tag{8}$$

$$\delta(\overset{\nearrow 0}{\langle v\rangle^2}) = -\delta\langle p\rangle/\rho - \delta\langle v^{02}\rangle. \tag{9}$$

In this representation, total mass flow through the permeable boundary and shear force on it are locally equivalent (over the averaging area) between the discrete and continuous representations. The average mass flux is reduced from that in the discrete jets by the ratio of open to total surface area. The average shear stress is reduced from that on the solid interstices by the ratio of solid surface area to total surface area. Some new features appear, however. Most importantly the average streamwise velocity at the boundary is nonzero and related to that in the boundary (allowing for the possibility of obliquely-oriented jets) by equation (8). The subtleties of such a situation (whether due to geometrical or flow-induced obliquity) regarding effects of internal normal stresses versus surface shear stresses and interpretation of experiment-theory comparisons with the appropriate boundary conditions is clarified by equation (8). This relationship also embodies information on the injected flow vorticity and structure.

Applying the same decomposition, averaging and jump-type boundary control volume analysis to the full equations in vorticity variables results in:

$$\langle v\rangle\delta\langle\omega\rangle_{(z)} = -\delta\langle v^0\omega^0{}_{(z)} - w^0\omega^0{}_{(y)}\rangle + \nu\delta\langle\omega\rangle_{(z)y}, \quad \text{and} \tag{10}$$

$$\delta\langle v^0\omega^0{}_{(x)}\rangle = \delta\langle u^0\omega^0{}_{(y)}\rangle, \tag{11}$$

which provides often-needed information on flow curvature at the wall.

Discussion

Therefore, we have established a relationship between the discrete distribution of jets in experiments and the continuous mass flux/shear stress distributions in computational predictions, as long as $\langle u\rangle \neq 0$ at the boundary. If $\langle u\rangle$ is set equal to zero at the boundary, calibration of some aspects of the theoretical formulation with experimental data must compensate for the approximation. It may be that the magnitude of the slip is small, inherently or due to term cancellation in equation (8). However, the structure of the injected flow does now enter the problem. Possibly, the appropriate slip velocity (guided by equation (1)) may be obtained empirically by judicious iteration between observation and theory.

However, the formulation suggests several more systematic approaches. First, since jet structures may be reasonably parameterized, the situation is much simpler than turbulence in representing the nonlinear terms. Therefore, a quantitative assessment of the effect of differences in detailed structure between porous boundaries which are equivalent in the mean is possible. Secondly, it suggests that applying computational boundary conditions at some height off the wall for which $\langle u^0 v^0\rangle \simeq 0$, analogous to the flow over a wall film, may be more appropriate.

Consider these two uses of equation (8). Across the boundary, $\delta\langle u\rangle$ may be computed if we know something of the injected flow structure. It is clear that, over the openings u^0 and $v^0 > 0$ and over the solid portion u^0 and $v^0 < 0$. Therefore, $\langle u^0 v^0\rangle$ is a positive number. Given $\langle v\rangle$, $\langle u\rangle$ at the wall may be computed (as a function of $\langle\omega\rangle$ at the wall, as required computationally) by specifying typical detailed distributions of u^0 and v^0 of interest within the porous boundary, computing their jump across the boundary according to equation (1) and then averaging. The procedure is necessarily iterative, requiring an initial guess of the slip velocity.

Furthermore, assuming that the height above the boundary at which $\langle u^0 v^0\rangle \simeq 0$ is small, the jump expressions may be applied (to some lesser degree of accuracy) between it and the wall boundary. Note that the jump across the boundary must first be computed. In this manner the equations are used to provide the boundary conditions ($\langle v\rangle$ and $\langle u\rangle$) for computations at that level where the discrete jets have mixed out. This is reminiscent of using wall functions and, indeed, some profile hypothesis is required to do this accurately. If explicit account of the injected turbulence is of interest, the turbulence kinetic energy and length scale at the displaced height could be computed from model equations utilizing the jump-type control volume analysis. This is relevant to the comment in reference [5] in which the authors refer to blowing as "provoking the viscous sub-layer." Utilizing the approach developed here, the extent to which the injected flow structure totally disrupts the near wall conditions may be assessed.

Consider the two-equation k-ϵ model as an example only, not necessarily proposed here as a general computational tool for these flows. In this preliminary evaluation, we assume that the low Reynolds number postulates, relative to the near

[2] Note that the averaging weighting function was chosen to be a constant over the averaging domain and zero outside of it. In this manner Reynolds averaging rules are retained and the so-called Leonard terms do not appear.

[3] This formulation also significantly clarifies the effect of mass transfer on the wall vorticity flux. If $\langle u\rangle$ is nonzero (due to active vectoring or naturally with nominally normal injection), $\langle\omega\rangle_{(z)y}$ responds to the four advective terms in equation (5) even in constant pressure flows. If $\langle u\rangle$ is also nonsteady, the $\langle u\rangle_t$ term also modifies the vorticity flux at the wall.

wall region of the flow over an impermeable boundary [6, 7], are inappropriate here and the relevant form of the equations is that for which molecular effects are ignorable. By applying the jump conditions across the layer, δy, in which the jets "mix out," the following expressions for the turbulence kinetic energy and isotropic dissipation ensue:

$$\rho v \delta k = \delta q_k + \{P_k - D_k\}\delta y, \quad \text{and} \tag{12}$$

$$\rho v \delta \epsilon = \delta q_\epsilon + \{P_\epsilon - D_\epsilon\}\delta y, \tag{13}$$

where $\{\ \}$ indicates the vertical spatial average across the δy layer and the diffusive fluxes (q), production (P) and dissipation (D) are:

$$\begin{aligned} q_k &= (\mu_t/\sigma_k)\,\partial k/\partial y\,, & q_\epsilon &= (\mu_t/\sigma_\epsilon)\,\partial \epsilon/\partial y \\ P_k &= \mu_t (\partial u/\partial y)^2\,, & P_\epsilon/\epsilon &= C_1 \times P_k/k \\ D_k &= \epsilon\,, & D_\epsilon/\epsilon &= C_2 \times D_k/k \end{aligned} \tag{14}$$

Utilizing expressions or values for μ_t ($C_\mu \rho k^2/\epsilon$), σ_k, σ_ϵ, C_1, and C_2, the magnitudes of k and ϵ at δy may be computed in terms of k and ϵ injected through the boundary and the near wall profiles. Therefore, the formalism by which the external flow responds to the strucutre of the injected flow, which was observed earlier for nonturbulent vortical details, carries over to turbulence as well.

Note that, for flows with streamwise pressure gradients, injection of material which undergoes a phase change at the boundary complicates the discussion of injected vortical structure due to the $\nabla\langle p\rangle \times \nabla\langle \rho\rangle^{-1}$ vorticity generation effect. In addition, dilatation effects may be important if either phase is compressible. Finally, for integral formulation, the standard mass transfer term is modified to: $(1 - \langle u\rangle_w/u_e)$ $(\langle v\rangle_w/u_e)$ and $\langle u^0 v^0\rangle$ and the Reynolds stresses (if the flow is turbulent) at the wall are included. Utilizing such a formulation, the effects of slip/vectoring and the peculiarities of various walls on $\langle u^0 v^0\rangle$ may be examined with data such as that in reference [8].

Acknowledgment

This work was carried out under the sponsorship of the Aerospace Sciences Directorate, AFOSR and the Office of Basic Energy Sciences, Department of Energy.

References

1 Beavers, G. S., and Joseph, D. D., "Boundary Conditions at a Naturally Permeable Wall," *JFM*, 1967, Vol. 30, Part 1, pp. 197–207.

2 Taylor, G. I., "A Model for the Boundary Condition of a Porous Material," Part 1, *JFM*, 1971, Vol. 49, Part 2, pp. 319–336.

3 Saffman, P. G., "On the Boundary Condition at the Surface of a Porous Medium," *Studies in Applied Mathematics*, Vol. 1, No. 2, June 1971, pp. 93–101.

4 Hokenson, G. J., "Boundary Conditions with Heat/Mass Transfer and Velocity Slip," *AIAA Journal*, Vol. 15, No. 3, March 1977, pp. 438–439.

5 Kutateladze, S. S., and Leont'ev, A. I., *Boundary Layers in Compressible Gases*, tranlated by D. B. Spalding, Academic Press, New York, 1964.

6 Jones, W. P., and Launder, B. E., "The Prediction of Laminarization with a Two-Equation Model of Turbulence," *International Journal of Heat and Mass Transfer*, Pergamon Press, London, England, Vol. 15, 1972, pp. 301–314.

7 Chien, K.-Y., "Predictions of Channel and Boundary-Layer Flows with a Low-Reynolds-Number Turbulence Model," *AIAA Journal*, Vol. 20, No. 1, Jan. 1982, pp. 33–38.

8 Collier, Jr., F. S., and Schetz, J. A., "Injection into a Turbulent Boundary Layer Through Different Porous Surfaces," *AIAA Journal*, Vol. 22, No. 6, June 1984, pp. 839–841.